UNIVERSITY OF CALIFORNIA,
IRVINE

Targeting endolysosomal trafficking with synthetic sphingolipid analogs to improve the delivery of oligonucleotide therapeutics

DISSERTATION

submitted in partial satisfaction of the requirements
for the degree of

DOCTOR OF PHILOSOPHY

in Biological Sciences

by

Brendan Tyler Finicle

Dissertation Committee:
Professor Aimee L. Edinger, Chair
Professor David A. Fruman
Associate Professor Claudia A. Benavente
Associate Professor Wenqi Wang

2023

TABLE OF CONTENTS

LIST OF FIGURES

LIST OF TABLES

ACKNOWLEDGEMENTS

First and foremost, I would like to thank my mentor Dr. Aimee Edinger. I came to Aimee's lab having no background in research. I've learned everything about science from Aimee, and I could not consider myself any luckier. Aimee is a true mentor and leader in science. Her electric enthusiasm is contagious and was the reason I stayed in science and pursued a PhD. Her grit for proceeding through the tough times combined with her ingenuity is inspiring and has kept me going when research felt hopeless. I hope to keep Aimee as a life-long mentor and friend.

I would also like to thank my committee members Dr. David Fruman, Dr. Claudia Benavente, and Dr. Wenqi Wang. I am grateful to these scientists for their technical expertise and their commitment to my growth as a scientist. I also thank Punit Seth for his technical expertise and valuable connections to reagents and collaborators.

I am very thankful to all the past and current members of the Edinger Lab. In my early days in the lab, it was the commitment to teamwork and excitement for the science that inspired long hours and made them bearable. I thank Manuel "Mannie" Ramirez for being a generous and encouraging teacher. A big thank you to Alison McCracken, Seong Kim, Tricia Nguyen, Vaishali Jayashankar, and Kazumi Eckenstein for making the lab environment so special. I am grateful to the great people of the Edinger lab that have made this experience special. Another big thank you to Rebecca Kattan of the Wang lab, who has been a good friend to me throughout this PhD.

Financial support was provided under the National Cancer Institute of the National Institutes of Health award numbers NCI T32 CA009054, F31 CA261085, and F99 CA264430. I would also like to acknowledge the support of the Chao Family Comprehensive Cancer Center Optical Biology Center shared resource, supported by the National Cancer Institute of the National Institutes of Health under award number P30 CA062203. The content of this thesis is solely the responsibility of the authors and does not necessarily represent the official views of the NIH.

The text of Chapter 1 is a reprint of the material as it appears in *J Cell Sci.* 2018. 131(12). pii: jcs213314., used with permission from The Company of Biologists. The co-authors listed in this publication are Manuel U. Ramirez, Gang Liu, Elizabeth M. Selwan, Alison N. McCracken, Jingwen Yu, Yoosun Joo, Jannett Nguyen, Kevin Ou, Saurabh G. Roy, Victor D. Mendoza, Dania Virginia Corrales, Aimee L. Edinger. Link to the article: https://doi.org/10.1242/jcs.213314.

The text of Chapter 2 is a reprint of the material as it appears in *Mol Cell Proteomics. 2019 Mar;18(3):408-422.*, used with permission from American Society for Biochemistry and Molecular Biology. The co-authors listed in this publication are Peter Kubiniok, Fanny Piffaretti, Alison N. McCracken, Michael Perryman, Stephen Hanessian, Aimee L. Edinger, and Pierre Thibault. Link to the article: https://doi.org/10.1074/mcp.RA118.001053.

The text of Chapter 3 is a reprint of the material that has been accepted for publication in *Nucleic Acids Research*, used with permission from Oxford University Press. The co-authors listed in this publication are Kazumi H. Eckenstein, Alexey S. Revenko, Brooke A. Anderson, W. Brad Wan, Alison N. McCracken, Daniel Gil, David A. Fruman, Stephen Hanessian, Punit P. Seth, and Aimee L. Edinger.

Finally, but most importantly, I want to thank my friends, family, and partner for being my rock and always supporting me. I could not have done this without all of you. Thank you for understanding my long work hours and providing me with a safe space to be my true self.

VITA

Brendan Tyler Finicle

EDUCATION

2017 – 2023	University of California, Irvine School of Biological Sciences	PhD	Cellular & Molecular Biology Cumulative GPA: 4.0
2012 - 2016	University of California, Irvine School of Biological Sciences	B.S. (with Honors)	Developmental & Cell Biology Cumulative GPA: 3.9

RESEARCH EXPERIENCE

2017 - 2023 **PhD student**, University of California, Irvine, Edinger Lab

- Characterized small molecules that improve delivery of oligonucleotides (ASOs and siRNAs) to extrahepatic tissues by disrupting intracellular trafficking, leading to a first-author manuscript in review and a US patent
- Characterized the endocytosis and subsequent vesicular trafficking of nutrient transporter proteins and other cell surface receptors in response to sphingolipids, leading to a co-first author manuscript
- Characterized novel small molecules that block coronavirus cell entry by disrupting endolysosomal trafficking, leading to a manuscript in final stages of preparation and a US patent application covering this technology
- Collaborated with protein chemistry experts to characterize phosphorylation changes caused by sphingolipids through a kinetic phospho-proteome screen, leading to a co-first author manuscript
- Collaborated with medicinal chemists on structure-activity relationship studies to facilitate medicinal chemistry optimization of sphingolipid-based small molecules, leading to multiple co-author publications

2016 - 2017 **Lab Technician & Lab Manager**, University of California, Irvine, Edinger Lab

- Applied cutting-edge quantitative microscopy techniques to assess endocytosis and GTPase activity in cells

2014 - 2016 **Undergraduate Researcher**, University of California, Irvine, Edinger Lab

- Extensively characterized intracellular trafficking of nutrient transporters using fluorescence microscopy

MANUSCRIPTS UNDER PEER REVIEW, SUBMITTED, OR IN LATE-STAGE PREPARATION

1. Jayashankar V*, Kubiniok P*, McCracken AN*, Eckenstein KH, Sernissi L, Vece V, Garsi JB, **Finicle BT**, Fruman DA, Jung S, Pitman M, Lin D, Kaiser P, Mobley D, Jang C, Hanessian S#, Thibault P#, Edinger AL#. (Paper title obscured for confidentiality). **Submitted.** (*Co-first authors, #co-corresponding authors)

2. **Finicle BT**, Vu W, Edinger AL. Sphingosine analog SH-BC-893 inhibits endosomal entry of multiple coronavirus strains in vitro and in vivo. **In preparation.**

PUBLICATIONS

1. **Finicle BT**, Eckenstein KH, Revenko AS, Anderson BA, Wan WB, McCracken AN, Gil D, Hanessian S, Seth PS, Edinger AL. Simultaneous inhibition of endocytic recycling and lysosomal fusion sensitizes cells and tissues to oligonucleotide therapeutics. ***Nucleic Acids Research*.** Accepted for publication.
2. Bachollet SPJT, Vece V, McCracken AN, **Finicle BT**, Selwan E, Romdhane NB, Dahal A, Ramirez C, Edinger AL, Hanessian S. Synthetic Sphingolipids With 1,2-Pyridazine Appendages Improve Antiproliferative Activity in Human Cancer Cell Lines. ***ACS Med Chem Lett.*** 2020. 11(5):686-690.
3. Garsi JB, Vece V, Sernissi L, Auger-Morin C, Hanessian S, McCracken AN, Selwan E, Ramirez C, Dahal A, Rhomdhane NB, **Finicle BT**, Edinger AL. Design, synthesis and anticancer activity of constrained sphingolipid-phenoxazine/phenothiazine hybrid constructs targeting protein phosphatase 2A. ***Bioorg Med Chem Lett.*** 2019. 29(18):2681-2685.
4. Kubiniok P*, **Finicle BT***, Piffaretti F, McCracken AN, Perryman M, Hanessian S, Edinger AL#, Thibault P#. Dynamic Phosphoproteomics Uncovers Signaling Pathways Modulated by Anti-oncogenic Sphingolipid Analogs. ***Mol Cell Proteomics.*** 2019. 18(3):408-422. (*Co-first authors, #co-corresponding authors)
5. **Finicle BT**, Jayashankar V, Edinger AL. Nutrient scavenging in cancer. ***Nat Rev Cancer.*** 2018. 18(10):619-633.
6. Jayashankar V, **Finicle BT**, Edinger AL. Starving PTEN-deficient prostate cancer cells thrive under nutrient stress by scavenging corpses for their supper. ***Mol Cell Oncol.*** 2018. 5(4):e1472060.
7. Kim SM*, Nguyen TT*, Ravi A*, Kubiniok P, **Finicle BT**, Jayashankar V, Malacrida L, Hou J, Robertson J, Gao D, Chernoff J, Digman MA, Potma EO, Tromberg BJ, Thibault P, Edinger AL. PTEN Deficiency and AMPK Activation Promote Nutrient Scavenging and Anabolism in Prostate Cancer Cells. ***Cancer Discov.*** 2018. 8(7):866-883. (*Co-first authors)
8. **Finicle BT***, Ramirez MU*, Liu G, Selwan EM, McCracken AN, Yu J, Joo Y, Nguyen J, Ou K, Roy SG, Mendoza VD, Corrales DV, Edinger AL. Sphingolipids inhibit endosomal recycling of nutrient transporters by inactivating ARF6. ***J Cell Sci.*** 2018. 131(12). pii: jcs213314. (*Co-first authors)
9. Kim SM, Roy SG, Chen B, Nguyen TM, McMonigle RJ, McCracken AN, Zhang Y, Kofuji S, Hou J, Selwan E, **Finicle BT**, Nguyen TT, Ravi A, Ramirez MU, Wiher T, Guenther GG, Kono M, Sasaki AT, Weisman LS, Potma EO, Tromberg BJ, Edwards RA, Hanessian S, Edinger AL. Targeting cancer metabolism by simultaneously disrupting parallel nutrient access pathways. ***J Clin Invest.*** 2016. 126(11):4088-4102.
10. Selwan EM, **Finicle BT**, Kim SM, Edinger AL. Attacking the supply wagons to starve cancer cells to death. ***FEBS Lett***. 2016. 590(7):885-907.

PATENTS

1. Edinger AL, Hanessian S, Tanowitz M, Seth PS, and **Finicle BT**. WO2022094615 - COMPOUNDS AND METHODS FOR INCREASED ANTISENSE ACTIVITY. International Application No. PCT/US2021/072140
2. Edinger AL, and **Finicle BT**. WO2022133494 - ANTIVIRAL COMPOUNDS AND APPLICATIONS THEREOF. International Application No. PCT/US2021/073013

TEACHING & PROFESSIONAL EXPERIENCE

2017 - 2023 **Laboratory Safety Officer** in the Edinger lab, UC Irvine

- In this role, I write SOPs for using chemical or biological agents and operating lab equipment & communicate with Environmental Health & Safety (EH&S) to implement and educate safety standards to the entire lab.

2018, 2019 **Teaching Assistant** to Honors Introduction to Biology (Bio93H) course at UCI

- In this role, I led class discussions, designed exam questions and active learning coursework, & independently led two lectures when professor was out of town.

HONORS & AWARDS

2022 Howard Schneiderman Fund award

- This award is the biggest award offered to UCI PhD students for excellence in research, providing $10,000.

2021 - 2023 NCI Predoctoral to Postdoctoral Fellow Transition Awardee (F99/K00), 1F99 CA264430

- The first nominee from UCI to ever receive this award, this fellowship supports completion of PhD research ($83,216 over two years) and up to 4 years of postdoctoral studies (up to $369,843 over four years).

2021 - 2022 ARCS Foundation Scholar

- This award is intended to recognize and reward “academically superior doctoral students exhibiting outstanding promise as scientists, researchers, and leaders.” Provided $10,000.

2021 Selection for Lindau Nobel Laureate Meeting

- After being nominated by the UC system, I was then selected by the Council for the Lindau Nobel Laureate Meetings to be one of 600 scientists around the world to attend this meeting.

2021 - 2022 NCI Ruth L. Kirschstein National Research Service Award (NRSA) (F31), 1F31 CA261085

- This award supports PhD candidates in a scientific health-related field relevant to the mission of the NCI.

2020 - 2021 NCI T32 Cancer Biology & Therapeutics Trainee, T32 CA009054-40

- Fellowship funding to gain additional training in both the basic biology of cancer and translational and/or clinical cancer research; grant terminated in 2021 to accept the F31 award.

2019 **Joseph H. Stephens Memorial Fellowship Award**
- This award is for "displaying excellence in the field of biochemistry and molecular biology" & provided $1,000

2017 **Francisco J. Ayala Graduate Fellowship**
- This award is for "recruitment and recognition of academically superior doctoral students exhibiting outstanding promise as scientists, researchers, and public leaders," providing $10,000.

2017 **UC Irvine Graduate Dean's Recruitment Fellowship**
- This award is to recruit "exceptional students admitted into doctoral programs at UC Irvine," providing $5,000

2016 **Laurence J. Mehlman Memorial Scholar**
- This award is for "demonstrating achievement in both scholarship and service to the school, extraordinary character and integrity, and esteemed by peers for ethical and moral strength," providing $1,000.

2016 **Dean's Award for Excellence in Research**
- This award is for "an outstanding project presented and defended at UCI's excellence in research program"

2016 **Chancellor's Award for Excellence in Undergraduate Research**
- This award is given to a student for "outstanding research accomplishments"

2016 **Phi Beta Kappa**
- Prestigious honors society for excellence in the liberal arts and sciences

SELECT EXTERNAL PRESENTATIONS

- *Ionis Pharmaceuticals.* Carlsbad, CA. "Increasing antisense oligonucleotide activity in tumors by targeting endocytic trafficking." 2017.
- *Ionis Pharmaceuticals*. Carlsbad, CA. "Increasing antisense oligonucleotide delivery." 2018.
- *Ionis Pharmaceuticals.* Carlsbad, CA. "Using small molecules to boost antisense activity in tumors." 2019.
- *Cancer Biology & Therapeutics group retreat joint with UC Davis & UC Irvine.* Los Angeles, CA. "Using small molecules to boost antisense activity in tumors." 2019.
- *Interdisciplinary Cancer Research group retreat joint with UCSD, Salk Institute, & UCI.* La Jolla, CA. "Breaking the delivery barrier for oligonucleotide therapeutics by targeting endolysosomal trafficking." 2022.

SELECT EXTERNAL POSTER PRESENTATIONS

- *RNA at the Bench and Bedside III, Nature conferences.* San Diego, CA. Simultaneous inhibition of endocytic recycling and lysosomal fusion sensitizes cells and tissues to oligonucleotide therapeutics. 2022.
- *18th Annual Oligonucleotide Therapeutics Society Conference*. Phoenix, CA. Simultaneous inhibition of endocytic recycling and lysosomal fusion sensitizes cells and tissues to oligonucleotide therapeutics. 2022.
- *UC, Drug Discovery Consortium (UCDDC) Conference.* Irvine, CA. “A drug-like sphingolipid breaks the delivery barrier for antisense oligonucleotides by disrupting endolysosomal trafficking.” 2021.

ABSTRACT OF THE DISSERTATION

Targeting endolysosomal trafficking with synthetic sphingolipid analogs to improve the delivery of oligonucleotide therapeutics

By

Brendan Tyler Finicle

Doctor of Philosophy in Biological Sciences

University of California, Irvine, 2023

Professor Aimee L. Edinger, Chair

Endolysosomal trafficking determines the ultimate destination of molecules that enter cells and therefore has great impact on multiple cellular processes. Our lab has established that bioactive lipids called sphingolipids can rewire endolysosomal trafficking to result in accumulation of endocytosed material in pre-lysosomal compartments. In this thesis research, the impact of disrupted endolysosomal trafficking caused by sphingolipids on the activity of oligonucleotide therapeutics will be discussed. Therapeutic oligonucleotides include large RNA molecules such as mRNA vaccines and those that target RNA such as single-stranded antisense oligonucleotides (ASOs) or the double-stranded small interfering RNAs (siRNAs). ASOs base pair with a target RNA to elicit RNaseH-dependent degradation, inhibition of translation, or changes to splicing. siRNAs can produce prolonged target RNA silencing after being loaded into Ago2 to form the RNA-induced silencing complex (RISC). Given that all of these oligonucleotide therapeutic platforms require cytoplasmic entry for activity, inefficient endosomal escape remains the primary barrier to the broad application of oligonucleotide therapeutics. Liver uptake after systemic administration is sufficiently robust that a therapeutic effect can be achieved but targeting extrahepatic tissues remains challenging. Prior attempts to improve oligonucleotide

activity using small molecules that increase the leakiness of endosomes have failed due to unacceptable toxicity. This thesis will discuss the development and characterization of a well-tolerated and orally bioavailable synthetic sphingolipid analog called SH-BC-893 that increases the activity of antisense oligonucleotides (ASOs) and small interfering RNAs (siRNAs) up to 200-fold in vitro without permeabilizing endosomes. SH-BC-893 treatment trapped endocytosed oligonucleotides within extra-lysosomal compartments thought to be more permeable due to frequent membrane fission and fusion events. Simultaneous disruption of ARF6-dependent endocytic recycling and PIKfyve-dependent lysosomal fusion was necessary and sufficient for SH-BC-893 to increase non-lysosomal oligonucleotide levels and enhance activity. In mice, oral administration of SH-BC-893 increased ASO potency in the liver by 15-fold. More importantly, SH-BC-893 enabled target RNA knockdown in the CNS and lungs of mice treated subcutaneously with cholesterol-functionalized duplexed oligonucleotides or unmodified ASOs, respectively. Together, these results establish the feasibility of using a small molecule that disrupts multiple endolysosomal trafficking steps to improve the activity of oligonucleotide therapeutics in extrahepatic tissues.

INTRODUCTION

Oligonucleotide therapeutics: a modular platform to treat any disease

Oligonucleotides targeting RNA include antisense oligonucleotides (ASOs) and small interfering RNAs (siRNAs). ASOs are single-stranded oligonucleotides that base pair with a target RNA and depending how they are designed can elicit RNaseH-dependent degradation, inhibition of translation, or changes to splicing (Roberts et al., 2020; Shen and Corey, 2018). siRNAs are double-stranded duplexed RNAs that degrade target RNAs after being loaded into Ago2 to form the RNA-induced silencing complex (RISC). Because they can alter expression of any RNA, oligonucleotide therapeutics have the potential to revolutionize medicine.

Historical problems with stability and rapid clearance have plagued the initial success of these platform therapeutics. Not only are unmodified and unformulated nucleic acids quickly broken down by endogenous nucleases present in circulation, but they also have minimal plasma protein binding and are therefore quickly removed by the kidneys and excreted in the urine (Bennett and Swayze, 2010; Geary et al., 2015). In addition, unmodified oligonucleotides lack sufficient affinity for the target RNA to successfully compete against the secondary structures present in target RNAs. Over the past 20-30 years, key advances in medicinal chemistry have solved these critical problems. For example, converting the native phosphodiester (PO) backbone into a phosphorothioate (PS) backbone dramatically improves the resistance to nucleases and protein binding, facilitating uptake into cells and limiting excretion (Bailey et al., 2017; Brown et al., 1994; Crooke et al., 2017; Liang et al., 2015; Stein et al., 1988). Sugar modifications have not only led to further increased nuclease resistance but have also improved affinity for target RNAs. Examples of successful sugar modifications include the conversion of the 2'-H (in DNA) or -OH (in RNA) into a 2'-O-methoxyethyl group (2'MOE) (Altmann et al., 1996; Geary et al., 2001; Teplova et al., 1999) or the locking of the 2' and 4' positions of the

ribose ring into a C_3-endo conformation with a (S)-constrained ethyl group (cEt) (Pallan et al., 2012; Seth et al., 2008, 2010). Exemplifying the success of these medicinal chemistry programs, today there are at least thirteen therapeutic oligonucleotides that have been FDA-approved with hundreds in preclinical development (Hong et al., 2015; Odate et al., 2017; Raal et al., 2010; Ross et al., 2017; De Velasco et al., 2019; Yamamoto et al., 2015).

The success of many therapeutic oligonucleotides is due to the ability to target the liver. The primary route of administration for oligonucleotides is intravenous (IV) infusion or subcutaneous injection (Geary et al., 2015). Following systemic administration, PS-ASOs quickly transfer from the injection site to blood, achieving peak plasma concentrations within 3-4 h with near complete absorption into tissues immediately following. Following the areas with the most direct blood flow, ASOs accumulate mostly in the liver and kidney after systemic administration. Additionally, ASOs and siRNAs do not cross the blood brain barrier. Therefore, the FDA-approved ASOs and siRNAs developed for targets expressed in the central nervous system (CNS) must be dosed via intrathecal injection.

Although ASOs accumulate to high degrees in the liver, the major cell types that are sensitive are Kupffer cells and endothelial cells rather than hepatocytes (Graham et al., 1998, 2001). In order to target hepatocytes, ASOs and siRNAs are conjugated to the sugar group N-acetyl galactosamine (GalNAc) which targets the oligonucleotides to the asialoglycoprotein receptor (ASGPR) expressed in hepatocytes (Wang et al., 2019). The invention of the GalNAc conjugates has revolutionized the therapeutic development of hepatocyte-targeted ASOs and siRNAs, producing many FDA-approved oligonucleotides along with >dozens in late-stage clinical development.

Delivery barriers for oligonucleotide therapeutics

While liver and CNS-targeted ASOs and siRNAs have had success, other extrahepatic tissues remain elusive. This is due to the delivery of oligonucleotides being incredibly inefficient, with only 1% of the oligonucleotide that is delivered to patients engaging its target. As a result, high concentrations are required in target tissues, levels that are readily achieved in the liver after subcutaneous administration. Extrahepatic tissues generally require local (e.g. intrathecal or aerosol) delivery or frequent administration of high doses to achieve significant target engagement (Gökirmak et al., 2021). Conjugation to ligands that bind to cell surface receptors can increase oligonucleotide activity by increasing cellular uptake (Gökirmak et al., 2021; Seth et al., 2019; Tanowitz et al., 2017). However, targeted delivery is not available for all target tissues and does not overcome the constraints that inefficient endosomal release places on oligonucleotide activity. Therefore, inefficient delivery to targets in the cytosol and nucleus of cells remains a major barrier to the broader application of oligonucleotide therapeutics (Corey et al., 2022; Dowdy, 2017; Gökirmak et al., 2021; Roberts et al., 2020). New approaches that address post-endocytic blocks to delivery could extend the range of tissues and cells that are accessible to systemically delivered oligonucleotide therapeutics even in the absence of a ligand-receptor targeting strategy. Lowering the required dose would also reduce sequence-independent toxicities and the high cost of goods that limits the accessibility of oligonucleotide therapies to patients.

As large (4-14 kDa) polar molecules, ASOs and siRNAs do not readily diffuse across lipid bilayers; both receptor-targeted and unconjugated oligonucleotides enter cells via endocytosis (Dowdy, 2017; Gökirmak et al., 2021). Oligonucleotide-containing endocytic vesicles are sorted between pathways that recycle material back to the extracellular space through exocytosis or that end in the lysosome, the degradative compartment of the cell (Crooke et al., 2017; Gökirmak et al., 2021; Grant and Donaldson, 2009). Chemical modifications render therapeutic

oligonucleotides resistant to lysosomal nucleases (Dowdy, 2017; Gökirmak et al., 2021; Roberts et al., 2020). Therefore, the majority of endocytosed oligonucleotides accumulate within lysosomes where they are stable but unable to reach their cytosolic targets, although recent evidence suggests slow leakage from lysosomes supports long-term oligonucleotide activity in the liver (Brown et al., 2020).

Many groups have attempted to improve the release of oligonucleotides from endosomes and lysosomes without clinical success. High throughput, small molecule screens have identified several compounds that increase the activity of splice-switching oligonucleotides (SSOs). For example, the GSK3 inhibitor 6BIO increases SSO activity by ~2-3-fold in vitro through an unknown mechanism (Zhang et al., 2017). Another molecule called Retro-1 that is known to block retrograde endosomal trafficking increases SSO activity in vitro by ~10-fold and in xenograft tumors by almost 2-fold (Ming et al., 2013). The most promising small molecule, UNC10217938A, increases SSO activity by up to 60-fold in vitro but only ~3-fold in vivo (Yang et al., 2015). However, UNC10217938A is highly toxic and cells can only tolerate exposure for 2 h before dying. This toxicity is due to this molecule's mechanism of action: permeabilizing endosomes and lysosomes to release oligonucleotides into the cytoplasm. Endosome permeabilization is cytotoxic due to the release of many hydrolytic enzymes contained within endolysosomes into the cytoplasmic space. It is also important to note that all of these studies measured oligonucleotide activity using a splice switching oligonucleotide (SSO). This SSO activity assay uses a GFP reporter that contains a splice-defective intron and a SSO that corrects the splicing deficit to produce fluorescence (Sazani et al., 2002). By going from zero to any positive signal, these assays produce a large-fold change in reporter signal and therefore overestimate ASO activity. Therefore, it is not clear that the fold-changes observed with Retro-1 or UNC10217938A will translate into clinically meaningful levels of splicing. Because the targets of these published molecules are unknown, optimization is challenging. Molecules that increase

the leakiness of endosomes produce large increases in oligonucleotide activity but have a narrow therapeutic index due to toxicities associated with endosome and lysosome permeabilization (Gilleron et al., 2015; Juliano, 2021; Kendall et al., 2012; Ming et al., 2013; Osborn et al., 2015; Yang et al., 2015; Zhang et al., 2017). Therefore, novel approaches that improve oligonucleotide escape into the cytosol without lysing endocytic compartments are required to solve the delivery problem that limits the therapeutic use of oligonucleotides.

Traditional strategies to deliver ASOs to cells such as packaging into nanoparticles or coupling to cell-penetrating peptides are prohibitively toxic and mainly increase activity in the liver, an organ that is already sensitive to ASOs (Juliano, 2016; Seth et al., 2019). No proteins have been identified that could be targeted to enhance ASO delivery; genetic knockdown screens directed against proteins involved in endolysosomal trafficking did not yield viable hits (Linnane et al., 2019; Wagenaar et al., 2015). Similarly, mass spectrometry studies cataloging the proteins that directly bind ASO molecules have failed to identify targetable proteins (Bailey et al., 2017; Crooke et al., 2017; Liang et al., 2015). Defining the specific molecular pathways that control ASO uptake and release could open new therapeutic avenues. Despite decades of study, these pathways remain poorly defined.

A logical model for oligonucleotide escape from endocytic compartments is that it occurs at sites of membrane fission and fusion (Juliano, 2018; Wagenaar et al., 2015; Wang et al., 2017; Wittrup et al., 2015). During these dynamic membrane remodeling events, the lipid bilayer is deformed to create non-bilayer regions that have increased permeability (Bennett and Tieleman, 2014; Cullis et al., 1986; Renard et al., 2018; Wang et al., 2009; Wickner and Rizo, 2017). Consistent with this model, pre-lysosomal compartments that undergo high rates of vesicle budding and fusion have been identified as sites of oligonucleotide escape (Liang et al., 2020; Linnane et al., 2019; Paramasivam et al., 2022; Wang et al., 2016). Escape from lysosomes is

much less efficient because the limiting membrane is heavily decorated with glycoproteins (e.g., LAMP1 and LAMP2) and glycolipids that reduce permeability relative to other endocytic structures (Rudnik and Damme, 2021; Wilke et al., 2012). While this lysosomal glycocalyx helps to prevent hydrolytic enzymes in the lysosome from leaking into the cytoplasm, it also contributes to inefficient endosomal escape. Therefore, approaches that increase oligonucleotide uptake and/or residency time in pre-lysosomal compartments where oligonucleotide escape is most efficient could offer significant gains in potency that would make extrahepatic tissues therapeutically accessible.

Introduction to the pathways and mechanisms of endolysosomal trafficking.

Evolution has selected for the endomembrane system, which selectively controls what material can pass through membranes and/or enter cells via the process known as endocytosis. Endocytosis encapsulates extracellular material within a vesicle made from the plasma membrane of cells and occurs by many distinct mechanisms (Donaldson et al., 2009; Ferreira and Boucrot, 2018; Mayor and Pagano, 2007). Some pathways require the protein clathrin to shape and coat the resulting vesicles (Figure 0.1). Other endocytic processes are known as clathrin-independent and include pathways such as fast endophilin-mediated endocytosis (FEME), macropinocytosis, and phagocytosis. However, regardless of the mode of entry, most endocytosed cargo is delivered to the early endosome, where sorting to final destinations occurs. Cargo can be routed from early endosomes to the late endosomes characterized by multivesicular bodies and eventually to the lysosome for degradation. Other cargo could be destined for a process called endocytic recycling (Cullen and Steinberg, 2018; Donaldson et al., 2009; Grant and Donaldson, 2009; Maxfield and McGraw, 2004). Endocytic recycling involves the delivery of endosomal vesicles back to the plasma membrane to return cell surface proteins

and lipids to the plasma membrane and expel internalized material to the extracellular space (Figure 0.1).

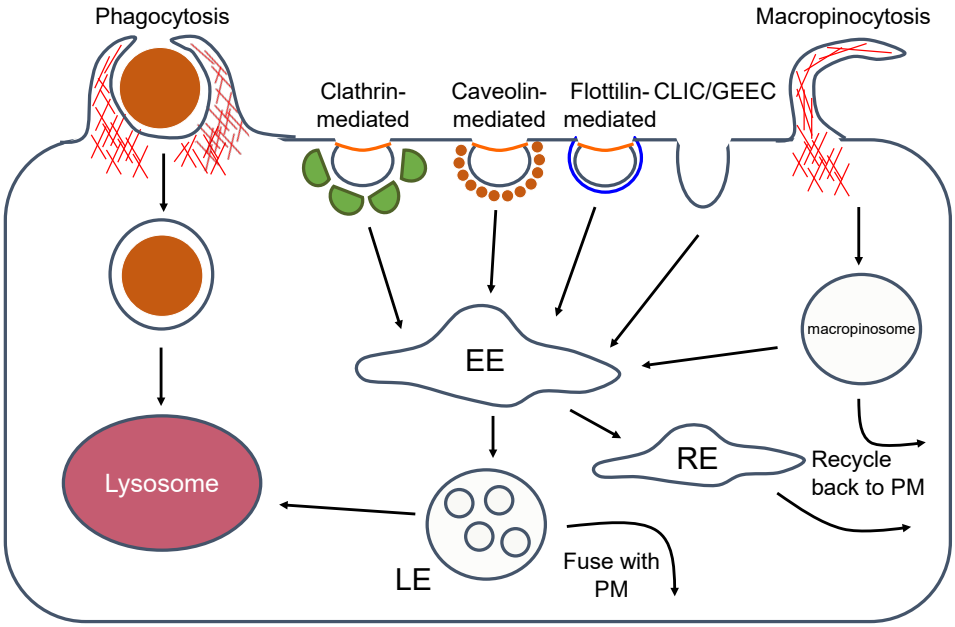

Figure 0.1: Introduction to endolysosomal trafficking pathways. Endocytic pathways converge at the early endosome where material is sent to back to the plasma membrane and extracellular environment via endocytic recycling or sent to the lysosome for degradation. Acronyms: CLIC/GEEC = clathrin-independent carriers and glycosylphosphotidylinositol-anchored protein enriched compartments; EE = early endosome; RE = recycling endosome; LE = late endosome; PM = plasma membrane.

As the ultimate destination impacts the interactions and activity of the endocytic cargo (Figure 0.1), the ultimate sorting route can dramatically impact multiple cellular processes. For example, many therapeutics, especially oligonucleotides, depend on these pathways to target cell types of interest and be released into the interior of cells where they are active. Therefore, it is essential to understand how cells balance trafficking towards the lysosome versus recycling back to the cell surface and exterior in order to identify approaches that could favor

oligonucleotide uptake and increase residency time in pre-lysosomal compartments, as discussed in the last section.

Sphingolipids are evolutionarily conserved regulators of endolysosomal trafficking. Sphingolipids like ceramide and sphingosine are bioactive lipids that play an evolutionarily conserved role in the response to stress by regulating intracellular trafficking (Dickson et al., 1997; Hannun and Obeid, 2008; Ogretmen and Hannun, 2004). For example, heat-stressed yeast produce the sphingolipid phytosphingosine which triggers the loss of cell surface nutrient transporters (e.g., the tryptophan transporters TAT1 and TAT2, the uracil transporter FUR4, and the general amino acid permease GAP1) to limit anabolic processes during times where proteins are likely to misfold (Bultynck et al., 2006; Chung et al., 2001; Dickson et al., 1997; Skrzypek et al., 1998; Welsch et al., 2004). The same mechanism is conserved in mammalian cells where the sphingolipids ceramide and sphingosine limit cell growth and proliferation in part by reducing cell surface localization of nutrient transport proteins that promote amino acid, carbohydrate, and lipid uptake into cells (Finicle et al., 2018; Guenther et al., 2008; Kim et al., 2016; Romero Rosales et al., 2011).

Attributing cellular phenotypes to specific endogenous sphingolipids is difficult due to the presence of enzymes that rapidly metabolize sphingolipids into derivatives that can have different, and even opposing, effects on cells (Hannun and Obeid, 2008). Using synthetic, sphingolipid-like molecules that cannot be metabolized but share structural features with endogenous sphingolipids can overcome this problem. For example, the FDA-approved sphingolipid drug FTY720 phenocopies ceramide and sphingosine by triggering the down-regulation of nutrient transporters from the surface and producing a starvation-like response in both yeast and mammalian cells (Barthelemy et al., 2017; Romero Rosales et al., 2011; Welsch et al., 2004). However, FTY720 is a pro-drug built for treatment of multiple sclerosis (MS). As

intended for treatment of MS, FTY720 is phosphorylated by sphingosine kinase into FTY720-phosphate, which is responsible for FTY720's immunosuppressive actions through stimulation of sphingosine-1-phosphate (S1P) receptors (Brinkmann et al., 2010). In order for FTY720 to disrupt endolysosomal trafficking similar to ceramide and sphingosine, FTY720 must be dosed at significantly higher concentrations than what it is used for MS treatment. Consequently, high levels of FTY720-phosphate are sufficient to produce dose-limiting bradycardia by activating the $S1P_1$ (in humans) and $S1P_3$ (in mice) receptors (Fryer et al., 2012). Unphosphorylated FTY720, in contrast, produces PP2A-dependent inhibition of endolysosomal trafficking similar to ceramide and sphingosine (Kim et al., 2016; Romero Rosales et al., 2011). Therefore, FTY720 analogs that fail to get phosphorylated and/or activate S1P receptors would have value as endolysosomal trafficking inhibitors.

Limiting the flexibility of the aminodiol on FTY720 prevents S1P receptor activation (Chen et al., 2016; Hanessian et al., 2007). The conformationally-constrained azacyclic FTY720 analog SH-BC-893 does not activate S1P receptors even in its phosphorylated form (Chen et al., 2016; Kim et al., 2016; Perryman et al., 2016). Importantly, SH-BC-893 produces identical disruptions in intracellular trafficking to FTY720, indicating that S1P receptor activation is not responsible for blocking endolysosomal trafficking (Kim et al., 2016; Romero Rosales et al., 2011). Like ceramide, SH-BC-893 reduces the surface localization of multiple nutrient transporters, including transporters for glucose (GLUT1, also known as SLC2A1), pyruvate, lactate and acetate (MCT1, also known as SLC16A1; MCT4, also known as SLC16A3), glutamine (ASCT2, also known as SLC1A5), and leucine (LAT1, also known as SLC7A5) (Barthelemy et al., 2017; Kim et al., 2016). In summary, the synthetic molecules SH-BC-893 phenocopies the growth suppressive effects of endogenous sphingolipids on endocytic trafficking while minimizing the confounding effects of sphingolipid metabolism.

The mechanism by which sphingolipids induce cell surface nutrient transporter loss has been dissected in yeast. Phytosphingosine triggers actin-dependent endocytosis of nutrient transporters by inducing TORC2-dependent phosphorylation of SLM1 and SLM2 and RPS5-dependent ubiquitination of the transporters (Bultynck et al., 2006; Chung et al., 2000; Daquinag et al., 2007; Fadri et al., 2005). Unfortunately, the molecular details are not completely conserved in mammalian cells. Our unpublished preliminary studies could not detect a role for the RSP5 homolog NEDD4 in mammalian cells treated with FTY720 or ceramide. In addition, these sphingolipids did not induce ubiquitination of nutrient transporters. The yeast proteins SLM1 and SLM2 contain a pleckstrin-homology domain and promote actin polarization, eisosome organization, and endocytic recycling in yeast (Douglas and Konopka, 2014; Kamble et al., 2011; Olivera-Couto et al., 2011; Walther et al., 2006). While there are no clear mammalian orthologs of SLM1 or SLM2, a DELTA-BLAST search against the human proteome indicates that the PH domains of SLM1 and SLM2 have high similarity to the PH domains present in the ARF6 GTPase activating proteins (GAP) ACAP2 (centaurin beta 2) and in the cytohesin family of ARF6 guanine nucleotide exchange factors (GEFs) (cytohesin-1, cytohesin-2/ARNO, cytohesin-3/GRP1, cytohesin-4). This similarity is interesting because the mammalian protein ARF6 regulates the same processes controlled by the SLM proteins (e.g., actin dynamics, endocytosis, and recycling) (Donaldson and Jackson, 2011; Schweitzer et al., 2011).

Our previous studies suggest that sphingolipids down-regulate nutrient transporter proteins in mammalian cells by activating the serine and threonine protein phosphatase 2A (PP2A). The bioactive sphingolipids ceramide, FTY720, and SH-BC-893 activate PP2A in vitro (Dobrowsky et al., 1993; Guenther et al., 2008; Kim et al., 2016; Romero Rosales et al., 2011); the biologically-inert sphingolipid that does not have any anti-proliferative effects, dihydroceramide, does not activate PP2A (Chalfant et al., 2004). PP2A inhibition with calyculin A or SV40 small t antigen expression maintains transporters on the cell surface in the presence of ceramide,

FTY720, or SH-BC-893, suggesting that PP2A activation is necessary (Guenther et al., 2008; Kim et al., 2016; Romero Rosales et al., 2011). The mechanism by which PP2A activation triggers transporter loss is not understood. Intriguingly, many of the proteins that are down-regulated by sphingolipids are also cargo whose recycling is controlled by ARF6 (Eyster et al., 2009; Maldonado-Báez et al., 2013), leading to the hypothesis that PP2A may regulate ARF6-dependent trafficking.

Rationale for utilizing the sphingosine analog SH-BC-893 as a potentiating agent for oligonucleotide therapeutics.

As mentioned above, approaches that increase oligonucleotide uptake and/or residency time in pre-lysosomal compartments where oligonucleotide escape is most efficient could offer significant gains in oligonucleotide potency that would make extrahepatic tissues therapeutically accessible. The work described in this thesis characterizes the synthetic sphingosine analog SH-BC-893's effects on endolysosomal trafficking. Specifically, we show that SH-BC-893 disrupts endocytic recycling by inactivating the small GTPase ARF6 (discussed in Chapter 1, also published in (Finicle et al., 2018)) and blocks lysosomal fusion reactions that depend on the lipid kinase PIKfyve (Kim et al., 2016). Both of these trafficking disruptions occur downstream of activation of the serine/threonine protein phosphatase known as PP2A; Chapter 2 investigates the potential substrates responsible for these trafficking disruptions (also published in (Kubiniok et al., 2019)). In Chapter 3, we test the hypothesis that simultaneous disruption of these endolysosomal trafficking pathways by SH-BC-893 would synergize to enhance the activity of oligonucleotide therapeutics by increasing oligonucleotide accumulation within pre-lysosomal compartments where endosomal release is most efficient. Because SH-BC-893 is orally bioavailable and safe even with chronic administration (Finicle et al., 2018; Jayashankar et al., 2021; Kim et al., 2016), we also evaluate the ability for SH-BC-893 to sensitize extrahepatic tissues to oligonucleotide therapeutics.

References for the Introduction

Altmann, K.H., Fabbro, D., Dean, N.M., Geiger, T., Monia, B.P., Müller, M., and Nicklin, P. (1996). Second-generation antisense oligonucleotides: structure-activity relationships and the design of improved signal-transduction inhibitors. Biochem. Soc. Trans. *24*, 630–637.

Bailey, J.K., Shen, W., Liang, X.-H., and Crooke, S.T. (2017). Nucleic acid binding proteins affect the subcellular distribution of phosphorothioate antisense oligonucleotides. Nucleic Acids Res. *45*, 10649–10671.

Barthelemy, C., Barry, A.O., Twyffels, L., and André, B. (2017). FTY720-induced endocytosis of yeast and human amino acid transporters is preceded by reduction of their inherent activity and TORC1 inhibition. Sci. Rep. *7*, 13816.

Bennett, C.F., and Swayze, E.E. (2010). RNA targeting therapeutics: molecular mechanisms of antisense oligonucleotides as a therapeutic platform. Annu. Rev. Pharmacol. Toxicol. *50*, 259–293.

Bennett, W.F.D., and Tieleman, D.P. (2014). The importance of membrane defects-lessons from simulations. Acc. Chem. Res. *47*, 2244–2251.

Brinkmann, V., Billich, A., Baumruker, T., Heining, P., Schmouder, R., Francis, G., Aradhye, S., and Burtin, P. (2010). Fingolimod (FTY720): discovery and development of an oral drug to treat multiple sclerosis. Nat. Rev. Drug Discov. *9*, 883–897.

Brown, C.R., Gupta, S., Qin, J., Racie, T., He, G., Lentini, S., Malone, R., Yu, M., Matsuda, S., Shulga-Morskaya, S., et al. (2020). Investigating the pharmacodynamic durability of GalNAc-siRNA conjugates. Nucleic Acids Res. *48*, 11827–11844.

Brown, D.A., Kang, S.H., Gryaznov, S.M., DeDionisio, L., Heidenreich, O., Sullivan, S., Xu, X., and Nerenberg, M.I. (1994). Effect of phosphorothioate modification of oligodeoxynucleotides on specific protein binding. J. Biol. Chem. *269*, 26801–26805.

Bultynck, G., Heath, V.L., Majeed, A.P., Galan, J.-M., Haguenauer-Tsapis, R., and Cyert, M.S. (2006). Slm1 and slm2 are novel substrates of the calcineurin phosphatase required for heat stress-induced endocytosis of the yeast uracil permease. Mol. Cell. Biol. *26*, 4729–4745.

Chalfant, C.E., Szulc, Z., Roddy, P., Bielawska, A., and Hannun, Y.A. (2004). The structural requirements for ceramide activation of serine-threonine protein phosphatases. J. Lipid Res. *45*, 496–506.

Chen, B., Roy, S.G., McMonigle, R.J., Keebaugh, A., McCracken, A.N., Selwan, E., Fransson, R., Fallegger, D., Huwiler, A., Kleinman, M.T., et al. (2016). Azacyclic FTY720 analogues that limit nutrient transporter expression but lack S1P receptor activity and negative chronotropic effects offer a novel and effective strategy to kill cancer cells in vivo. ACS Chem. Biol. *11*, 409–414.

Chung, N., Jenkins, G., Hannun, Y.A., Heitman, J., and Obeid, L.M. (2000). Sphingolipids signal heat stress-induced ubiquitin-dependent proteolysis. J. Biol. Chem. *275*, 17229–17232.

Chung, N., Mao, C., Heitman, J., Hannun, Y.A., and Obeid, L.M. (2001). Phytosphingosine as a specific inhibitor of growth and nutrient import in Saccharomyces cerevisiae. J. Biol. Chem. *276*, 35614–35621.

Corey, D.R., Damha, M.J., and Manoharan, M. (2022). Challenges and opportunities for nucleic acid therapeutics. Nucleic Acid Ther. *32*, 8–13.

Crooke, S.T., Wang, S., Vickers, T.A., Shen, W., and Liang, X.-H. (2017). Cellular uptake and trafficking of antisense oligonucleotides. Nat. Biotechnol. *35*, 230–237.

Cullen, P.J., and Steinberg, F. (2018). To degrade or not to degrade: mechanisms and significance of endocytic recycling. Nat. Rev. Mol. Cell Biol. *19*, 679–696.

Cullis, P.R., Hope, M.J., and Tilcock, C.P. (1986). Lipid polymorphism and the roles of lipids in membranes. Chem Phys Lipids *40*, 127–144.

Daquinag, A., Fadri, M., Jung, S.Y., Qin, J., and Kunz, J. (2007). The yeast PH domain proteins Slm1 and Slm2 are targets of sphingolipid signaling during the response to heat stress. Mol. Cell. Biol. *27*, 633–650.

Dickson, R.C., Nagiec, E.E., Skrzypek, M., Tillman, P., Wells, G.B., and Lester, R.L. (1997). Sphingolipids are potential heat stress signals in Saccharomyces. J. Biol. Chem. *272*, 30196–30200.

Dobrowsky, R.T., Kamibayashi, C., Mumby, M.C., and Hannun, Y.A. (1993). Ceramide activates heterotrimeric protein phosphatase 2A. J. Biol. Chem. *268*, 15523–15530.

Donaldson, J.G., and Jackson, C.L. (2011). ARF family G proteins and their regulators: roles in membrane transport, development and disease. Nat. Rev. Mol. Cell Biol. *12*, 362–375.

Donaldson, J.G., Porat-Shliom, N., and Cohen, L.A. (2009). Clathrin-independent endocytosis: a unique platform for cell signaling and PM remodeling. Cell Signal. *21*, 1–6.

Douglas, L.M., and Konopka, J.B. (2014). Fungal membrane organization: the eisosome concept. Annu. Rev. Microbiol. *68*, 377–393.

Dowdy, S.F. (2017). Overcoming cellular barriers for RNA therapeutics. Nat. Biotechnol. *35*, 222–229.

Eyster, C.A., Higginson, J.D., Huebner, R., Porat-Shliom, N., Weigert, R., Wu, W.W., Shen, R.-F., and Donaldson, J.G. (2009). Discovery of new cargo proteins that enter cells through clathrin-independent endocytosis. Traffic *10*, 590–599.

Fadri, M., Daquinag, A., Wang, S., Xue, T., and Kunz, J. (2005). The pleckstrin homology domain proteins Slm1 and Slm2 are required for actin cytoskeleton organization in yeast and bind phosphatidylinositol-4,5-bisphosphate and TORC2. Mol. Biol. Cell *16*, 1883–1900.

Ferreira, A.P.A., and Boucrot, E. (2018). Mechanisms of Carrier Formation during Clathrin-Independent Endocytosis. Trends Cell Biol. *28*, 188–200.

Finicle, B.T., Ramirez, M.U., Liu, G., Selwan, E.M., McCracken, A.N., Yu, J., Joo, Y., Nguyen, J., Ou, K., Roy, S.G., et al. (2018). Sphingolipids inhibit endosomal recycling of nutrient transporters by inactivating ARF6. J. Cell Sci. *131*.

Fryer, R.M., Muthukumarana, A., Harrison, P.C., Nodop Mazurek, S., Chen, R.R., Harrington, K.E., Dinallo, R.M., Horan, J.C., Patnaude, L., Modis, L.K., et al. (2012). The clinically-tested S1P receptor agonists, FTY720 and BAF312, demonstrate subtype-specific bradycardia ($S1P_1$) and hypertension ($S1P_3$) in rat. PLoS One *7*, e52985.

Geary, R.S., Watanabe, T.A., Truong, L., Freier, S., Lesnik, E.A., Sioufi, N.B., Sasmor, H., Manoharan, M., and Levin, A.A. (2001). Pharmacokinetic properties of 2'-O-(2-methoxyethyl)-modified oligonucleotide analogs in rats. J. Pharmacol. Exp. Ther. *296*, 890–897.

Geary, R.S., Norris, D., Yu, R., and Bennett, C.F. (2015). Pharmacokinetics, biodistribution and cell uptake of antisense oligonucleotides. Adv. Drug Deliv. Rev. *87*, 46–51.

Gilleron, J., Paramasivam, P., Zeigerer, A., Querbes, W., Marsico, G., Andree, C., Seifert, S., Amaya, P., Stöter, M., Koteliansky, V., et al. (2015). Identification of siRNA delivery enhancers by a chemical library screen. Nucleic Acids Res. *43*, 7984–8001.

Gökirmak, T., Nikan, M., Wiechmann, S., Prakash, T.P., Tanowitz, M., and Seth, P.P. (2021). Overcoming the challenges of tissue delivery for oligonucleotide therapeutics. Trends Pharmacol. Sci. *42*, 588–604.

Graham, M.J., Crooke, S.T., Monteith, D.K., Cooper, S.R., Lemonidis, K.M., Stecker, K.K., Martin, M.J., and Crooke, R.M. (1998). In vivo distribution and metabolism of a phosphorothioate oligonucleotide within rat liver after intravenous administration. J. Pharmacol. Exp. Ther. *286*, 447–458.

Graham, M.J., Crooke, S.T., Lemonidis, K.M., Gaus, H.J., Templin, M.V., and Crooke, R.M. (2001). Hepatic distribution of a phosphorothioate oligodeoxynucleotide within rodents following intravenous administration. Biochem. Pharmacol. *62*, 297–306.

Grant, B.D., and Donaldson, J.G. (2009). Pathways and mechanisms of endocytic recycling. Nat. Rev. Mol. Cell Biol. *10*, 597–608.

Guenther, G.G., Peralta, E.R., Rosales, K.R., Wong, S.Y., Siskind, L.J., and Edinger, A.L. (2008). Ceramide starves cells to death by downregulating nutrient transporter proteins. Proc. Natl. Acad. Sci. USA *105*, 17402–17407.

Hanessian, S., Charron, G., Billich, A., and Guerini, D. (2007). Constrained azacyclic analogues of the immunomodulatory agent FTY720 as molecular probes for sphingosine 1-phosphate receptors. Bioorg. Med. Chem. Lett. *17*, 491–494.

Hannun, Y.A., and Obeid, L.M. (2008). Principles of bioactive lipid signalling: lessons from sphingolipids. Nat. Rev. Mol. Cell Biol. *9*, 139–150.

Hong, D., Kurzrock, R., Kim, Y., Woessner, R., Younes, A., Nemunaitis, J., Fowler, N., Zhou, T., Schmidt, J., Jo, M., et al. (2015). AZD9150, a next-generation antisense oligonucleotide inhibitor of STAT3 with early evidence of clinical activity in lymphoma and lung cancer. Sci. Transl. Med. *7*, 314ra185.

Jayashankar, V., Selwan, E., Hancock, S.E., Verlande, A., Goodson, M.O., Eckenstein, K.H., Milinkeviciute, G., Hoover, B.M., Chen, B., Fleischman, A.G., et al. (2021). Drug-like sphingolipid SH-BC-893 opposes ceramide-induced mitochondrial fission and corrects diet-induced obesity. EMBO Mol. Med. *13*, e13086.

Juliano, R.L. (2016). The delivery of therapeutic oligonucleotides. Nucleic Acids Res. *44*, 6518–6548.

Juliano, R.L. (2018). Intracellular trafficking and endosomal release of oligonucleotides: what we know and what we don't. Nucleic Acid Ther. *28*, 166–177.

Juliano, R.L. (2021). Chemical manipulation of the endosome trafficking machinery: implications for oligonucleotide delivery. Biomedicines *9*.

Kamble, C., Jain, S., Murphy, E., and Kim, K. (2011). Requirements of Slm proteins for proper eisosome organization, endocytic trafficking and recycling in the yeast Saccharomyces cerevisiae. J. Biosci. *36*, 79–96.

Kendall, G.C., Mokhonova, E.I., Moran, M., Sejbuk, N.E., Wang, D.W., Silva, O., Wang, R.T., Martinez, L., Lu, Q.L., Damoiseaux, R., et al. (2012). Dantrolene enhances antisense-mediated exon skipping in human and mouse models of Duchenne muscular dystrophy. Sci. Transl. Med. *4*, 164ra160.

Kim, S.M., Roy, S.G., Chen, B., Nguyen, T.M., McMonigle, R.J., McCracken, A.N., Zhang, Y., Kofuji, S., Hou, J., Selwan, E., et al. (2016). Targeting cancer metabolism by simultaneously disrupting parallel nutrient access pathways. J. Clin. Invest. *126*, 4088–4102.

Kubiniok, P., Finicle, B.T., Piffaretti, F., McCracken, A.N., Perryman, M., Hanessian, S., Edinger, A.L., and Thibault, P. (2019). Dynamic Phosphoproteomics Uncovers Signaling Pathways Modulated by Anti-oncogenic Sphingolipid Analogs. Mol. Cell Proteomics *18*, 408–422.

Liang, X., Sun, H., Shen, W., and Crooke, S.T. (2015). Identification and characterization of intracellular proteins that bind oligonucleotides with phosphorothioate linkages. Nucleic Acids Res. *43*, 2927–2945.

Liang, X.-H., Sun, H., Hsu, C.-W., Nichols, J.G., Vickers, T.A., De Hoyos, C.L., and Crooke, S.T. (2020). Golgi-endosome transport mediated by M6PR facilitates release of antisense oligonucleotides from endosomes. Nucleic Acids Res. *48*, 1372–1391.

Linnane, E., Davey, P., Zhang, P., Puri, S., Edbrooke, M., Chiarparin, E., Revenko, A.S., Macleod, A.R., Norman, J.C., and Ross, S.J. (2019). Differential uptake, kinetics and mechanisms of intracellular trafficking of next-generation antisense oligonucleotides across human cancer cell lines. Nucleic Acids Res. *47*, 4375–4392.

Maldonado-Báez, L., Williamson, C., and Donaldson, J.G. (2013). Clathrin-independent endocytosis: a cargo-centric view. Exp. Cell Res. *319*, 2759–2769.

Maxfield, F.R., and McGraw, T.E. (2004). Endocytic recycling. Nat. Rev. Mol. Cell Biol. *5*, 121–132.

Mayor, S., and Pagano, R.E. (2007). Pathways of clathrin-independent endocytosis. Nat. Rev. Mol. Cell Biol. *8*, 603–612.

Ming, X., Carver, K., Fisher, M., Noel, R., Cintrat, J.-C., Gillet, D., Barbier, J., Cao, C., Bauman, J., and Juliano, R.L. (2013). The small molecule Retro-1 enhances the pharmacological actions of antisense and splice switching oligonucleotides. Nucleic Acids Res. *41*, 3673–3687.

Odate, S., Veschi, V., Yan, S., Lam, N., Woessner, R., and Thiele, C.J. (2017). Inhibition of STAT3 with the Generation 2.5 Antisense Oligonucleotide, AZD9150, Decreases Neuroblastoma Tumorigenicity and Increases Chemosensitivity. Clin. Cancer Res. *23*, 1771–1784.

Ogretmen, B., and Hannun, Y.A. (2004). Biologically active sphingolipids in cancer pathogenesis and treatment. Nat. Rev. Cancer *4*, 604–616.

Olivera-Couto, A., Graña, M., Harispe, L., and Aguilar, P.S. (2011). The eisosome core is composed of BAR domain proteins. Mol. Biol. Cell *22*, 2360–2372.

Osborn, M.F., Alterman, J.F., Nikan, M., Cao, H., Didiot, M.C., Hassler, M.R., Coles, A.H., and Khvorova, A. (2015). Guanabenz (Wytensin™) selectively enhances uptake and efficacy of hydrophobically modified siRNAs. Nucleic Acids Res. *43*, 8664–8672.

Pallan, P.S., Allerson, C.R., Berdeja, A., Seth, P.P., Swayze, E.E., Prakash, T.P., and Egli, M. (2012). Structure and nuclease resistance of 2’,4'-constrained 2'-O-methoxyethyl (cMOE) and 2'-O-ethyl (cEt) modified DNAs. Chem. Commun. *48*, 8195–8197.

Paramasivam, P., Franke, C., Stöter, M., Höijer, A., Bartesaghi, S., Sabirsh, A., Lindfors, L., Arteta, M.Y., Dahlén, A., Bak, A., et al. (2022). Endosomal escape of delivered mRNA from endosomal recycling tubules visualized at the nanoscale. J. Cell Biol. *221*.

Perryman, M.S., Tessier, J., Wiher, T., O’Donoghue, H., McCracken, A.N., Kim, S.M., Nguyen, D.G., Simitian, G.S., Viana, M., Rafelski, S., et al. (2016). Effects of stereochemistry, saturation, and hydrocarbon chain length on the ability of synthetic constrained azacyclic sphingolipids to trigger nutrient transporter down-regulation, vacuolation, and cell death. Bioorg. Med. Chem. *24*, 4390–4397.

Raal, F.J., Santos, R.D., Blom, D.J., Marais, A.D., Charng, M.-J., Cromwell, W.C., Lachmann, R.H., Gaudet, D., Tan, J.L., Chasan-Taber, S., et al. (2010). Mipomersen, an apolipoprotein B synthesis inhibitor, for lowering of LDL cholesterol concentrations in patients with homozygous familial hypercholesterolaemia: a randomised, double-blind, placebo-controlled trial. Lancet *375*, 998–1006.

Renard, H.-F., Johannes, L., and Morsomme, P. (2018). Increasing diversity of biological membrane fission mechanisms. Trends Cell Biol. *28*, 274–286.

Roberts, T.C., Langer, R., and Wood, M.J.A. (2020). Advances in oligonucleotide drug delivery. Nat. Rev. Drug Discov. *19*, 673–694.

Romero Rosales, K., Singh, G., Wu, K., Chen, J., Janes, M.R., Lilly, M.B., Peralta, E.R., Siskind, L.J., Bennett, M.J., Fruman, D.A., et al. (2011). Sphingolipid-based drugs selectively kill cancer cells by down-regulating nutrient transporter proteins. Biochem. J. *439*, 299–311.

Ross, S.J., Revenko, A.S., Hanson, L.L., Ellston, R., Whalley, N., Pandey, S.K., Revill, M., Rooney, C., Buckett, K., Klein, S.K., et al. (2017). Targeting KRAS dependent tumors with AZD4785 , a high-affinity therapeutic antisense oligonucleotide inhibitor of KRAS. Sci Trans Med *5253*, 1–14.

Rudnik, S., and Damme, M. (2021). The lysosomal membrane-export of metabolites and beyond. FEBS J. *288*, 4168–4182.

Sazani, P., Gemignani, F., Kang, S.-H., Maier, M.A., Manoharan, M., Persmark, M., Bortner, D., and Kole, R. (2002). Systemically delivered antisense oligomers upregulate gene expression in mouse tissues. Nat. Biotechnol. *20*, 1228–1233.

Schweitzer, J.K., Sedgwick, A.E., and D’Souza-Schorey, C. (2011). ARF6-mediated endocytic recycling impacts cell movement, cell division and lipid homeostasis. Semin. Cell Dev. Biol. *22*, 39–47.

Seth, P.P., Siwkowski, A., Allerson, C.R., Vasquez, G., Lee, S., Prakash, T.P., Kinberger, G., Migawa, M.T., Gaus, H., Bhat, B., et al. (2008). Design, synthesis and evaluation of constrained methoxyethyl (cMOE) and constrained ethyl (cEt) nucleoside analogs. Nucleic Acids Symp. Ser. 553–554.

Seth, P.P., Vasquez, G., Allerson, C.A., Berdeja, A., Gaus, H., Kinberger, G.A., Prakash, T.P., Migawa, M.T., Bhat, B., and Swayze, E.E. (2010). Synthesis and biophysical evaluation of 2’,4'-constrained 2'O-methoxyethyl and 2',4'-constrained 2'O-ethyl nucleic acid analogues. J. Org. Chem. *75*, 1569–1581.

Seth, P.P., Tanowitz, M., and Bennett, C.F. (2019). Selective tissue targeting of synthetic nucleic acid drugs. J. Clin. Invest. *129*, 915–925.

Shen, X., and Corey, D.R. (2018). Chemistry, mechanism and clinical status of antisense oligonucleotides and duplex RNAs. Nucleic Acids Res. *46*, 1584–1600.

Skrzypek, M.S., Nagiec, M.M., Lester, R.L., and Dickson, R.C. (1998). Inhibition of amino acid transport by sphingoid long chain bases in Saccharomyces cerevisiae. J. Biol. Chem. *273*, 2829–2834.

Stein, C.A., Subasinghe, C., Shinozuka, K., and Cohen, J.S. (1988). Physicochemical properties of phosphorothioate oligodeoxynucleotides. Nucleic Acids Res. *16*, 3209–3221.

Tanowitz, M., Hettrick, L., Revenko, A., Kinberger, G.A., Prakash, T.P., and Seth, P.P. (2017). Asialoglycoprotein receptor 1 mediates productive uptake of N-acetylgalactosamine-conjugated and unconjugated phosphorothioate antisense oligonucleotides into liver hepatocytes. Nucleic Acids Res. *45*, 12388–12400.

Teplova, M., Minasov, G., Tereshko, V., Inamati, G.B., Cook, P.D., Manoharan, M., and Egli, M. (1999). Crystal structure and improved antisense properties of 2'-O-(2-methoxyethyl)-RNA. Nat. Struct. Biol. *6*, 535–539.

De Velasco, M.A., Kura, Y., Sakai, K., Hatanaka, Y., Davies, B.R., Campbell, H., Klein, S., Kim, Y., MacLeod, A.R., Sugimoto, K., et al. (2019). Targeting castration-resistant prostate cancer with androgen receptor antisense oligonucleotide therapy. JCI Insight *4*.

Wagenaar, T.R., Tolstykh, T., Shi, C., Jiang, L., Zhang, J., Li, Z., Yu, Q., Qu, H., Sun, F., Cao, H., et al. (2015). Identification of the endosomal sorting complex required for transport-I (ESCRT-I) as an important modulator of anti-miR uptake by cancer cells. Nucleic Acids Res. *43*, 1204–1215.

Walther, T.C., Brickner, J.H., Aguilar, P.S., Bernales, S., Pantoja, C., and Walter, P. (2006). Eisosomes mark static sites of endocytosis. Nature *439*, 998–1003.

Wang, S., Sun, H., Tanowitz, M., Liang, X.-H., and Crooke, S.T. (2016). Annexin A2 facilitates endocytic trafficking of antisense oligonucleotides. Nucleic Acids Res. *44*, 7314–7330.

Wang, S., Sun, H., Tanowitz, M., Liang, X.-H., and Crooke, S.T. (2017). Intra-endosomal trafficking mediated by lysobisphosphatidic acid contributes to intracellular release of phosphorothioate-modified antisense oligonucleotides. Nucleic Acids Res. *45*, 5309–5322.

Wang, T., Smith, E.A., Chapman, E.R., and Weisshaar, J.C. (2009). Lipid mixing and content release in single-vesicle, SNARE-driven fusion assay with 1-5 ms resolution. Biophys. J. *96*, 4122–4131.

Wang, Y., Yu, R.Z., Henry, S., and Geary, R.S. (2019). Pharmacokinetics and Clinical Pharmacology Considerations of GalNAc3-Conjugated Antisense Oligonucleotides. Expert Opin Drug Metab Toxicol *15*, 475–485.

Welsch, C.A., Roth, L.W.A., Goetschy, J.F., and Movva, N.R. (2004). Genetic, biochemical, and transcriptional responses of Saccharomyces cerevisiae to the novel immunomodulator FTY720 largely mimic those of the natural sphingolipid phytosphingosine. J. Biol. Chem. *279*, 36720–36731.

Wickner, W., and Rizo, J. (2017). A cascade of multiple proteins and lipids catalyzes membrane fusion. Mol. Biol. Cell *28*, 707–711.

Wilke, S., Krausze, J., and Büssow, K. (2012). Crystal structure of the conserved domain of the DC lysosomal associated membrane protein: implications for the lysosomal glycocalyx. BMC Biol. *10*, 62.

Wittrup, A., Ai, A., Liu, X., Hamar, P., Trifonova, R., Charisse, K., Manoharan, M., Kirchhausen, T., and Lieberman, J. (2015). Visualizing lipid-formulated siRNA release from endosomes and target gene knockdown. Nat. Biotechnol. *33*, 870–876.

Yamamoto, Y., Loriot, Y., Beraldi, E., Zhang, F., Wyatt, A.W., Al Nakouzi, N., Mo, F., Zhou, T., Kim, Y., Monia, B.P., et al. (2015). Generation 2.5 antisense oligonucleotides targeting the androgen receptor and its splice variants suppress enzalutamide-resistant prostate cancer cell growth. Clin. Cancer Res. *21*, 1675–1687.

Yang, B., Ming, X., Cao, C., Laing, B., Yuan, A., Porter, M.A., Hull-Ryde, E.A., Maddry, J., Suto, M., Janzen, W.P., et al. (2015). High-throughput screening identifies small molecules that enhance the pharmacological effects of oligonucleotides. Nucleic Acids Res. *43*, 1987–1996.

Zhang, X., Castanotto, D., Nam, S., Horne, D., and Stein, C. (2017). 6BIO Enhances Oligonucleotide Activity in Cells: A Potential Combinatorial Anti-androgen Receptor Therapy in Prostate Cancer Cells. Mol. Ther. *25*, 79–91.

CHAPTER 1

Sphingolipids inhibit endosomal recycling of nutrient transporters by inactivating ARF6

Brendan T. Finicle*, Manuel U. Ramirez*, Gang Liu, Elizabeth M. Selwan, Alison N. McCracken, Jingwen Yu, Yoosun Joo, Jannett Nguyen, Kevin Ou, Saurabh Ghosh Roy, Victor D. Mendoza, Dania Virginia Corrales, and Aimee L. Edinger

Affiliations

Department of Developmental and Cell Biology, University of California Irvine, Irvine, California 92697

* denotes equal contribution

This chapter is derived from the manuscript published in *Journal of Cell Science*:
J Cell Sci. 2018 Jun 25;131(12):jcs213314. doi: 10.1242/jcs.213314.

1.1 Abstract

Endogenous sphingolipids (ceramide) and related synthetic molecules (FTY720, SH-BC-893) reduce nutrient access by decreasing cell surface expression of a subset of nutrient transporter proteins. Here, we report that these sphingolipids disrupt endocytic recycling by inactivating the small GTPase ARF6. Consistent with reported roles for ARF6 in maintaining the tubular recycling endosome, MICAL-L1-positive tubules were lost from sphingolipid-treated cells. ARF6 inactivation may occur downstream of PP2A activation. Sphingolipids that fail to activate PP2A

did not reduce ARF6-GTP levels, a structurally unrelated PP2A activator disrupted tubular recycling endosome morphology and transporter localization, and over-expression of a phosphomimetic mutant of the ARF6 GEF GRP1 prevented nutrient transporter loss. ARF6 inhibition alone was not toxic. However, the ARF6 inhibitors SecinH3 and NAV2729 dramatically enhanced cancer cell killing by SH-BC-893 without increasing toxicity to peripheral blood mononuclear cells, suggesting that ARF6 inactivation contributes to the anti-neoplastic actions of sphingolipids. Taken together, these studies provide mechanistic insight into how ceramide and sphingolipid-like molecules limit nutrient access and suppress tumor cell growth and survival.

1.2 Introduction

Sphingolipids induce an evolutionarily conserved adaptive quiescence program in stressed cells that depends on nutrient transporter down-regulation. Phytosphingosine starves heat-stressed yeast into growth arrest by triggering the internalization of several nutrient permeases including the tryptophan transporters TAT1 and TAT2, the uracil transporter FUR4, and the general amino acid permease GAP1 (Bultynck et al., 2006; Chung et al., 2001; Dickson et al., 1997; Skrzypek et al., 1998; Welsch et al., 2004). In mammalian cells, ceramide produced in response to a variety of stresses antagonizes growth and proliferation, in part by down-regulating nutrient transporter proteins and reducing amino acid and glucose import (Guenther et al., 2008, 2014; Hannun and Obeid, 2008; Summers et al., 1998). Attributing cellular phenotypes to specific endogenous sphingolipids is complicated by the fact that a large number of enzymes rapidly metabolize sphingolipids into derivatives that can have different, and even opposing, effects on cells (Hannun and Obeid, 2008). Using synthetic, sphingolipid-like molecules can help to overcome this problem. Similar to the endogenous sphingolipids phytosphingosine and ceramide, the FDA-approved sphingolipid drug FTY720 triggers transporter down-regulation and induces a starvation-like response in both yeast and mammalian cells (Barthelemy et al., 2017; Romero Rosales et al., 2011; Welsch et al., 2004). FTY720 is a pro-drug, and FTY720-phosphate produced intracellularly is responsible for FTY720's therapeutic, immunosuppressive actions through stimulation of sphingosine-1-phosphate (S1P) receptors (Brinkmann et al., 2010). Unphosphorylated FTY720, in contrast, limits tumor cell growth and survival in vitro and in vivo by activating PP2A and disrupting endocytic trafficking (Kim et al., 2016; Romero Rosales et al., 2011). Unlike FTY720, the conformationally constrained FTY720 analog SH-BC-893 (893) does not activate S1P receptors even in its phosphorylated form (Chen et al., 2016; Kim et al., 2016; Perryman et al., 2016). However, FTY720 and 893 produce identical disruptions in intracellular trafficking, and their IC50's are closely matched suggesting that

effects on trafficking, not S1P receptors, are responsible for FTY720's anti-cancer activity (Kim et al., 2016; Romero Rosales et al., 2011). FTY720 and 893 disrupt the trafficking of transporters for glucose (GLUT1, also known as SLC2A1), pyruvate, lactate and acetate (MCT1, also known as SLC16A1; MCT4, also known as SLC16A3), glutamine (ASCT2, also known as SLC1A5), and leucine (LAT1, also known as SLC7A5) (Barthelemy et al., 2017; Kim et al., 2016). Down-regulation of multiple mammalian nutrient transporters by sphingolipids is consistent with the observation that both phytosphingosine and FTY720 promote internalization of permeases for multiple amino acids (tryptophan, leucine, histidine, and proline) and uracil in yeast (Barthelemy et al., 2017; Bultynck et al., 2006; Chung et al., 2000, 2001; Skrzypek et al., 1998). In summary, synthetic molecules like FTY720 and 893 phenocopy the growth suppressive effects of endogenous sphingolipids on endocytic trafficking while minimizing the confounding effects of sphingolipid metabolism.

The molecular mechanism underlying sphingolipid-induced nutrient transporter loss has been dissected in yeast. Phytosphingosine triggers actin-dependent endocytosis of nutrient transporters by inducing TORC2-dependent phosphorylation of the pleckstrin-homology (PH) domain containing proteins SLM1 and SLM2 and RSP5-dependent ubiquitination of the transporters (Bultynck et al., 2006; Chung et al., 2000; Daquinag et al., 2007; Fadri et al., 2005). Unfortunately, while sphingolipid-induced transporter loss is conserved in mammalian cells, the molecular details are not. We have thus far been unable to detect ubiquitination of nutrient transporters or a role for the RSP5 homolog NEDD4 in mammalian cells treated with FTY720 or ceramide, and there are no clear mammalian orthologs of the SLM1 or SLM2 proteins that promote actin polarization, eisosome organization, and endocytic recycling in yeast (Douglas and Konopka, 2014; Kamble et al., 2011; Olivera-Couto et al., 2011; Walther et al., 2006). However, a DELTA-BLAST search against the human proteome indicates that the PH domains

of SLM1 and SLM2 bear homology to the PH domains present in the ARF6 GAP ACAP2 (centaurin beta 2) and in the cytohesin family of ARF6 GEFs (cytohesin-1, cytohesin-2/ARNO, cytohesin-3/GRP1, cytohesin-4). This similarity is interesting because ARF6 regulates actin dynamics, endocytosis, and recycling, the same processes controlled by the SLM proteins (Donaldson and Jackson, 2011; Schweitzer et al., 2011). Sphingolipids have not previously been linked to ARF6 regulation. Rather, the available evidence suggests that sphingolipids down-regulate nutrient transporter proteins in mammalian cells by activating the serine and threonine protein phosphatase 2A (PP2A). Ceramide, FTY720, and 893 activate PP2A in vitro while dihydroceramide, a sphingolipid that does not kill cells, does not (Chalfant et al., 2004; Dobrowsky et al., 1993; Kim et al., 2016). PP2A activation is necessary for sphingolipid-induced nutrient transporter loss as PP2A inhibition with calyculin A or SV40 small t antigen expression maintains transporters on the cell surface in the presence of ceramide, FTY720, or 893 (Guenther et al., 2008; Kim et al., 2016; Romero Rosales et al., 2011). How PP2A activation triggers transporter loss is not understood. Intriguingly, many of the proteins that are down-regulated by sphingolipids are also cargo for the ARF6-dependent, clathrin-independent endocytic trafficking pathway (Eyster et al., 2009; Maldonado-Báez et al., 2013), leading to the hypothesis that PP2A may regulate ARF6-dependent trafficking. Here we show that the “tumor suppressor lipid” ceramide and the anti-neoplastic, sphingolipid-like small molecules FTY720 and 893 decrease cell surface nutrient transporter levels in mammalian cells by reducing ARF6-GTP levels, dissolving the tubular recycling endosome, and disrupting endocytic recycling.

1.3 Results

Natural and synthetic sphingolipids trap cell surface nutrient transporters in a recycling compartment. CD98 (4F2hc, SLC3A2) is a chaperone protein for LAT1 (SLC7A5) and xCT (SLC7A11), two amino acid transporter proteins whose over-expression in cancer cells is correlated with poor prognosis (Selwan et al., 2016). FTY720 down-regulates CD98 and LAT1 in mammalian cells (Barthelemy et al., 2017; Kim et al., 2016; Romero Rosales et al., 2011). Surface levels of CD98 are readily quantified using flow cytometry while antibodies recognizing the exofacial domains of other nutrient transporters are not generally available, most likely because glycosylation of the extracellular regions of these proteins sterically hinders antibody binding. As expected, the sphingolipids ceramide, sphingosine, FTY720, and 893 down-regulate CD98 in mammalian cells ((Guenther et al., 2008; Kim et al., 2016; Perryman et al., 2016; Romero Rosales et al., 2011), Fig. 1.1A,B and S1.1). Importantly, bacterial sphingomyelinase, an enzyme that converts plasma membrane sphingomyelin into physiologic long-chain ceramides, also reduces cell surface transporter levels indicating that natural ceramides, not just more soluble short chain analogs, share this activity ((Guenther et al., 2008), Fig. 1.1A,B). As small molecule and protein inhibitors of PP2A block transporter loss (Guenther et al., 2008; Kim et al., 2016; Romero Rosales et al., 2011), this phenotype is not due to the direct effects of sphingolipids on membranes (Trajkovic et al., 2008).

To begin to dissect the mechanism underlying sphingolipid-induced nutrient transporter loss in mammalian cells, a kinetic study of transporter co-localization with markers for different endocytic compartments was performed. In sphingolipid-treated cells, internalized CD98 did not co-localize with the early endosome marker EEA1 at any time point (Fig. 1.1C and S1.2A,B). Sphingolipids induced co-localization of intracellular CD98 and the trans Golgi network marker TGN46, however TGN46 localization was itself altered by sphingolipids (Fig. 1.1D, S1.2C-D,

and S1.3A-B). In control cells, TGN46 was mostly co-localized with GM130 as expected (Fig. S1.3A). In FTY720-treated cells, some TGN46 still co-localized with GM130, but most TGN46 molecules were redistributed to peripheral, vesicular structures. GM130 localization was not altered suggesting that the cis-Golgi remained intact. While TGN46's steady state localization pattern is predominantly in the trans Golgi network, TGN46 traffics between the trans Golgi network and the plasma membrane along tubular endosome intermediates (Ghosh et al., 1998; Maxfield and McGraw, 2004; Prescott et al., 1997). The punctate, peripheral distribution of both TGN46 and CD98 in sphingolipid-treated cells (Fig. 1.1D and S1.2C-D) suggested that both were trapped in a recycling intermediate. Consistent with this hypothesis, a subset of internalized transferrin receptor (TfR) co-localized with GLUT1 in sphingolipid-treated cells, most likely in recycling endosomes that receive cargo from both the clathrin-independent endocytosis (CIE) and clathrin-mediated endocytosis (CME) pathways (Fig. 1.1E and S1.4A-B). Sphingolipids also increased co-localization of TGN46 and TfR, again suggesting that recycling pathways are disrupted (Fig. S1.3B). CD98 partially co-localized with the late endosome/lysosome marker LAMP1 only at late timepoints (Fig. 1.1F, S1.4C,D) suggesting that nutrient transporters that fail to recycle may eventually be rerouted towards the degradative pathway. In ceramide-treated cells, CD98 was present in the interior of the LAMP1-positive endosomes suggesting it was present in the limiting membrane of intraluminal vesicles that have budded into the multivesicular body (MVB) prior to lysosomal degradation (Fig. 1.1F). In 893-treated cells where intraluminal budding is disrupted due to the mislocalization of the lipid kinase PIKfyve and the loss of $PI(3,5)P_2$ from MVB membranes (Kim et al., 2016), CD98 remained associated with the limiting membranes of LAMP1-positive endosomes (Fig. 1.1F). Taken together, these co-localization studies suggest that natural and synthetic sphingolipids trap endocytosed nutrient transporters in recycling endosomes, but these proteins are eventually sent to the lysosome for degradation when they fail to recycle.

As mentioned above, small molecule inhibitors of PP2A rescue from the trafficking defects induced by sphingolipids indicating PP2A activation is necessary to produce these phenotypes. Consistent with this model, dihydroceramide, which differs from ceramide by a single unsaturated bond (Fig. S1.1) and does not activate PP2A (Chalfant et al., 2004; Dobrowsky et al., 1993; Kowluru and Metz, 1997) also did not alter the localization of CD98, TGN46, GLUT1, or the TfR (Fig. S1.5A-B). An 893 analog, 893-lactam, that lacks a charge on the pyrrolidine nitrogen fails to down-regulate nutrient transporter proteins or induce vacuolation, both PP2A-dependent phenotypes (Fig. S1.1, (Chen et al., 2016; Perryman et al., 2016)). 893-lactam also did not affect the localization of these recycling proteins (Fig. S1.5A-B). In summary, a subset of sphingolipids that activate PP2A trap several proteins in what appears to be a recycling compartment.

Sphingolipids increase internalization and block endosomal recycling of nutrient transporters downstream of PP2A activation. The down-regulation of nutrient transporter proteins in sphingolipid-treated cells could result from an increased rate of endocytosis, a decreased rate of endosomal recycling, or a combination of the two. Internalization of cell surface transporters in response to sphingolipids was quantified using a flow cytometry-based assay. Briefly, live cells were incubated with unlabeled primary antibody on ice, washed, and then shifted to 37°C in the presence or absence of FTY720 for various intervals before staining with fluorochrome-conjugated secondary antibodies on ice. Using this approach, down-regulation of molecules that were initially present on the cell surface can be selectively measured. Cell lines that grow in suspension were used for these assays to minimize artifacts that might result from loss of adhesion-dependent signal transduction after trypsinization and to simplify the experimental design. Over the course of the experiment, minimal CD98 was lost from the surface of murine FL5.12 hematopoetic cells in the absence of exogenous sphingolipids confirming that antibody binding does not itself trigger CD98 endocytosis (Fig.

1.2A). Internalization of cell surface CD98 was dramatically enhanced by FTY720 with only 48% of the CD98 molecules that were initially on the surface remaining after 30 min of exposure. Similar results were obtained in human SupB15 leukemia cells. In contrast, FTY720 did not increase transferrin (Tf) internalization in either FL5.12 or SupB15 cells suggesting that CME is not stimulated by sphingolipids (Fig. 1.2B). These results suggest that sphingolipids selectively increase the internalization of plasma membrane-localized CD98 but not the TfR.

Endocytic recycling also controls the surface level of plasma membrane proteins. The results in Fig. 1.2A could have been obtained if CD98 has a high basal internalization rate that was not affected by FTY720 and this sphingolipid selectively blocks recycling. To evaluate whether sphingolipids impede endosomal recycling, a modified version of this flow cytometry assay was utilized. In these recycling studies, surface CD98 was again selectively labeled with primary antibodies, but cells were washed and transferred to FTY720-free medium at 1 h, a time point after CD98 loss had plateaued. As expected, the initial treatment with FTY720 triggered the internalization of about 35% of the cell-surface CD98 in SupB15 cells (Fig. 1.2A&C). However, washing out FTY720 after 1 h led to the complete restoration of the internalized CD98 to the cell surface within 30 min (Fig. 1.2C). In control samples where FTY720 was replenished after washing, internalized CD98 did not return to the surface. Consistent with the co-localization studies presented in Fig. 1.1D&E, these results suggest that sphingolipids trap CD98 in a recycling compartment. As TfR was trapped intracellularly along with GLUT1 and TGN46 in sphingolipid-treated cells (Fig. 1.1E, S1.3B, and S1.4A-B), Tf recycling was also evaluated. Internalized Tf was recycled more slowly in FTY720-treated cells (Fig. 1.2D). As TfR internalization was not altered by FTY720 (Fig. 1.2B), sphingolipids may increase the internalization of a subset of clathrin-independent cargo while having a more global negative impact on endocytic recycling.

Sphingolipid-induced nutrient transporter down-regulation requires PP2A activation (Guenther et al., 2008; Kim et al., 2016; Romero Rosales et al., 2011). As expected, the PP2A inhibitors calyculin A and cantharidin blocked FTY720-induced nutrient transporter loss (Fig. 1.2E). Calyculin A and cantharidin inhibit PP1 at ~2- and ~10-fold higher concentrations than they inhibit PP2A, respectively (Swingle et al., 2007). However, the PP1-specific inhibitor tautomycin did not block CD98 loss in response to FTY720 (Fig. 1.2E). In an internalization assay selectively monitoring cell surface CD98, PP2A inhibition with calyculin A maintained plasma membrane localized CD98 at initial levels (Fig. 1.2F). Moreover, the CD98 recycling defect could be attributed to PP2A activation. In recycling assays where cell surface CD98 was labeled and then 1 h was allowed for internalization, calyculin A resulted in the return of internalized CD98 to the cell surface even in the continued presence of FTY720 (Fig. 1.2G). Taken together, these experiments suggest that PP2A activation by sphingolipids blocks endocytic recycling.

Sphingolipids disrupt the tubular recycling endosome that receives CIE cargo. Several of the nutrient transporter proteins affected by sphingolipids, including CD98, LAT1, GLUT1, and MCT1, are ARF6 cargo proteins that are internalized by CIE and recycled back to the plasma membrane via the tubular recycling endosome (TRE) (Eyster et al., 2009; Maldonado-Báez et al., 2013). The recycling of these cargo from the TRE depends on ARF6-GTP; expressing the dominant-negative ARF6 mutant T27N or knocking-down the ARF6 GEF cytohesin-3/GRP1 ablates endosomal recycling from the TRE (D'Souza-Schorey et al., 1998; Eyster et al., 2009; Li et al., 2012; Maldonado-Báez et al., 2013; Rahajeng et al., 2012; Schweitzer et al., 2011; Zimmermann et al., 2005). The molecular scaffold MICAL-L1 recruits ARF6 to the TRE along with additional proteins involved in membrane tubulation and scission (Cai et al., 2014; Giridharan et al., 2013; Rahajeng et al., 2012; Sharma et al., 2009). Given that the proteins down-regulated by sphingolipids are ARF6 cargo that move through the TRE during recycling,

we evaluated the effect of sphingolipids on the morphology of this recycling compartment by monitoring MICAL-L1 localization.

HeLa cells are commonly used to study TRE function (Cai et al., 2014; Giridharan et al., 2012, 2013; Rahajeng et al., 2012; Reinecke et al., 2015; Sharma et al., 2009). An extensive TRE is also present in COS7, COS1, MCF7, dendritic cells, and intestinal cells of *Caenorhabditis elegans* (Chen et al., 2014; Grant and Donaldson, 2009; Montesinos et al., 2005; Vidal-Quadras et al., 2011; Walseng et al., 2008; Zimmermann et al., 2005); less elaborate forms of an ARF6-regulated tubular recycling compartment likely exist in all mammalian cells. Consistent with the effect of sphingolipids on CD98 internalization and recycling (Fig. 1.2), both FTY720 and 893 triggered a dramatic re-localization of CD98 to tubular structures within 30 min in HeLa cells (Fig. 1.3A and not shown). Additional CIE cargo proteins that are down-regulated by sphingolipids, GLUT1 and MCT1, also accumulated in tubules in response to FTY720 or 893 (data not shown). To confirm that these tubules represented the TRE, cells were stained for both CD98 and MICAL-L1. Because the antibodies to CD98 and MICAL-L1 were both generated in mice, GFP-tagged MICAL-L1 was expressed to facilitate co-localization studies. As expected, tubules containing CD98 were also positive for MICAL-L1 (Fig. 1.3B). Moreover, consistent with this structure receiving an enhanced endocytic load, the MICAL-L1-positive TRE expanded upon exposure to 893 (Fig. 1.3C,D). Following this initial expansion, tubular MICAL-L1 staining was completely lost, shifting to a diffuse, cytoplasmic pattern after 3 h with no decrease in total cellular MICAL-L1 (Fig. 1.3C-E). Similar to MICAL-L1, CD98 lost its tubular distribution at 3 h (Fig. 1.3A) and no longer co-localized with MICAL-L1 at 6 h (Fig. 1.3F). MICAL-L1 is essential for proper TRE function as it recruits many proteins required for recycling, including ARF6, RAB35, syndapin2, RAB8, RAB10, and EHD1 (Giridharan et al., 2012, 2013; Rahajeng et al., 2012; Sharma et al., 2009). Loss of the molecular scaffold MICAL-L1 suggests that proteins critical for endocytic recycling from the TRE would not be recruited. Indeed,

tubular ARF6 and RAB35 staining and co-localization with MICAL-L1 was eliminated after 6 h of exposure to ceramide or 893 (Fig. S1.6A-B). These results suggest that the failure to retain MICAL-L1 on the TRE contributes to the disruption in endocytic recycling in sphingolipid-treated cells.

In marked contrast to results obtained with FTY720 and 893 (Fig. 1.3A-C), ceramide did not induce a tubular MICAL-L1 or CD98 staining pattern at early time points (Fig. 1.4A-B). While tubular MICAL-L1 persisted until 3 h in cells treated with FTY720 or 893 (Fig. 1.3C-D), tubular MICAL-L1 localization was lost within 30 min of ceramide addition (Fig. S1.6A-B). Loss of tubular MICAL-L1 staining in ceramide-exposed cells was not due to degradation as MICAL-L1 total protein levels were not reduced (Fig. 1.3E). As FTY720, 893, and ceramide induce nutrient transporter loss with similar kinetics and to a similar extent (Fig. 1.1A-F, (Guenther et al., 2008; Kim et al., 2016; Romero Rosales et al., 2011)), this discrepancy in their effects on the TRE was unexpected. However, FTY720 and 893 have effects on intracellular trafficking that are not shared with ceramide (Kim et al., 2016). FTY720 and 893 induce profound cytoplasmic vacuolation by mislocalizing the phosphatidyl inositol kinase PIKfyve and its product $PI(3,5)P_2$ to an abnormal compartment, inhibiting activation of the effector protein TRMPL1 and the release of Ca^{2+} necessary for lysosomal fusion. Ceramide, in contrast, does not alter PIKfyve localization or inhibit lysosomal fusion reactions. To assess whether the loss of $PI(3,5)P_2$ from the MVB could account for the disparate effects of ceramide and FTY720/893 on MICAL-L1 localization (Fig. 1.4A), MICAL-L1 localization was evaluated in cells treated with the PIKfyve kinase inhibitor YM201636 alone or in combination with ceramide. Intriguingly, MICAL-L1 positive tubules were longer and more numerous in cells treated with YM201636, a phenotype similar to that seen with FTY720 and 893 at early timepoints (Figs. 1.3C-D, 1.4A&C and S1.6A-B). Whereas about half of the cells normally contain a well-elaborated TRE, nearly 100% of the cells treated with FTY720, 893, or YM201636 contain a TRE structure with extended tubules

(Fig. 1.4A,C&D and S1.6A-B). YM201636 did not prevent ceramide-induced dispersion of MICAL-L1 suggesting that FTY720 and 893 may trigger additional trafficking disruptions that affect TRE morphology (Fig. 1.4D). As YM201636 does not reduce surface nutrient transporter levels as a single agent and does not increase the transporter loss induced by ceramide (Fig. 1.4C and (Kim et al., 2016)), it seems unlikely that hypertubulation interferes with recycling or contributes to transporter loss. Rather, the dispersion of MICAL-L1 that is triggered by ceramide immediately or by FTY720 and 893 after 3 h is more likely to be associated with a transporter recycling defect.

Endogenous and synthetic sphingolipids that down-regulate nutrient transporters inactivate the ARF6 GTPase. ARF6 activation is required for recycling of a number of cargo proteins that localize to the TRE (D'Souza-Schorey et al., 1998; Donaldson, 2003; Maldonado-Báez et al., 2013). ARF6 is also necessary to maintain the TRE (Rahajeng et al., 2012). Thus, the observed effects of sphingolipids on endocytic recycling and the TRE suggest that sphingolipids might inactivate ARF6. To test this model, ARF6-GTP levels were measured using a published ARF6 effector pulldown assay (Cohen and Donaldson, 2010). The ARF6 inhibitor SecinH3 inactivates the cytohesin family of ARF6 GEFs and reduced ARF6-GTP to about 60% of basal levels; C_2-ceramide, bSMase, FTY720, and 893 decreased ARF6-GTP levels to a similar degree in a dose-responsive and time-dependent manner (Fig. 1.5A-C). FTY720 inactivated ARF6 in multiple cell types including MDA-MB-231 (human breast cancer), HeLa (human cervical carcinoma), SW620 (human colorectal cancer), PC3 (human prostate cancer), and SupB15 (human acute lymphoblastic leukemia) cells (Fig. 1.5D). Sphingolipids induce nutrient transporter loss in all of these cell types (Guenther et al., 2008; Kim et al., 2016; Romero Rosales et al., 2011). Moreover, sphingolipids that do not down-regulate CD98 failed to inactivate ARF6. C_2-dihydroceramide did not trigger CD98 down-regulation, TGN46 mislocalization, GLUT1 and transferrin receptor colocalization, or dissolution of MICAL-L1-

positive TRE (Fig. 1.5E and S1.5A-C). C_2-dihydroceramide also failed to kill cells (Fig. 1.5F). Consistent with the expectation that loss of MICAL-L1 on the TRE and mislocalization of recycling cargo TGN46 and the transferrin receptor is due to ARF6 inactivation, dihydroceramide failed to reduce ARF6-GTP levels (Fig. 1.5G). Similar results were obtained with the inactive analog 893-lactam (Fig. S1.5A-D). As C_2-dihydroceramide also fails to activate PP2A in vitro (Chalfant et al., 2004; Kim et al., 2016), these results are consistent with placement of ARF6 inactivation downstream of PP2A activation. Also consistent with this model, a structurally unrelated small molecule activator of PP2A, perphenazine (PPZ), was sufficient to trigger mislocalization of CD98 and TGN46 and to eliminate tubular MICAL-L1 staining (Fig. S1.7A-B). As YM201636 did not alter ARF6-GTP levels or disrupt ARF6 recruitment to the TRE (Fig. S1.7C-D), ARF6 inactivation is unlikely to lie downstream of PIKfyve mislocalization by FTY720 or 893. Together, these data support the model that PP2A activation leads to ARF6 inactivation and a block in endocytic recycling.

If PP2A activation is upstream of ARF6 inactivation, then inhibition of PP2A should maintain ARF6-GTP levels in sphingolipid-treated cells. Unexpectedly, the PP2A inhibitor calyculin A that blocked transporter internalization and restored endocytic recycling (Fig. 1.2E-G) inactivated ARF6 even in the absence of exogenous sphingolipids (Fig. 1.5H). This result may reflect the fact that PP2A is a heterotrimeric enzyme that can take over 50 different forms with distinct subunit composition and substrate preferences (Sangodkar et al., 2016). Sphingolipids may activate only a subset of PP2A isoforms, but calyculin A inhibits all PP2A heterotrimers including sphingolipid-insensitive PP2A heterotrimers that might promote ARF6 activation. Off-target effects on proteins other than PP2A may also contribute to the inactivation of ARF6 by calyculin A. Our efforts to measure ARF6-GTP levels in cells where PP2A was genetically inhibited were unsuccessful. Loss of PP2A catalytic activity is cell lethal, and sufficient quantities of viable cells with PP2A-A or –C subunit knockdown could not be generated for use in effector pulldown

assays. Knocking down individual PP2A B subunits was a less toxic approach, but failed to protect from transporter loss (data not shown). While SV40 small t antigen blocked sphingolipid-induced nutrient transporter loss in transient transfection assays (Kim et al., 2016), expression levels achieved in stable populations or cell clones were not sufficient to protect from transporter loss; similar results were obtained in cells stably over-expressing the PP2A inhibitor I_2PP2A/SET (data not shown). Given these technical difficulties, a definitive test of whether ARF6 inactivation lies down-stream of sphingolipid-induced PP2A activation will require additional mechanistic insight. Nonetheless, the correlation between the ability of sphingolipids to trigger nutrient transporter loss, starve cells, reduce ARF6-GTP levels, and activate PP2A suggests that PP2A activation is likely upstream of ARF6 inactivation.

ARF6 inactivation is necessary and sufficient to account for reduced nutrient transporter recycling in sphingolipid-treated cells. Dominant-negative and constitutively-active mutants are routinely used to study GTPase function. Constitutively-active mutants exist preferentially in the GTP-bound state due to mutations that prevent GTP hydrolysis, while dominant-negative mutants are preferentially in the GDP-bound state and compete with the endogenous GTPase for GEFs. While these mutants can provide key insights, GTPase cycling between the GDP- and GTP-bound forms is required for normal GTPase function. Indeed, the constitutively-active ARF6 mutant ARF6-Q67L causes nutrient transporter proteins to accumulate intracellularly in large, perinuclear vesicles and, not surprisingly, failed to restore nutrient transporters to the surface in sphingolipid-treated cells ((Eyster et al., 2009) and not shown). However, consistent with our finding that sphingolipids inactivate ARF6, the dominant-negative mutant ARF6-T27N drove CD98 into tubular endosomes and cytoplasmic puncta similar to the phenotype in sphingolipid-treated cells (Figs. 1.3A, 1.4B, and 1.6A-B). ARF6-T27N also mislocalized the recycling cargo TGN46 to peripheral, vesicular structures suggesting that ARF6 inactivation was sufficient to explain the recycling defects observed with sphingolipids (Fig. S1.7E). Both the

cytohesin inhibitor SecinH3 and the allosteric ARF6 inhibitor NAV2729 also disrupted the localization pattern of CD98 (Fig. 1.6C-D) and TGN46 (Fig. S1.7F) and phenocopied the effects of sphingolipids on MICAL-L1, eliminating tubular MICAL-L1 localization (Fig. 1.6E-F) and blocking ARF6 and RAB35 recruitment to the TRE similar to 893 and ceramide (Fig. S1.6A-C). If ARF6 activity is necessary for nutrient transporter recycling from the TRE, then reducing ARF6-GTP with SecinH3 should recapitulate the recycling block induced by sphingolipids. To measure recycling, HeLa cells were treated with ceramide or 893 to induce CD98 and GLUT1 internalization and cytoplasmic levels of transporters were compared to untreated controls (Fig. 1.6G). Washing out sphingolipids after 1 h reduced the amount of intracellular transporter analogous to results obtained in SupB15 leukemia cells (Figs. 1.2C and 1.6G). Inclusion of SecinH3 in the medium after 893/ceramide washout was sufficient to retain both CD98 and GLUT1 in swollen endosomal structures (Fig. 1.6G). Taken together, genetic and small molecule inhibitor studies indicate that reducing ARF6-GTP levels is sufficient to account for the sphingolipid-induced defect in nutrient transporter recycling.

To determine whether ARF6 inactivation was necessary for sphingolipid-induced nutrient transporter loss, we attempted to maintain ARF6-GTP in sphingolipid-treated cells. As mentioned above, the ARF6 GTPase cycle is critical for its normal function, and the constitutively-active ARF6-Q67L mutant disrupts rather than facilitates ARF6-dependent recycling (Cohen et al., 2007; D'Souza-Schorey et al., 1998; Donaldson, 2003; Donaldson et al., 2009; Eyster et al., 2009; Maldonado-Báez et al., 2013; Santy, 2002). Over-expression of ARF6 GEFs is commonly employed as a more physiologic means to activate ARF6 (Cohen and Donaldson, 2010; Kanamarlapudi, 2014; Santy and Casanova, 2001). However, GEF over-expression can also lead to ARF6 hyper-activation, inducing abnormal, non-physiologic phenotypes similar to the ARF6-Q67L mutant (Cohen et al., 2007; Li et al., 2012; Monier et al., 1998). The PH domain of SLM proteins bears significant homology to the PH domain of

cytohesin family GEFs, the cytohesin inhibitor SecinH3 recapitulated many of the effects of sphingolipids on endocytic trafficking (Figs. 1.6C-G), and cytohesin-3/GRP1 promotes GLUT4 recycling in response to insulin (Li et al., 2012). Thus, we attempted to maintain ARF6-GTP levels in sphingolipid-treated cells by over-expressing GRP1. GRP1 is activated by insulin-dependent, AKT-mediated phosphorylation of Ser155 and Thr280 (Li et al., 2012). Because we suspected that PP2A activation was upstream of ARF6 inactivation, a constitutively-active, phosphomimetic mutant where these serine and threonine residues were converted to aspartic acid (GRP1-DD) was also evaluated. HeLa cells were transfected with GFP (negative control), wildtype GRP1, or GRP1-DD and CD98 localization with or without 893 was monitored by immunofluorescence microscopy. As expected, 893 down-regulated CD98 in GFP-expressing cells leading to its accumulation in swollen endocytic structures (Fig. 1.7A). Over-expression of wild type GRP1 led to an unexpected phenotype: CD98 was no longer evenly distributed along the plasma membrane but rather collected in membrane ruffles and in small endosomes that accumulated in the perinuclear region. While CD98 localization to plasma membrane ruffles was not observed in cells expressing the activated mutant ARF6-Q67L, accumulation of CD98 in perinuclear vesicles is consistent with ARF6 hyper-activation (data not shown and (Eyster et al., 2009)). Given its basal effects on CD98 localization, it was not surprising that over-expression of wildtype GRP1 failed to protect from sphingolipid-induced nutrient transporter loss (Fig. 1.7A). Intriguingly, CD98 localization was not basally altered in GRP1-DD expressing cells despite the reported constitutive activity of this mutant (Fig. 1.7A and (Li et al., 2012)); sequencing of the plasmids used in this experiment confirmed the identity of the wildtype and mutant constructs. The increased localization of GRP1-DD to endosomes might contribute to its differential activity (Li et al., 2012). Importantly, GRP1-DD eliminated the endosomal CD98 signal in 893-treated cells (Fig. 1.7A), suggesting GRP1-DD might maintain recycling in sphingolipid-treated cells. Given that ARF6 inhibition destabilizes the TRE and GRP1-DD restores recycling, this mutant might also stabilize the TRE in 893-treated cells. Indeed, while MICAL-L1 positive tubules were

absent in GFP- and GRP1-expressing cells exposed to 893, MICAL-L1 tubules were readily detectable in GRP1-DD expressing cells exposed to 893 (Fig. 1.7B). Disappointingly, populations or clones stably expressing GRP1-DD had markedly lower expression levels of exogenous GRP1 compared to the transient over-expressing cells and were not protected from CD98 loss (data not shown). As a result, the ability of GRP1-DD to rescue cells from 893-induced ARF6 inactivation and cell death could not be evaluated. Moreover, changes in GRP1 phosphorylation in response to sphingolipids could not be detected using an antibody that recognizes phosphorylated AKT substrates (Li et al., 2012) (data not shown). In summary, these studies suggest that sphingolipids disrupt endocytic recycling by activating PP2A and inactivating ARF6 (Fig. 1.7C).

ARF6 inhibition contributes to the anti-neoplastic effects of synthetic sphingolipids. Sphingolipids selectively kill cancer cells in part by starving them secondary to nutrient transporter down-regulation (Guenther et al., 2008; Kim et al., 2016; Romero Rosales et al., 2011). If ARF6 inactivation blocks access to nutrients by limiting nutrient transporter recycling, then small molecules that inactivate ARF6 may sensitize cancer cells to suboptimal, non-cytotoxic concentrations of anti-neoplastic sphingolipids. In SupB15 leukemia cells, SecinH3 was not cytotoxic or even cytostatic as a single agent (Fig. 1.8A and not shown). At 5 μM, FTY720 blocked SupB15 cell proliferation but did not induce cell death. However, the combination of 5 μM FTY720 with a dose of SecinH3 that inactivates ARF6 (Fig. 1.5A) killed >60% of the leukemia cells in 72 h (Fig. 1.8A). As a single agent, SecinH3 did not affect the proliferation or viability of SW620 colorectal cancer cells, PC3 prostate cancer cells, MDA-MB-231 breast cancer cells, or MCF7 breast cancer cells (Fig. 1.8B-E and data not shown). However, in each of these cell lines, SecinH3 dramatically potentiated the effect of a suboptimal concentration of 893 suggesting that ARF6 inactivation contributes to sphingolipid-induced cell death. Similar results were obtained with the allosteric ARF6 inhibitor NAV2729 in MDA-MB-231

cells (Fig. 1.8F). *In vitro*, cancer cells are at least 10-fold more sensitive than non-transformed cells to the cytotoxic effects of 893, most likely because their oncogenic mutations drive anabolism and limit their ability to make adaptive metabolic changes that would compensate for reduced nutrient access (Kim et al., 2016). To test whether combining SecinH3 with 893 would reduce or expand this therapeutic index, colony formation by peripheral blood mononuclear cells was measured in the presence or absence of SecinH3 and 893. In contrast to our results in five different human cancer cell lines (Fig. 1.8A-E), SecinH3 did not sensitize PBMCs to 893 (Fig. 1.8G). In fact, SecinH3 may have partially protected normal cells from 893 although this effect was not statistically significant. These studies suggest that ARF6 inactivation contributes to the anti-neoplastic activity of sphingolipids and that combining ARF6 inhibitors with 893 could extend the dose range over which 893 is effective without increasing toxicity to normal proliferating cells.

1.4 Discussion

While we and others have previously shown that a subset of sphingolipids down-regulate glucose and amino acid transporters (Barthelemy et al., 2017; Bultynck et al., 2006; Chung et al., 2001; Guenther et al., 2008; Kim et al., 2016; Romero Rosales et al., 2011; Skrzypek et al., 1998; Summers et al., 1998), the molecular mechanism is incompletely defined. As restricting nutrient access is a key mode of action for both endogenous and synthetic anti-neoplastic sphingolipids, understanding the molecular mechanism underlying this phenotype will provide insight into normal cell biology and clarify which tumor cells will be sensitive and resistant to therapeutic approaches that involve sphingolipid delivery or generation. Studies in yeast suggest that both internalization and recycling of nutrient transporter proteins are affected by sphingolipids (Barthelemy et al., 2017; Bultynck et al., 2006; Chung et al., 2001; Kamble et al., 2011; Welsch et al., 2004). The work presented here demonstrates that sphingolipids block transporter recycling in mammalian cells. While the molecular details of sphingolipid-induced nutrient transporter loss differ between yeast and mammalian cells, there are several interesting parallels. SLM1/2 are localized to both the plasma membrane and eisosomes, structures composed of multiple BAR domain proteins that promote membrane tubulation and endocytosis (Olivera-Couto et al., 2011). Intriguingly, expression of yeast eisosome proteins in COS-7 cells resulted in a tubular staining pattern highly reminiscent of the MICAL-L1-positive TRE (Olivera-Couto et al., 2011). While the precise molecular relationships between the yeast and mammalian sphingolipid-responsive pathways are not yet clear, it is interesting to speculate that the eisosome endocytic recycling pathway is paralleled in mammalian cells by the ARF6-dependent TRE.

Although over-expression of a phosphomimetic mutant of GRP1 (GRP1-DD) rescued from both sphingolipid-induced nutrient transporter down-regulation and loss of the MICAL-L1-positive TRE (Fig. 1.7A-B), other ARF6-regulatory proteins may be affected by sphingolipids (Fig. 1.7C).

For example, RAB35-GTP negatively regulates ARF6 activity by recruiting the ARF6 GAP ACAP2 to the recycling endosome (Chesneau et al., 2012; Kobayashi and Fukuda, 2012; Rahajeng et al., 2012). RAB35 activation also leads to the loss of MICAL-L1-positive tubular endosomes similar to what was observed in sphingolipid-treated cells (Fig. 1.3C-F and 1.4A) (Rahajeng et al., 2012). However, using a published RAB35 effector pulldown assay (Chesneau et al., 2012), we were unable to detect reproducible changes in RAB35-GTP levels following sphingolipid treatment (not shown). This negative result is consistent with our finding that ACAP2 siRNA did not restore ARF6-GTP levels or CD98 trafficking in sphingolipid-treated cells (not shown). We were unable to demonstrate that PP2A activation is necessary for sphingolipid-induced ARF6 inactivation. However, the inability of C_2-dihydroceramide to activate PP2A (Chalfant et al., 2004; Kim et al., 2016) or trigger trafficking disruptions associated with ARF6 inactivation, our finding that the non-sphingolipid small molecule PP2A activator perphenazine (PPZ) recapitulates phenotypes associated with ARF6 inactivation, and the selective protection from sphingolipid-induced phenotypes by a phosphomimetic GRP1 mutant provide support for the model shown in Fig. 1.7C.

ARF6 has multiple pro-oncogenic roles and establishing a connection between tumor suppressive sphingolipids and this GTPase has implications beyond the effects on nutrient transporter trafficking. ARF6 activity is important for primary tumor growth in some models, although the mechanism is incompletely defined and may vary with tumor type. ARF6 is activated downstream of a variety of receptor tyrosine kinases that drive tumor growth (Hongu et al., 2015; Hu et al., 2013; Li et al., 2017; Morishige et al., 2008). ARF6 promotes recycling of the MET receptor tyrosine kinase (Parachoniak et al., 2011), and thus decreasing ARF6-GTP may reduce MET surface levels with important consequences for the highly invasive MET-driven cancers like hereditary kidney cancers, sporadic papillary renal cancer, hepatocellular carcinoma, and gastric cancer (Boccaccio and Comoglio, 2006; Danilkovitch-Miagkova and

Zbar, 2002). MET and ARF6 promote tumor angiogenesis by stimulating β1-integrin recycling in a GRP1-dependent manner (Hongu et al., 2015). Melanoma and lung tumor isograft growth is compromised in mice lacking ARF6 selectively in endothelial cells, and treatment with the cytohesin inhibitor SecinH3 limited tumor growth and blocked angiogenesis in vivo (Bill et al., 2012; Hongu et al., 2015). SecinH3 has also been shown to limit primary tumor growth in other models, including breast cancer and colorectal cancer (Pan et al., 2014; Zhao et al., 2016). The structurally unrelated allosteric ARF6 inhibitor NAV-2729 was recently shown to inhibit tumor growth in a uveal melanoma model (Yoo et al., 2016). These studies with small molecule ARF6 inhibitors indicate that ARF6 is an actionable target in cancer. The results presented here suggest that endogenous sphingolipids and sphingolipid-like small molecules such as 893 may selectively kill cancer cells in part through ARF6 inactivation (Fig. 1.8; (Kim et al., 2016)). Moreover, sphingolipid-like agents or chemotherapies that increase ceramide generation (Dimanche-Boitrel et al., 2011; Morad and Cabot, 2013; Ogretmen and Hannun, 2001, 2004) may be even more effective when used in combination with SecinH3 or NAV-2729.

ARF6 also has a well-documented role in metastasis in breast cancer, melanoma, and clear cell renal carcinoma (Grossmann et al., 2013; Hashimoto et al., 2004, 2016; Hu et al., 2013; Loskutov et al., 2015; Morishige et al., 2008; Muralidharan-Chari et al., 2009a, 2009b; Tague et al., 2004; Yoo et al., 2016). Invadopodia are actin-rich cellular protrusions enriched with various matrix proteases that form cell-ECM contacts for matrix degradation and subsequent tumor cell intravasation into the vasculature (Paz et al., 2014). ARF6 activity is required for invadopodia formation and subsequent localized matrix degradation (Hashimoto et al., 2004). Membrane-tethered membrane type 1-matrix metalloproteinase (MT1-MMP) is secreted from cancer cells and promotes metastasis secondary to collagen breakdown (Marchesin et al., 2015; Paz et al., 2014; Sodek et al., 2007). ARF6 activity promotes recycling of MT1-MMP to the plasma membrane for release to the extracellular matrix (Loskutov et al., 2015; Marchesin et al., 2015).

Lastly, tumor-derived microvesicles can promote angiogenesis, immune suppression, tumor invasion, and metastasis (D'Souza-Schorey and Clancy, 2012). ARF6 activation also promotes the release of microvesicles containing matrix proteases like MT1-MMP (Muralidharan-Chari et al., 2009b). Given the multi-faceted roles of ARF6 in tumor cell invasion and metastasis, whether ceramide and synthetic sphingolipids like 893 limit metastasis as a consequence of ARF6 inactivation merits further evaluation.

1.5 Materials and Methods

Cell culture. SupB15, MDA-MB-231, SW620, and PC3 cells were obtained from the ATCC. Normal, non-transformed hematopoietic FL5.12 cells were obtained from Craig B. Thompson (Memorial Sloan Kettering Cancer Center, New York, NY, USA), HeLa cells from Steve Caplan (University of Nebraska Medical Center, Omaha, NE, USA), and MCF7 cells from the Translational Oncology Research Laboratory at UCLA (University of California Los Angeles, Los Angeles, CA, USA). PBMCs were obtained through the CTSA-supported Institute for Clinical and Translational Science at UCI under IRB protocols 2015-1883 (Edinger) and 2001-2058 (ICTS). FL5.12 and SupB15 cells were maintained in RPMI 1640 supplemented with 10% fetal bovine serum (FBS), 10 mM HEPES, 55 μM β-mercaptoethanol, 2 mM L-glutamine, and 1% antibiotics. FL5.12 media was additionally supplemented with 500 pg/ml recombinant murine IL-3. HeLa cells were maintained in DMEM with 4.5 g/L glucose and L-glutamine supplemented with 10% FBS and antibiotics. MDA-MB-231 and SW620 cells were cultured in DMEM containing 4.5 g/L glucose and L-glutamine supplemented with 10% FBS, 1 mM sodium pyruvate, and antibiotics. PC3 cells were cultured in F12-K medium supplemented with 10% FBS and antibiotics. MCF7 cells were cultured in RPMI 1640 supplemented with 10% FBS and 1% antibiotics. Cells were screened for *Mycoplasma* contamination at least every 6 months using the LookOut Mycoplasma PCR Detection Kit (Sigma, Cat# MP0035-1KT); the cell lines utilized in this study tested negative in all screens.

Antibodies. Antibodies were purchased from: BD Biosciences (PE Rat IgG1 κ isotype Cat #551979, unconjugated anti-mouse CD98 Cat #557479, unconjugated anti-human CD98 Cat #556074, unconjugated Mu IgG1 κ isotype Cat #554121, PE anti-human CD98 Cat #556077; PE Mu IgG1 κ isotype Cat #555749, Transferrin Receptor/CD71 Cat# 555534); Biolegend (PE anti-mouse CD98 Cat #128208, unconjugated anti-mouse CD98 Cat #128202); Cell Signaling

Technology (ARF6 Cat #5740, HA-tag Cat #2367, Myc-tag Cat #2276, EEA1 Cat# 3288, Lamp1 Cat# 9091, GM130 Cat#12480); Novus Biologicals (MICAL-L1 Cat# H00085377-B01P, GLUT1 Cat# NB300-666); LI-COR (IRDye 800CW Gt-α-Rb Cat #926-32211, IRDye 680LT Gt-α-Mu Cat #926-68020, IRDye 800CW Dk-α-Gt Cat #926-32214, IRDye 800CW Gt-α-Mu Cat #926-32210, IRDye 800CW Gt-α-Rt Cat #926-32219, IRDye 680LT Dk-α-Rb Cat #926-68023); BIO-RAD (TGN46 cat #AHP500G); Invitrogen (Alexa Fluor 488 goat anti-mouse Cat #A-11029, Alexa Fluor 488 goat anti-rabbit Cat #A-11008, Alexa Fluor 488 donkey anti-sheep Cat#A-11015, Alexa Fluor 594 goat anti-mouse Cat #A-11032, Alexa Fluor 594 donkey anti-mouse Cat#A-21203, Alexa Fluor 594 goat anti-rabbit Cat #R37117); Santa Cruz Biotechnology (ARF6 Cat #SC-7971).

Plasmids and transfection. GFP-tagged MICAL-L1 was a kind gift from Dr. Steve Caplan (University of Nebraska Medical Center, Omaha, NE, USA); pCDNA3-HA-ARF6-WT, -ARF6-Q67L and -ARF6-T27N were generously provided by Julie Donaldson (NIH, Bethesda, USA). pEF6-Myc-GRP1-WT and -GRP1-S155D/T240D were kind gifts of Dr. Victor W. Hsu (Harvard Medical School, Boston, MA, USA). Transient transfections were performed using a calcium phosphate transfection protocol as lipid transfection reagents interfere with the cellular response to sphingolipids (not shown).

Confocal microscopy. Microscopy samples were prepared by plating cells on glass cover slips, upon which cells were treated, fixed with 4% paraformaldehyde (10 min, RT), then permeablized and blocked with block solution (10% FCS, 0.3% saponin, azide in PBS) (30 min, 37°C). Coverslips were incubated in block solution with primary antibody overnight, rocking, at 4°C, then washed once with wash solution (0.03% saponin and azide in PBS), twice with PBS,

and incubated in secondary antibody at RT for 1 h while rocking. Cells were again washed, incubated in 1 mg/mL DAPI in wash solution, washed and mounted on slides using Vectashield Mounting Medium (Vector Laboratories Cat #H-1000). Confocal microscopy images were collected with Zeiss LSM780 confocal microscope with Plan Apochromat 63x/1.40 Oil DIC or Plan-Apochromat 100x/1.40 Oil DIC objectives and using Zeiss ZEN digital imaging software. ImageJ software was used for image processing. All images were collected with the same microscope and image processing settings. Cytoplasmic intensity in Fig. 1.6B and 1.6G was measured using ImageJ. A region of interest (ROI) beneath the plasma membrane and excluding the nucleus was selected and the mean gray value (MGV) measured. Fluorescence intensity is expressed as the MGV within the ROI after subtracting the background MGV. To measure percent of cells containing tubular MICAL-L1 staining (Fig. 1.3D, 1.6F, S1.7B), at least 20 different fields of view containing between 5-10 cells were measured.

Flow cytometry. Viability was measured by vital dye exclusion using 1 mg/ml DAPI. For CD98 surface staining, 50,000-200,000 cells were incubated for 30 min on ice with primary antibody diluted in FACS block (10% FBS and 0.05% NaN_3 in PBS). Cells were washed twice with FACS wash (2% FBS and 0.05% NaN_3 in PBS) and suspended in FACS wash containing 1 mg/ml DAPI. Analysis was restricted to live cells. For the transferrin internalization assay, 100,000 cells were incubated on ice for 1 h with biotinylated transferrin (100 µg/ml) in blocking buffer (1% BSA in PBS). Cells were washed twice with blocking buffer, resuspended in complete growth medium on ice, and warmed to 37°C for the indicated intervals. Following internalization, cells were fixed with 1% paraformaldehyde and stained with APC-tagged streptavidin. For the transferrin recycling assay, cells were incubated with vehicle or FTY720 (5 µM) and Alexa Fluor 488-transferrin (1 µg/ml). Following internalization, cells were resuspended in vehicle or FTY720

without transferrin for the indicated intervals. Surface transferrin was stripped with pH 5.0 buffer. Samples were evaluated on a Becton Dickinson LSRII flow cytometer.

Measurement of ARF6-GTP levels. ARF6-GTP was quantified as previously described (Cohen and Donaldson, 2010). Briefly, pGEX plasmid expressing GST (control) or GST-VHS-GAT (effector pull-down construct) was transformed into BL21 cells. Protein expression was induced with IPTG (0.6 mM). Proteins were isolated using glutathione Sepharose 4B beads (Sigma-Aldrich, Cat #17-0756-01). Protein was quantified using a BCA assay (Thermo Scientific Cat #23223). Depending on ARF6 protein expression level, 50-200 µg cell lysate protein was combined with 40 µg of GST-bound or GST-GGA3-VHS-GAT-bound beads and rocked at 4°C for 1 h. Beads were washed three times with lysis buffer and protein eluted in 10 µL 2X NuPAGE loading buffer. Total ARF6 protein levels were evaluated using 10% of the pull-down lysate.

Western blotting. Cell lysates were prepared in Triton X-100 or RIPA lysis buffer containing 1X c0mplete protease inhibitor (ROCHE Cat. #11697498001 or Pierce Cat. #88265). Protein concentration was quantified using Pierce BCA protein assay (Thermo Scientific Cat. #23223). Western blot samples were prepared in 1X NuPAGE sample buffer (Invitrogen Cat. #NP0007) supplemented with 1X protease inhibitor and 50 mM DTT. Samples were run on Invitrogen NuPAGE 4-12% Bis-Tris Gels (Cat #NP0336BOX) and transferred to BioTrace NT nitrocellulose membrane (Pall Cat #66485). Nitrocellulose blots were incubated in blocking solution (5% bovine serum albumin, 0.05% NaN_3 in 1X TBST) for 1 h then incubated overnight at 4°C in blocking solution containing primary antibody at the recommended dilution. Blots were washed three times in 1X TBST, incubated at RT for 1 h in blocking solution containing secondary

antibody (1:10,000), then washed three times in TBST. Blots were imaged and quantified using a LI-COR Odyssey SA imaging system.

1.6 Acknowledgements

The authors would like to thank Lee Bardwell, David Fruman, Anand Ganesan, Grant MacGregor, and Christine Sütterlin for input, assistance and access to equipment; and Julie Donaldson, Steve Caplan, and Victor Hsu for generously sharing plasmids.

1.7 Competing interests statement

A.L.E. is an inventor on a patent application covering the synthesis of SH-BC-893 and its use as an anti-cancer agent.

1.8 Author contributions

Conceptualization: B.T.F., M.U.R., E.M.S., A.L.E.; Methodology: B.T.F., M.U.R., E.M.S, A.N.M., A.L.E.; Validation: B.T.F., M.U.R.; Formal analysis: B.T.F., M.U.R., A.L.E.; Investigation: B.T.F., M.U.R., G.L., E.M.S., A.N.M., J.Y., Y.J., J.N., K.O., S.G.R., V.D.M., D.V.C.; Resources: A.L.E.; Data curation: B.T.F., M.U.R., A.L.E.; Writing - original draft: B.T.F., M.U.R., A.L.E.; Writing - review & editing: B.T.F., M.U.R., A.L.E.; Visualization: B.T.F., M.U.R., A.L.E.; Supervision: A.L.E.; Project administration: B.T.F., M.U.R., A.L.E.; Funding acquisition: A.L.E.

1.9 Funding

This work was supported by grants to ALE from the NIH (R01 GM089919, R21 CA178230), CDMRP (W81XWH-11-1-0535 and W81XWH-15-1-0010), the American Cancer Society (RSG-11-111-01-CDD), the William Lawrence and Blanche Hughes Foundation, and the UCI CORCL.

MUR was funded by NIH Ruth L. Kirschstein Minority Fellowship (1F31GM106702). ES was supported by NIH T32-CA009054-37.

1.10 References

Barthelemy, C., Barry, A.O., Twyffels, L., and André, B. (2017). FTY720-induced endocytosis of yeast and human amino acid transporters is preceded by reduction of their inherent activity and TORC1 inhibition. Sci. Rep. *7*, 13816.

Bill, A., Schmitz, A., König, K., Heukamp, L.C., Hannam, J.S., and Famulok, M. (2012). Anti-proliferative effect of cytohesin inhibition in gefitinib-resistant lung cancer cells. PLoS One *7*, e41179.

Boccaccio, C., and Comoglio, P.M. (2006). Invasive growth: a MET-driven genetic programme for cancer and stem cells. Nat. Rev. Cancer *6*, 637–645.

Brinkmann, V., Billich, A., Baumruker, T., Heining, P., Schmouder, R., Francis, G., Aradhye, S., and Burtin, P. (2010). Fingolimod (FTY720): discovery and development of an oral drug to treat multiple sclerosis. Nat. Rev. Drug Discov. *9*, 883–897.

Bultynck, G., Heath, V.L., Majeed, A.P., Galan, J.-M., Haguenauer-Tsapis, R., and Cyert, M.S. (2006). Slm1 and slm2 are novel substrates of the calcineurin phosphatase required for heat stress-induced endocytosis of the yeast uracil permease. Mol. Cell. Biol. *26*, 4729–4745.

Cai, B., Xie, S., Caplan, S., and Naslavsky, N. (2014). GRAF1 forms a complex with MICAL-L1 and EHD1 to cooperate in tubular recycling endosome vesiculation. Front. Cell Dev. Biol. *2*, 22.

Chalfant, C.E., Szulc, Z., Roddy, P., Bielawska, A., and Hannun, Y.A. (2004). The structural requirements for ceramide activation of serine-threonine protein phosphatases. J. Lipid Res. *45*, 496–506.

Chen, B., Roy, S.G., McMonigle, R.J., Keebaugh, A., McCracken, A.N., Selwan, E., Fransson, R., Fallegger, D., Huwiler, A., Kleinman, M.T., et al. (2016). Azacyclic FTY720 analogues that limit nutrient transporter expression but lack S1P receptor activity and negative chronotropic effects offer a novel and effective strategy to kill cancer cells in vivo. ACS Chem. Biol. *11*, 409–414.

Chen, S., Li, L., Li, J., Liu, B., Zhu, X., Zheng, L., Zhang, R., and Xu, T. (2014). SEC-10 and RAB-10 coordinate basolateral recycling of clathrin-independent cargo through endosomal tubules in Caenorhabditis elegans. Proc. Natl. Acad. Sci. USA *111*, 15432–15437.

Chesneau, L., Dambournet, D., Machicoane, M., Kouranti, I., Fukuda, M., Goud, B., and Echard, A. (2012). An ARF6/Rab35 GTPase cascade for endocytic recycling and successful cytokinesis. Curr. Biol. *22*, 147–153.

Chung, N., Jenkins, G., Hannun, Y.A., Heitman, J., and Obeid, L.M. (2000). Sphingolipids signal heat stress-induced ubiquitin-dependent proteolysis. J. Biol. Chem. *275*, 17229–17232.

Chung, N., Mao, C., Heitman, J., Hannun, Y.A., and Obeid, L.M. (2001). Phytosphingosine as a specific inhibitor of growth and nutrient import in Saccharomyces cerevisiae. J. Biol. Chem. *276*, 35614–35621.

Cohen, L.A., and Donaldson, J.G. (2010). Analysis of Arf GTP-binding protein function in cells. Curr. Protoc. Cell Biol. *Chapter 3*, Unit 14.12.1–17.

Cohen, L.A., Honda, A., Varnai, P., Brown, F.D., Balla, T., and Donaldson, J.G. (2007). Active Arf6 recruits ARNO/cytohesin GEFs to the PM by binding their PH domains. Mol. Biol. Cell *18*, 2244–2253.

D'Souza-Schorey, C., and Clancy, J.W. (2012). Tumor-derived microvesicles: shedding light on novel microenvironment modulators and prospective cancer biomarkers. Genes Dev. *26*, 1287–1299.

D'Souza-Schorey, C., van Donselaar, E., Hsu, V.W., Yang, C., Stahl, P.D., and Peters, P.J. (1998). ARF6 targets recycling vesicles to the plasma membrane: insights from an ultrastructural investigation. J. Cell Biol. *140*, 603–616.

Danilkovitch-Miagkova, A., and Zbar, B. (2002). Dysregulation of Met receptor tyrosine kinase activity in invasive tumors. J. Clin. Invest. *109*, 863–867.

Daquinag, A., Fadri, M., Jung, S.Y., Qin, J., and Kunz, J. (2007). The yeast PH domain proteins Slm1 and Slm2 are targets of sphingolipid signaling during the response to heat stress. Mol. Cell. Biol. *27*, 633–650.

Dickson, R.C., Nagiec, E.E., Skrzypek, M., Tillman, P., Wells, G.B., and Lester, R.L. (1997). Sphingolipids are potential heat stress signals in Saccharomyces. J. Biol. Chem. *272*, 30196–30200.

Dimanche-Boitrel, M.-T., Rebillard, A., and Gulbins, E. (2011). Ceramide in chemotherapy of tumors. Recent Pat. Anticancer. Drug Discov. *6*, 284–293.

Dobrowsky, R.T., Kamibayashi, C., Mumby, M.C., and Hannun, Y.A. (1993). Ceramide activates heterotrimeric protein phosphatase 2A. J. Biol. Chem. *268*, 15523–15530.

Donaldson, J.G. (2003). Multiple roles for Arf6: sorting, structuring, and signaling at the plasma membrane. J. Biol. Chem. *278*, 41573–41576.

Donaldson, J.G., and Jackson, C.L. (2011). ARF family G proteins and their regulators: roles in membrane transport, development and disease. Nat. Rev. Mol. Cell Biol. *12*, 362–375.

Donaldson, J.G., Porat-Shliom, N., and Cohen, L.A. (2009). Clathrin-independent endocytosis: a unique platform for cell signaling and PM remodeling. Cell Signal. *21*, 1–6.

Douglas, L.M., and Konopka, J.B. (2014). Fungal membrane organization: the eisosome concept. Annu. Rev. Microbiol. *68*, 377–393.

Eyster, C.A., Higginson, J.D., Huebner, R., Porat-Shliom, N., Weigert, R., Wu, W.W., Shen, R.-F., and Donaldson, J.G. (2009). Discovery of new cargo proteins that enter cells through clathrin-independent endocytosis. Traffic *10*, 590–599.

Fadri, M., Daquinag, A., Wang, S., Xue, T., and Kunz, J. (2005). The pleckstrin homology domain proteins Slm1 and Slm2 are required for actin cytoskeleton organization in yeast and bind phosphatidylinositol-4,5-bisphosphate and TORC2. Mol. Biol. Cell *16*, 1883–1900.

Ghosh, R.N., Mallet, W.G., Soe, T.T., McGraw, T.E., and Maxfield, F.R. (1998). An endocytosed TGN38 chimeric protein is delivered to the TGN after trafficking through the endocytic recycling compartment in CHO cells. J. Cell Biol. *142*, 923–936.

Giridharan, S.S.P., Cai, B., Naslavsky, N., and Caplan, S. (2012). Trafficking cascades mediated by Rab35 and its membrane hub effector, MICAL-L1. Commun Integr Biol *5*, 384–387.

Giridharan, S.S.P., Cai, B., Vitale, N., Naslavsky, N., and Caplan, S. (2013). Cooperation of MICAL-L1, syndapin2, and phosphatidic acid in tubular recycling endosome biogenesis. Mol. Biol. Cell *24*, 1776–90, S1.

Grant, B.D., and Donaldson, J.G. (2009). Pathways and mechanisms of endocytic recycling. Nat. Rev. Mol. Cell Biol. *10*, 597–608.

Grossmann, A.H., Yoo, J.H., Clancy, J., Sorensen, L.K., Sedgwick, A., Tong, Z., Ostanin, K., Rogers, A., Grossmann, K.F., Tripp, S.R., et al. (2013). The small GTPase ARF6 stimulates β-catenin transcriptional activity during WNT5A-mediated melanoma invasion and metastasis. Sci. Signal. *6*, ra14.

Guenther, G.G., Peralta, E.R., Rosales, K.R., Wong, S.Y., Siskind, L.J., and Edinger, A.L. (2008). Ceramide starves cells to death by downregulating nutrient transporter proteins. Proc. Natl. Acad. Sci. USA *105*, 17402–17407.

Guenther, G.G., Liu, G., Ramirez, M.U., McMonigle, R.J., Kim, S.M., McCracken, A.N., Joo, Y., Ushach, I., Nguyen, N.L., and Edinger, A.L. (2014). Loss of TSC2 confers resistance to ceramide and nutrient deprivation. Oncogene *33*, 1776–1787.

Hannun, Y.A., and Obeid, L.M. (2008). Principles of bioactive lipid signalling: lessons from sphingolipids. Nat. Rev. Mol. Cell Biol. *9*, 139–150.

Hashimoto, S., Onodera, Y., Hashimoto, A., Tanaka, M., Hamaguchi, M., Yamada, A., and Sabe, H. (2004). Requirement for Arf6 in breast cancer invasive activities. Proc. Natl. Acad. Sci. USA *101*, 6647–6652.

Hashimoto, S., Mikami, S., Sugino, H., Yoshikawa, A., Hashimoto, A., Onodera, Y., Furukawa, S., Handa, H., Oikawa, T., Okada, Y., et al. (2016). Lysophosphatidic acid activates Arf6 to promote the mesenchymal malignancy of renal cancer. Nat. Commun. *7*, 10656.

Hongu, T., Funakoshi, Y., Fukuhara, S., Suzuki, T., Sakimoto, S., Takakura, N., Ema, M., Takahashi, S., Itoh, S., Kato, M., et al. (2015). Arf6 regulates tumour angiogenesis and growth through HGF-induced endothelial β1 integrin recycling. Nat. Commun. *6*, 7925.

Hu, Z., Xu, R., Liu, J., Zhang, Y., Du, J., Li, W., Zhang, W., Li, Y., Zhu, Y., and Gu, L. (2013). GEP100 regulates epidermal growth factor-induced MDA-MB-231 breast cancer cell invasion through the activation of Arf6/ERK/uPAR signaling pathway. Exp. Cell Res. *319*, 1932–1941.

Kamble, C., Jain, S., Murphy, E., and Kim, K. (2011). Requirements of Slm proteins for proper eisosome organization, endocytic trafficking and recycling in the yeast Saccharomyces cerevisiae. J. Biosci. *36*, 79–96.

Kanamarlapudi, V. (2014). Exchange factor EFA6R requires C-terminal targeting to the plasma membrane to promote cytoskeletal rearrangement through the activation of ADP-ribosylation factor 6 (ARF6). J. Biol. Chem. *289*, 33378–33390.

Kim, S.M., Roy, S.G., Chen, B., Nguyen, T.M., McMonigle, R.J., McCracken, A.N., Zhang, Y., Kofuji, S., Hou, J., Selwan, E., et al. (2016). Targeting cancer metabolism by simultaneously disrupting parallel nutrient access pathways. J. Clin. Invest. *126*, 4088–4102.

Kobayashi, H., and Fukuda, M. (2012). Rab35 regulates Arf6 activity through centaurin-β2 (ACAP2) during neurite outgrowth. J. Cell Sci. *125*, 2235–2243.

Kowluru, A., and Metz, S.A. (1997). Ceramide-activated protein phosphatase-2A activity in insulin-secreting cells. FEBS Lett. *418*, 179–182.

Li, J., Malaby, A.W., Famulok, M., Sabe, H., Lambright, D.G., and Hsu, V.W. (2012). Grp1 plays a key role in linking insulin signaling to glut4 recycling. Dev. Cell *22*, 1286–1298.

Li, R., Peng, C., Zhang, X., Wu, Y., Pan, S., and Xiao, Y. (2017). Roles of Arf6 in cancer cell invasion, metastasis and proliferation. Life Sci. *182*, 80–84.

Loskutov, Y.V., Kozyulina, P.Y., Kozyreva, V.K., Ice, R.J., Jones, B.C., Roston, T.J., Smolkin, M.B., Ivanov, A.V., Wysolmerski, R.B., and Pugacheva, E.N. (2015). NEDD9/Arf6-dependent endocytic trafficking of matrix metalloproteinase 14: a novel mechanism for blocking mesenchymal cell invasion and metastasis of breast cancer. Oncogene *34*, 3662–3675.

Maldonado-Báez, L., Williamson, C., and Donaldson, J.G. (2013). Clathrin-independent endocytosis: a cargo-centric view. Exp. Cell Res. *319*, 2759–2769.

Marchesin, V., Castro-Castro, A., Lodillinsky, C., Castagnino, A., Cyrta, J., Bonsang-Kitzis, H., Fuhrmann, L., Irondelle, M., Infante, E., Montagnac, G., et al. (2015). ARF6-JIP3/4 regulate endosomal tubules for MT1-MMP exocytosis in cancer invasion. J. Cell Biol. *211*, 339–358.

Maxfield, F.R., and McGraw, T.E. (2004). Endocytic recycling. Nat. Rev. Mol. Cell Biol. *5*, 121–132.

Monier, S., Chardin, P., Robineau, S., and Goud, B. (1998). Overexpression of the ARF1 exchange factor ARNO inhibits the early secretory pathway and causes the disassembly of the Golgi complex. J. Cell Sci. *111 (Pt 22)*, 3427–3436.

Montesinos, M.L., Castellano-Muñoz, M., García-Junco-Clemente, P., and Fernández-Chacón, R. (2005). Recycling and EH domain proteins at the synapse. Brain Res Brain Res Rev *49*, 416–428.

Morad, S.A.F., and Cabot, M.C. (2013). Ceramide-orchestrated signalling in cancer cells. Nat. Rev. Cancer *13*, 51–65.

Morishige, M., Hashimoto, S., Ogawa, E., Toda, Y., Kotani, H., Hirose, M., Wei, S., Hashimoto, A., Yamada, A., Yano, H., et al. (2008). GEP100 links epidermal growth factor receptor signalling to Arf6 activation to induce breast cancer invasion. Nat. Cell Biol. *10*, 85–92.

Muralidharan-Chari, V., Hoover, H., Clancy, J., Schweitzer, J., Suckow, M.A., Schroeder, V., Castellino, F.J., Schorey, J.S., and D'Souza-Schorey, C. (2009a). ADP-ribosylation factor 6 regulates tumorigenic and invasive properties in vivo. Cancer Res. *69*, 2201–2209.

Muralidharan-Chari, V., Clancy, J., Plou, C., Romao, M., Chavrier, P., Raposo, G., and D'Souza-Schorey, C. (2009b). ARF6-regulated shedding of tumor cell-derived plasma membrane microvesicles. Curr. Biol. *19*, 1875–1885.

Ogretmen, B., and Hannun, Y.A. (2001). Updates on functions of ceramide in chemotherapy-induced cell death and in multidrug resistance. Drug Resist Updat *4*, 368–377.

Ogretmen, B., and Hannun, Y.A. (2004). Biologically active sphingolipids in cancer pathogenesis and treatment. Nat. Rev. Cancer *4*, 604–616.

Olivera-Couto, A., Graña, M., Harispe, L., and Aguilar, P.S. (2011). The eisosome core is composed of BAR domain proteins. Mol. Biol. Cell *22*, 2360–2372.

Pan, T., Sun, J., Hu, J., Hu, Y., Zhou, J., Chen, Z., Xu, D., Xu, W., Zheng, S., and Zhang, S. (2014). Cytohesins/ARNO: the function in colorectal cancer cells. PLoS One *9*, e90997.

Parachoniak, C.A., Luo, Y., Abella, J.V., Keen, J.H., and Park, M. (2011). GGA3 functions as a switch to promote Met receptor recycling, essential for sustained ERK and cell migration. Dev. Cell *20*, 751–763.

Paz, H., Pathak, N., and Yang, J. (2014). Invading one step at a time: the role of invadopodia in tumor metastasis. Oncogene *33*, 4193–4202.

Perryman, M.S., Tessier, J., Wiher, T., O'Donoghue, H., McCracken, A.N., Kim, S.M., Nguyen, D.G., Simitian, G.S., Viana, M., Rafelski, S., et al. (2016). Effects of stereochemistry, saturation, and hydrocarbon chain length on the ability of synthetic constrained azacyclic sphingolipids to trigger nutrient transporter down-regulation, vacuolation, and cell death. Bioorg. Med. Chem. *24*, 4390–4397.

Prescott, A.R., Lucocq, J.M., James, J., Lister, J.M., and Ponnambalam, S. (1997). Distinct compartmentalization of TGN46 and beta 1,4-galactosyltransferase in HeLa cells. Eur. J. Cell Biol. *72*, 238–246.

Rahajeng, J., Giridharan, S.S.P., Cai, B., Naslavsky, N., and Caplan, S. (2012). MICAL-L1 is a tubular endosomal membrane hub that connects Rab35 and Arf6 with Rab8a. Traffic *13*, 82–93.

Reinecke, J.B., Katafiasz, D., Naslavsky, N., and Caplan, S. (2015). Novel functions for the endocytic regulatory proteins MICAL-L1 and EHD1 in mitosis. Traffic *16*, 48–67.

Romero Rosales, K., Singh, G., Wu, K., Chen, J., Janes, M.R., Lilly, M.B., Peralta, E.R., Siskind, L.J., Bennett, M.J., Fruman, D.A., et al. (2011). Sphingolipid-based drugs selectively kill cancer cells by down-regulating nutrient transporter proteins. Biochem. J. *439*, 299–311.

Sangodkar, J., Farrington, C.C., McClinch, K., Galsky, M.D., Kastrinsky, D.B., and Narla, G. (2016). All roads lead to PP2A: exploiting the therapeutic potential of this phosphatase. FEBS J. *283*, 1004–1024.

Santy, L.C. (2002). Characterization of a fast cycling ADP-ribosylation factor 6 mutant. J. Biol. Chem. *277*, 40185–40188.

Santy, L.C., and Casanova, J.E. (2001). Activation of ARF6 by ARNO stimulates epithelial cell migration through downstream activation of both Rac1 and phospholipase D. J. Cell Biol. *154*, 599–610.

Schweitzer, J.K., Sedgwick, A.E., and D'Souza-Schorey, C. (2011). ARF6-mediated endocytic recycling impacts cell movement, cell division and lipid homeostasis. Semin. Cell Dev. Biol. *22*, 39–47.

Selwan, E.M., Finicle, B.T., Kim, S.M., and Edinger, A.L. (2016). Attacking the supply wagons to starve cancer cells to death. FEBS Lett. *590*, 885–907.

Sharma, M., Giridharan, S.S.P., Rahajeng, J., Naslavsky, N., and Caplan, S. (2009). MICAL-L1 links EHD1 to tubular recycling endosomes and regulates receptor recycling. Mol. Biol. Cell *20*, 5181–5194.

Skrzypek, M.S., Nagiec, M.M., Lester, R.L., and Dickson, R.C. (1998). Inhibition of amino acid transport by sphingoid long chain bases in Saccharomyces cerevisiae. J. Biol. Chem. *273*, 2829–2834.

Sodek, K.L., Ringuette, M.J., and Brown, T.J. (2007). MT1-MMP is the critical determinant of matrix degradation and invasion by ovarian cancer cells. Br. J. Cancer *97*, 358–367.

Summers, S.A., Garza, L.A., Zhou, H., and Birnbaum, M.J. (1998). Regulation of insulin-stimulated glucose transporter GLUT4 translocation and Akt kinase activity by ceramide. Mol. Cell. Biol. *18*, 5457–5464.

Swingle, M., Ni, L., and Honkanen, R.E. (2007). Small-molecule inhibitors of ser/thr protein phosphatases: specificity, use and common forms of abuse. Methods Mol. Biol. *365*, 23–38.

Tague, S.E., Muralidharan, V., and D'Souza-Schorey, C. (2004). ADP-ribosylation factor 6 regulates tumor cell invasion through the activation of the MEK/ERK signaling pathway. Proc. Natl. Acad. Sci. USA *101*, 9671–9676.

Trajkovic, K., Hsu, C., Chiantia, S., Rajendran, L., Wenzel, D., Wieland, F., Schwille, P., Brügger, B., and Simons, M. (2008). Ceramide triggers budding of exosome vesicles into multivesicular endosomes. Science *319*, 1244–1247.

Vidal-Quadras, M., Gelabert-Baldrich, M., Soriano-Castell, D., Lladó, A., Rentero, C., Calvo, M., Pol, A., Enrich, C., and Tebar, F. (2011). Rac1 and calmodulin interactions modulate dynamics of ARF6-dependent endocytosis. Traffic *12*, 1879–1896.

Walseng, E., Bakke, O., and Roche, P.A. (2008). Major histocompatibility complex class II-peptide complexes internalize using a clathrin- and dynamin-independent endocytosis pathway. J. Biol. Chem. *283*, 14717–14727.

Walther, T.C., Brickner, J.H., Aguilar, P.S., Bernales, S., Pantoja, C., and Walter, P. (2006). Eisosomes mark static sites of endocytosis. Nature *439*, 998–1003.

Welsch, C.A., Roth, L.W.A., Goetschy, J.F., and Movva, N.R. (2004). Genetic, biochemical, and transcriptional responses of Saccharomyces cerevisiae to the novel immunomodulator FTY720 largely mimic those of the natural sphingolipid phytosphingosine. J. Biol. Chem. *279*, 36720–36731.

Yoo, J.H., Shi, D.S., Grossmann, A.H., Sorensen, L.K., Tong, Z., Mleynek, T.M., Rogers, A., Zhu, W., Richards, J.R., Winter, J.M., et al. (2016). ARF6 Is an Actionable Node that Orchestrates Oncogenic GNAQ Signaling in Uveal Melanoma. Cancer Cell *29*, 889–904.

Zhao, H., Ahirwar, D.K., Oghumu, S., Wilkie, T., Powell, C.A., Nasser, M.W., Satoskar, A.R., Li, D.Y., and Ganju, R.K. (2016). Endothelial Robo4 suppresses breast cancer growth and metastasis through regulation of tumor angiogenesis. Mol. Oncol. *10*, 272–281.

Zimmermann, P., Zhang, Z., Degeest, G., Mortier, E., Leenaerts, I., Coomans, C., Schulz, J., N'Kuli, F., Courtoy, P.J., and David, G. (2005). Syndecan recycling [corrected] is controlled by syntenin-PIP2 interaction and Arf6. Dev. Cell *9*, 377–388.

1.11 Figures

Figure 1.1

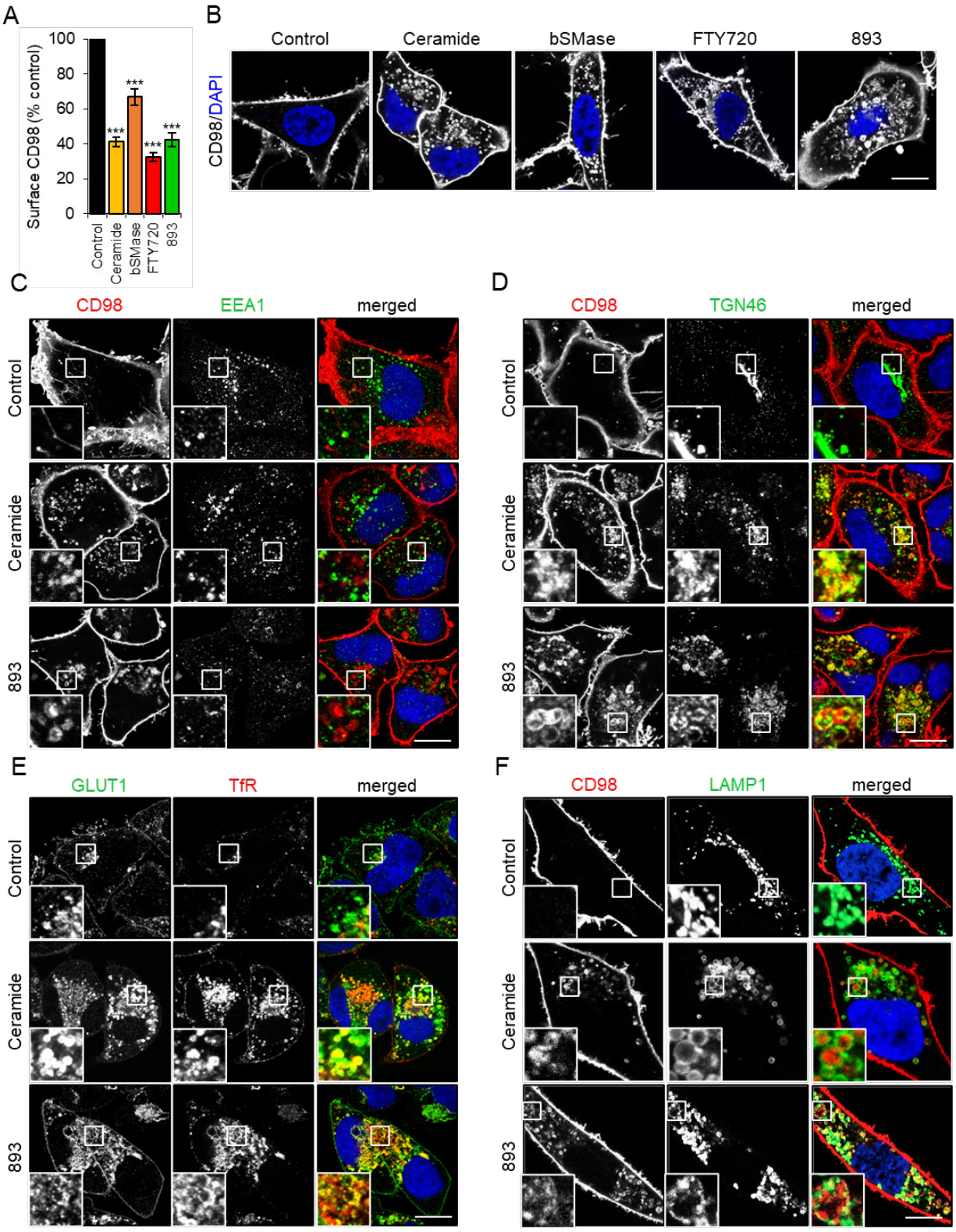

Figure 1.1: Natural and synthetic sphingolipids trap plasma membrane nutrient transporters along with recycling cargo. (A) FL5.12 cells were treated with vehicle, C_2-ceramide (50 μM), bacterial sphingomyelinase (bSMase; 100 mU/mL), FTY720 (5 μM), or SH-BC-893 (893, 5 μM) for 3 h then stained for surface CD98. (B) HeLa cells were treated as in (A) for 12 h then stained for CD98. All images were collected with the same microscope and image processing settings. (C-F) HeLa cells were treated with vehicle, C_2-ceramide (50 μM), or 893 (10 μM) for 12 h, then stained for CD98 and EEA1 (C), CD98 and TGN46 (D), GLUT1 and transferrin receptor (TfR) (E), or CD98 and LAMP1 (F). $n \geq 3$ in all panels. In (A), Means ± SEM are shown; using an ordinary one-way ANOVA to compare treated samples to control, *** = $p \leq 0.001$. Dunnett's test was used to correct for multiple comparisons. Scale bar, 10 μm. See also Supplementary Figures S1.1-S1.4.

Figure 1.2

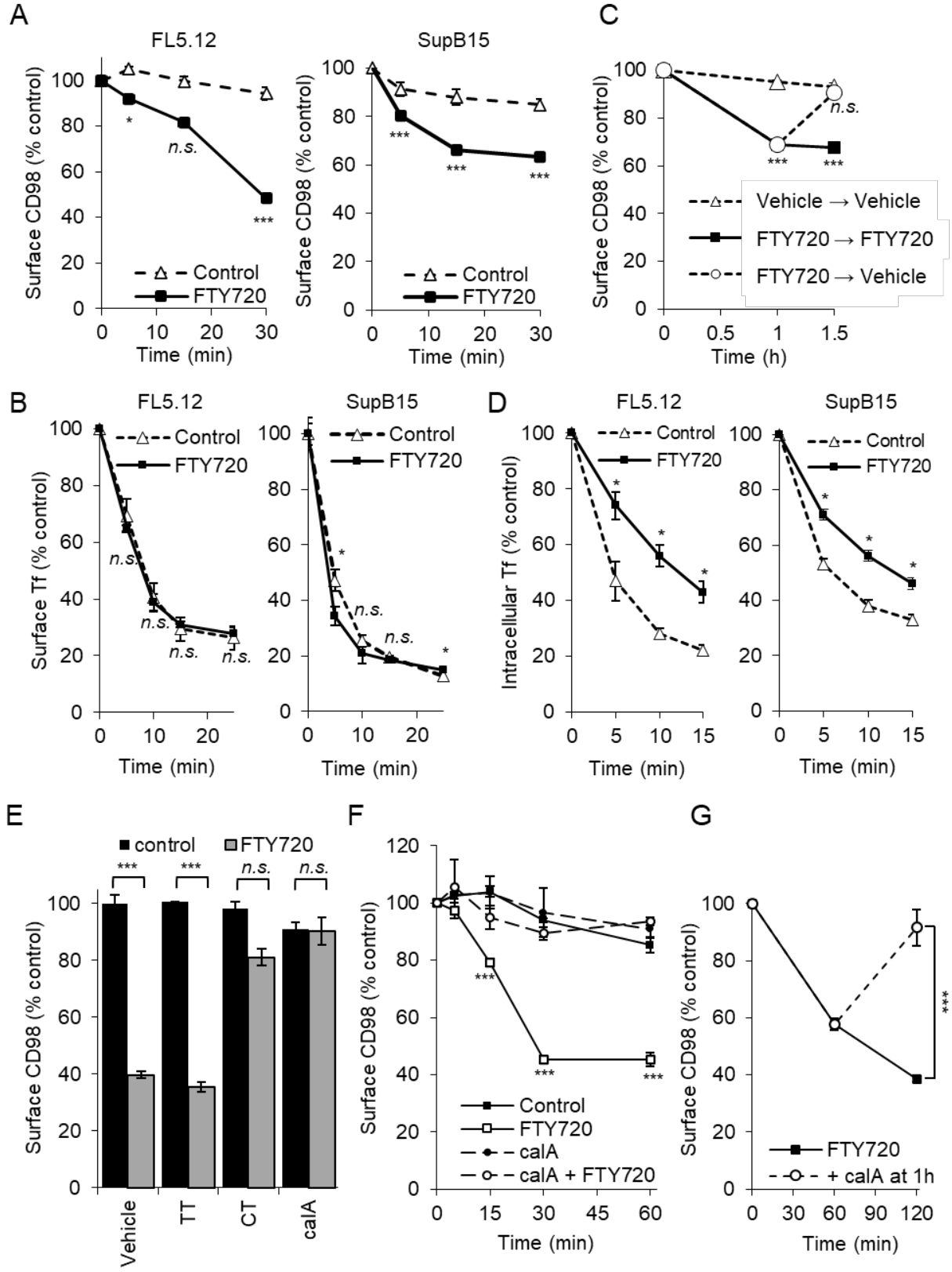
A
FL5.12
SupB15
Surface CD98 (% control)
Time (min)
Control
FTY720
C
Vehicle → Vehicle
FTY720 → FTY720
FTY720 → Vehicle
Time (h)
B
Surface Tf (% control)
D
Intracellular Tf (% control)
E
control
FTY720
Vehicle
TT
CT
calA
F
Control
FTY720
calA
calA + FTY720
G
FTY720
+ calA at 1h

Figure 1.2: Sphingolipids inhibit recycling of nutrient transporters in a PP2A-dependent manner. (A) Surface CD98 loss in FL5.12 and SupB15 cells. Cells were incubated with a primary, unconjugated CD98 antibody on ice for 30 min. Cells were then treated with vehicle or FTY720 at 37°C for the indicated times, incubated on ice with secondary antibody for 30 min, and surface CD98 measured by flow cytometry. (B) Transferrin uptake in FL5.12 and SupB15 cells with or without FTY720. (C) CD98 recycling in SupB15 cells. Cells were incubated with primary CD98 antibody as in (A) then treated with vehicle or FTY720 for 1 h at which point cells were washed and returned to vehicle- or FTY720-containing medium for 0.5 h. Surface CD98 levels were then measured by flow cytometry. (D) Tf recycling assay conducted in the presence or absence of FTY720. (E) FL5.12 cells pre-treated (1.5 h) with PP1 inhibitor tautomycin (TT, 200 nM) or PP2A inhibitors cantharidin (CT, 10 μM) or calyculin A (calA, 5 nM) were treated with FTY720 for 1 h and surface CD98 quantified by flow cytometry. (F) Internalization of surface CD98 was measured as in (A), cells were pre-treated with calyculinA (5 nM) for 1 h where indicated. (G) Following surface labeling with a primary antibody, FL5.12 cells were treated with FTY720 for 1 h at which point vehicle or calyculin A (10 nM) was added for an additional 1 h. Cells were then stained with secondary antibody and surface CD98 measured using flow cytometry. FTY720 was used at 5 μM, means ± SEM shown, $n \geq 3$ in all panels. Using two-tailed t test to compare sphingolipid-treated timepoints to vehicle timepoints, *n.s.* = not significant; * = $p \leq 0.05$; *** = $p \leq 0.001$.

Figure 1.3

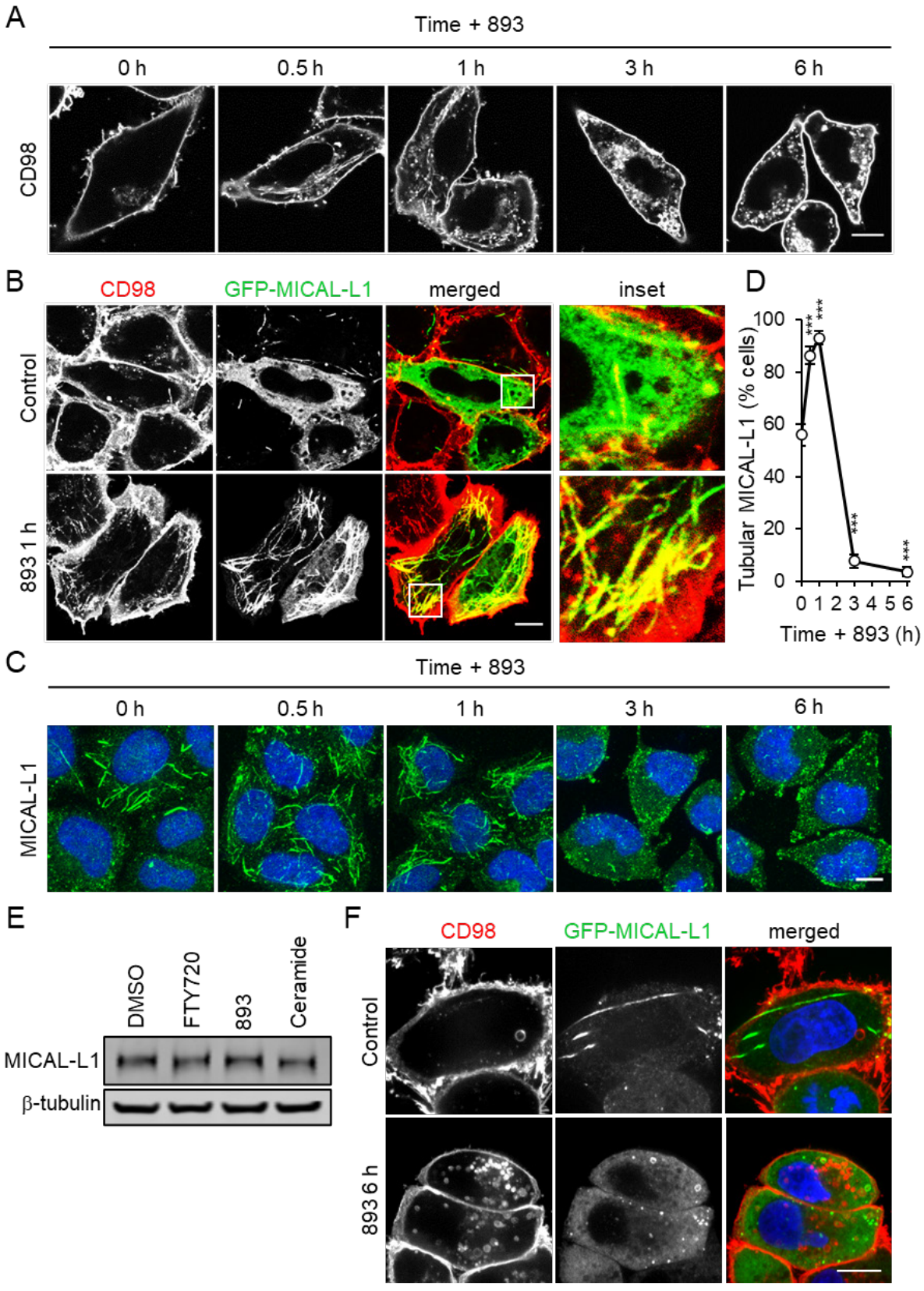
A
Time + 893
0 h
0.5 h
1 h
3 h
6 h
CD98
B
CD98
GFP-MICAL-L1
merged
inset
Control
893 1 h
D
Tubular MICAL-L1 (% cells)
100
80
60
40
20
0
***
0 1 2 3 4 5 6
Time + 893 (h)
C
Time + 893
0 h
0.5 h
1 h
3 h
6 h
MICAL-L1
E
DMSO
FTY720
893
Ceramide
MICAL-L1
β-tubulin
F
CD98
GFP-MICAL-L1
merged
Control
893 6 h

Figure 1.3: Sphingolipids send nutrient transporters to the tubular recycling endosome prior to its dissolution. (A) HeLa cells treated with 893 (10 μM) for 0.5, 1, 3, or 6 h were stained for CD98. (B) HeLa cells expressing GFP-MICAL-L1 were treated with 893 (10 μM) for 1 h and stained for CD98. (C) HeLa cells treated as in (A) but stained for MICAL-L1. (D) Quantification of (C); the percent of cells that exhibit tubular MICAL-L1 staining is graphed. Means ± SEM shown. Using an ordinary one-way ANOVA to compare to time zero, *** = p≤ 0.001. Dunnett's test was used to correct for multiple comparisons. (E) Representative blot for HeLa cells treated with FTY720 (10 μM), 893 (10 μM), C_2-ceramide (50 μM) for 6 h, lysed, and blotted for MICAL-L1 and tubulin. (F) HeLa cells expressing GFP-MICAL-L1 treated with 893 (10 μM) for 6 h and stained for CD98. Scale bar, 10 μm.

Figure 1.4

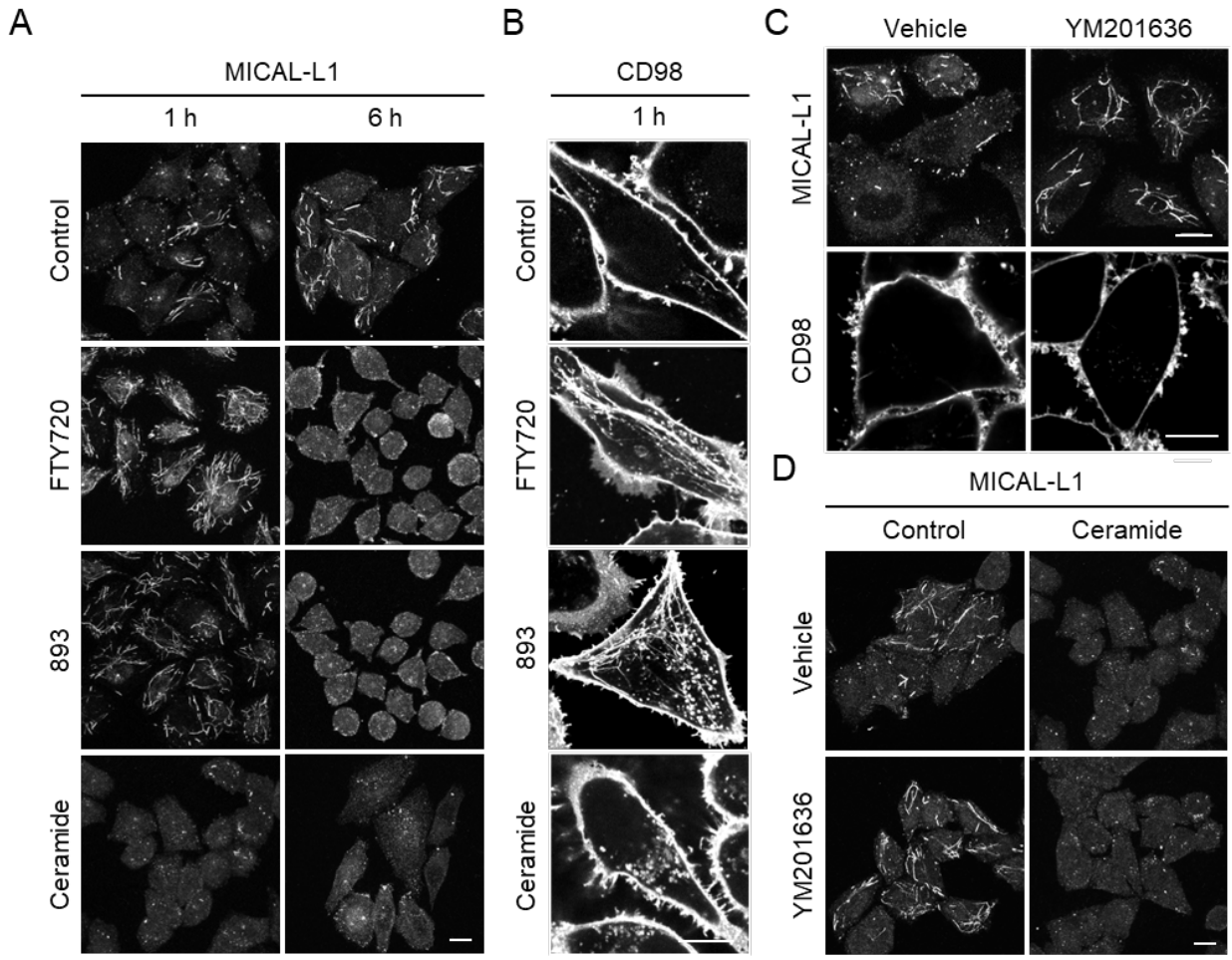

Figure 1.4: Hyper-tubulation of the TRE occurs downstream of PIKfyve inhibition. (A) HeLa cells treated with vehicle, FTY720 (10 μM), 893 (10 μM), or C_2-ceramide (50 μM) for 1 h or 6 h were stained for MICAL-L1. (B) HeLa cells treated with vehicle, FTY720 (10 μM), 893 (10 μM), or C_2-ceramide (50 μM) for 1 h and stained for CD98. (C) HeLa cells treated with PIKfyve inhibitor YM201636 (800 nM) for 1 h and stained for MICAL-L1 or CD98. (D) HeLa cells treated with C_2-ceramide (50 μM) or YM201636 (800 nM) alone or in combination for 1 h were stained for MICAL-L1. Scale bar, 10 μm.

Figure 1.5

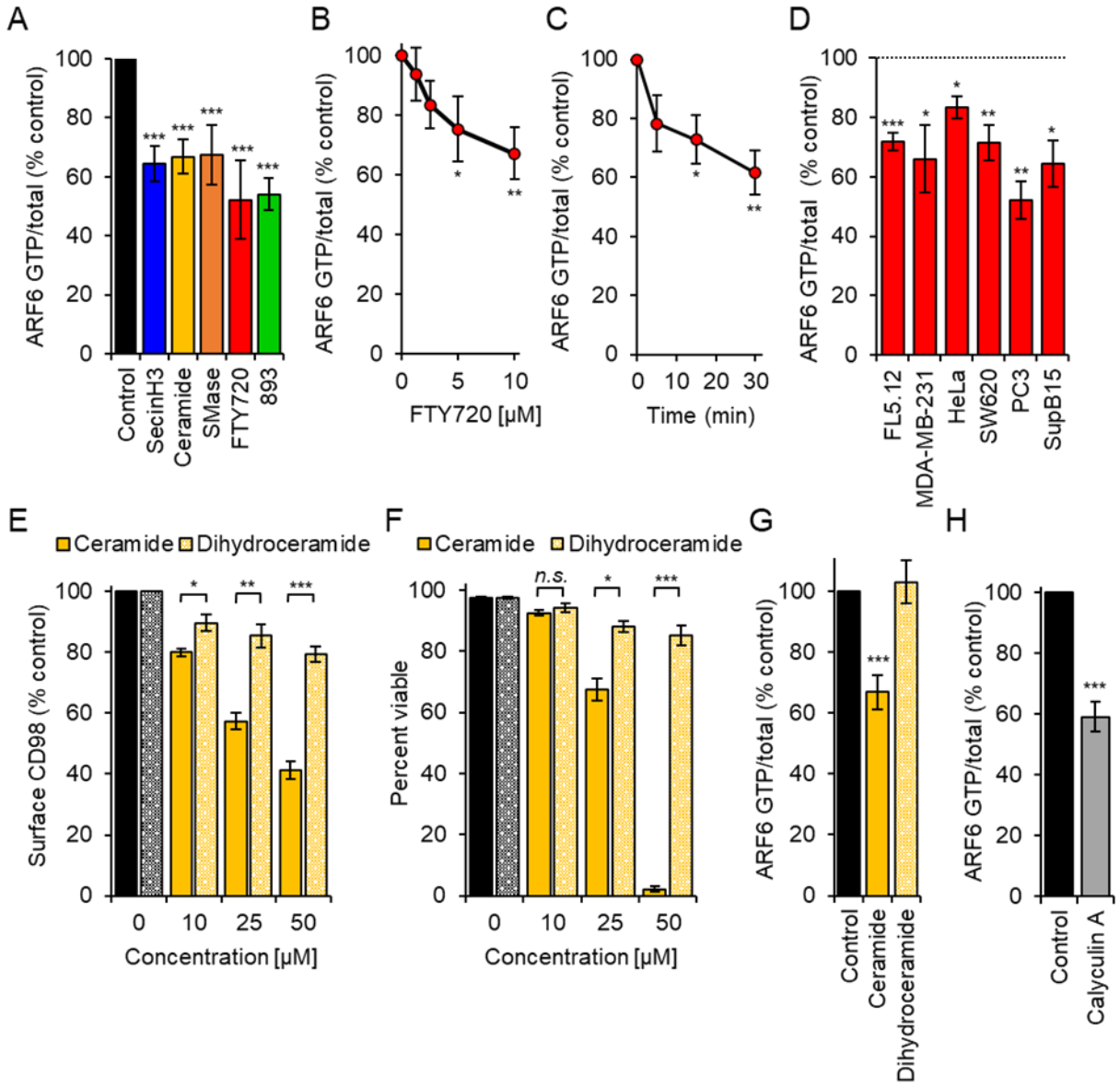

Figure 1.5: Endogenous and synthetic sphingolipids that down-regulate nutrient transporters also inactivate the ARF6 GTPase. (A) ARF6-GTP levels normalized to total ARF6 in FL5.12 cells treated with the cytohesin inhibitor SecinH3 (30 μM), C_2-ceramide (50 μM), bacterial sphingomyelinase (bSMase; 100 mU/mL), FTY720 (5 μM), or 893 (5 μM) for 3 h. (B,C) ARF6-GTP levels in FL5.12 cells treated with FTY720 (0, 1.25, 2.5, 5, or 10 μM) for 30 min (B) or with 10 μM FTY720 for 5, 15, or 30 min (C). (D) ARF6-GTP levels in FL5.12, MDA-

MB-231, HeLa, SW620, PC3, or SupB15 treated for 3 h with FTY720 (10 μM). (E) Steady state surface CD98 levels in FL5.12 cells treated with C_2-ceramide or C_2-dihydroceramide at the indicated concentrations for 3 h. (F) Viability of C_2-ceramide- or C_2-dihydroceramide-treated FL5.12 cells at 48 h. (G) ARF6-GTP levels in FL5.12 cells treated with C_2-ceramide (50 μM) or C_2-dihydroceramide (50 μM). (H) ARF6-GTP levels in FL5.12 cells treated with CalyculinA (10 nM) for 1 h. Means ± SEM shown, $n \geq 3$ in all panels. Using two-tailed t test (D-F,H) or ordinary one-way ANOVA (A-C,G), *n.s.* = not significant; * = $p \leq 0.05$; ** = $p \leq 0.01$; *** = $p \leq 0.001$. Dunnett's test was used to correct for multiple comparisons (A-C,G). See also Supplementary Figure S1.5.

Figure 1.6

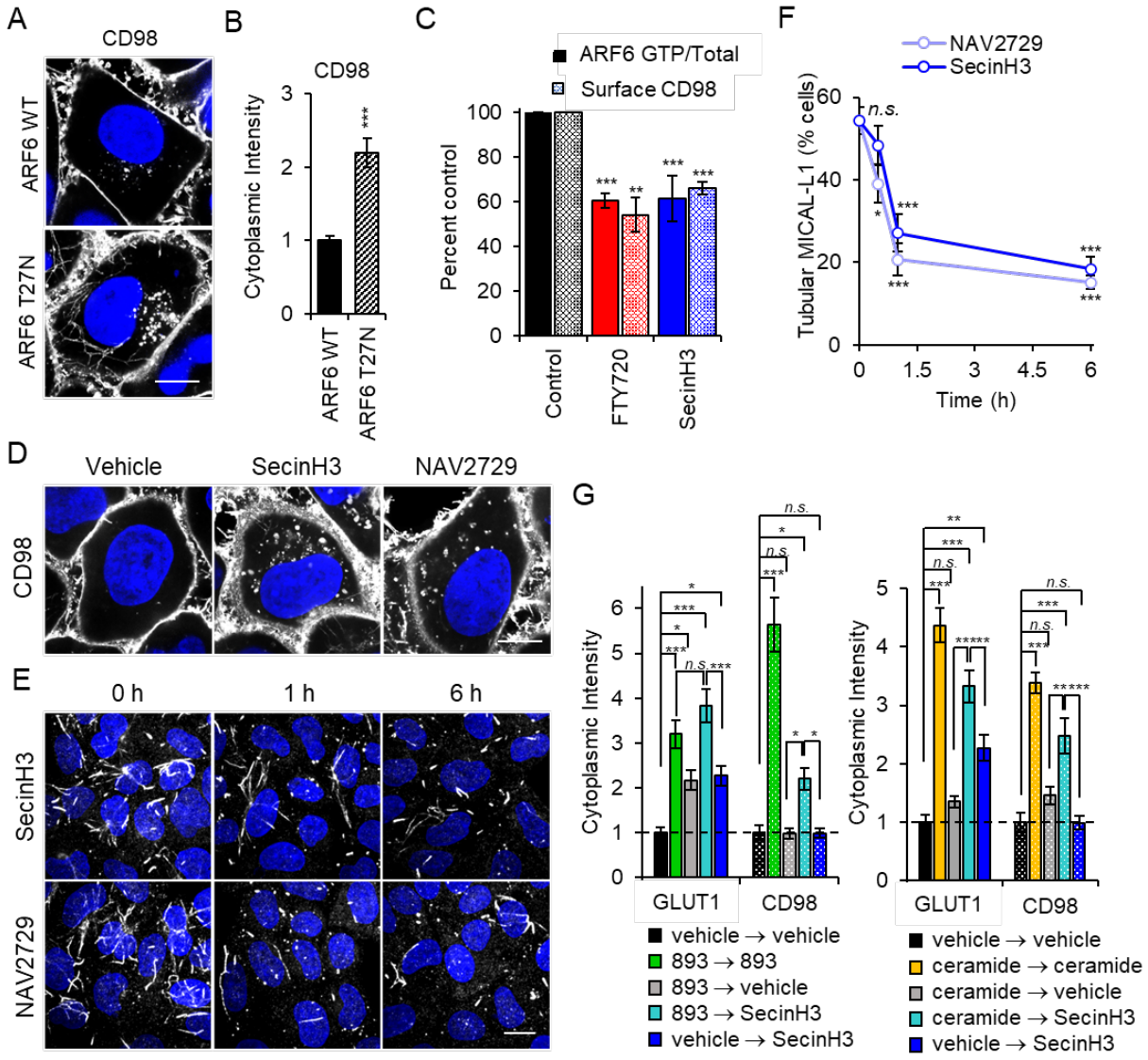

Figure 1.6: ARF6 inactivation is sufficient to inhibit nutrient transporter recycling. (A) HeLa cells expressing HA-ARF6 or HA-ARF6-T27N stained for CD98. (B) Quantification of intracellular CD98 intensity in (A). (C) Surface CD98 quantification and ARF6-GTP levels in FL5.12 cells treated with FTY720 (5 μM) or SecinH3 (30 μM) for 3 h. (D) HeLa cells treated with SecinH3 (30 μM) or NAV2729 (12.5 μM) for 16 h and stained for CD98. (E) HeLa cells treated with SecinH3 (30 μM) or NAV2729 (12.5 μM) for 1 or 6 h and stained for MICAL-L1. (F) Quantification of (E). (G) Cytoplasmic intensity quantification of CD98 and GLUT1 in HeLa cells

treated with vehicle, 893 (10 μM), or C_2-ceramide (50 μM) for 1 h, washed with PBS, then returned to 893 (10 μM) or placed in vehicle or SecinH3 (30 μM) for 2 h. Means ± SEM shown, $n \geq 3$ in all panels. Using a two-tailed t test (B) or an ordinary one-way ANOVA (C,F,G) to compare treated samples to controls, *n.s.* = not significant; * = $p \leq 0.05$; ** = $p \leq 0.01$; *** = $p \leq 0.001$. Dunnett's test was used in Fig. 1.6C and F and Tukey's test was used in Fig. 1.6G to correct for multiple comparisons. Scale bar, 10 μm. See also Supplementary Figures S1.6 and S1.7.

Figure 1.7

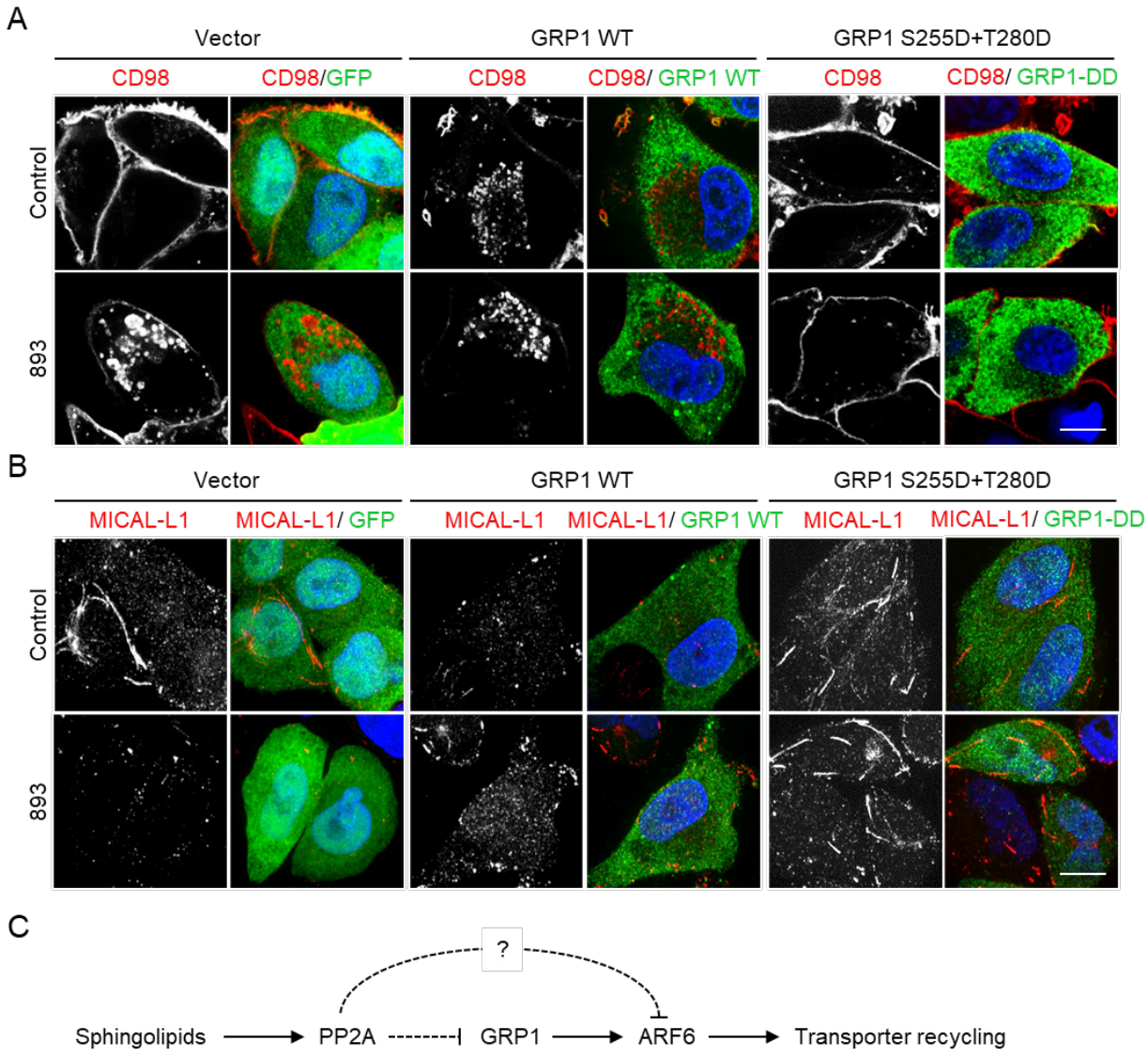

Figure 1.7: A phosphomimetic mutant of GRP1 protects nutrient transporter recycling from inhibition by 893. (A) HeLa cells expressing GFP alone, myc-tagged wildtype GRP1, or myc-tagged GRP1 S155D+T280D (GRP1-DD) were treated with 893 (5 μM) for 6 h and stained for GFP or myc tag and CD98. (B) As in (A), except stained for MICAL-L1 and myc tag or GFP. Scale bar, 10 μm. (C) Model for regulation of endocytic recycling by sphingolipids.

Figure 1.8

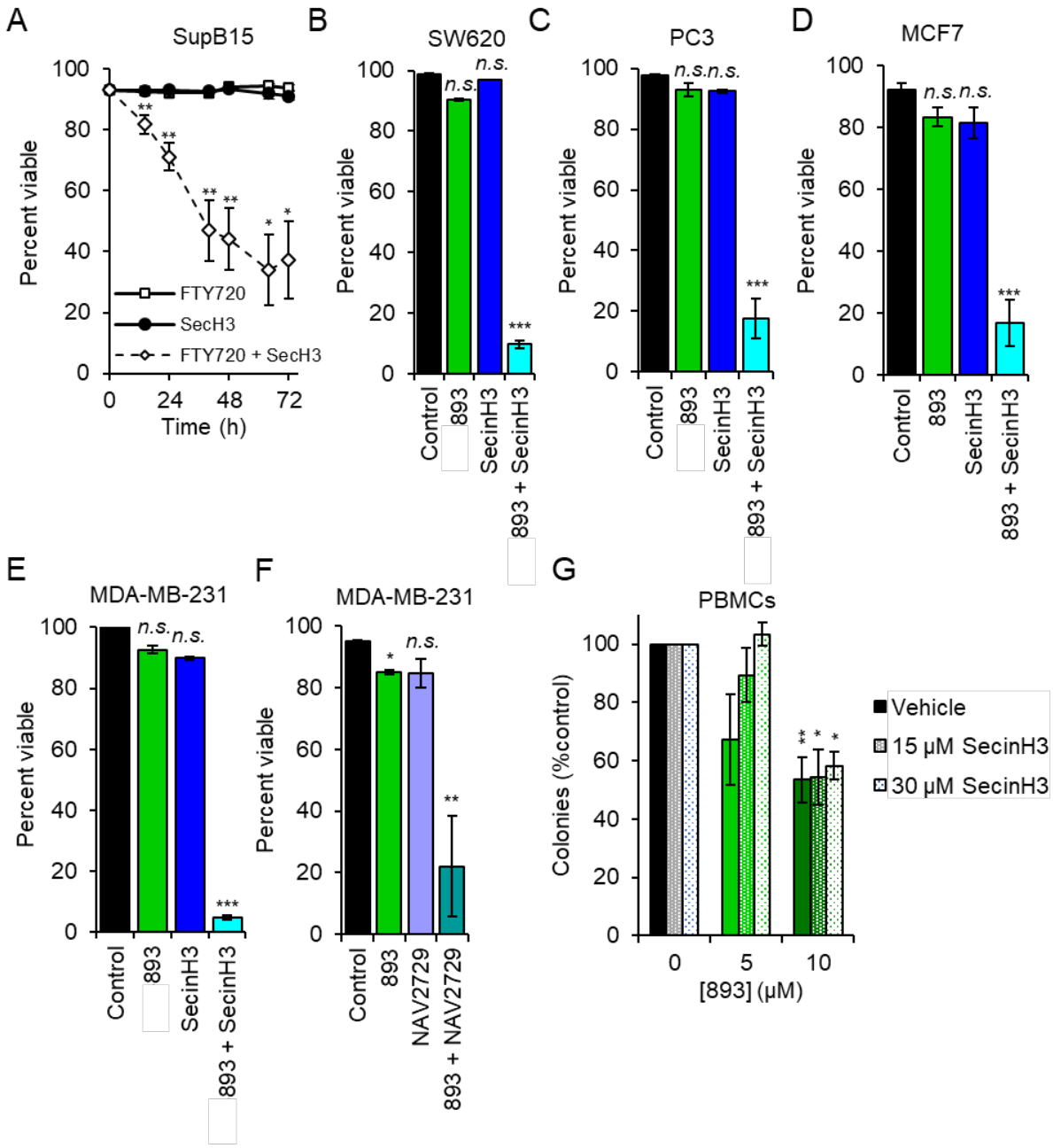

Figure 1.8: ARF6 inhibition enhances the anti-neoplastic effects of synthetic sphingolipids. (A) Viability of SupB15 cells treated with FTY720 (5 μM), SecinH3 (30 μM), or the combination. (B) Viability of SW620 cells treated with 893 (4 μM), SecinH3 (30 μM), or the combination for 120 h. (C) As in (B), but using PC3 cells at 144 h. (D) As in (B), except MCF7

cells at 120 h. (E) As in (B), but using MDA-MB-231 cells at 96 h. (F) As in (E), but using NAV2729 (6.25 μM) rather than SecinH3. (G) Peripheral blood mononuclear cell (PBMC) colony formation assay at the indicated doses of 893 and SecinH3. Means ± SEM shown, $n \geq 3$ in all panels. Using two-tailed t test (A) or ordinary one-way ANOVA (B-G) to compare to controls, *n.s.* = not significant; * = $p \leq 0.05$; ** = $p \leq 0.01$; *** = $p \leq 0.001$. Tukey's test was used to correct for multiple comparisons in B-G; statistics are relative to the respective control.

1.12 Supplementary Figures

Supplementary Fig. S1.1

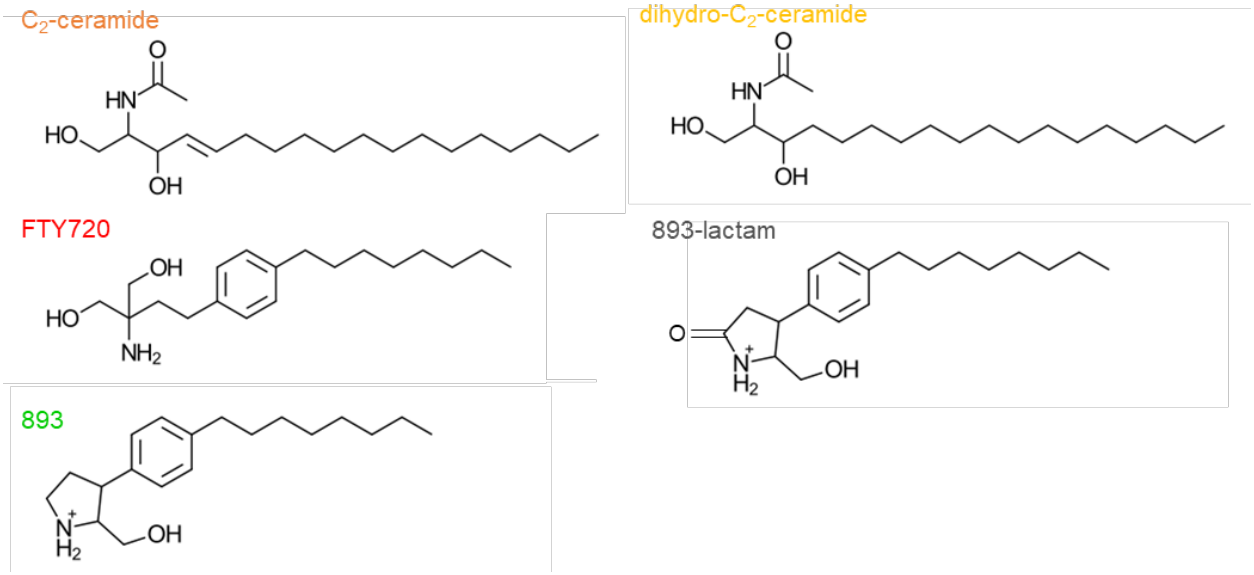

Supplementary Fig. S1.1: Sphingolipids used in this study. Related to Figures 1.1-1.8.

Structures of sphingolipids used in these studies.

Supplementary Fig. S1.2

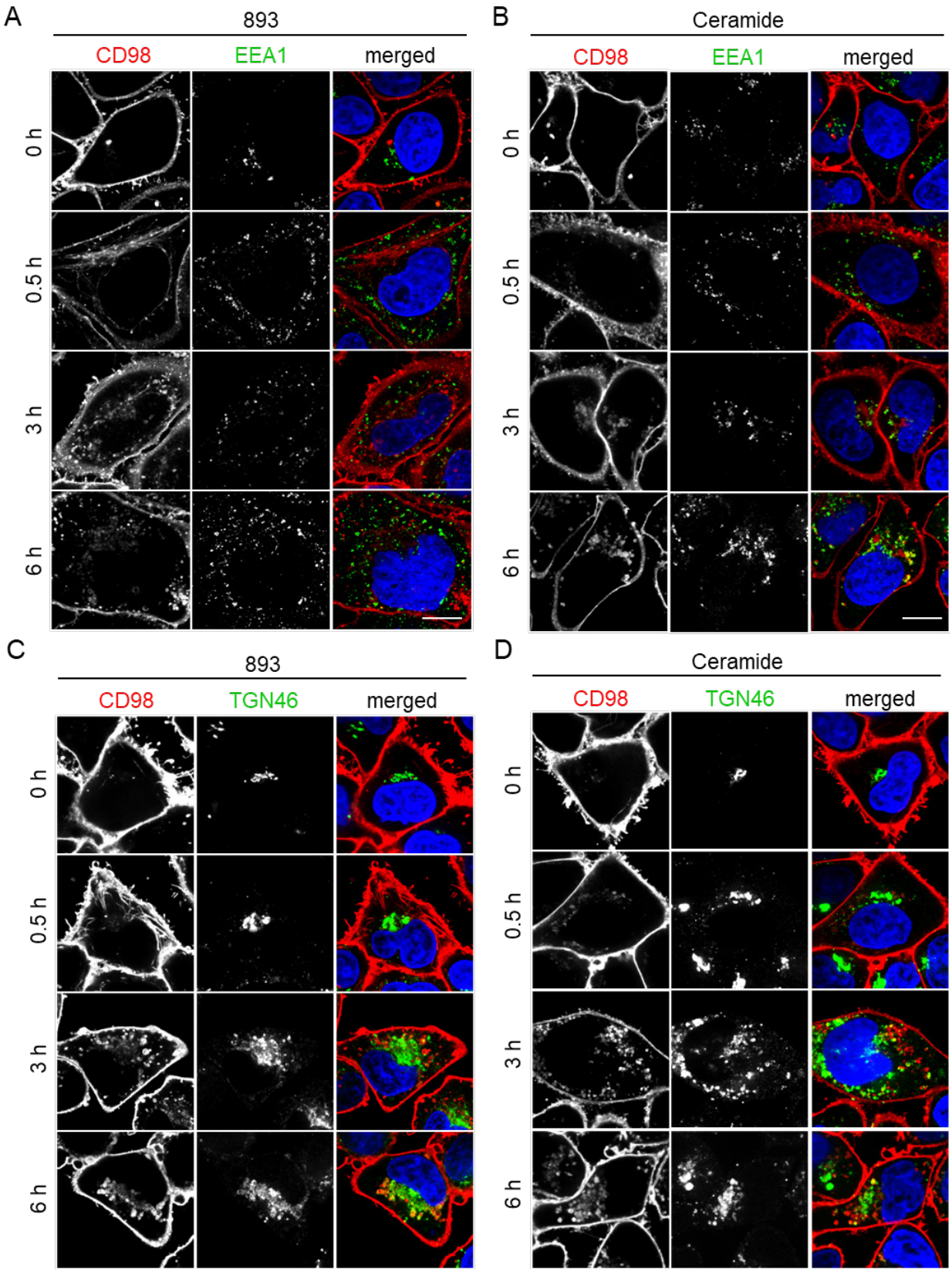

Supplementary Fig. S1.2: Transporters do not enter the early endosome or colocalize with TGN46 until late timepoints. Related to Figure 1.1. (A-B) HeLa cells were treated with 893 (10 μM) or C2-ceramide (50 μM) for 0.5, 3, or 6 h then stained for CD98 and EEA1. (C-D) HeLa cells were treated as in A&B and stained for CD98 and TGN46. Scale bar, 10 μm.

Supplementary Fig. S1.3

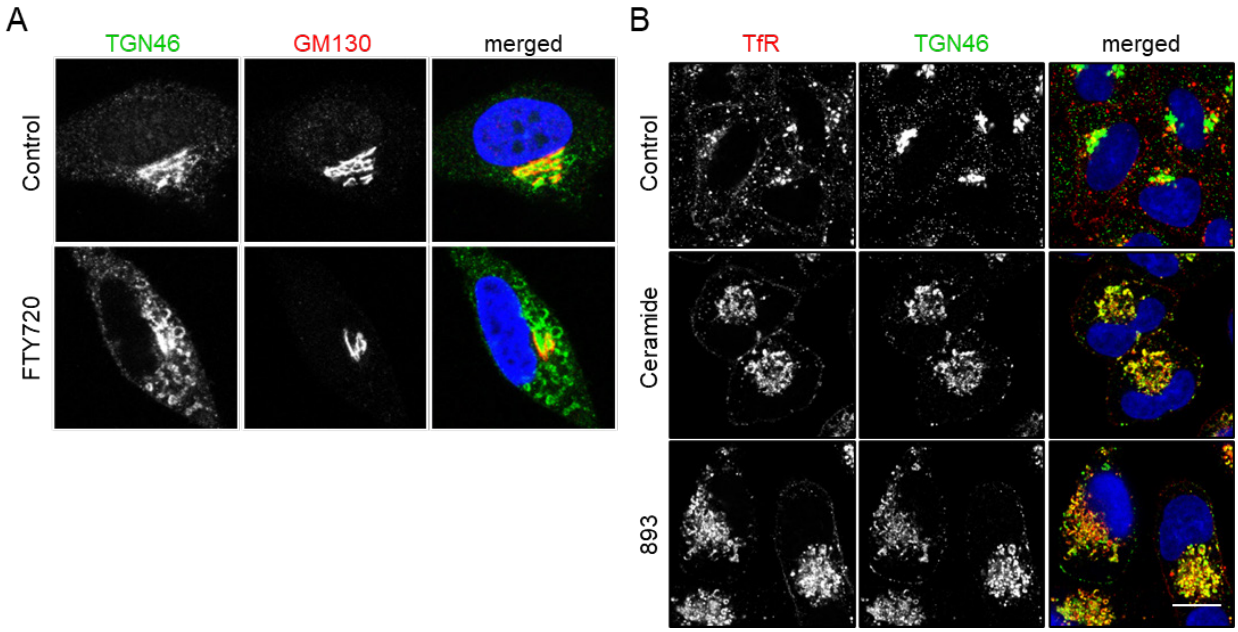

Supplementary Figure S1.3: TGN46 is mislocalized in sphingolipid-treated cells. Related to Figure 1.1. (A) HeLa cells were treated with FTY720 (5 μM) for 12 h and stained for TGN46 and GM130. (B) HeLa cells were treated with vehicle, C_2-ceramide (50 μM), or 893 (10 μM) for 12 h and stained for TfR and TGN46. Scale bar, 10 μm.

Supplementary Fig. S1.4

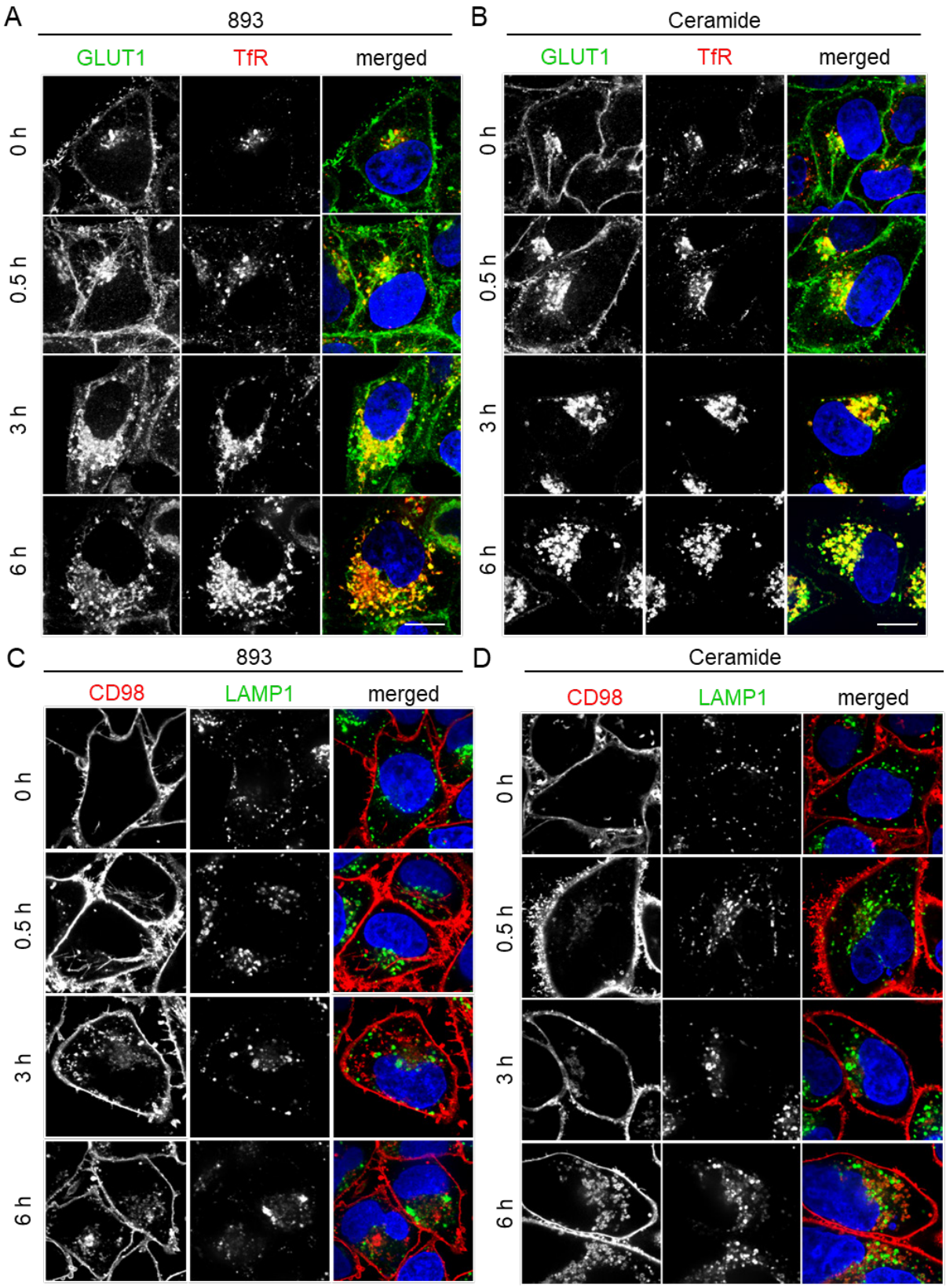

Supplementary Figure S1.4: Nutrient transporters are trapped with other recycled cargo at late timepoints. Related to Figure 1.1. (A-B) HeLa cells were treated with 893 (10 μM) or C_2-ceramide (50 μM) for 0.5, 3, or 6 h then stained for GLUT1 and the transferrin receptor (TfR). (C-D) HeLa cells were treated as in A&B and stained for CD98 and LAMP1. Scale bar, 10 μm.

Supplementary Fig. S1.5

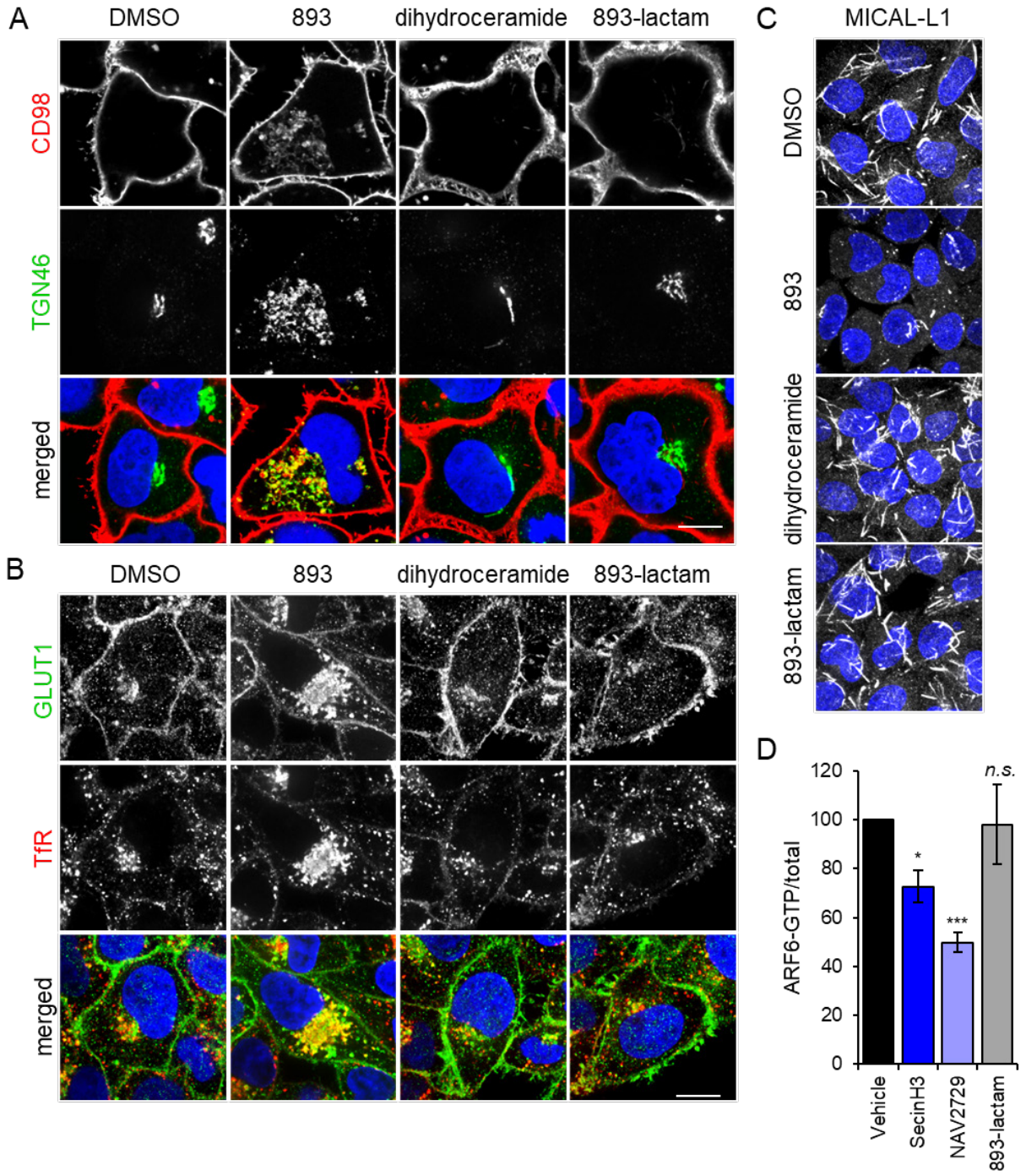

Supplementary Figure S1.5: Structurally-similar sphingolipids that do not activate PP2A or reduce ARF6-GTP levels fail to cause nutrient transporter trafficking defects. Related to Figure 1.5. (A-C) HeLa cells were treated with 893 (10 μM), C_2-dihydroceramide (50 μM), or

893-lactam (10 μM) for 12 h and then stained for CD98 and TGN46 (in A) or for GLUT1 and TfR (in B) or for MICAL-L1 (in C). (D) ARF6-GTP levels normalized to total in HeLa cells treated with SecinH3 (30 μM), NAV2729 (25 μM), or 893-lactam (10 μM) for 3 h. Means ± SEM shown, n ≥ 4 for SecinH3 and NAV2729; n = 2 for 893-lactam. Using ordinary one-way ANOVA, n.s. = not significant; * = p≤ 0.05; *** = p≤ 0.001. Dunnett's test was used to correct for multiple comparisons.

Supplementary Fig. S1.6

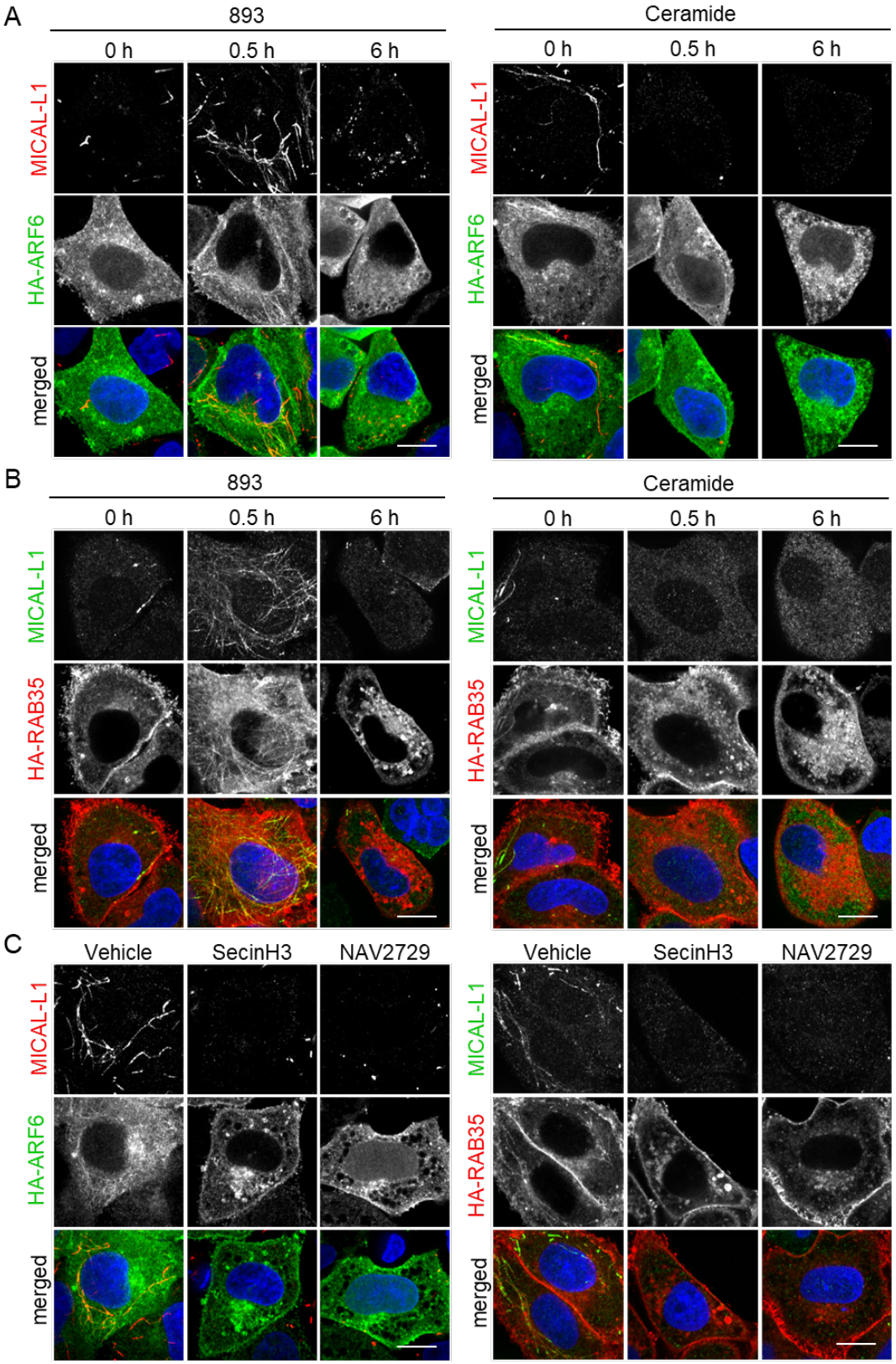

Supplementary Figure S1.6: ARF6 inhibition by sphingolipids is sufficient to block recruitment of ARF6, RAB35, and their scaffold MICAL-L1 to the tubular recycling endosome. Related to Figure 1.6. (A) HeLa cells transfected with HA-ARF6 were treated with 893 (10 μM) or C_2-ceramide (50 μM) for 0.5 or 6 h and then stained for MICAL-L1 and HA tag. (B) HeLa cells transfected with HA-RAB35 were treated with 893 (10 μM) or C_2-ceramide (50 μM) for 0.5 or 6 h and then stained for MICAL-L1 and HA tag. (C) HeLa cells transfected with HA-ARF6 or HA-RAB35 were treated with SecinH3 (30 μM) or NAV2729 (12.5 μM) for 6 h and then stained for MICAL-L1 and HA tag. Scale bar, 10 μm.

Supplementary Fig. S1.7

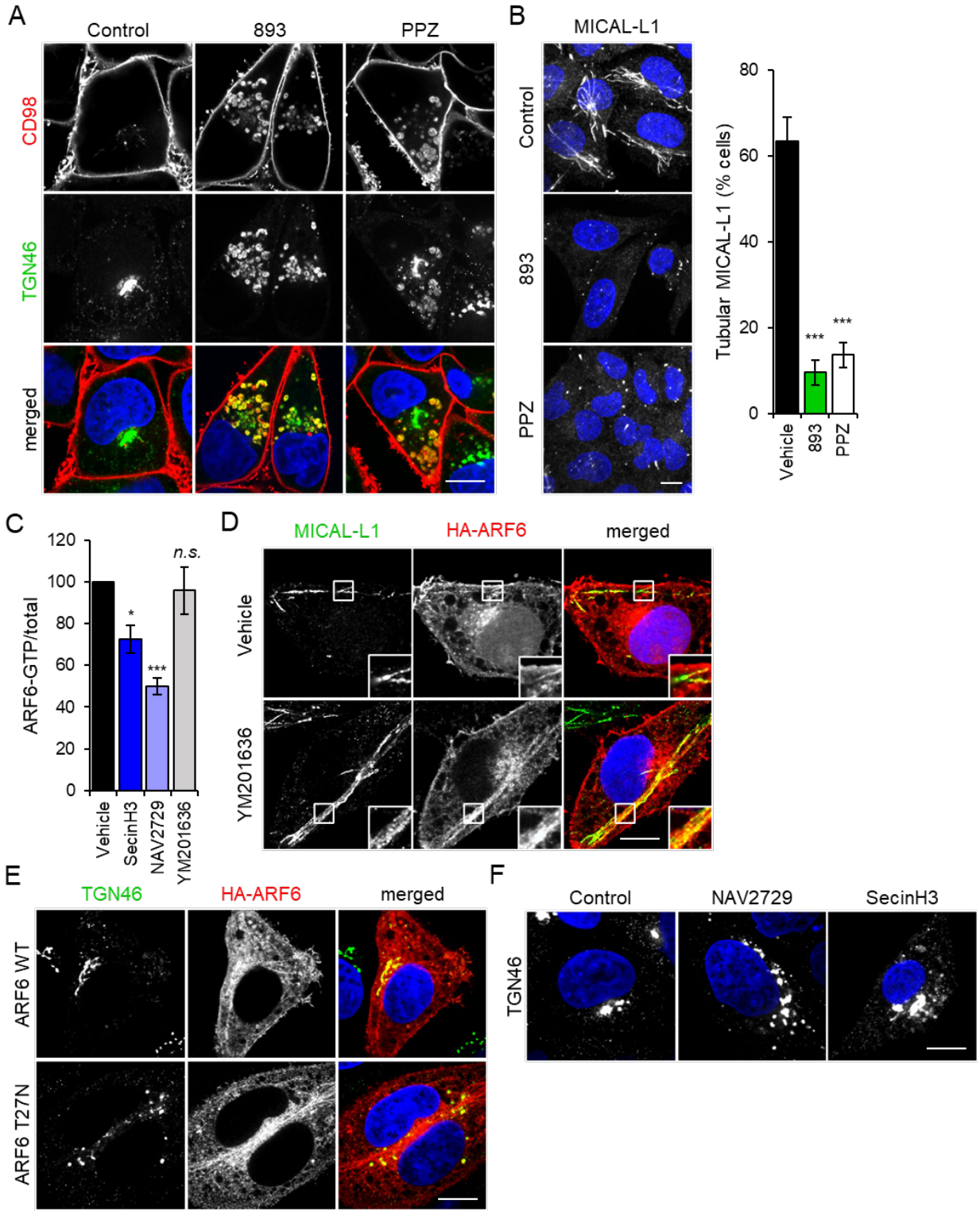

Supplementary Figure S1.7: PP2A activation or ARF6 inhibition but not PIKfyve inhibition is sufficient to disrupt endocytic recycling. Related to Figure 1.6. (A-B) HeLa cells were treated with 893 (10 μM) or perphenazine (PPZ; 12.5 μM) for 16 h and then stained for CD98 and TGN46 (A) or MICAL-L1 (B). The percent of cells per field of view with tubular MICAL-L1 staining is shown in (B). (C) ARF6-GTP normalized to total in HeLa cells treated with SecinH3 (30 μM), NAV2729 (25 μM), or YM201636 (800 nM) for 1 h. (D) HeLa cells transfected with HA-ARF6 were treated with YM201636 (800 nM) for 1 h and then stained for MICAL-L1 and HA tag. (E) HeLa cells transfected with HA-ARF6 wildtype (WT) or the dominant negative ARF6 mutant (HA-ARF6 T27N) were stained for TGN46 and HA tag. (F) HeLa cells were treated with SecinH3 (30 μM) or NAV2729 (12.5 μM) for 16 h and then stained for TGN46. Scale bar, 10 μm. Means ± SEM shown (B,C), n ≥ 4. Using ordinary one-way ANOVA (B,C), n.s. = not significant; * = p≤ 0.05; ** = p≤ 0.01; *** = p≤ 0.001. Dunnett's test was used to correct for multiple comparisons.

CHAPTER 2

Dynamic phosphoproteomics uncovers signaling pathways modulated by anti-oncogenic sphingolipid analogs

Peter Kubiniok[1,2,#], Brendan T. Finicle[3,#], Fanny Piffaretti[1], Alison N. McCracken[3], Michael Perryman[2], Stephen Hanessian[2], Aimee L. Edinger[3*] and Pierre Thibault[1,2,4*]

Affiliations

[1] Institute for Research in Immunology and Cancer, Université de Montréal, C.P. 6128, Succursale centre-ville, Montréal, Québec, H3C 3J7, Canada.

[2] Department of Chemistry, Université de Montréal, Quebec, Canada H3C 3J7

[3] Department of Developmental and Cell Biology, University of California Irvine, Irvine CA 92697

[4] Department of Biochemistry, Université de Montréal, C.P. 6128, Succursale centre-ville, Montréal, Québec, H3C 3J7, Canada.

# These authors contributed equally to this work; * These are co-corresponding authors.

This chapter is derived from the manuscript published in Molecular & Cellular Proteomics: Mol Cell Proteomics. 2019 Mar;18(3):408-422. doi: 10.1074/mcp.RA118.001053.

2.1 Abstract

The anti-neoplastic sphingolipid analog SH-BC-893 starves cancer cells to death by down-regulating cell surface nutrient transporters and blocking lysosomal trafficking events. These

effects are mediated by the activation of protein phosphatase 2A (PP2A). To identify putative PP2A substrates, we used quantitative phosphoproteomics to profile the temporal changes in protein phosphorylation in FL5.12 cells following incubation with SH-BC-893 or the specific PP2A inhibitor LB-100. These analyses enabled the profiling of more than 15,000 phosphorylation sites, of which 958 sites on 644 proteins were dynamically regulated. We identified 114 putative PP2A substrates including several nutrient transporter proteins, GTPase regulators (e.g., Agap2, Git1), and proteins associated with actin cytoskeletal remodeling (e.g., Vim, Pxn). To identify SH-BC-893-induced cell signaling events that disrupt lysosomal trafficking, we compared phosphorylation profiles in cells treated with SH-BC-893 or C2-ceramide, a non-vacuolating sphingolipid that does not impair lysosomal fusion. These analyses combined with functional assays uncovered the differential regulation of Akt and Gsk3b by SH-BC-893 (vacuolating) and C2-ceramide (non-vacuolating). Dynamic phosphoproteomics of cells treated with compounds affecting PP2A activity thus enabled the correlation of cell signaling with phenotypes to rationalize their mode of action.

2.2 Introduction

Oncogenic mutations selected during the tumorigenic process rewire the metabolic circuitry to meet the increased anabolic demands of cancer cells. Because oncogenic mutations constitutively drive growth and proliferation, cancer cells depend on a steady influx of nutrients via cell surface transporters and receptors and on the lysosomal degradation of internalized macromolecules into subunits that can be used for biosynthesis and/or the production of ATP (Selwan et al., 2016). Because cancer cells are constitutively anabolic, they are unable to tolerate nutrient stress that causes quiescence and catabolism in normal cells. Restricting nutrient access using sphingolipid-inspired compounds is an appealing therapeutic strategy to impede cancer cell proliferation and survival. Previous reports indicated that endogenous and synthetic sphingolipids starve many different cancer cell types to death by triggering the down regulation of multiple nutrient transporter proteins and/or blocking lysosomal fusion reactions (Barthelemy et al., 2017; Guenther et al., 2008, 2014; Hyde et al., 2005; Kim et al., 2016; Romero Rosales et al., 2011).

In mammalian cells, ceramides can function as tumor suppressors, mediating signaling events associated with apoptosis, autophagic responses and cell cycle arrest (Morad and Cabot, 2013). Several sphingolipids activate protein phosphatase 2A (PP2A) and negatively regulate multiple signaling pathways that promote nutrient transporter expression (Chalfant et al., 1999; Dobrowsky et al., 1993; Edinger, 2007; Habrukowich et al., 2010; Kim et al., 2016; Oaks and Ogretmen, 2014). Although the mechanism underlying sphingolipid regulation of PP2A activity is not entirely clear, previous reports suggest that ceramides can bind to endogenous protein inhibitors of PP2A to enhance its catalytic activity (Oaks and Ogretmen, 2014). Interestingly, while Fingolimod (FTY720, Gilenya), pyrrolidine analogs such as SH-BC-893, and ceramide all induce nutrient transporter down-regulation downstream of PP2A activation, only FTY720 and

SH-BC-893 produce PP2A-dependent cytoplasmic vacuolation (Kim et al., 2016). Ceramide, on the other hand, produces distinct effects from FTY720 and SH-BC-893 on the tubular recycling endosome, although whether these effects are PP2A-dependent is less certain (Finicle et al., 2018; Kim et al., 2016). These observations suggest that these structurally-related molecules differentially activate PP2A, resulting in distinct patterns of dephosphorylation and different endolysosomal trafficking phenotypes.

To determine how PP2A activity induces nutrient transporter loss and cytosolic vacuolation, we profiled the dynamic changes in protein phosphorylation in the murine prolymphocytic cell line FL5.12 following incubation with SH-BC-893, the specific PP2A inhibitor LB-100, or C2-ceramide. Metabolic labeling and quantitative phosphoproteomics (Kanshin et al., 2015a, 2015b; Kubiniok et al., 2017) identified kinetic profiles that could be correlated with putative PP2A substrates. This approach identified 15,607 phosphorylation sites, of which 958 were dynamically regulated by the treatments. While 265 putative PP2A sites were common to both PP2A agonists, our analyses also revealed 467 sites uniquely regulated by either SH-BC-893 or C2-ceramide that provided further insights into the SH-BC-893-specific phenotype, vacuolation.

2.3 Results

SH-BC-893 and C2-ceramide produce distinct, PP2A-dependent alterations in endolysosomal trafficking.

Ceramide is an endogenous tumor suppressor lipid that limits cellular growth and proliferation (Guenther et al., 2008; Morad and Cabot, 2013). Despite its antineoplastic actions, ceramide cannot be used to treat cancer patients because it is readily metabolized into inactive forms. While the synthetic sphingolipid FTY720 overcomes this problem, it also produces dose-limiting bradycardia at the concentrations required for tumor suppression by activating sphingosine-1-phosphate receptor 1 (S1PR1) (Camm et al., 2014; Chen et al., 2016). SH-BC-893 is a structurally constrained analog of FTY720 that limits tumor growth in multiple model systems, including prostate and colorectal cancer, without activating S1PR1 (Chen et al., 2016; Fransson et al., 2013; Kim et al., 2016; Perryman et al., 2016). Both SH-BC-893 and C2-ceramide (N-Acetyl-sphingosine, Figure 2.1A) suppress cell growth and survival in part by down-regulating nutrient transporter proteins through the activation of the cytosolic serine/threonine protein phosphatase PP2A (Chen et al., 2016; Finicle et al., 2018; Guenther et al., 2008; Kim et al., 2016). The cell surface antigen 4F2 heavy chain (solute carrier family 3 member 2, Slc3a2 or CD98) is a chaperone required for the surface expression of several associated light chains that transport amino-acids (Bröer and Bröer, 2017). Incubation with either 2.5 μM SH-BC-893 or 50 μM C2-ceramide resulted in a 40% down regulation of 4F2hc that was reversed by the selective PP2A inhibitor LB-100 (Figure 2.1B). These observations are consistent with published studies in multiple cell types (Chen et al., 2016; Finicle et al., 2018; Guenther et al., 2008; Kim et al., 2016; Perryman et al., 2016). In addition to limiting cell surface CD98 expression, SH-BC-893, but not ceramide, prevented the fusion of endocytic vesicles and autophagosomes with lysosomes resulting in enlarged multivesicular bodies, MVB (Kim et al., 2016); LB-100 reversed this effect (Figure 2.1C). These results confirm that disruptions in endolysosomal trafficking that

starve cancer cells to death (Kim et al., 2016) are PP2A-dependent in FL5.12 cells.

Dynamic phosphoproteomics deconvolves signaling events associated with changes in PP2A activity

To investigate the molecular mechanisms underlying nutrient transporter loss and vacuolation, we profiled the temporal changes in protein phosphorylation in FL5.12 cells treated with SH-BC-893, C2-ceramide, or LB-100 using quantitative phosphoproteomics and metabolic labeling (Figure 2.2). Changes in the phosphoproteome associated with SH-BC-893 or LB-100 treatment were analyzed in triple SILAC experiments. LB-100 was selected for these studies as it is more selective towards PP2A than other serine/threonine protein phosphatase inhibitors such as calyculin A or okadaic acid which affect both PP1 and PP2A (Cohen et al., 1989; Ishihara et al., 1989). In a parallel set of experiments, C2-ceramide's effects on the phosphoproteome were compared to those of SH-BC-893 using a similar strategy. Unstimulated cells (^{0}Lys, ^{0}Arg, light), and cells treated with LB-100/C2-ceramide or SH-BC-893 (^{4}Lys, ^{6}Arg, medium or ^{8}Lys, ^{10}Arg, heavy) were collected every 5 min for 60 min, and combined together in pre-cooled ethanol (-80˚C) at each time point. Cells were centrifuged, lysed, and digested with trypsin prior to phosphopeptide enrichment on TiO_2 affinity media. The eluted phosphopeptides were subsequently fractionated on strong cation exchange (SCX) spin columns and analyzed by liquid chromatography tandem mass spectrometry (LC-MS/MS). Phosphopeptide identification and quantification was performed using MaxQuant (Cox et al., 2011; Tyanova et al., 2016) and kinetic trends and clusters identified using R (http://www.r-project.org/). A total of 15,607 unique phosphopeptides were identified corresponding to an average phosphopeptide enrichment level of 85% for all experiments. SILAC experiments enabled the identification of 12,137 and 9,738 unique phosphopeptides on 2,949 and 2,550 proteins for LB-100/SH-BC-893 and C2-ceramide/SH-BC-893 experiments, respectively (Supplementary Table 2). On average, 70% of

phosphosites were localized with high confidence (8,559 sites for LB-100/SH-BC-893 and 6,704 sites for C2-ceramide/SH-BC-893). Closer examination of these data revealed that 3,928 phosphosites in LB-100/SH-BC-893 and 2,919 phosphosites in C2-ceramide/SH-BC-893 experiments were quantified in at least 6 time points, and were classified as high-quality kinetic profiles (Supplementary Figures S2.1 and 2 and Supplementary Table 3). Of the 5,029 high quality profiles, 1,818 were common to both experiments (Supplementary Figure S2.3). A list of phosphopeptides corresponding to these profiles is presented in Supplementary Table 3 for both triple SILAC experiments. As described previously, curve fitting with a polynomial model and a false discovery rate (FDR) of 1% distinguished dynamic from static profiles (Kubiniok et al., 2017). These analyses identified 629 and 428 dynamic profiles corresponding to regulated phosphosites in LB-100/SH-BC-893 and C2-ceramide/SH-BC-893 experiments, respectively (Supplementary Table 4). A comparison of these regulated phosphosites revealed that only 54 phosphopeptides were common to all three conditions suggesting that many of the changes in cell signaling taking place were not regulated by all three stimuli (Supplementary Figure S2.3).

Phosphorylation events that vary in opposite directions in cells treated with SH-BC-893 and LB-100 are likely to be PP2A-dependent. The dynamic profiles showed a progressive broadening of fold change (FC) values with a gradual shift in the median distribution toward a decrease or an increase in phosphorylation for cells treated with SH-BC-893 or LB-100, respectively. The width of this distribution was calculated from the inter quartile range (IQR) of the Log_2 (FC) distribution of phosphopeptides at each time point and plotted over the entire cell stimulation period (Figure 2.3A). The resulting curve showed a progressive increase in the IQR, in contrast to the trend observed from non-phosphorylated peptides that remained unaffected with time. Also, the extent of changes in protein phosphorylation was more pronounced for cells treated with LB-100 compared to those incubated with SH-BC-893.

Fuzzy clustering separated these dynamic profiles into those that displayed rapid or progressive increases or decreases in phosphorylation or showed an adaptation-like response (Figures 2.3B-C). From the 629 dynamic profiles identified in experiments comparing SH-BC-893 and LB-100 treatments, 384 were regulated by SH-BC-893, and are represented in Figure 2.3B. The majority of profiles in SH-BC-893-treated cells showed a progressive dephosphorylation (200 of 384 profiles), consistent with the expected agonist activity of this compound (Figure 2.3C). In contrast, profiles from cells treated with the PP2A inhibitor LB-100 displayed a progressive increase in phosphorylation with time (349 of 534 profiles). Fifty-two profiles in cells treated with SH-BC-893 exhibited adaptation characterized by a rapid dephosphorylation over the first 20 min post-stimulation followed by a recovery phase that extended over the remaining time period (Figure 2.3C). Interestingly, phosphosites that displayed transient dephosphorylation were more highly conserved than static sites ($p<0.001$) or dynamic sites that changed unidirectionally ($p<0.05$) suggesting that the adaptation cluster may define a subset of functionally important phosphorylation events (Supplementary Figure S2.4).

To identify putative PP2A substrates, we compared phosphorylation profiles that changed in opposite directions when FL5.12 cells were treated with LB-100 and SH-BC-893. Out of the 629 dynamic profiles identified in the triple SILAC experiment, 289 profiles were common to both treatments, and 114 of these profiles showed reciprocal (bidirectional) behavior (Figure 2.4A). We also noted that a subset of 175 profiles common to both LB-100 and SH-BC-893 displayed comparable trends that were either increasing or decreasing in phosphorylation with time, and were referred to as monodirectional. Linear motif analysis of monodirectional or bidirectional phosphopeptides with motif-X revealed that an RxxS motif was mainly represented in bidirectionally regulated sites while proline directed phosphorylation (SP and PxSP) was mainly

found amongst monodirectional phosphorylated sites (Figure 2.4B). To decipher which phosphorylation events are associated with changes in PP2A activity, we selected phosphosites that exhibited reciprocal trends with SH-BC-893 and LB-100 together with those uniquely regulated by SH-BC-893 (209 sites), and performed Gene Ontology (GO) enrichment using DAVID (Figure 2.4C). Proteins associated with guanosine triphosphate hydrolase (GTPase) regulators and actin filament reorganization were significantly enriched; GTPases and actin dynamics both play critical roles in regulating intracellular trafficking.

A literature analysis was performed to determine whether dynamic profiles had been previously identified as PP2A interactors (St-Denis et al., 2016; Wiredja et al., 2017; Wlodarchak and Xing, 2016). This analysis revealed that 30 proteins (37 phosphosites) identified in our screen were common with PP2A-interactors identified in other reports (St-Denis et al., 2016; Wiredja et al., 2017; Wlodarchak and Xing, 2016) (Figure 2.5A, Supplementary Table 5). Closer examination of these data indicated that 15 of these proteins are interconnected through a protein-protein interaction network and that 6 of these members (Vim, Pxn, Pak2, Gsk3b, Cfl1, Arhgef2) are known regulators of cytoskeleton organization (Figure 2.5B). Phosphorylation profiles of these substrates are shown in Figure 2.5C. Previous reports have indicated that Vimentin (Vim) phosphorylation at several residues, including Ser42 and Ser430, is regulated by PP2A and functionally important (Ando et al., 1989; Eriksson et al., 2004); inactivation of vimentin leads to increased actin stress fiber assembly (Jiu et al., 2017). The cytoskeletal protein Paxillin (Pxn) that regulates the actin-membrane attachment showed a rapid dephosphorylation at site Ser83 upon the first 5 min of SH-BC-893 treatment followed by a recovery and a more gradual decrease in phosphorylation that extended over the entire stimulation period. The closely located phosphorylation sites Pxn Thr31 and Thr118 have previously been reported to regulate cell migration in a RhoA dependent manner (Chen et al., 2004; Iwasaki et al., 2002). The

cytoskeleton organizing kinase Pak2 showed strong dephosphorylation on Ser141. Furthermore, Arhgef2 Ser122 showed a rapid dephosphorylation upon SH-BC-893 treatment. This site is proximal to Ser143 previously described to impact F-actin based morphological changes (Callow et al., 2005). The actin depolymerizing protein Cofilin1 (Cfl1) showed a progressive increase in phosphorylation at Ser3, a site whose phosphorylation inactivates the actin-depolymerizing activity of cofilin (Arber et al., 1998). Similarly, SH-BC-893 induces phosphorylation of the glycogen synthase kinase 3 b (Gsk3b) on Ser9, a site that has previously been reported to regulate the reorganization of the microtubule cytoskeleton (Wakatsuki et al., 2011). With the exception of Cfl1 Ser3, all sites described above showed differential regulation upon SH-BC-893 and LB-100 treatments.

Dynamic phosphoproteomics identifies distinct cell signaling events associated with C2-ceramide and SH-BC-893.

While both SH-BC-893 and C2-ceramide down-regulate nutrient transporters in a PP2A-dependent manner, only SH-BC-893 promotes cytoplasmic vacuolation (Figure 2.1). Quantitative phosphoproteomics experiments performed on FL5.12 cells treated with SH-BC-893 or C2-ceramide enabled the identification of cell signaling events differentially associated with these compounds. Dynamic profiles again formed three distinct clusters according to fuzzy clustering, displaying rapid or progressive increases or decreases in phosphorylation or an adaptation-like response (Figures 2.6A-B). In total, we identified 428 dynamic profiles, of which 254 profiles were common to SH-BC-893 and C2-ceramide (Figure 2.6C). It is noteworthy that temporal changes in protein phosphorylation for cells treated with SH-BC-893 (Figures 2.3B and 2.6C) yield comparable trends with Pearson coefficient of 0.68 on average between biological replicates (Supplementary Figure S2.5). Approximately 80% of common profiles between SH-BC-893 and C2-ceramide (203 of 254 profiles) showed a mono-directional trend where

progressive changes in protein phosphorylation were similar both in magnitude and direction for these two compounds consistent with the fact that these agents produce largely overlapping phenotypes in cells. Interestingly, 51 of the 254 common profiles showed opposite trends, while 126 or 48 profiles were uniquely regulated by C2-ceramide or SH-BC-893, respectively. These differentially regulates sites could be responsible for divergent phenotypes such as vacuolation.

To correlate phosphorylation changes with the distinct vacuolation phenotypes associated with C2-ceramide and SH-BC-893, dynamic profiles were separated into three groups: 1) Common and mono-directional profiles, 2) Bi-directional profiles or dynamic profiles unique to SH-BC-893 and 3) Dynamic profiles unique to C2-ceramide. GO term enrichment analyses were performed to determine if these groups were related to specific cellular compartments and molecular functions. Results from the corresponding analyses are displayed in the radar plots of Figure 2.6D. The majority of profiles identified belong to group 1 (203 shared monodirectional profiles) and are likely to account for phenotypes induced by both C2-ceramide and SH-BC-893 (e.g. nutrient transporter down-regulation). These profiles correspond to substrates that are largely involved in the regulation GTPase activity and actin cytoskeleton organization. Profiles from group 2 that showed opposite trends or are specific to SH-BC-893 treatment (99 profiles) were associated with the GO terms: endosome, intracellular membrane bound organelle and plasma membrane. Amongst these we found 11 phosphorylation sites on 9 proteins involved in vesicle trafficking and lysosomal fusion (Supplementary Figure S2.6). This result is consistent with finding that SH-BC-893 but not C2-ceramide inhibits lysosomal trafficking events (Kim et al., 2016). Group 3 comprises 126 profiles that are unique to C2-ceramide treatment. Phosphorylated substrates associated with this group are mostly localized in the nucleus with functional GO terms enriched for DNA binding, Chromatin binding and “DNA-directed DNA polymerase activity.” A protein-protein interaction network of the corresponding phosphoproteins

highlights several of the corresponding members and regroups proteins involved in DNA replication, DNA repair, nucleotide synthesis, and ribosome assembly (Supplementary Figure S2.7).

Next, we analyzed dynamic profiles from each group with Motif-X to determine if a specific phosphorylation consensus sequence was over-represented in these datasets (Supplementary Figure S2.8A). These analyses indicated that a large proportion of dynamic profiles were represented by proline-directed and basophilic phosphorylation motifs. Further analyses performed with the kinase prediction software available from the Group-based Prediction System (GPS) (Xue et al., 2008) identified Akt as a putative kinase targeting dynamic basophilic motifs. Interestingly, bidirectional sites from group 2 comprised the largest proportion of putative Akt substrates from all groups (Figure 2.6E and Supplementary Figure S2.8B). Among the 21 putative Akt substrates from group 2, we identified 6 proteins (Vim, Slc33a1, Gsk3b, Pikfyve, Acly, Pi4kb) that are known to interact with each other, including 3 proteins (Gsk3b, Pikfyve, Acly) previously reported as Akt substrates (Cross et al., 1995; Hill et al., 2010; Osinalde et al., 2016) (Figure 2.6F). For convenience, Supplementary Figure S2.9 presents the kinetic phosphorylation profiles of several Akt substrates. Together, these results suggest that a subset of bidirectional sites are putative Akt substrates associated with vesicle trafficking and could account for the vacuolation phenotype observed only with SH-BC-893.

SH-BC-893 and C2-ceramide stimulate actin polymerization that is necessary for cytoplasmic vacuolation but not surface nutrient transporter loss.

To gain a systems-level view of changes in protein phosphorylation observed for C2-ceramide and SH-BC-893, we used GO terms enriched in our datasets (Figure 2.6D, Supplementary

Table 4) combined with manual curation of gene lists to generate a pictogram of regulated phosphosites (Supplementary Figure S2.10). Protein groups of interest included membrane transport, endocytosis/cell adhesion, actin reorganization, nutrient transport and GTPase regulation (GTPase activators, GAPs and guanidine nucleotide exchange factors, GEFs).

Because dynamic phosphorylation sites similarly affected by SH-BC-893 and C2-ceramide were clustered in proteins that modulate actin dynamics (Figure 2.6D), actin polymerization was monitored in SH-BC-893- or C2-ceramide-treated FL5.12 cells using fluorescently-conjugated phalloidin. Both SH-BC-893 and C2-ceramide robustly increased F-actin formation in the cell cortex and in a cytosolic, likely endosomal, compartment (Figure 2.7A). Similar effects were observed in murine embryonic fibroblasts (MEFs) and in HeLa cells (data not shown). Consistent with a role for PP2A activation in this phenotype, the PP2A inhibitors LB-100 and calyculinA (CalyA) blocked actin polymerization at both locations (Figure 2.7B). The actin polymerization inhibitor Latrunculin A (LatA) also prevented actin polymerization with SH-BC-893 and C2-ceramide (Figure 2.7C). However, while LB-100 blocked CD98 down-regulation induced by SH-BC-893 or ceramide (Figure 2.1B), LatA did not suggesting that the loss of surface transporters depends on PP2A activation but not actin polymerization (Figure 2.7D). This result was unexpected, as actin polymerization is essential for nutrient permease downregulation by sphingolipids in yeast (Dickson, 2010). Interestingly, LatA reversed vacuolation by SH-BC-893 (Figure 2.7E). The actin polymerization stimulator Jasplakinolide did not promote vacuolation on its own (data not shown). Together, these data suggest that both C2-ceramide and SH-BC-893 stimulate actin polymerization in a PP2A-dependent manner and that actin polymerization is necessary but not sufficient to produce cytoplasmic vacuolation.

Ceramide inhibits SH-BC-893-induced vacuolation by inactivating Akt.

The finding that ceramide results in the dephosphorylation of more proteins than SH-BC-893 suggested that, rather than failing to induce vacuolation, ceramide may dephosphorylate and inactivate proteins necessary for vacuolation. In support of this model, co-addition of C2-ceramide inhibited cytoplasmic vacuolation by SH-BC-893 in FL5.12 cells (Figure 2.8A). Similar results were obtained in HeLa cells and murine prostate cancer epithelial cells (Supplementary Figure 2.11A-B). As highlighted in Supplementary Figure S2.9, multiple Akt substrates were dephosphorylated in cells treated with C2-ceramide but not SH-BC-893. That the effect of C2-ceramide was dominant was confirmed in Figure 2.8B and Supplementary Figures S2.11C,D by monitoring the Akt-dependent phosphorylation of PRAS40 at threonine 246 (Kovacina et al., 2003). These observations suggested that C2-ceramide may block vacuolation by inactivating Akt. Consistent with this model, the allosteric Akt inhibitor MK2206 reduced both Akt activity and vacuolation in FL5.12 cells treated with SH-BC-893 (Figures 2.8B,C); similar results were obtained in HeLa and mPCE prostate cancer cells (Supplementary Figures S2.11B,E). The deletion of Rictor, an mTORC2 component necessary for Akt activation (Sarbassov et al., 2005), also blocked vacuolation in the presence of SH-BC-893 again suggesting that Akt activity is essential for this phenotype (Figure 2.8D). Together, these data suggest that C2-ceramide does not vacuolate cells because Akt inactivation prevents the manifestation of this phenotype.

Two Akt substrates that are dephosphorylated in the presence of C2-ceramide but not SH-BC-893, Pikfyve and Pik4b, regulate late endocytic trafficking (Clayton et al., 2013; Kim et al., 2014). Gsk3b also localizes to MVBs and lysosomes and may regulate their function (Taelman et al., 2010). Consistent with its phosphorylation by Akt, GSK3b Ser9 phosphorylation increases with SH-BC-893 but decreases with C2-ceramide (Supplementary Figure S2.9). Because Ser9 phosphorylation inhibits Gsk3b activity (Sutherland et al., 1993), Gsk3b inhibition may contribute

to vacuolation. To test this, SH-BC-893 or C2-ceramide was combined with the Gsk3b inhibitor CHIR99021 and vacuolation monitored. While CHIR99021 did not vacuolate on its own or induce vacuolation in C2-ceramide-treated cells, CHIR99021 enhanced vacuolation of FL5.12 cells by SH-BC-893 (Figure 2.8E). This effect was much more dramatic in HeLa cells where CHIR99021 also sensitized cells to SH-BC-893 induced death despite its complete lack of toxicity as a single agent (Supplementary Figures S2.11F,G). These data suggest that SH-BC-893, but not C2-ceramide, vacuolates cells because Akt continues to inhibit Gsk3b.

2.4 Discussion

In this study, quantitative phosphoproteomics was used to identify phosphoproteins that responded differentially to pharmacological compounds that modulate PP2A activity and to correlate the PP2A-dependent phenotypes that affect intracellular trafficking and nutrient transporter loss. Time-resolved phosphoproteome analyses of FL5.12 cells treated with the PP2A agonist SH-BC-893 or the PP2A inhibitor LB-100 enabled the identification of putative PP2A substrates and phosphorylation events specific to each compound. These analyses confirmed that SH-BC-893 affected PP2A activity as approximately 75% of phosphorylation sites (289 out of 384 sites) were also targeted by LB-100. A more detailed analysis of the dynamic changes in protein phosphorylation common to LB-100 and SH-BC-893 revealed that 40% of these profiles displayed the expected reciprocal response and could represent putative PP2A substrates. A significant proportion of these targets are involved in the regulation of cell migration and actin cytoskeleton organization, including previously known PP2A substrates such as Vim, Pxn, Pak2, and Arhgef2.

Gene ontology analysis of phosphoproteins that were dynamically regulated monodirectionally by SH-BC-893 and C2-ceramide suggested that changes in actin dynamics contribute to the intracellular trafficking defects observed in sphingolipid-treated cells (Figure 2.6D) and led to the discovery that both SH-BC-893 and C2-ceramide promote PP2A-dependent actin polymerization at the cell cortex and in the cytoplasm (Figures 2.7A,B). Given that actin polymerization plays an important role in sphingolipid-induced nutrient transporter internalization in yeast (Dickson, 2010), it was surprising that actin polymerization was not necessary for down-regulation of nutrient transporter proteins by SH-BC-893 and C2-ceramide (Figures 2.7C,D). Moreover, rather than contributing the shared phenotype, loss of surface nutrient transporters, actin polymerization was necessary for a phenotype observed uniquely in SH-BC-893-treated

cells, vacuolation (Figure 2.7E). As vacuolation contributes to the anti-neoplastic activity of SH-BC-893 *in vitro* and *in vivo* (Kim et al., 2016), the molecular mechanism underlying this phenotype is of significant interest.

The differential ability of SH-BC-893 and C2-ceramide to produce vacuolation (Figure 2.1C) led us to hypothesize that cell signaling events responsible for vacuolation would be encompassed in phosphosites that varied in opposite manner in SH-BC-893- and C2-ceramide-treated cells. A basophilic phosphorylation motif typical of Akt substrates was enriched among these differentially regulated dynamic sites; multiple Akt substrates were dephosphorylated in C2-ceramide-, but not SH-BC-893-treated, cells (Figure 2.6F and Supplementary Figure S2.8). It has been widely reported that ceramide reduces the phosphorylation and activity of Akt (Chavez and Summers, 2012). In contrast, Akt Ser473 phosphorylation was maintained in SH-BC-893-treated cells not just in this study (Supplementary Figure S2.10A,B), but also in vivo in autochthonous prostate tumors (Kim et al., 2016). Differential regulation of Akt activity by SH-BC-893 and C2-ceramide might result if these sphingolipids activate PP2A through distinct mechanisms. Alternatively, as SH-BC-893 is water soluble to >60 mM while C2-ceramide is poorly soluble in aqueous solutions, these compounds may activate PP2A in different subcellular compartments. Membrane-localized C2-ceramide may activate plasma-membrane localized PP2A more effectively than SH-BC-893; Akt is activated by kinases found at the plasma membrane (Manning and Toker, 2017). It is also possible that SH-BC-893 and C2-ceramide differentially regulate the phosphorylation of the PP2A regulatory subunit B56β (Ppp2r5b) by Clk2 thereby affecting the interaction between Akt and PP2A (Kuo et al., 2008; Rodgers et al., 2011). Regardless of the mechanism underlying differential Akt activation by these sphingolipids, the reduction in vacuolation when Akt was inhibited by MK2206, Rictor deletion, or C2-ceramide demonstrate that Akt activity is necessary for SH-BC-893-induced

vacuolation (Figures 2.8A-D and Supplementary Figures S2.10A-D). In summary, these phosphoproteomics studies led to the unexpected discovery that C2-ceramide was dominant over SH-BC-893 in vacuolation assays (Figure 2.8A and Supplementary Figure S2.10A) and the conclusion that, rather lacking an activity possessed by SH-BC-893, ceramide fails to vacuolate cells because it inactivates Akt.

A detailed mechanistic understanding of how Akt activity supports vacuolation will require additional studies. However, the almost 2-fold increase or decrease in the phosphorylation of the Akt substrate Gsk3b phosphorylation at its inhibitory site Ser9 with SH-BC-893 or C2-ceramide, respectively (Supplementary Figure S2.8), and the accentuation of vacuolation by the Gsk3b inhibitor CHIR99021 (Figure 2.8E and Supplementary Figure S2.10E) suggest that Gsk3b may suppress vacuolation by positively regulating MVB function. Because CHIR99021 was not sufficient to induce vacuolation in C2-ceramide treated cells (Figure 2.8E), it is likely that additional Akt substrates besides Gsk3b contribute to the vacuolation phenotype. Consistent with published studies showing that vacuolation contributes to the anti-neoplastic effects of SH-BC-893 (Kim et al., 2016), inhibition of Gsk3b also sensitized cells to SH-BC-893-induced death (Supplementary Figure S2.10F). Gsk3b inhibitors are currently being developed for treatment of acute myeloid leukemia and breast cancer. Considering these findings, there may be a strong rationale for combining Gsk3b inhibitors and SH-BC-893 in cancer treatment. In conclusion, global, kinetic phosphoproteomic screens utilizing PP2A-activating sphingolipids helped to elucidate signaling pathways necessary for cellular starvation by sphingolipids, and highlighted a key role for Akt and Gsk3b signaling in regulating lysosomal trafficking events.

2.5 Materials and Methods

Cell culture. FL5.12 cells were maintained in RPMI-1640 medium supplemented with 10% fetal bovine serum (FBS), 10 mM HEPES buffer, 55 μM 2-mercaptoethanol, 2 mM L-glutamine, 500 pg/mL murine recombinant IL-3, and antibiotics. HeLa cells were cultured in DMEM with 4.5 g/L glucose and L-glutamine supplemented with 10% FBS and antibiotics. For proteomic analyses FL5.12 cells were grown in triple SILAC SD-Media (Thermo Fisher Scientific, Rockford, IL) containing 10% FBS, 500 pg/mL murine recombinant IL-3, 164 μM Lysine (K), 95 μM Arginine (R), 4.3 μM proline (Silantes, Munich, Germany) with additional nutrients consistent with Bendall *et al.* (Bendall et al., 2008). Cells were incubated at 37°C and 5% CO_2. Cells were counted using a Leica microscope with a 10 x 0.25 objective. Approximately 500 million cells per SILAC channel were grown in 500 mL spinner flasks. Incubation with small molecules was performed by adding 1 mL of small molecule or DMSO (Sigma Aldrich Co.) diluted in SILAC RPMI 1640/10% FBS to reach the final concentration. Cells were harvested every 5 min during the first hour of treatment with either 5 μM SH-BC-893 (heavy label) or 50 μM C2-ceramide (medium label) or 10 μM LB-100 (medium label) or DMSO (light label). Drug concentrations used for treatments are based on previously published references (Dai et al., 2017; Guenther et al., 2008; Kim et al., 2016). Cells were collected by pipetting 75 mL (25 mL per SILAC channel) of culture into 425 mL of -80°C pre-cooled ethanol.

Flow cytometry. For quantification of cell surface CD98, 400,000 FL5.12 cells were stained with either PE-conjugated rat IgG2a k isotype control (Biolegend, cat. no. 400508) or PE-conjugated rat anti-mouse CD98 (Biolegend, cat. no. 128208) in blocking buffer (PBS with 10% FBS and 0.05% sodium azide) for 30 min on ice. Cells were washed twice in ice-cold wash buffer (PBS with 2% FCS and 0.05% sodium azide), resuspended in wash buffer containing 1

μg/mL DAPI, and returned to ice. Analysis was restricted to live cells (DAPI-negative) and data normalized to the untreated control after background subtraction.

Vacuolation assay. Vacuoles were quantified as in Perryman et al. (Perryman et al., 2016). Briefly, FL5.12 cells were treated as indicated for 3 h then pelleted by centrifuging at 2,000 rpm for 3 min in a microfuge. The cell pellet was resuspended in 10 μL, and 3 μL of the cell suspension was examined under a 0.13 to 0.17 mm thick coverglass (VWR Micro cover glass, square, No.1, cat. no. 48366-045) on a microscope slide. FL5.12 cells were evaluated by differential interference microscopy (DIC) using a 100x oil-immersion objective with a Nikon TE2000-S fluorescence microscope. To calculate the vacuolation score, at least 10 different fields of view containing 5-12 cells per field were assessed. Scores were assigned to individual cells as follows: 0 = no vacuoles, 1 = very small vacuoles, 2 = multiple well-defined vacuoles, 3 = multiple large vacuoles. To calculate the vacuolation score, the following formula was used:

$$\text{score} = \frac{(3 \times \%\ \text{cells in cat. } 3) + (2 \times \%\ \text{cells in cat. } 2) + (1 \times \%\ \text{cells in cat. } 1)}{3}$$

Fluorescence microscopy. To monitor F-actin, FL5.12 cells were fixed with 4% paraformaldehyde for 10 min, washed, and incubated in permeabilization and blocking buffer (PBS with 10% FBS, 0.3% saponin, and 0.05% sodium azide) containing Alexa Fluor 488 conjugated phalloidin (Cell Signalling Technologies, 1:100 dilution). Cells were then imaged on a Nikon Eclipse Ti spinning-disk confocal microscope using a 100x oil-immersion objective. Images were analyzed using ImageJ; fluorescence intensity was normalized between all images and displayed using the LUT “16 colors.”

Immunoblotting. Cells were lysed in RIPA buffer containing protease (Pierce, Cat #88265) and phosphatase inhibitors (Sigma, Cat #4906845001). Protein concentration was quantified using a BCA protein assay (Thermo Scientific, Cat #23223). Samples were prepared in NuPAGE sample buffer (Invitrogen, Cat #NP0007) and 50 mM DTT, run on Invitrogen NuPAGE 4-12% Bis-Tris gels (Cat #NP0336BOX), and transferred to BioTrace NT nitrocellulose membranes (Pall, Cat #66485). After transfer, membranes were dried at room temperature for 30 min, incubated in blocking solution (5% bovine serum albumin, 0.05% NaN_3 in TBST) for 1 h, and then incubated overnight at 4°C in blocking solution containing primary antibody. Blots were washed three times in TBST (TBS with 0.1% Tween 20), incubated at RT for 1 h in blocking solution containing IRDye-conjugated secondary antibodies (1:10,000), and then washed three times in TBST. Blots were imaged using a LI-COR Odyssey CLx imaging system.

Digestion and desalting of cell extracts. Heavy, medium and light cells from each time point were combined in 500 mL collection tubes (Sorvall centrifuge bottles), separated by centrifugation at 1,200 rpm (Sorvall Legend RT centrifuge) and washed first with 35 mL PBS, then 5 mL PBS, and finally 3 times with 1 mL PBS while transferring from 500 mL collection tubes to 50 mL falcon tubes to 1.7mL Eppendorf tubes, respectively. Cell lysis was performed by sonication for 15 seconds with a sonic dismembrator (Thermo Fisher Scientific; Rockford, IL) after adding 1 mL lysis buffer (8M Urea, 50mM TRIS, pH 8, HALT phosphatase inhibitor (Thermo Fisher Scientific). Cells were maintained at 0°C to prevent protein degradation. Protein concentration was measured by BCA assay (Thermo Fisher Scientific). Protein disulfide bonds were reduced by incubating lysates in 5 mM dithiothreitol (DTT, Sigma-Aldrich, St-Louis, MO) for 30 min at 56°C while shaking at 1,000 rpm. Alkylation of cysteine residues was achieved by incubation with iodoacetamide (IAA, Sigma-Aldrich) at a concentration of 15 mM for 30 min at

RT in the dark. Excess IAA was quenched for 15 min at RT by adding DTT to 5 mM. All samples were diluted 5 times with 20 mM TRIS (Bioshop Burlington ON), 1 mM $CaCl_2$, pH 8 and mixed with 2 µg/µL trypsin (Sigma-Aldrich) (protein: trypsin 50:1 w:w) and incubated for 12 h at 37°C. Trypsin was kept at -80 °C and thawed only once. Desalting was performed on 60 mg solid phase extraction (SPE) reverse phase cartridges (Oasis HLB 3cc cartridge, 60 mg, 30 µm particle size, Waters Mississauga, ON) previously conditioned with 3 mL methanol, SPE Buffer (50% acetonitrile, ACN, 1% formic acid, FA) and finally with 1% aqueous FA. Peptide samples were loaded, washed with 3 mL 1% FA, eluted in 1 mL SPE buffer and dried on a vacuum centrifuge (Thermo Fisher Scientific) at RT.

Phosphopeptide enrichment. Phosphopeptide enrichment was performed on 5 µm titansphere particles (Canadian Life Science, Peterborough, ON) according to published protocols (Kanshin et al., 2012, 2013). Loading of protein extracts on the titansphere beads, washing, and elution steps were performed using custom spin columns (Ishihama et al., 2006) made from 200 µl pipette tip containing a SDB-XC membrane (Empore, 3M) frit and filled with TiO_2 beads. Peptides were desalted in 50 µL of 1% FA and subsequently eluted from spin columns using 50 µL of 50% ACN 0.5% FA.

Offline strong cation exchange chromatography. To achieve high reproducibility and parallel sample fractionation in high throughput proteomics experiments, we used strong cation fractionation (SCX) on homemade spin columns packed with 18 to 22 mg (for cell lysate of 3 to 8 mg protein extract) of polysulfoethyl A 300Å particle, (Canada Life Science; Peterborough, ON). After equilibrating the SCX particles with each 100 µL of SCX Buffer A (10% ACN/0.2%FA v/v), Buffer B (1 M NaCl in 10% ACN/0.2%FA v/v) and finally 200 µL SCX Buffer A. Peptides

were resuspended in 100 µL Buffer A, loaded on the SCX column and eluted in six salt step fractions of 100 µL each with 0, 30, 50, 80, 120 and 500 mM NaCl in SCX Buffer A. Prior to LC-MS/MS analyses all fractions were dried on a SpeedVac centrifuge at RT (Thermo Fisher Scientific) and resuspended in 4% FA. All centrifugation steps were performed at 4°C except where indicated.

Mass spectrometry analysis. LC-MS/MS analyses were performed on a Q-Exactive HF (SH-BC-893 vs. C2-ceramide experiments) or an Orbitrap tribrid Fusion (SH-BC-893 vs. LB-100 experiments) mass spectrometer using homemade capillary LC columns (18 cm length, 150 µm ID, 360 µm OD). Capillary LC columns were packed with C18 Jupiter 3 µm particles (Phenomenex, Torrance, CA) at 1,000 psi. Samples were directly injected on LC-columns and separations were performed at a flow rate of 0.6 µL/min using a linear gradient of 5-35 % aqueous ACN (0.2% FA) in 150 minutes. MS spectra were acquired with a resolution of 60,000 using a lock mass (m/z: 445.120025) followed by up to 20 MS/MS data dependent scans on the most intense ions using high energy dissociation (HCD). AGC target values for MS and MS/MS scans were set to $1x10^6$ (max fill time 100 ms) and $5x10^5$ (max fill time 200 ms), respectively. The precursor isolation window was set to m/z 1.6 with a HCD normalized collision energy of 25. The dynamic exclusion window was set to 20 s.

Data processing and analysis. Raw data analysis of SILAC experiments was performed using Maxquant software 1.5.3.8 and the Andromeda search engine (Tyanova et al., 2016). The false discovery rate (FDR) for peptide, protein, and site identification was set to 1%, the minimum peptide length was set to 6, and the ‘peptide requantification’ function was enabled. Precursor ions detected as 3D peaks (m/z, intensity and retention time) were considered as peptide

features. Precursor mass accuracies were then estimated by MaxQuant in a feature specific fashion as described previously (Cox and Mann, 2008). Briefly, mass accuracy of peptide features were determined for each 2D peak (m/z and intensity) across the 3D peak and an intensity weighted bootstrap analysis estimated mass accuracies for each precursor ion. Minimum reporter ion mass accuracy was set to 20 ppm. The option match between runs (2 min time tolerance) was enabled to correlate identification and quantitation results across different runs. Up to 2 missed cleavages per peptide were allowed. To adjust for any systematic quantification errors, SILAC ratios were normalized by time point. All additional parameters are reported in MaxQuant parameters.txt and experimentalDesign.txt provided in Supplementary Table 1. The Uniprot mouse proteome database (September 2015 containing 35,281 entries) was used for all searches. Protein groups were formed by MaxQuant, and all identified peptides were used to make pair-wise comparison between proteins in the database. Proteins containing an equal or overlapping set of peptides were merged together to form a protein group and ranked according to the highest number of peptides.

In addition to an FDR of 1% set for peptide, protein and phosphosite identification levels, we used additional criteria to increase data quality. The Andromeda score threshold for the identification of phosphopeptides was set to 40 with a delta score to the second best match of 8, as optimized by Sharma K et al. (Sharma et al., 2014). We selected only peptides for which abundance ratios (FC=Drug/Control) were measured in at least 6 time points. Then we set a cut-off for maximum phosphosite localization confidence across experiments (time points) to 0.75. Next, we distinguished dynamic from static phosphosites by calculating an FDR based on curve fitting as recently described (Kubiniok et al., 2017). We further performed clustering analysis using the fuzzy means package (Baker and Chalkley, 2014) which is implemented to the R environment (https://cran.r-project.org/).

Gene Ontology (GO) enrichment analyses were performed using the database DAVID version 6.7 (Sharma et al., 2014). Protein interaction networks were defined using the STRING database and interacting proteins were visualized with Cytoscape version 2.8. A protein-protein interaction network was built in STRING version 9.1 for all proteins containing dynamic phosphosites. All interaction predictions were based on experimental evidences with a minimal confidence score of 0.7 (considered as a “high confidence” filter in STRING). Linear motif analysis was done using Motif-x (Huang et al., 2009; Kumar and E Futschik, 2007). Conservation of phosphorylation sites across species was assessed using the CPhos program (Zhao et al., 2012).

Experimental Design and Statistical Rationale. For time resolved phosphoproteomics experiments, FL5.12 cells were collected from one large cell culture (500 mL) per SILAC channel. Time course experiments (SH-BC-893 and LB-100; SH-BC-893 and C2-ceramide) were conducted on different days. Sample processing for each time course experiment was performed in parallel and from the same batch of materials and chemicals to maximize reproducibility of peptide digestion, phosphopeptide enrichment and fractionation. All time points of each SCX fraction were consecutively loaded onto the LC-MS system to ensure similar peptide coverage for all time points. SCX fractions were injected with increasing salt concentration. All data were analyzed using the same FASTA file (Uniprot Mouse proteome, accessed September 2015, 35,281 entries) and MaxQuant version 1.5.8.3.

Microscopy experiments (e.g., phalloidin staining in Fig. 2.7A-C, vacuolation images in Fig. 2.1C, 2.7E, and 2.8A,C-E) were completed in 2-3 biological replicates performed on separate

days to account for biological variation. Microscopy images representative of the >100 cells per condition per biological replicate were used in figures. For quantitation of cytoplasmic vacuolation (Fig. 2.8A,C-E), at least 400 cells per condition from three biological replicates were evaluated and means calculated, error bars show the 95% confidence interval. Statistical significance was evaluated with a Student's t test (two-tailed, paired), as described in each figure legend.

For flow cytometry experiments quantifying the surface levels of CD98 (Fig. 2.1B and 2.7D), at least three biological replicates were performed on different days to account for biological variation. Surface CD98 levels are normalized to vehicle within each experiment, and the normalized values are averaged. Variation is shown as standard error of the mean and statistical significance was assessed by Student's t test (two-tailed, paired), as described in the figure legends.

2.6 Acknowledgements

This work was funded in part by the Natural Sciences and Engineering Research Council (NSERC) (P.T. 311598; S.H. 04726), grants to A.L.E. from the NIH (R01 GM089919, R21 CA178230), CDMRP (W81XWH-15-1-0010), the American Cancer Society (RSG-11-111-01-CDD), and the UCI CORCL. The Institute for Research in Immunology and Cancer (IRIC) receives infrastructure support from the Canadian Center of Excellence in Commercialization and Research, the Canadian Foundation for Innovation, and the Fonds de recherche du Québec - Santé (FRQS). Proteomics analyses were performed at the Center for Advanced Proteomic and Chemogenomics Analyses (CAPCA), a Node of the Genomic Technology Platform supported by the Canadian Government through Genome Canada. Imaging was performed in the Optical Biology Core at UCI which is supported in part by NIH P30 CA062203. The authors would like to thank David Sabatini (Whitehead Institute, MIT) for generously providing Rictor knockout MEFs.

2.7 Competing interests statement

A.L.E. is an inventor on a patent application covering the synthesis of SH-BC-893 and its use as an anti-cancer agent.

2.8 Author contributions

P.T., A.L.E., S.H. designed the research; P.K., B.F., F.P., A.N.M, M.P. performed the research, conducted the experiments. P.K., B.F., analyzed the data; and P.K., B.F., A.L.E. and P.T. wrote the paper. All authors approved the content and submission of the paper.

2.9 Funding

This work was funded in part by the Natural Sciences and Engineering Research Council (NSERC) (P.T. 311598; S.H. 04726), grants to A.L.E. from the NIH (R01 GM089919, R21 CA178230), CDMRP (W81XWH-15-1-0010), the American Cancer Society (RSG-11-11101-CDD), and the UCI CORCL. The Institute for Research in Immunology and Cancer (IRIC) receives infrastructure support from the Canadian Center of Excellence in Commercialization and Research, the Canadian Foundation for Innovation, and the Fonds de recherche du Que´bec - Sante´ (FRQS). Proteomics analyses were performed atthe Center for Advanced Proteomic and Chemogenomics Analyses (CAPCA), a Node of the Genomic Technology Platform supported by the Canadian Government through Genome Canada. Imaging was performed in the Optical Biology Core at UCI which is supported in part by NIH P30 CA062203.

2.10 Data availability

All raw LC-MS/MS data and MaxQuant output files can beaccessed from the PeptideAtlas (http://www.peptideatlas.org/) with the dataset identifier PASS01168. In addition, all MS/MS spectra of identified peptides and phosphopeptides can be accessed through the MS viewer consortium (http://msviewer.ucsf.edu/prospector/cgi-bin/msform.cgi?formmsviewer). The “SH-BC-893 vs. LB-100” and the “SH-BC-893 vs. C2-ceramide” data sets can be retrieved with the search keys “scuimnsogi” and “emvfcljjhs,” respectively.

Supplementary Tables available on https://www.mcponline.org/article/S1535-9476(20)31847-8/fulltext#supplementaryMaterial

2.11 References

Ando, S., Tanabe, K., Gonda, Y., Sato, C., and Inagaki, M. (1989). Domain- and sequence-specific phosphorylation of vimentin induces disassembly of the filament structure. Biochemistry *28*, 2974–2979.

Arber, S., Barbayannis, F.A., Hanser, H., Schneider, C., Stanyon, C.A., Bernard, O., and Caroni, P. (1998). Regulation of actin dynamics through phosphorylation of cofilin by LIM-kinase. Nature *393*, 805–809.

Baker, P.R., and Chalkley, R.J. (2014). MS-viewer: a web-based spectral viewer for proteomics results. Mol. Cell Proteomics *13*, 1392–1396.

Barthelemy, C., Barry, A.O., Twyffels, L., and André, B. (2017). FTY720-induced endocytosis of yeast and human amino acid transporters is preceded by reduction of their inherent activity and TORC1 inhibition. Sci. Rep. *7*, 13816.

Bendall, S.C., Hughes, C., Stewart, M.H., Doble, B., Bhatia, M., and Lajoie, G.A. (2008). Prevention of amino acid conversion in SILAC experiments with embryonic stem cells. Mol. Cell Proteomics *7*, 1587–1597.

Bröer, S., and Bröer, A. (2017). Amino acid homeostasis and signalling in mammalian cells and organisms. Biochem. J. *474*, 1935–1963.

Callow, M.G., Zozulya, S., Gishizky, M.L., Jallal, B., and Smeal, T. (2005). PAK4 mediates morphological changes through the regulation of GEF-H1. J. Cell Sci. *118*, 1861–1872.

Camm, J., Hla, T., Bakshi, R., and Brinkmann, V. (2014). Cardiac and vascular effects of fingolimod: mechanistic basis and clinical implications. Am. Heart J. *168*, 632–644.

Chalfant, C.E., Kishikawa, K., Mumby, M.C., Kamibayashi, C., Bielawska, A., and Hannun, Y.A. (1999). Long chain ceramides activate protein phosphatase-1 and protein phosphatase-2A. Activation is stereospecific and regulated by phosphatidic acid. J. Biol. Chem. *274*, 20313–20317.

Chavez, J.A., and Summers, S.A. (2012). A ceramide-centric view of insulin resistance. Cell Metab. *15*, 585–594.

Chen, B., Roy, S.G., McMonigle, R.J., Keebaugh, A., McCracken, A.N., Selwan, E., Fransson, R., Fallegger, D., Huwiler, A., Kleinman, M.T., et al. (2016). Azacyclic FTY720 analogues that limit nutrient transporter expression but lack S1P receptor activity and negative chronotropic effects offer a novel and effective strategy to kill cancer cells in vivo. ACS Chem. Biol. *11*, 409–414.

Chen, H.-Y., Shen, C.-H., Tsai, Y.-T., Lin, F.-C., Huang, Y.-P., and Chen, R.-H. (2004). Brk activates rac1 and promotes cell migration and invasion by phosphorylating paxillin. Mol. Cell. Biol. *24*, 10558–10572.

Clayton, E.L., Minogue, S., and Waugh, M.G. (2013). Mammalian phosphatidylinositol 4-kinases as modulators of membrane trafficking and lipid signaling networks. Prog. Lipid Res. *52*, 294–304.

Cohen, P., Klumpp, S., and Schelling, D.L. (1989). An improved procedure for identifying and quantitating protein phosphatases in mammalian tissues. FEBS Lett. *250*, 596–600.

Cox, J., and Mann, M. (2008). MaxQuant enables high peptide identification rates, individualized p.p.b.-range mass accuracies and proteome-wide protein quantification. Nat. Biotechnol. *26*, 1367–1372.

Cox, J., Neuhauser, N., Michalski, A., Scheltema, R.A., Olsen, J.V., and Mann, M. (2011). Andromeda: a peptide search engine integrated into the MaxQuant environment. J. Proteome Res. *10*, 1794–1805.

Cross, D.A., Alessi, D.R., Cohen, P., Andjelkovich, M., and Hemmings, B.A. (1995). Inhibition of glycogen synthase kinase-3 by insulin mediated by protein kinase B. Nature *378*, 785–789.

Dai, C., Zhang, X., Xie, D., Tang, P., Li, C., Zuo, Y., Jiang, B., and Xue, C. (2017). Targeting PP2A activates AMPK signaling to inhibit colorectal cancer cells. Oncotarget *8*, 95810–95823.

Dickson, R.C. (2010). Roles for sphingolipids in Saccharomyces cerevisiae. Adv. Exp. Med. Biol. *688*, 217–231.

Dobrowsky, R.T., Kamibayashi, C., Mumby, M.C., and Hannun, Y.A. (1993). Ceramide activates heterotrimeric protein phosphatase 2A. J. Biol. Chem. *268*, 15523–15530.

Edinger, A.L. (2007). Controlling cell growth and survival through regulated nutrient transporter expression. Biochem. J. *406*, 1–12.

Eriksson, J.E., He, T., Trejo-Skalli, A.V., Härmälä-Braskén, A.-S., Hellman, J., Chou, Y.-H., and Goldman, R.D. (2004). Specific in vivo phosphorylation sites determine the assembly dynamics of vimentin intermediate filaments. J. Cell Sci. *117*, 919–932.

Finicle, B.T., Ramirez, M.U., Liu, G., Selwan, E.M., McCracken, A.N., Yu, J., Joo, Y., Nguyen, J., Ou, K., Roy, S.G., et al. (2018). Sphingolipids inhibit endosomal recycling of nutrient transporters by inactivating ARF6. J. Cell Sci. *131*.

Fransson, R., McCracken, A.N., Chen, B., McMonigle, R.J., Edinger, A.L., and Hanessian, S. (2013). Design, Synthesis, and Anti-leukemic Activity of Stereochemically Defined Constrained Analogs of FTY720 (Gilenya). ACS Med. Chem. Lett. *4*.

Guenther, G.G., Peralta, E.R., Rosales, K.R., Wong, S.Y., Siskind, L.J., and Edinger, A.L. (2008). Ceramide starves cells to death by downregulating nutrient transporter proteins. Proc. Natl. Acad. Sci. USA *105*, 17402–17407.

Guenther, G.G., Liu, G., Ramirez, M.U., McMonigle, R.J., Kim, S.M., McCracken, A.N., Joo, Y., Ushach, I., Nguyen, N.L., and Edinger, A.L. (2014). Loss of TSC2 confers resistance to ceramide and nutrient deprivation. Oncogene *33*, 1776–1787.

Habrukowich, C., Han, D.K., Le, A., Rezaul, K., Pan, W., Ghosh, M., Li, Z., Dodge-Kafka, K., Jiang, X., Bittman, R., et al. (2010). Sphingosine interaction with acidic leucine-rich nuclear phosphoprotein-32A (ANP32A) regulates PP2A activity and cyclooxygenase (COX)-2 expression in human endothelial cells. J. Biol. Chem. *285*, 26825–26831.

Hill, E.V., Hudson, C.A., Vertommen, D., Rider, M.H., and Tavaré, J.M. (2010). Regulation of PIKfyve phosphorylation by insulin and osmotic stress. Biochem. Biophys. Res. Commun. *397*, 650–655.

Huang, D.W., Sherman, B.T., and Lempicki, R.A. (2009). Systematic and integrative analysis of large gene lists using DAVID bioinformatics resources. Nat. Protoc. *4*, 44–57.

Hyde, R., Hajduch, E., Powell, D.J., Taylor, P.M., and Hundal, H.S. (2005). Ceramide down-regulates System A amino acid transport and protein synthesis in rat skeletal muscle cells. FASEB J. *19*, 461–463.

Ishihama, Y., Rappsilber, J., and Mann, M. (2006). Modular stop and go extraction tips with stacked disks for parallel and multidimensional Peptide fractionation in proteomics. J. Proteome Res. *5*, 988–994.

Ishihara, H., Martin, B.L., Brautigan, D.L., Karaki, H., Ozaki, H., Kato, Y., Fusetani, N., Watabe, S., Hashimoto, K., and Uemura, D. (1989). Calyculin A and okadaic acid: inhibitors of protein phosphatase activity. Biochem. Biophys. Res. Commun. *159*, 871–877.

Iwasaki, T., Nakata, A., Mukai, M., Shinkai, K., Yano, H., Sabe, H., Schaefer, E., Tatsuta, M., Tsujimura, T., Terada, N., et al. (2002). Involvement of phosphorylation of Tyr-31 and Tyr-118 of paxillin in MM1 cancer cell migration. Int. J. Cancer *97*, 330–335.

Jiu, Y., Peränen, J., Schaible, N., Cheng, F., Eriksson, J.E., Krishnan, R., and Lappalainen, P. (2017). Vimentin intermediate filaments control actin stress fiber assembly through GEF-H1 and RhoA. J. Cell Sci. *130*, 892–902.

Kanshin, E., Michnick, S., and Thibault, P. (2012). Sample preparation and analytical strategies for large-scale phosphoproteomics experiments. Semin. Cell Dev. Biol. *23*, 843–853.

Kanshin, E., Michnick, S.W., and Thibault, P. (2013). Displacement of N/Q-rich peptides on TiO2 beads enhances the depth and coverage of yeast phosphoproteome analyses. J. Proteome Res. *12*, 2905–2913.

Kanshin, E., Kubiniok, P., Thattikota, Y., D'Amours, D., and Thibault, P. (2015a). Phosphoproteome dynamics of Saccharomyces cerevisiae under heat shock and cold stress. Mol. Syst. Biol. *11*, 813.

Kanshin, E., Bergeron-Sandoval, L.-P., Isik, S.S., Thibault, P., and Michnick, S.W. (2015b). A cell-signaling network temporally resolves specific versus promiscuous phosphorylation. Cell Rep. *10*, 1202–1214.

Kim, G.H.E., Dayam, R.M., Prashar, A., Terebiznik, M., and Botelho, R.J. (2014). PIKfyve inhibition interferes with phagosome and endosome maturation in macrophages. Traffic *15*, 1143–1163.

Kim, S.M., Roy, S.G., Chen, B., Nguyen, T.M., McMonigle, R.J., McCracken, A.N., Zhang, Y., Kofuji, S., Hou, J., Selwan, E., et al. (2016). Targeting cancer metabolism by simultaneously disrupting parallel nutrient access pathways. J. Clin. Invest. *126*, 4088–4102.

Kovacina, K.S., Park, G.Y., Bae, S.S., Guzzetta, A.W., Schaefer, E., Birnbaum, M.J., and Roth, R.A. (2003). Identification of a proline-rich Akt substrate as a 14-3-3 binding partner. J. Biol. Chem. *278*, 10189–10194.

Kubiniok, P., Lavoie, H., Therrien, M., and Thibault, P. (2017). Time-resolved Phosphoproteome Analysis of Paradoxical RAF Activation Reveals Novel Targets of ERK. Mol. Cell Proteomics *16*, 663–679.

Kumar, L., and E Futschik, M. (2007). Mfuzz: a software package for soft clustering of microarray data. Bioinformation *2*, 5–7.

Kuo, Y.-C., Huang, K.-Y., Yang, C.-H., Yang, Y.-S., Lee, W.-Y., and Chiang, C.-W. (2008). Regulation of phosphorylation of Thr-308 of Akt, cell proliferation, and survival by the B55alpha

regulatory subunit targeting of the protein phosphatase 2A holoenzyme to Akt. J. Biol. Chem. *283*, 1882–1892.

Manning, B.D., and Toker, A. (2017). AKT/PKB signaling: navigating the network. Cell *169*, 381–405.

Morad, S.A.F., and Cabot, M.C. (2013). Ceramide-orchestrated signalling in cancer cells. Nat. Rev. Cancer *13*, 51–65.

Oaks, J., and Ogretmen, B. (2014). Regulation of PP2A by sphingolipid metabolism and signaling. Front. Oncol. *4*, 388.

Osinalde, N., Mitxelena, J., Sánchez-Quiles, V., Akimov, V., Aloria, K., Arizmendi, J.M., Zubiaga, A.M., Blagoev, B., and Kratchmarova, I. (2016). Nuclear Phosphoproteomic Screen Uncovers ACLY as Mediator of IL-2-induced Proliferation of CD4+ T lymphocytes. Mol. Cell Proteomics *15*, 2076–2092.

Perryman, M.S., Tessier, J., Wiher, T., O'Donoghue, H., McCracken, A.N., Kim, S.M., Nguyen, D.G., Simitian, G.S., Viana, M., Rafelski, S., et al. (2016). Effects of stereochemistry, saturation, and hydrocarbon chain length on the ability of synthetic constrained azacyclic sphingolipids to trigger nutrient transporter down-regulation, vacuolation, and cell death. Bioorg. Med. Chem. *24*, 4390–4397.

Rodgers, J.T., Vogel, R.O., and Puigserver, P. (2011). Clk2 and B56β mediate insulin-regulated assembly of the PP2A phosphatase holoenzyme complex on Akt. Mol. Cell *41*, 471–479.

Romero Rosales, K., Singh, G., Wu, K., Chen, J., Janes, M.R., Lilly, M.B., Peralta, E.R., Siskind, L.J., Bennett, M.J., Fruman, D.A., et al. (2011). Sphingolipid-based drugs selectively kill cancer cells by down-regulating nutrient transporter proteins. Biochem. J. *439*, 299–311.

Sarbassov, D.D., Guertin, D.A., Ali, S.M., and Sabatini, D.M. (2005). Phosphorylation and regulation of Akt/PKB by the rictor-mTOR complex. Science *307*, 1098–1101.

Selwan, E.M., Finicle, B.T., Kim, S.M., and Edinger, A.L. (2016). Attacking the supply wagons to starve cancer cells to death. FEBS Lett. *590*, 885–907.

Sharma, K., D'Souza, R.C.J., Tyanova, S., Schaab, C., Wiśniewski, J.R., Cox, J., and Mann, M. (2014). Ultradeep human phosphoproteome reveals a distinct regulatory nature of Tyr and Ser/Thr-based signaling. Cell Rep. *8*, 1583–1594.

St-Denis, N., Gupta, G.D., Lin, Z.Y., Gonzalez-Badillo, B., Veri, A.O., Knight, J.D.R., Rajendran, D., Couzens, A.L., Currie, K.W., Tkach, J.M., et al. (2016). Phenotypic and interaction profiling of the human phosphatases identifies diverse mitotic regulators. Cell Rep. *17*, 2488–2501.

Sutherland, C., Leighton, I.A., and Cohen, P. (1993). Inactivation of glycogen synthase kinase-3 beta by phosphorylation: new kinase connections in insulin and growth-factor signalling. Biochem. J. *296 (Pt 1)*, 15–19.

Taelman, V.F., Dobrowolski, R., Plouhinec, J.-L., Fuentealba, L.C., Vorwald, P.P., Gumper, I., Sabatini, D.D., and De Robertis, E.M. (2010). Wnt signaling requires sequestration of glycogen synthase kinase 3 inside multivesicular endosomes. Cell *143*, 1136–1148.

Tyanova, S., Temu, T., and Cox, J. (2016). The MaxQuant computational platform for mass spectrometry-based shotgun proteomics. Nat. Protoc. *11*, 2301–2319.

Wakatsuki, S., Saitoh, F., and Araki, T. (2011). ZNRF1 promotes Wallerian degeneration by degrading AKT to induce GSK3B-dependent CRMP2 phosphorylation. Nat. Cell Biol. *13*, 1415–1423.

Wiredja, D.D., Ayati, M., Mazhar, S., Sangodkar, J., Maxwell, S., Schlatzer, D., Narla, G., Koyutürk, M., and Chance, M.R. (2017). Phosphoproteomics Profiling of Nonsmall Cell Lung Cancer Cells Treated with a Novel Phosphatase Activator. Proteomics *17*.

Wlodarchak, N., and Xing, Y. (2016). PP2A as a master regulator of the cell cycle. Crit Rev Biochem Mol Biol *51*, 162–184.

Xue, Y., Ren, J., Gao, X., Jin, C., Wen, L., and Yao, X. (2008). GPS 2.0, a tool to predict kinase-specific phosphorylation sites in hierarchy. Mol. Cell Proteomics *7*, 1598–1608.

Zhao, B., Pisitkun, T., Hoffert, J.D., Knepper, M.A., and Saeed, F. (2012). CPhos: a program to calculate and visualize evolutionarily conserved functional phosphorylation sites. Proteomics *12*, 3299–3303.

2.12 Figures

Figure 2.1

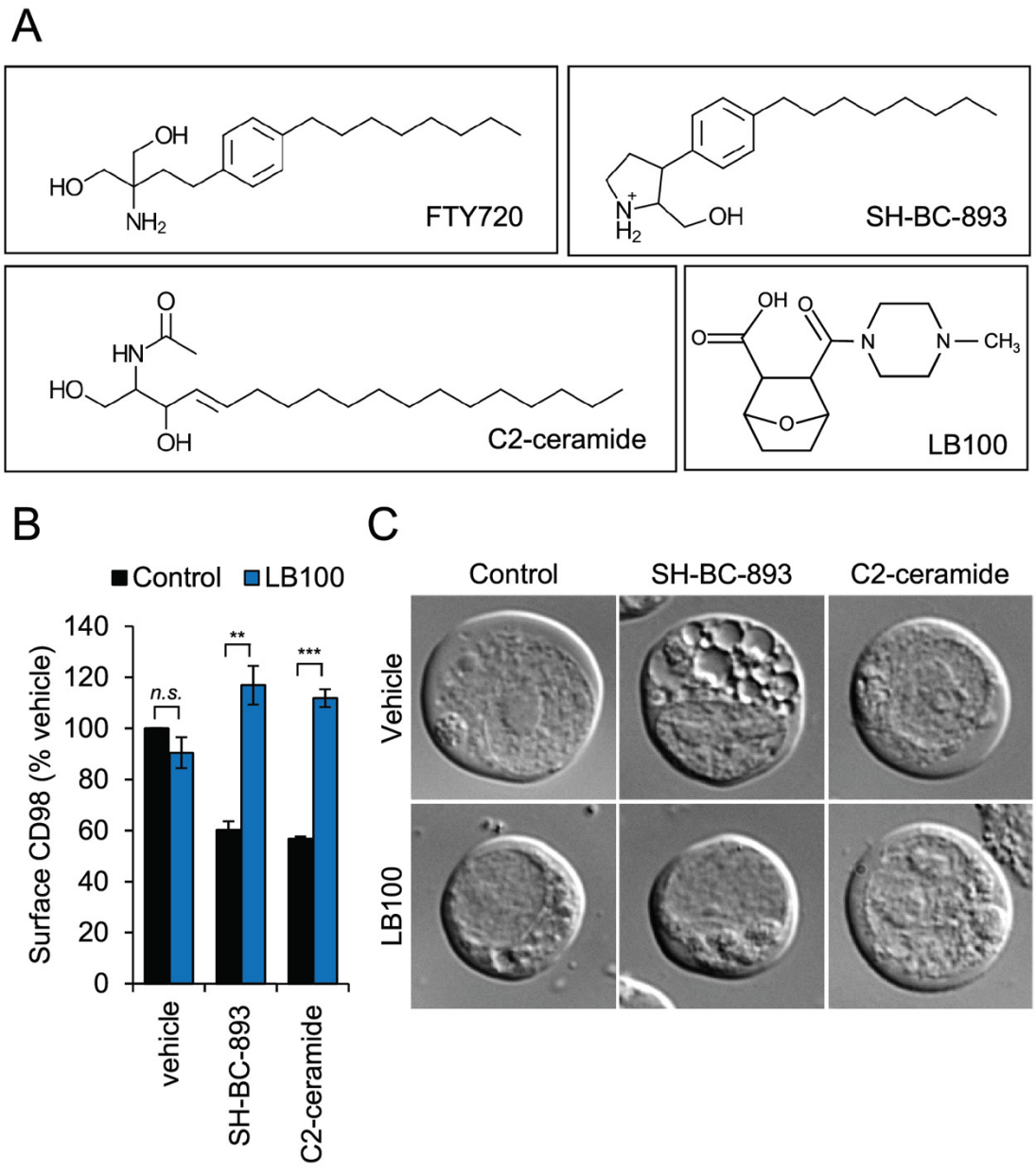

Figure 2.1. SH-BC-893 and C2-ceramide cause PP2A-dependent disruptions in endolysosomal trafficking. A) Structures of the PP2A activators FTY720 (Fingolimod), C2-ceramide, SH-BC-893 and the PP2A inhibitor LB-100. B) Surface CD98 levels in FL5.12 cells pre-treated with LB-100 (100 μM) for 1.5 h prior to addition of DMSO, SH-BC-893 (5 μM), or C2-

ceramide (50 μM) for 1 h. Using Student's t-test (n.s.) not significant; *,p ≤0.05;**, p≤0.01; and ***, p≤0.001 C) DIC microscopy of FL5.12 cells pre-treated with LB-100 (100 μM) for 1.5 h prior to addition of DMSO, vehicle, SH-BC-893 (5 μM), or C2-ceramide (50 μM) for 2 h.

Figure 2.2

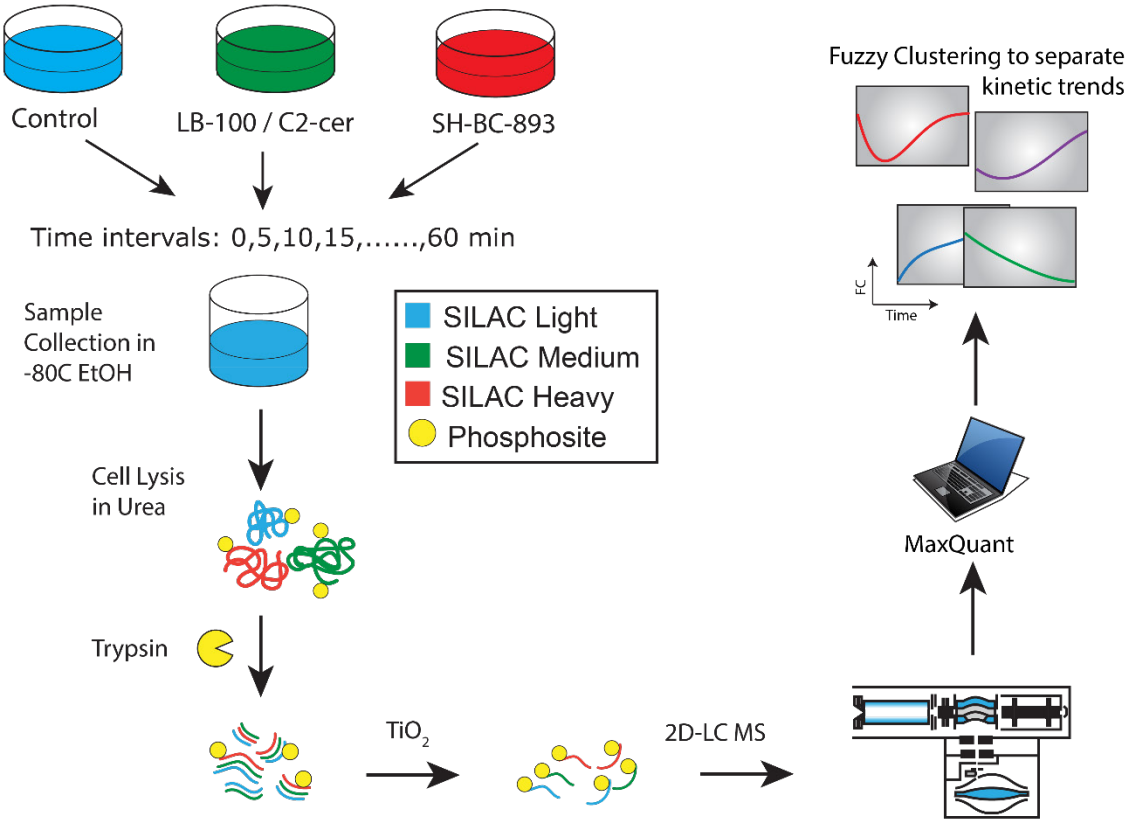

Figure 2.2. Triple SILAC phosphoproteomics workflow. Light cells are treated with vehicle, medium cells were treated with C2-ceramide (50 μM) or LB-100 (10 μM), and heavy cells were treated with SH-BC-893 (5 μM). Cells were collected every 5 min from 0-60 min of stimulation by snap freezing in pre-cooled ethanol. Cells were lysed in urea, digested with trypsin and phosphopeptides were enriched using titanium dioxide. Strong cation fractionation (SCX) was performed prior to LC-MS/MS analysis. Phosphopeptide identification and quantitation was performed using MaxQuant, and only kinetic profiles of sites with localisation confidence > 0.75 and measured in at least 6 time points were selected for further analysis. Polynomial fitting was used to define regulated phosphosites, and only phosphopeptide profiles with FDR < 1% were selected and used for fuzzy c-means clustering and subsequent analyses.

Figure 2.3

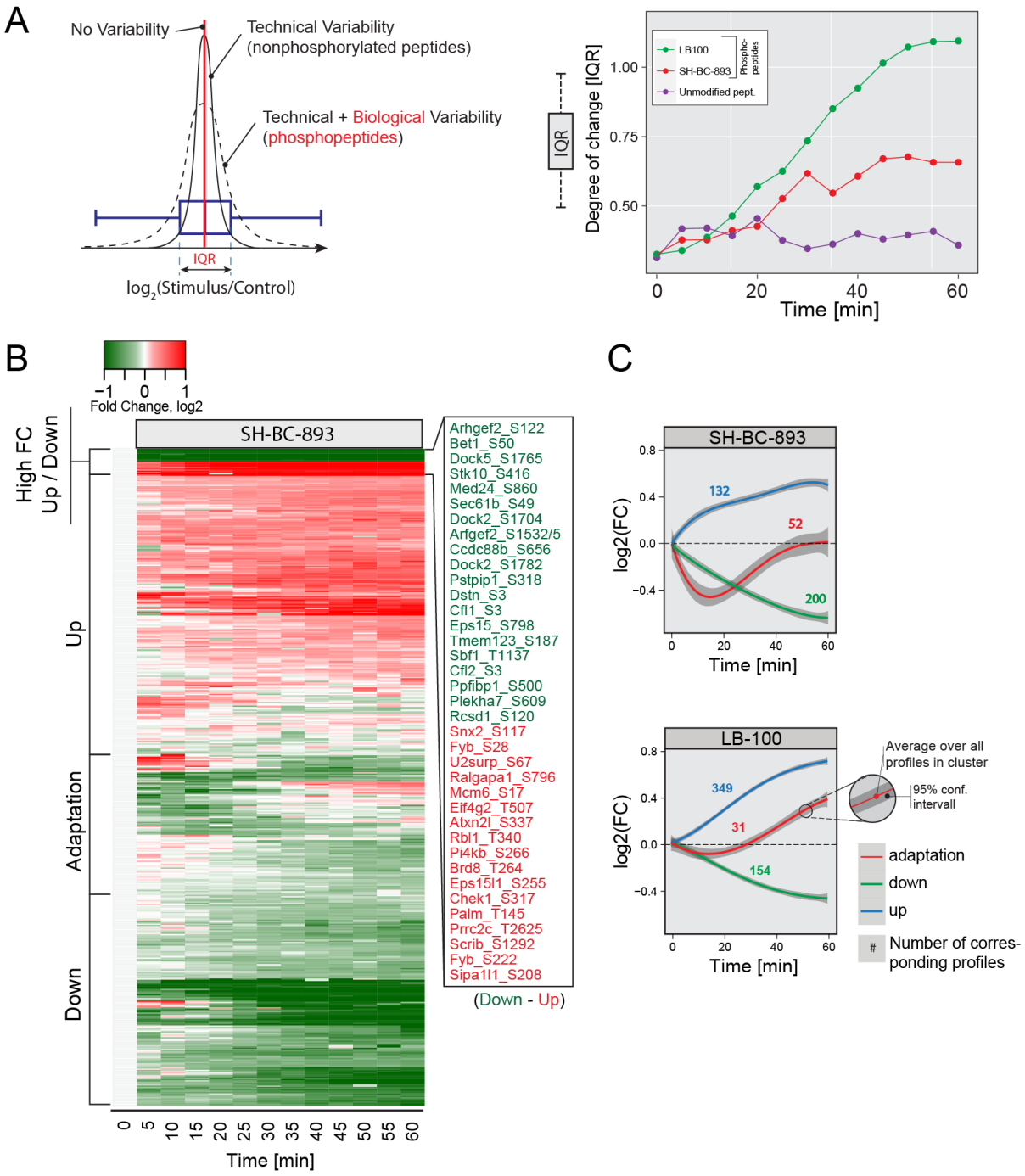

Figure 2.3. Phosphoproteomics results from the comparison of treatments with LB-100 (10 µM) and SH-BC-893 (5 µM). A) Inter quartile range (IQR) shows the global change in phosphorylation upon treatment. Unmodified peptides (control) do not change over time while

LB-100 and SH-BC-893 treatments show a progressive increase in IQR with time. B) Heatmap of all 390 phosphosites regulated by SH-BC-893. Different kinetic behaviors are indicated. C) Kinetic trends extracted from LB-100 and SH-BC-893 treatments using fuzzy means clustering, numbers correspond to profiles observed with a particular kinetic trend.

Figure 2.4

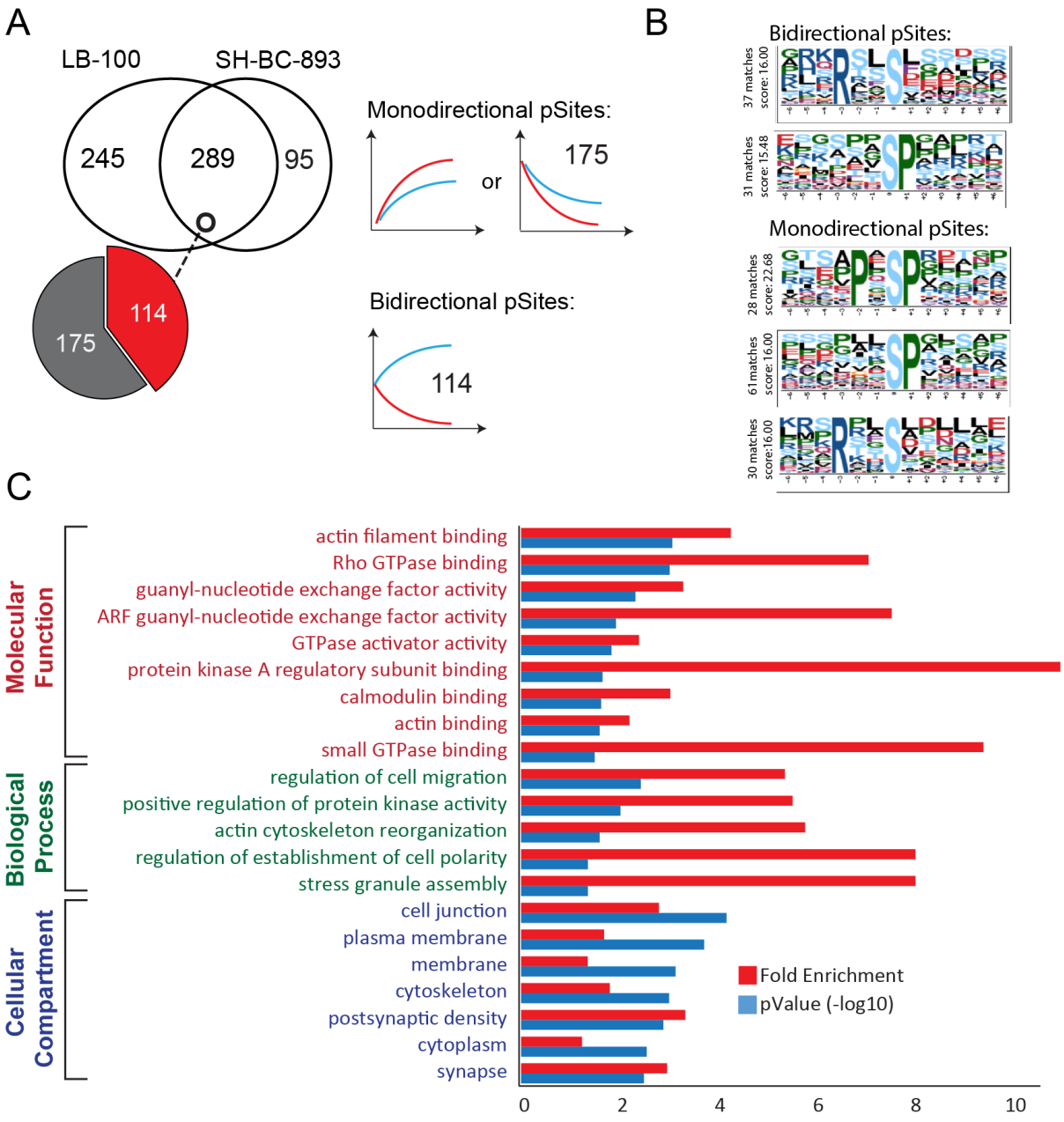

Figure 2.4. Comparison of dynamic phosphorylation sites following SH-BC-893 and LB-100 treatments. A) Venn diagram showing that 292 phosphosites are common to both treatments while 253 and 98 phosphosites are uniquely regulated by LB-100 and SH-BC-893, respectively. Of the 292 common sites, 116 sites showed opposite (Bidirectional) tends and 176 sites are regulated in the same direction (Monodirectional). B) Phosphorylation motifs extracted

from motif-X. Monodirectional phosphosites display PxSP and SP motifs. Bidirectional sites that show rapid changes in phosphorylation are present on Serine-rich peptides. C) Gene Ontology enrichment of proteins corresponding to the 214 bidirectional and unidirectional (for SH-BC-893) phosphosites.

Figure 2.5

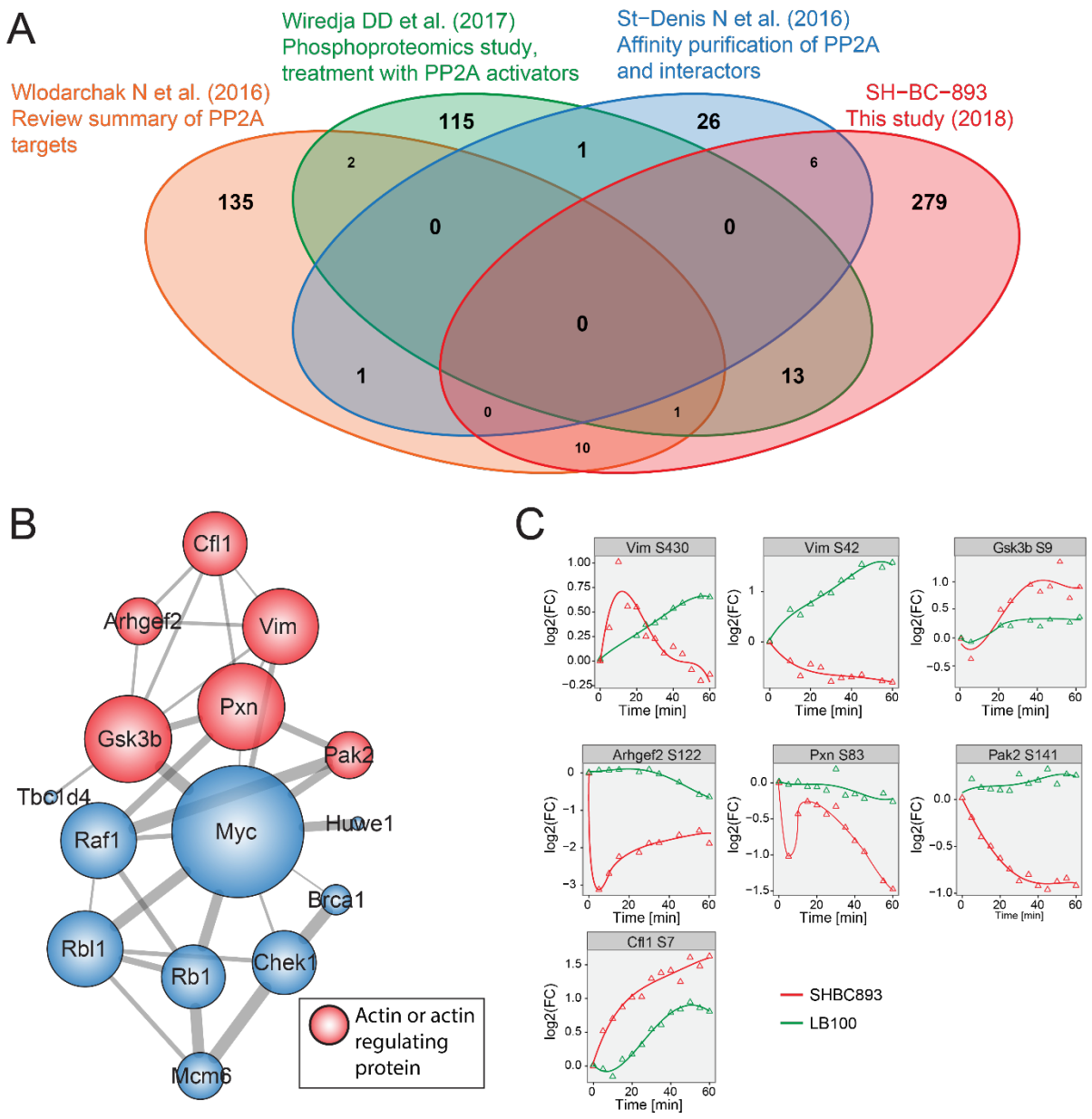

Figure 2.5. Identification of putative PP2A targets. A) Comparative analysis of the list of candidate PP2A substrates identified from various proteomic studies. The comparison was done at the protein level since not all datasets reported the position of the phosphorylated sites. B) A network of phosphorylation sites identified as direct PP2A targets based on comparative literature review. Color coding indicates if the proteins are involved in actin reorganization. C) Dynamic profiles of sites from putative PP2A targets involved in actin reorganization.

Figure 2.6

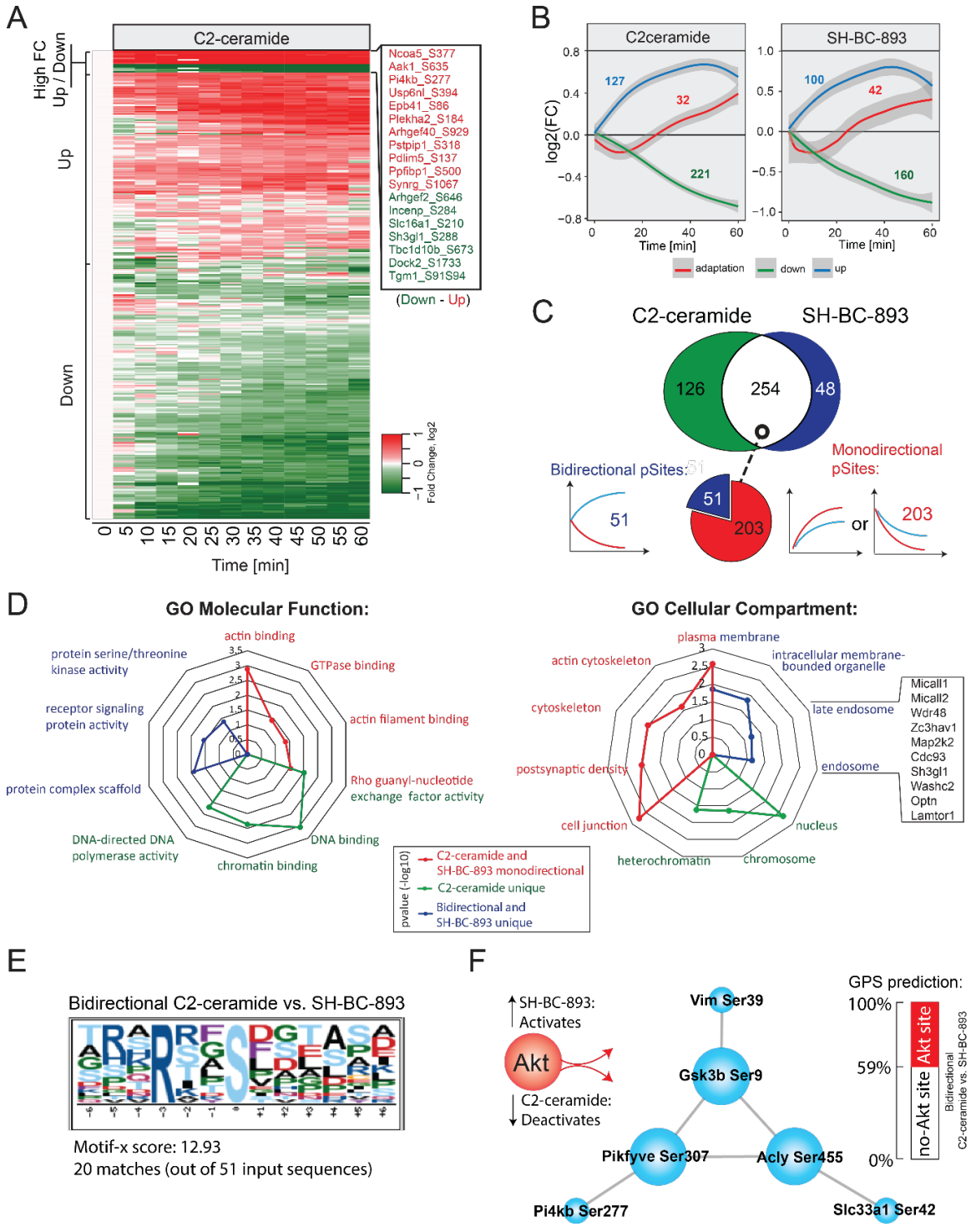

Figure 2.6. Dynamic phosphoproteomics identifies signaling events differently regulated by C2-ceramide and SH-BC-893 treatments. A) Heatmap corresponding to 380 phosphorylation sites that were dynamically phosphorylated upon C2-ceramide treatment.

Kinetic trends are indicated. B) Dynamic profiles extracted from C2-ceramide and SH-BC-893 treatments using fuzzy means clustering. Numbers correspond to profiles observed for a given cluster. C) Venn diagram of dynamic phosphosites showing that 254 phosphosites are common, 126 and 48 phosphosites are uniquely regulated by C2-ceramide and SH-BC-893, respectively. Of the 254 commonly regulated sites, 51 show opposite change in phosphorylation (bidirectional) and 203 are regulated in the same direction (monodirectional). D) Radar plot showing the enrichment of GO terms associated with specific groups highlighted in different colors. E) Motif-X analyses of bidirectional sites showing an over-representation of basophilic motifs. F) Network of putative Akt substrates and known interacting members.

Figure 2.7

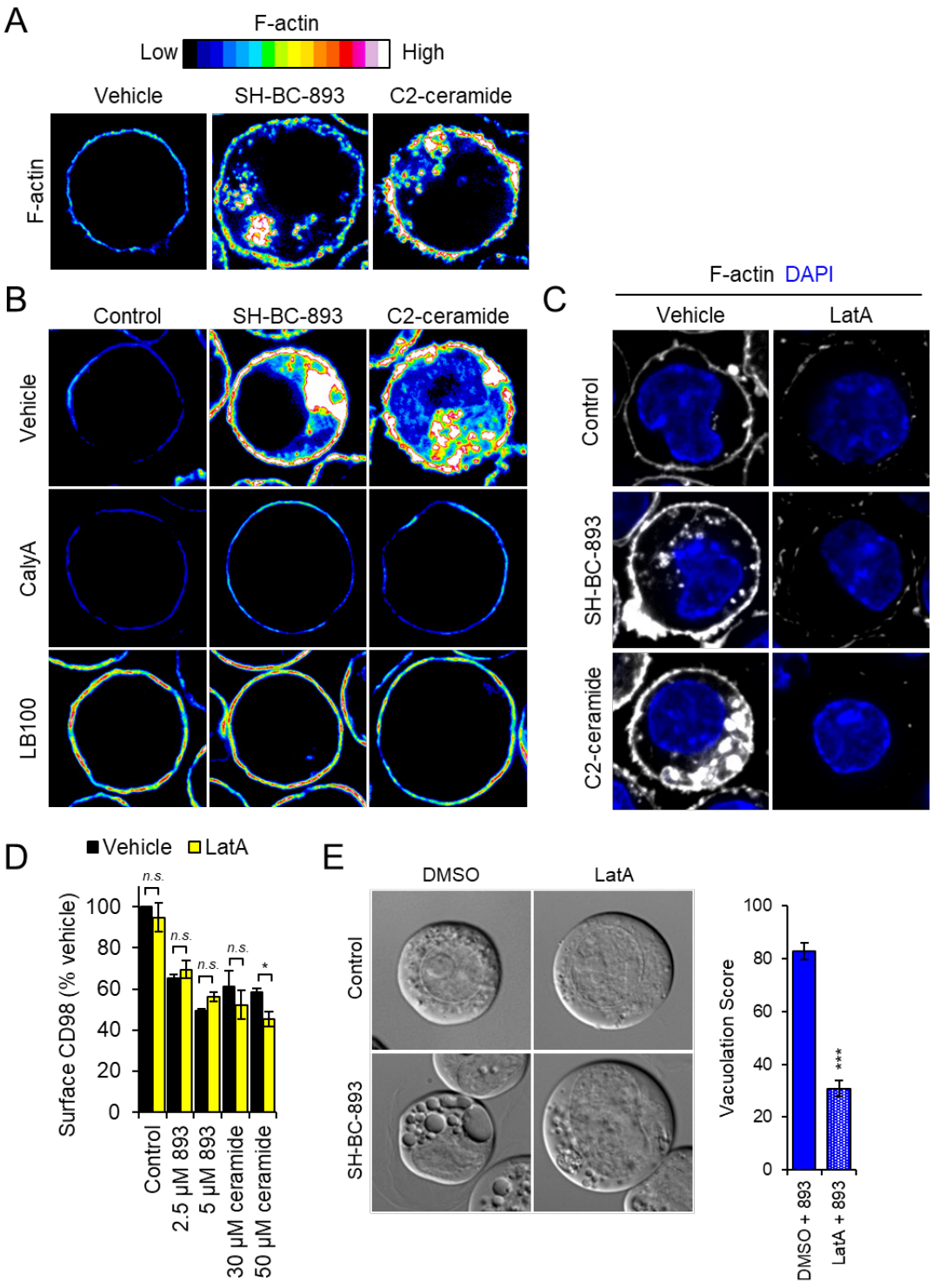

Figure 2.7. C2-ceramide and SH-BC-893 promote actin polymerization. A) FL5.12 cells treated with SH-BC-893 (10 µM) or C2-ceramide (50 µM) for 1 h and then stained for F-actin

with Alexa Fluor 488-conjugated phalloidin. B) Same as in A), except cells pre-treated with vehicle or PP2A inhibitors calyculinA (calyA, 5 nM) or LB-100 (100 μM) for 1.5 h prior to SH-BC-893 addition. C) Same as in A), except cells pre-treated with vehicle or actin polymerization inhibitor latrunculinA (LatA, 1 μM) for 30 min prior to SH-BC-893 (2.5 μM) or C2-ceramide (30 μM) addition. D) FL5.12 cells pre-treated (30 min) with LatA (1 μM) were treated with SH-BC-893 (2.5 or 5 μM) or C2-ceramide (30 or 50 μM) for 1 h and surface CD98 quantified by flow cytometry. E) FL5.12 cells pre-treated with LatA (30 min, 1 μM) were treated with SH-BC-893 (5 μM) for 2 h and imaged by DIC microscopy to visualize vacuoles. ($n = 3$ in D and $n \geq 30$ cells per condition in E). A two-tailed t-test was used to compare SH-BC-893 -treated cells to combination of LatA and SH-BC-893, *** = $p \leq 0.001$.

Figure 2.8

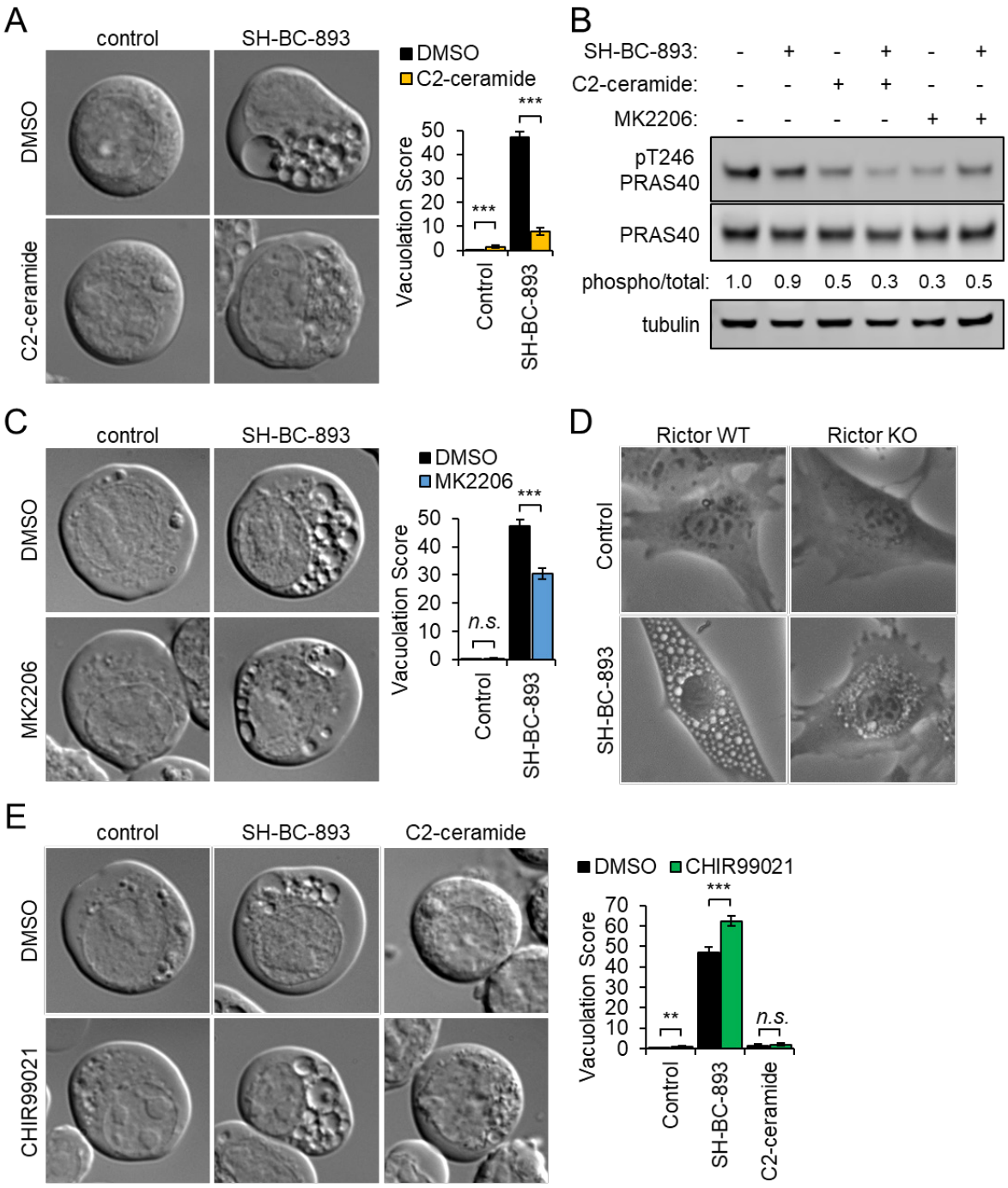

Figure 2.8. Ceramide inhibits vacuolation by reducing Akt activity. (A) FL5.12 cells were treated for 3 h with SH-BC-893 (2.5 μM) and/or C2-ceramide (50 μM) as indicated and imaged

by DIC microscopy. (B) Western blot measuring the phosphorylation of the AKT substrate PRAS40 (total and phospho-Thr246) in FL5.12 cells treated for 30 min with SH-BC-893 (5 μM), C2-ceramide (50 μM), and/or MK2206 (1 μM) as indicated. (C) FL5.12 cells treated for 3 h with SH-BC-893 (2.5 μM) and/or AKT inhibitor MK2206 (1 μM) as indicated and visualized as in (A). (D) Rictor WT and KO murine embryonic fibroblasts (MEFs) treated for 6 h with vehicle or SH-BC-893 (5 μM) then visualized by phase contrast microscopy. (E) FL5.12 cells treated for 3 h with SH-BC-893 (2.5 μM) or C2-ceramide (50 μM) and the Gsk3b inhibitor CHIR99021 (10 μM) as indicated; visualized as in (A). In (A,C,E), ≥ 400 cells per condition were analyzed from a total of three independent experiments; using a two-tailed t-test to compare either SH-BC-893 or C2-ceramide to the vehicle control (in E) or SH-BC-893 alone to the combination of SH-BC-893 with C2-ceramide (A), MK2206 (C), or CHIR99021 (E), *n.s.* = not significant, ** = $p \leq 0.01$, or *** = $p \leq 0.001$.

2.13 Supplementary Figures

Supplementary Fig. S2.1

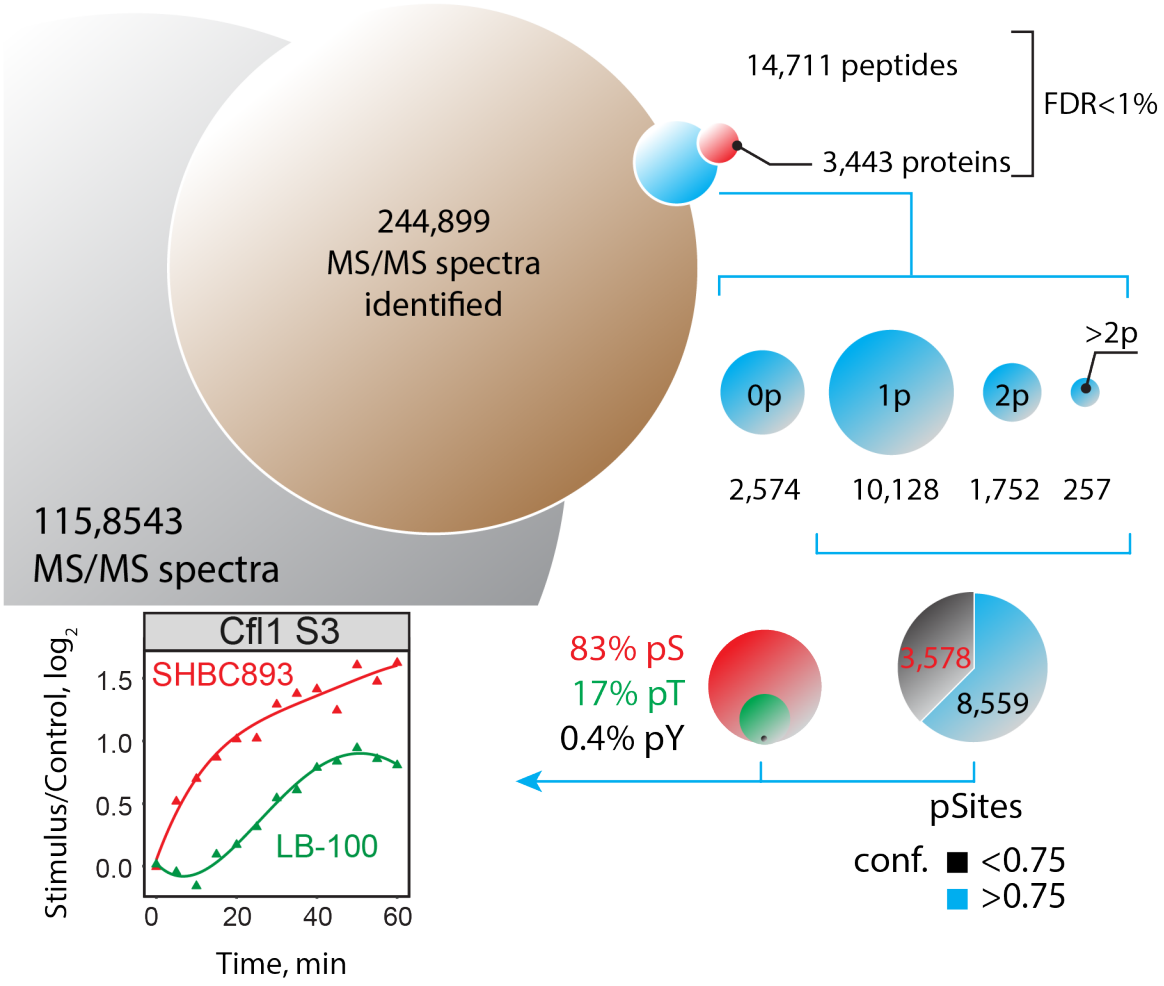

Supplementary Figure S2.1. Summary of statistics of triple SILAC phosphoproteomics experiment comparing LB-100 and SH-BC-893-treated FL5.12 cells.

Supplementary Fig. S2.2

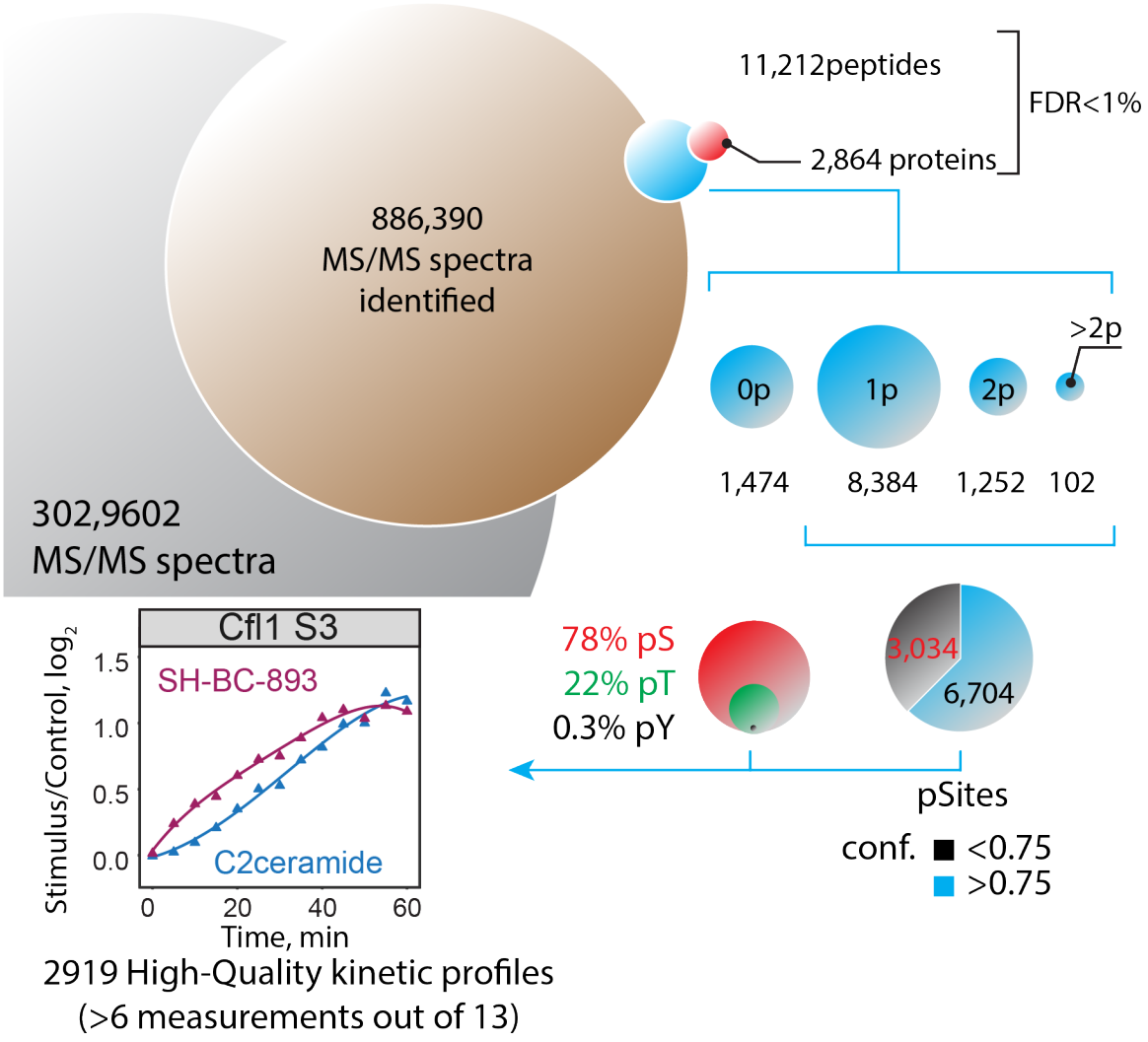

Supplementary Figure S2.2. Summary of statistics of triple SILAC phosphoproteomics experiment comparing C2-ceramide and SH-BC-893-treated FL5.12 cells.

Supplementary Fig. S2.3

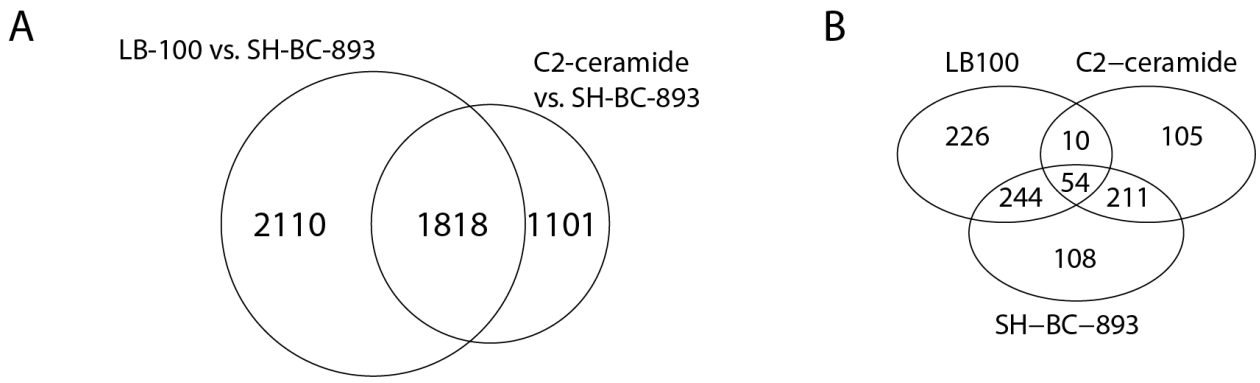

Supplementary Figure S2.3. Comparison of compounds affecting PP2A activity revealed different protein subsets affecting cell signaling. A) Overlap of high quality kinetic profiles obtained from both triple SILAC experiments comparing either SH-BC-893 and LB-100 or SH-BC-893 and C2-ceramide. 1860 profiles were common to both experiments. B) Overlap of dynamically regulated phosphosites.

Supplementary Fig. S2.4

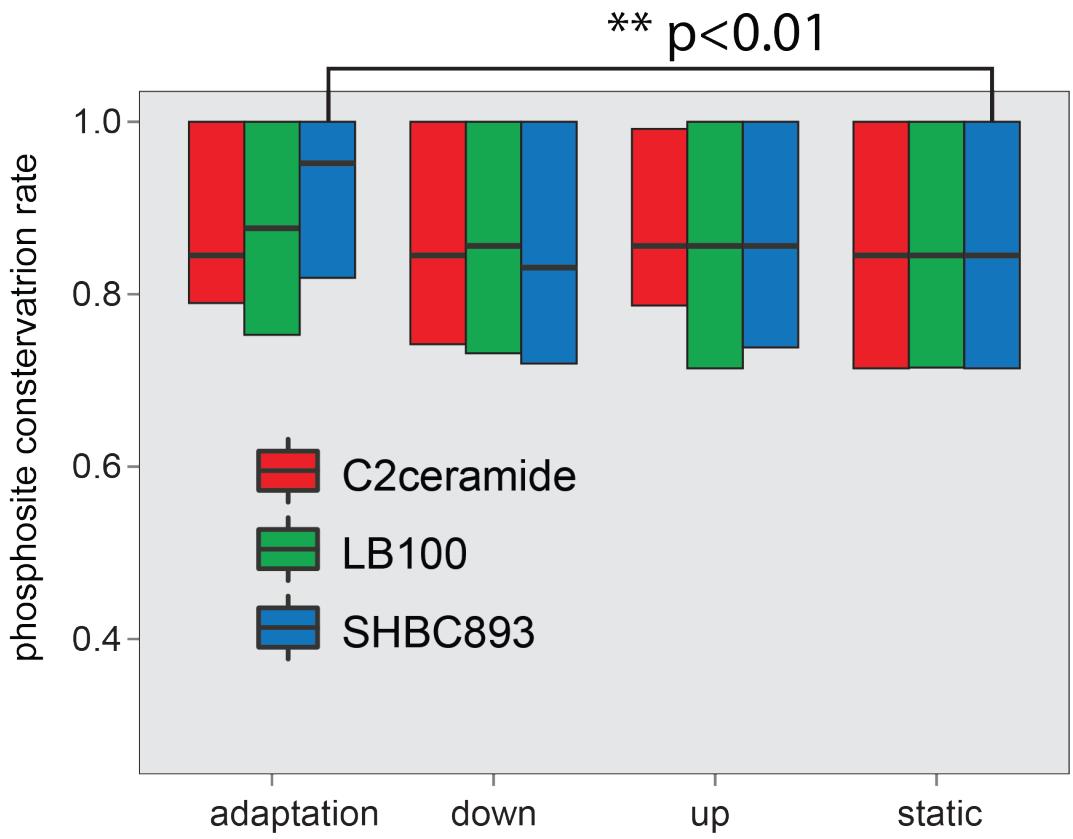

Supplementary Figure S2.4. Conservation rate analysis. Conservation of phosphorylation sites was compared based on grouping of the kinetic profiles observed for different treatments. Phosphorylation sites showing adaptation-like behavior upon treatment with SH-BC-893 are more conserved across species.

Supplementary Fig. S2.5

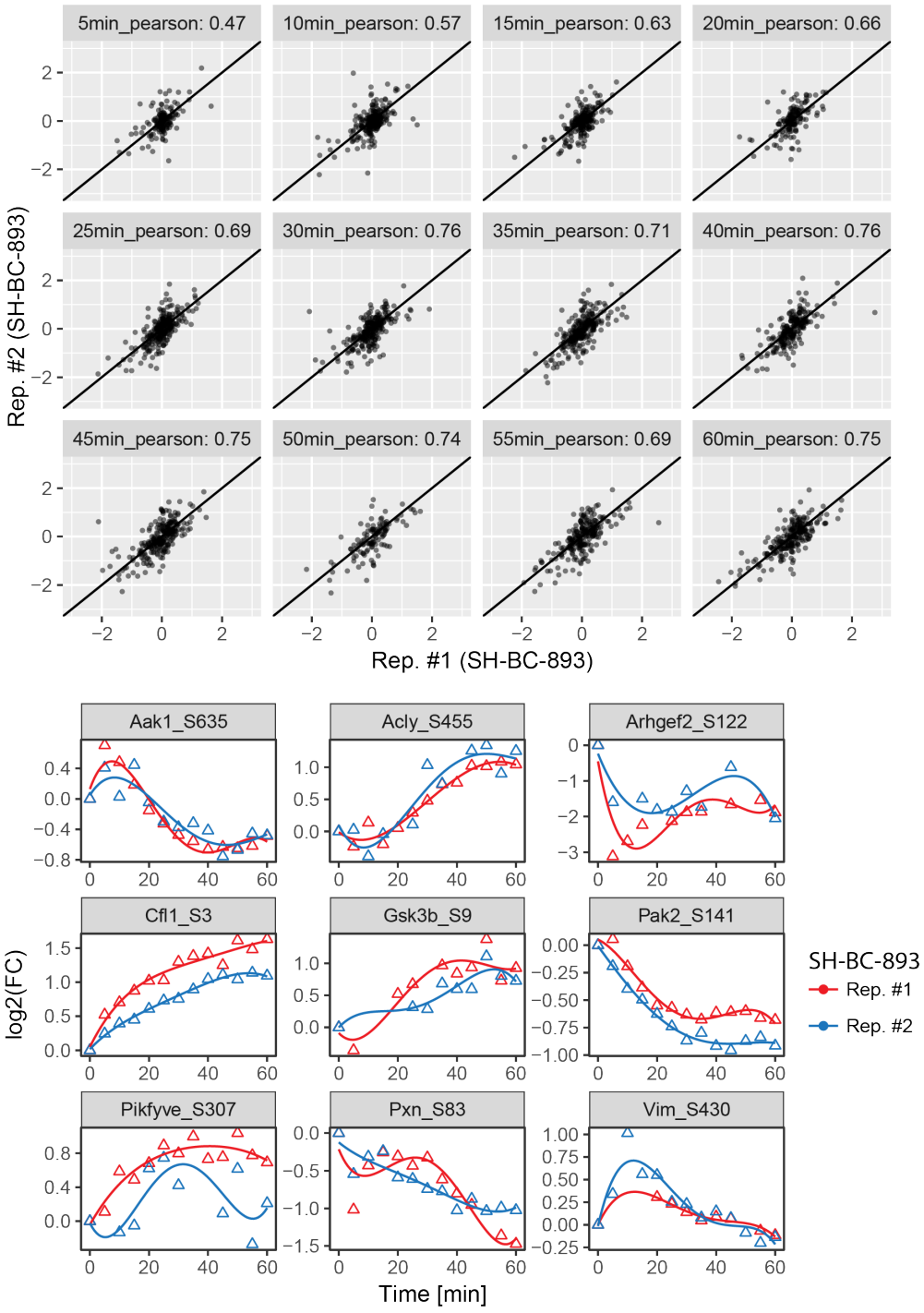

Supplementary Figure S2.5. Reproducibility between dynamic phosphoproteomics profiles between replicates. A) Reproducibility of fold change measurements for dynamic phosphoproteomic profiles taken at different time points following incubation of FL5.11 cells with

SH-BC-893. Replicates 1 and 2 correspond to experiments described in Figure 2.3C and Figure 2.6B, respectively. Pearson correlation coefficients are displayed for each time point. B) Comparison of dynamic profiles for 9 phosphopeptides obtained from two separate time course experiments (R1 and R2; SHBC893 treatments).

Supplementary Fig. S2.6

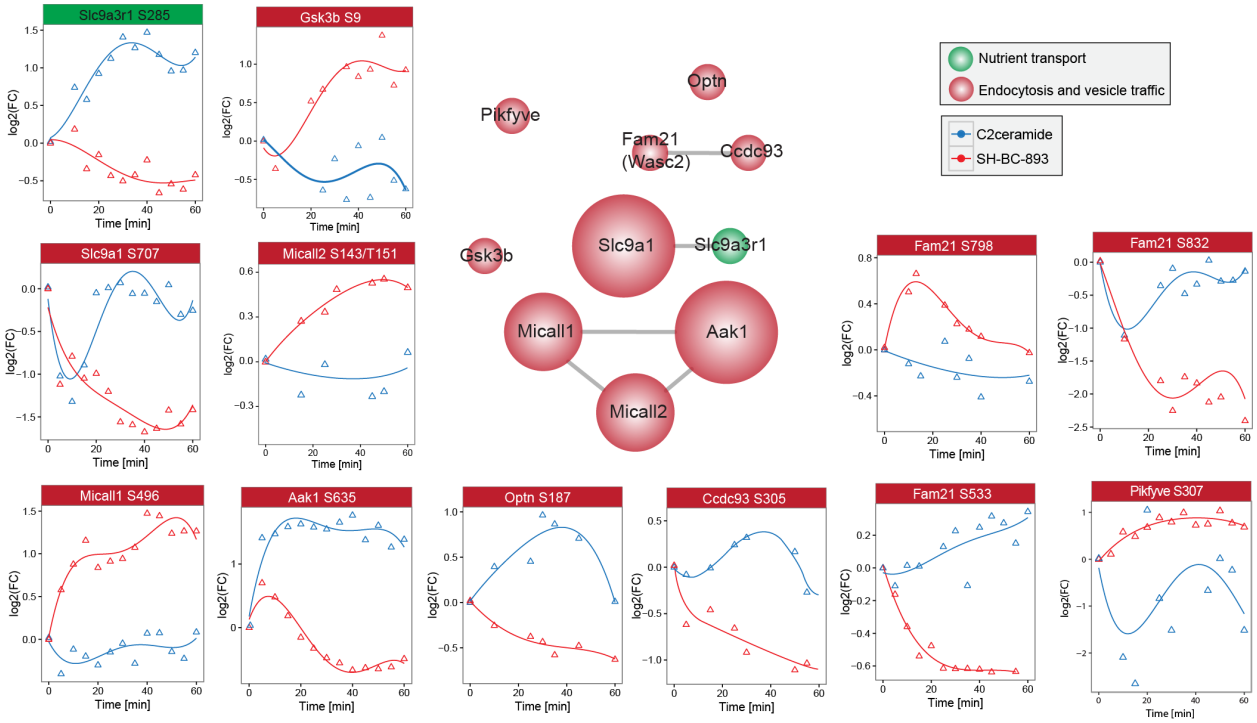

Supplementary Figure S2.6. Proteins from endosomes, late endosomes or intracellular membrane-bound organelles are differentially phosphorylated upon treatment with sphingolipids. Partial network and kinetic profiles of phosphorylation from proteins following cell treatment with SH-BC-893 and C2-ceramide.

Supplementary Fig. S2.7

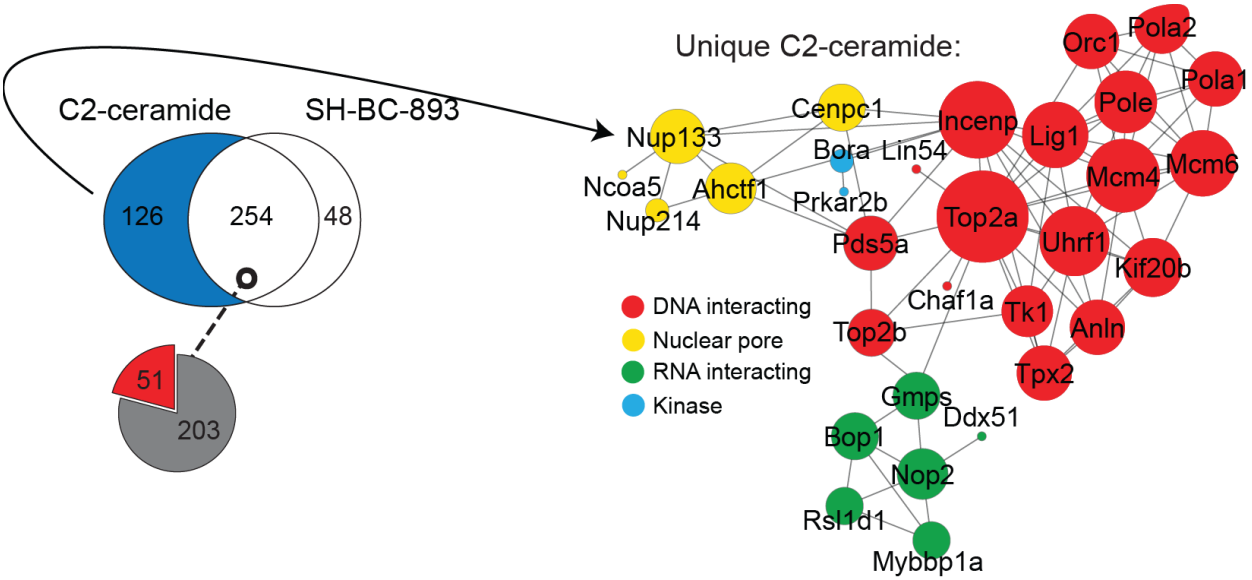

Supplementary Figure S2.7. Network of proteins that are uniquely phosphorylated upon C2-ceramide treatment.

Supplementary Fig. S2.8

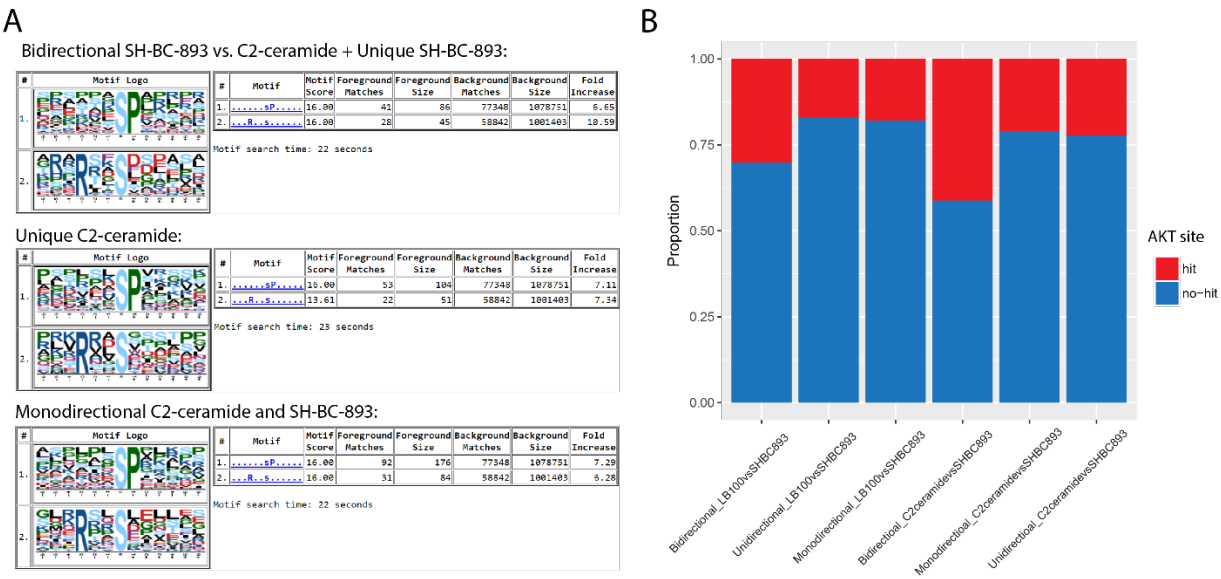

Supplementary Figure S2.8. Consensus motif of phosphorylation sites observed in dynamic profiles from C2-ceramide and SH-BC-893 phosphoproteomic experiments. A) Motif-X analyses of phosphorylation sites from three groups of dynamic profiles. B) Relative proportion of Akt sites within each group predicted from GPS 3.0 (http://gps.biocuckoo.org/).

Supplementary Fig. S2.9

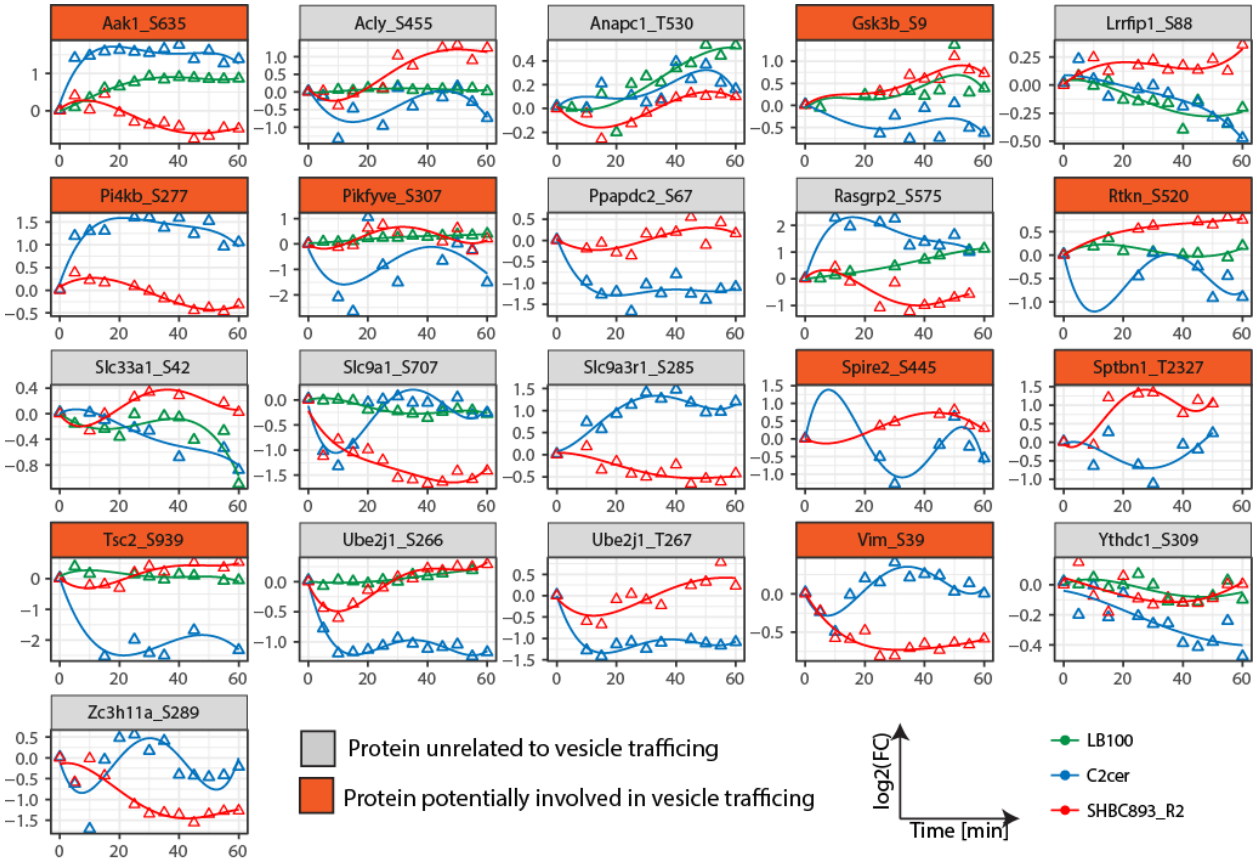

Supplementary Figure S2.9. Dynamic profiles of putative Akt substrates associated with vesicle trafficking.

Supplementary Fig. S2.10

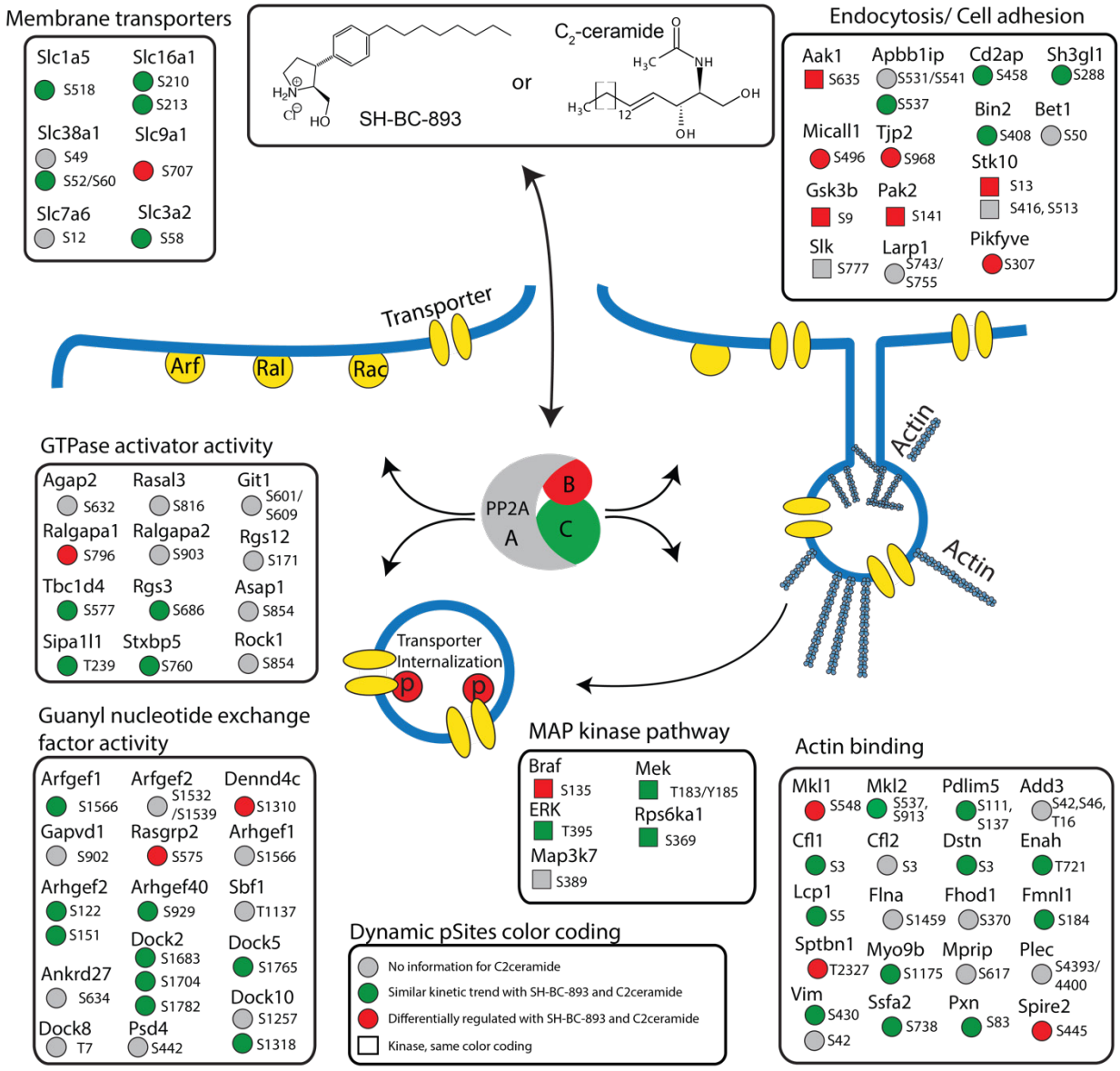

Supplementary Figure S2.10. Pictogram of proteins that are dynamically phosphorylated upon SH-BC-893 and C2-ceramide treatment. Only proteins associated to the main GO term molecular functions (Membrane transport, GTPase and GEF regulation, Actin binding, Endocytosis) are shown. Color coding indicates differences and similarities observed between C2-ceramide and SH-BC-893 treatments.

Supplementary Fig. S2.11

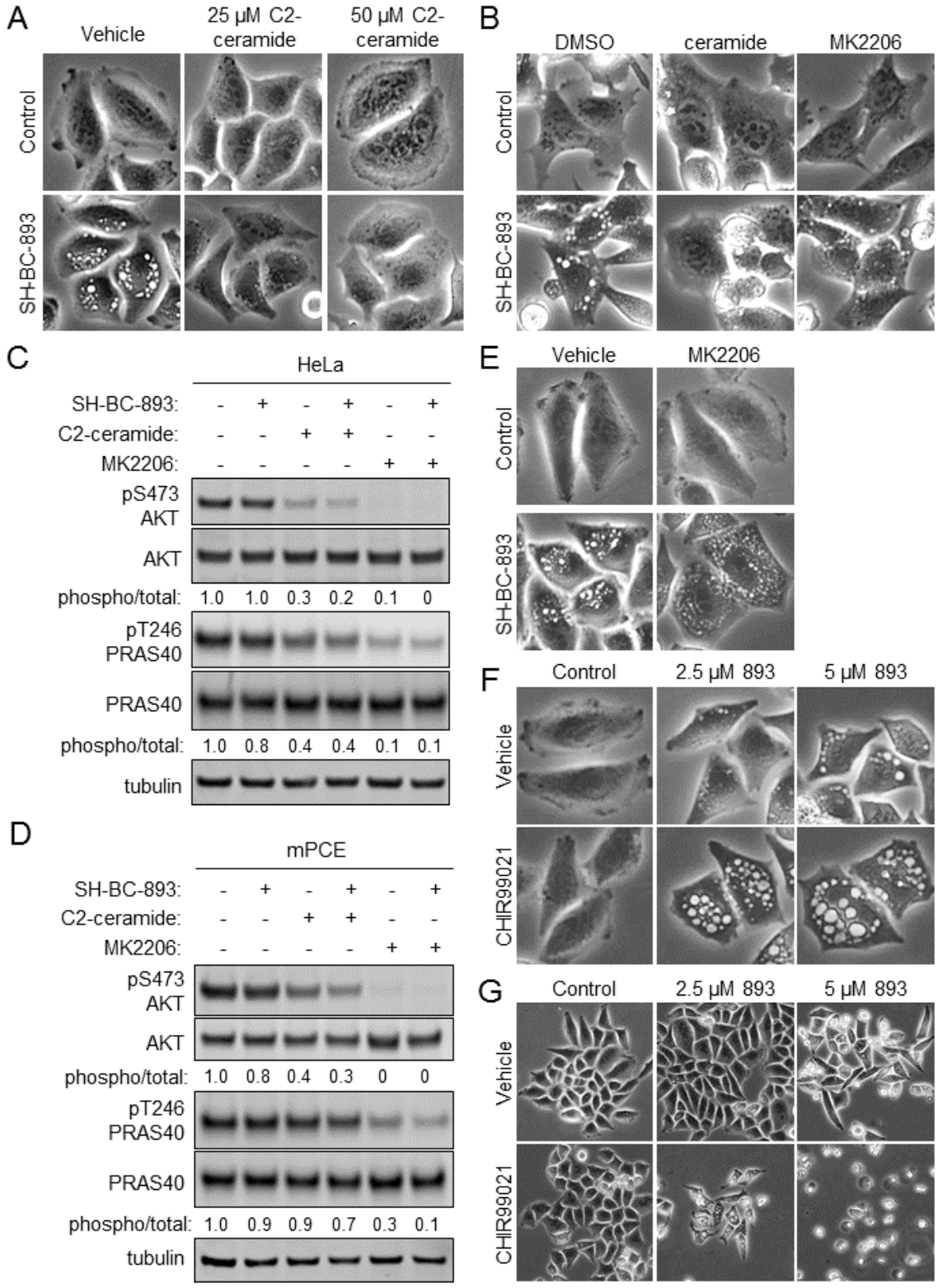

Supplementary Figure S2.11: Ceramide inhibits vacuolation in multiple cell lines by reducing Akt activity. (A) HeLa cells treated for 3 h with SH-BC-893 (5 μM) and the indicated concentrations of C2-ceramide were imaged by phase contrast microscopy to visualize vacuoles. (B) Murine prostate cancer epithelial (mPCE) cells co-treated with SH-BC-893 (5 μM) and C2-ceramide (50 μM) or the Akt inhibitor MK2206 (1 μM) and imaged as in A. (C) Western blot for AKT (total and phospho-Ser473), PRAS40 (total and phospho-Thr246) and tubulin (loading control) in HeLa cells treated for 30 min with SH-BC-893 (5 μM), C2-ceramide (50 μM), and/or MK2206 (1 μM). (D) As in (B), except with mouse prostate cancer epithelial cells (mPCE). (E) HeLa cells treated for 6 h with SH-BC-893 (5 μM) and/or the AKT inhibitor MK2206 (1 μM) were visualized as in (A). (F) HeLa cells were treated for 6 h with indicated concentrations of SH-BC-893 or C2-ceramide and/or CHIR99021 (10 μM) as indicated and visualized as in (A). (G) As in E, except at 24 h.

CHAPTER 3

Simultaneous inhibition of endocytic recycling and lysosomal fusion sensitizes cells and tissues to oligonucleotide therapeutics

Brendan T. Finicle[1], Kazumi H. Eckenstein[1], Alexey S. Revenko[2], Brooke A. Anderson[2], W. Brad Wan[2], Alison N. McCracken[3], Daniel Gil[3], David A. Fruman[4], Stephen Hanessian[5,6], Punit P. Seth[2,7], and Aimee L. Edinger[1,*]

Affiliations

[1] Department of Developmental and Cell Biology, University of California Irvine, Irvine, CA, USA
[2] Ionis Pharmaceuticals, Carlsbad, CA, USA
[3] Siege Pharmaceuticals, Irvine, CA, USA
[4] Department of Molecular Biology and Biochemistry, University of California Irvine, Irvine, CA, USA
[5] Department of Chemistry, Université de Montréal, Montréal, QC, Canada
[6] Department of Pharmaceutical Sciences, University of California Irvine, Irvine, CA, USA
[7] Current address: Alnylam Pharmaceuticals, Cambridge, MA, USA

This chapter is derived from the manuscript accepted for publication in *Nucleic Acids Research: Nucleic Acids Research.* 2023 Accepted for publication.

3.1 Abstract

Inefficient endosomal escape remains the primary barrier to the broad application of oligonucleotide therapeutics. Liver uptake after systemic administration is sufficiently robust that a therapeutic effect can be achieved but targeting extrahepatic tissues remains challenging. Prior attempts to improve

oligonucleotide activity using small molecules that increase the leakiness of endosomes have failed due to unacceptable toxicity. Here we show that the well-tolerated and orally bioavailable synthetic sphingolipid analog, SH-BC-893, increases the activity of antisense oligonucleotides (ASOs) and small interfering RNAs (siRNAs) up to 200-fold in vitro without permeabilizing endosomes. SH-BC-893 treatment trapped endocytosed oligonucleotides within extra-lysosomal compartments thought to be more permeable due to frequent membrane fission and fusion events. Simultaneous disruption of ARF6-dependent endocytic recycling and PIKfyve-dependent lysosomal fusion was necessary and sufficient for SH-BC-893 to increase non-lysosomal oligonucleotide levels and enhance their activity. In mice, oral administration of SH-BC-893 increased ASO potency in the liver by 15-fold without toxicity. More importantly, SH-BC-893 enabled target RNA knockdown in the CNS and lungs of mice treated subcutaneously with cholesterol-functionalized duplexed oligonucleotides or unmodified ASOs, respectively. Together, these results establish the feasibility of using a small molecule that disrupts endolysosomal trafficking to improve the activity of oligonucleotides in extrahepatic tissues.

3.2 Introduction

Oligonucleotide therapeutics have the potential to revolutionize medicine by making almost any target accessible. Oligonucleotides targeting RNA include single-stranded antisense oligonucleotides (ASOs) that base pair with a target RNA to elicit RNaseH-dependent degradation, inhibition of translation, or changes to splicing (Roberts et al., 2020; Shen and Corey, 2018). Double-stranded small interfering RNAs (siRNAs) degrade target RNAs after being loaded into the RNA-induced silencing complex (RISC). Medicinal chemistry optimization of the drug-like properties of ASOs and siRNAs solved historical problems with stability and rapid clearance. At least thirteen therapeutic oligonucleotides have been FDA-approved and hundreds are in preclinical development (Hong et al., 2015; Odate et al., 2017; Raal et al., 2010; Ross et al., 2017; De Velasco et al., 2019; Yamamoto et al., 2015).

Despite these successes, inefficient delivery to targets in the cytosol and nucleus of cells remains a major barrier to the broad application of oligonucleotide therapeutics (Corey et al., 2022; Dowdy, 2017; Gökirmak et al., 2021; Roberts et al., 2020). Only 1% of the oligonucleotide that is delivered to patients engages its target. The high concentrations required in target tissues are readily achieved in the liver after subcutaneous administration. Extrahepatic tissues generally require local (e.g. intrathecal or aerosol) delivery or frequent administration of high doses to achieve significant target engagement (Gökirmak et al., 2021). Conjugation to ligands that bind to cell surface receptors can increase oligonucleotide activity by increasing cellular uptake (Gökirmak et al., 2021; Seth et al., 2019; Tanowitz et al., 2017). Thus far, the only liganded oligonucleotides that are FDA-approved are N-acetylgalactosamine (GalNAc) conjugates that target hepatocytes. Other ligand-target pairs will require optimization for extrahepatic delivery. Approaches that address post-endocytic blocks to delivery offer an alternate strategy to extend the range of tissues and cells that are accessible to oligonucleotide therapeutics.

As large (4-14 kDa) polar molecules, ASOs and siRNAs do not readily diffuse across lipid bilayers; both receptor-targeted and unconjugated oligonucleotides enter cells via endocytosis (Dowdy, 2017; Gökirmak et al., 2021). Oligonucleotides in endocytic vesicles are either recycled back to the extracellular space through exocytosis or progress to lysosomes, the degradative compartment of the cell (Crooke et al., 2017; Gökirmak et al., 2021; Grant and Donaldson, 2009). Chemical modifications render therapeutic oligonucleotides resistant to lysosomal nucleases (Dowdy, 2017; Gökirmak et al., 2021; Roberts et al., 2020). Therefore, the majority of endocytosed oligonucleotides accumulate within lysosomes where they are stable but unable to reach their cytosolic targets, although recent evidence suggests slow leakage from lysosomes supports long-term oligonucleotide activity in the liver (Brown et al., 2020). Attempts to improve the escape of oligonucleotides from endosomes and lysosomes into the cytosol have met little success. Genetic knockdown screens have failed to identify targetable proteins that significantly enhance oligonucleotide activity (Linnane et al., 2019; Wagenaar et al., 2015). Molecules that increase the leakiness of endosomes produce large increases in oligonucleotide activity but have a narrow therapeutic index because permeabilizing endosomes and lysosomes is toxic (Gilleron et al., 2015; Juliano, 2021; Kendall et al., 2012; Ming et al., 2013; Osborn et al., 2015; Yang et al., 2015; Zhang et al., 2017). Therefore, novel approaches that improve oligonucleotide escape into the cytosol without lysing endocytic compartments are required to solve the delivery problem that limits the therapeutic use of oligonucleotides.

In the absence of permeabilizing agents, oligonucleotides likely escape from endocytic compartments at sites of membrane fission and fusion (Juliano, 2018; Wagenaar et al., 2015; Wang et al., 2017; Wittrup et al., 2015). During these dynamic membrane remodeling events, the lipid bilayer is deformed to create non-bilayer regions that have increased permeability (Bennett and Tieleman, 2014; Cullis et al., 1986; Renard et al., 2018; Wang et al., 2009; Wickner and Rizo, 2017). Consistent with this model, pre-lysosomal compartments that undergo high rates of vesicle budding and fusion have been identified

as sites of oligonucleotide escape (Liang et al., 2020; Linnane et al., 2019; Paramasivam et al., 2022; Wang et al., 2016). Escape from lysosomes is much less efficient because the limiting membrane is heavily decorated with glycoproteins (e.g., LAMP1 and LAMP2) and glycolipids that reduce permeability relative to other endocytic structures (Rudnik and Damme, 2021; Wilke et al., 2012). Approaches that increase oligonucleotide uptake and/or residency time in pre-lysosomal compartments where oligonucleotide escape is most efficient could offer significant gains in potency that would make extrahepatic tissues therapeutically accessible.

We have published that the synthetic sphingosine analog SH-BC-893 disrupts endocytic recycling by inactivating the small GTPase ARF6 and blocks lysosomal fusion reactions that depend on the lipid kinase PIKfyve (Finicle et al., 2018; Jayashankar et al., 2021; Kim et al., 2016; Kubiniok et al., 2019). We hypothesized that simultaneous disruption of these endolysosomal trafficking pathways would synergistically increase oligonucleotide activity by causing accumulation within pre-lysosomal compartments where endosomal release is most efficient (Fig. 3.1A). Importantly, these changes in trafficking are well tolerated as SH-BC-893 is non-toxic at the effective dose even with chronic administration (Finicle et al., 2018; Jayashankar et al., 2021; Kim et al., 2016). Here, we demonstrate that the parallel actions of SH-BC-893 on endocytic recycling and lysosomal fusion are necessary and sufficient to increase intracellular oligonucleotide levels in extra-lysosomal compartments and significantly enhance oligonucleotide activity both in vitro and in vivo with no toxicities detected.

3.3 Results

SH-BC-893 increases ASO delivery and activity in vitro

SH-BC-893 (Supplementary Fig. S3.1) disrupts endocytic recycling by inactivating the small GTPase ARF6 and blocks lysosomal fusion reactions that depend on the lipid kinase PIKfyve (Finicle et al., 2018; Jayashankar et al., 2021; Kim et al., 2016; Kubiniok et al., 2019), activities that we predicted would synergize to promote oligonucleotide delivery (Fig. 3.1A). HeLa cervical carcinoma cells were used initially to test this hypothesis because they are well suited to confocal microscopy and widely used to study both intracellular trafficking and oligonucleotide delivery. As expected, SH-BC-893 disrupted endolysosomal trafficking in HeLa cells at non-toxic concentrations (Fig. 3.1B,C). While toxic in vitro at high concentrations, SH-BC-893 is well tolerated in mice at the effective dose even with chronic administration (Jayashankar et al., 2021; Kim et al., 2016). Initial studies used a phosphorothioate (PS) gapmer complementary to the long non-coding RNA (lncRNA) *MALAT1* with 10 deoxynucleotides in the center flanked on each side by 3 nucleotides containing riboses with a 2',4' constrained ethyl (cEt) group (Supplementary Table 3.1); this modification is common among preclinical ASOs and is currently being evaluated in patients (Gökirmak et al., 2021). ASO localization was tracked using a polyclonal antibody specific for PS ASOs (Linnane et al., 2019).

ASO localization was evaluated by confocal fluorescence microscopy after gymnotic delivery ("free uptake"). In control cells, the majority of internalized ASOs colocalized with the lysosomal marker LAMP2 after 6 h (Fig. 3.1D,E and Supplementary Fig. S3.2A). Co-treatment with SH-BC-893 (5 μM) reduced the percent of ASOs in LAMP2-positive lysosomes from 70% to 9%. Moreover, SH-BC-893 treatment increased the total amount of intracellular ASOs by 4-fold (Fig. 3.1D,E). Reducing the delivery of ASOs to LAMP2-positive lysosomes and concomitantly increasing intracellular ASO levels translated to a more than 250-fold increase in the amount of ASOs in extra-lysosomal, LAMP2-negative compartments. Similar results were obtained with an untagged 2'-O-methoxyethyl (2'MOE) PS-gapmer,

an ASO tagged on the 5’ end with a 6-carboxyfluorescein (FAM) fluorophore, and an antibody against another lysosomal marker, LAMP1 (Supplementary Table 3.1 and Supplementary Fig. S3.2B-G). In sum, co-incubation with SH-BC-893 increased the total amount of intracellular ASOs and dramatically reduced colocalization with lysosomal markers.

ASOs must escape from endosomal structures to produce knockdown. It is estimated that 1-4% of the oligonucleotides that are endocytosed escape to the cytoplasm (Dowdy, 2017; Dowdy et al., 2022; He et al., 2021). Such a small quantity is hard to observe in fluorescence microscopy images that contain very bright endosomal signals. To better illustrate changes in the low, cytoplasmic levels of ASOs, the endosomal ASO signal was removed and the cytoplasmic signal quantified (Supplementary Data Fig. S3.3A). Background subtraction was performed using cells that were stained with both primary and secondary antibodies but not exposed to ASOs. In control cells, approximately 3% of the ASOs were cytoplasmic which is consistent with prior estimates (Supplementary Fig. S3.3B-C and (Dowdy, 2017; Dowdy et al., 2022; He et al., 2021)). SH-BC-893 treatment increased the cytosolic fraction to 10% which, given the increase in intracellular ASOs, translated to a 9-fold increase in the absolute amount of cytoplasmic ASO (Supplementary Fig. S3.3B-D). In summary, SH-BC-893 significantly increased the amount of ASO that reaches the cytoplasm.

Whether this increase in cytoplasmic ASOs translated into increased target RNA degradation was assessed by RT-qPCR under the same experimental conditions. Co-treatment with SH-BC-893 increased *MALAT1* knockdown in cells treated with a cEt gapmer ASO (2 μM) from 25% to 85% (Supplementary Fig. S3.4A); similar potentiation was observed with a 2’MOE gapmer ASO (Supplementary Fig. S3.4B). To quantify the degree of potentiation more rigorously (Gagnon and Corey, 2019), IC50s were determined for both cEt and 2’MOE ASOs in the presence or absence of SH-BC-893. With gymnotic delivery in HeLa cells, cEt and 2’MOE gapmer IC50s were 19 μM and 13 μM,

respectively (Fig. 3.2A-D). Co-incubation with SH-BC-893 shifted the dose response curves to the left by 2 logs, reducing the ASO IC50s to 171 nM (cEt) or 61 nM (2'MOE), a 111- or 215-fold increase in activity. ASO potentiation by SH-BC-893 was equally robust when normalized to total RNA or to the housekeeping gene *ACTB* (Fig. 3.2E). Additionally, ASO potentiation by SH-BC-893 was dose responsive, ranging from an 11-fold increase in ASO activity at 2.5 μM to a ~100-fold increase at 5 and 10 μM (Fig. 3.2F). Notably, SH-BC-893-mediated potentiation plateaued at 5 μM, a non-toxic concentration (Fig. 3.1C).

In our experience, the MALAT1 ASOs widely used in proof-of-concept studies are 2-3-fold more potent than most ASOs targeting other sequences. Importantly, SH-BC-893 increased the activity of oligonucleotides of other sequences in different cell types. SH-BC-893 enhanced the activity of a cEt gapmer targeting α-actinin-1 (ACTN1) >63-fold (Fig. 3.2G). In addition to HeLa cells, potentiation was observed in SH-BC-893-treated mouse embryonic fibroblasts and in cancer cell lines derived from tumors of the breast, colon, lung, or pancreas (Fig. 3.2H and Supplementary Fig. S3.5). The same barriers limit ASO and siRNA delivery to their targets in the cytosol and nucleus (Crooke et al., 2017; Dominska and Dykxhoorn, 2010). SH-BC-893 also improved the activity of a palmitate-conjugated, nuclease-resistant siRNA targeting *HPRT1* by 20-fold, shifting the IC50 from 1.9 μM to 97 nM (Fig. 3.2I,J). These results suggest that SH-BC-893 could improve oligonucleotide activity across multiple platforms and in extrahepatic tissues.

SH-BC-893 is less toxic or more effective than previously identified oligonucleotide-potentiating small molecules

Small molecules that enhance endosomal release of oligonucleotides through lysis have been described. For example, the small molecule UNC10217938A dramatically enhances the activity of

ASOs, siRNAs, and splice-switching oligonucleotides by permeabilizing endosomes and lysosomes (Yang et al., 2015). However, the therapeutic use of endolytic agents is limited by their toxicity. Under our standard assay conditions where cells are continuously exposed to ASOs and compound for 24 h, the effective dose of UNC10217938A (Yang et al., 2015) was cytotoxic, killing 90% of the cells (Supplementary Fig. S3.6A,B). In (Yang et al., 2015), toxicity was avoided by pre-loading cells with ASOs for 16 h and then pulsing cells with UNC10217938A for only 2 h. Under these conditions, UNC10217938A produced profound ASO potentiation without cell death (Supplementary Fig. S3.6C,D). In contrast, SH-BC-893 did not increase ASO activity when added after ASO had reached lysosomes. SH-BC-893's lack of toxicity at the efficacious dose (Supplementary Fig. S3.6B) and the observation that SH-BC-893 is not effective once ASO are sequestered in lysosomes suggests that SH-BC-893 does not function as an endolytic agent like UNC10217938A. To directly test whether SH-BC-893 permeabilizes endosomal membranes, cells pre-loaded with ASO and 10 kDa dextran were evaluated by microscopy for release into the cytosol and nucleus (Supplementary Fig. S3.6E,F). At their effective doses, UNC10217938A, but not SH-BC-893, released both ASOs and dextran from endosomes. Together, this data shows that SH-BC-893 does not enhance ASO activity by permeabilizing lysosomes and is consistent with our proposed mechanism of action: trapping ASOs in a pre-lysosomal compartment from which oligonucleotide escape is naturally more efficient (Fig. 3.1A).

Several other small molecules have been reported to enhance ASO and/or siRNA activity without permeabilizing endosomes or lysosomes. For example, the GSK3 inhibitor 6BIO enhances ASO and siRNA activity through an unknown mechanism (Zhang et al., 2017), the mTOR kinase inhibitor AZD8055 increases ASO activity by stimulating autophagy (Ochaba et al., 2019), and the retrograde trafficking inhibitor retro-1 increases the activity of ASOs (Ming et al., 2013). Because the assay conditions and cell lines used in these publications vary, we directly compared the ASO potentiating ability of these compounds and SH-BC-893 in HeLa cells treated with an RNaseH-dependent ASO.

Notably, many prior studies utilized splice-switching ASOs that trigger expression of luciferase or GFP, reporter assays that give a larger fold-change in activity than would an equivalent effect size in an RNaseH-dependent assay measuring RNA knockdown. Using the concentrations employed in the prior publications, 6BIO, AZD8055, and retro-2 enhanced ASO activity 3-, 4-, or 5-fold, respectively, while SH-BC-893 increased ASO activity 130-fold under the same conditions (Supplementary Fig. S3.6G-H); the structurally-related molecule retro-2 was utilized because retro-1 is not commercially available (Stechmann et al., 2010). None of these molecules were cytotoxic under these assay conditions (Supplementary Fig. S3.6I). In summary, SH-BC-893 is less toxic than endosome-permeabilizing agents and more effective than previously identified small molecule ASO potentiators that do not lyse endocytic structures.

Simultaneous PIKfyve and ARF6 inhibition is both necessary and sufficient for ASO potentiation by SH-BC-893

The mechanism by which SH-BC-893 promotes antisense activity was next evaluated. We hypothesized that the previously reported effects of SH-BC-893 on endocytic trafficking, disrupting ARF6-dependent endocytic recycling and PIKfyve-dependent lysosomal fusion reactions (Finicle et al., 2018; Kim et al., 2016), were responsible for the observed oligonucleotide potentiation (Fig. 3.1A). To test this model, the impact of selective PIKfyve (YM201636 and apilimod) or ARF6 (SecinH3 and NAV2729) inhibitors on ASO uptake and localization was compared to SH-BC-893 (structures provided in Supplementary Fig. S3.1). These structurally distinct inhibitors are unlikely to have the same off-target effects as each other or as SH-BC-893, thereby increasing confidence that any shared effects on oligonucleotide trafficking and activity are due to ARF6 or PIKfyve inhibition.

At concentrations previously established to fully inhibit their targets (Finicle et al., 2018; Kim et al., 2016), the two ARF6 inhibitors increased intracellular ASO levels to a similar extent as SH-BC-893 (Fig. 3.3A-B). In contrast, PIKfyve inhibition with YM201636 or apilimod slightly decreased ASO accumulation within cells. ARF6 promotes endosomal recycling (Finicle et al., 2018; Grant and Donaldson, 2009). To determine whether ARF6 inhibition increased intracellular ASO levels by reducing their recycling out of the cell (Fig. 3.1A), a pulse-chase protocol was designed. Cells were pulsed with ASOs for 1 h in the absence of inhibitors, washed, and then maintained in medium lacking ASOs but containing vehicle, SH-BC-893, an ARF6 inhibitor, or a PIKfyve inhibitor for an additional 2 h (Fig. 3.3C-D). Control cells treated with vehicle lost >80% of the ASO signal during the 2 h chase indicating that much of the ASO that enters cells is recycled. The loss of signal during the chase was not due to quenching of the 6-FAM fluorophore as similar results were obtained with untagged ASOs detected with an antibody recognizing PS ASOs (Supplementary Fig. S3.7A-B). In contrast to the >80% loss of signal in control cells, only 25-30% of the ASO signal was lost when cells were chased in medium containing SH-BC-893 or the ARF6 inhibitors SecinH3 and NAV2729 (Fig. 3.3C-D). Thus, ARF6 inhibition is sufficient to account for SH-BC-893's ability to increase intracellular ASO levels and reduce ASO recycling.

Results using ARF6 inhibitors were validated with genetic approaches. The classic knockdown/knockout target validation experiments could not be performed because knockdown of ARF6 compromised cellular health to an extent that would confound the interpretation of results. We have previously shown that inhibition of ARF6-mediated endocytic recycling by SH-BC-893 occurs downstream of activation of the serine and threonine protein phosphatase 2A (PP2A) (Finicle et al., 2018). ARF6 is activated by its guanine nucleotide exchange factor GRP1 which is in turn inactivated by PP2A-dependent dephosphorylation (Finicle et al., 2018; Li et al., 2012). Replacing serine 255 and threonine 280 with phosphomimetic aspartic acid residues ($GRP1^{DD}$) renders GRP1 resistant to

inactivation by PP2A and restores recycling in SH-BC-893-treated cells. Consistent with a model where SH-BC-893 increases intracellular ASO levels by inactivating ARF6, SH-BC-893 failed to block ASO recycling in GRP1^{DD} expressing cells (Fig. 3.3E-F). Thus, chemical and genetic approaches indicate that ARF6 inactivation is both necessary and sufficient to explain the ability of SH-BC-893 to boost intracellular ASO levels.

Although the ARF6 inhibitors SecinH3 and NAV2729 increased intracellular ASO levels, they did not block delivery to lysosomes like SH-BC-893 (Fig. 3.3A,G). In contrast, the PIKfyve inhibitors YM201636 and apilimod reduced the amount of ASOs within lysosomes by 80-90% similar to SH-BC-893. However, these PIKfyve inhibitors did not increase intracellular ASO levels and had only a minimal effect on recycling (Fig. 3.3A-D). In keeping with the model in Fig. 3.1A, combining ARF6 and PIKfyve inhibition was necessary and sufficient to recapitulate the full effects of SH-BC-893 on ASO localization. Cells treated with both the ARF6 inhibitor NAV2729 and the PIKfyve inhibitor YM201636 had more intracellular ASOs outside of lysosomes matching the effects of SH-BC-893. Taken together, these experiments indicate that inhibiting ARF6 and PIKfyve-dependent trafficking in parallel accounts for effects of SH-BC-893 on intracellular ASO accumulation and trafficking as proposed in Fig. 3.1A.

To determine the extent to which increased intracellular ASO levels and extra-lysosomal localization contribute to the improved ASO activity in SH-BC-893-treated cells (Fig. 3.2 and Supplementary Figs. S3.4 and S3.5), the effects of ARF6 inhibitors and PIKfyve inhibitors alone and in combination on ASO activity were assessed by RT-qPCR. Despite increasing the amount of intracellular ASOs to a similar extent as SH-BC-893 (Fig. 3.3A,B), the ARF6 inhibitors NAV2729 and SecinH3 failed to increase ASO activity (Fig. 3.4A,B and Supplementary Fig. S3.8A,B). Lack of potentiation most likely reflects ASO accumulation in lysosomes when only ARF6 is inhibited (Fig. 3.3A,G) as escape from this site is expected to be inefficient. Although they reduced lysosomal co-localization to a similar degree as SH-

BC-893 (Fig. 3.3A,G), the PIKfyve inhibitors YM201636 or apilimod increased ASO activity by only 3-4-fold (Fig. 3.4A,B and Supplementary Fig. S3.8A,B). The failure of PIKfyve inhibitors to increase ASO activity to a similar extent as SH-BC-893 likely reflects their inability to increase intracellular ASO accumulation (Fig. 3.3A-B). Combining the ARF6 inhibitor NAV2729 with the PIKfyve inhibitor YM201636 produced marked synergy, improving ASO activity to the same extent as SH-BC-893 (Fig. 3.4A,B). Importantly, SH-BC-893, the ARF6 inhibitors, the PIKfyve inhibitors, and the combination were not toxic to cells at the concentrations that disrupt endolysosomal trafficking and modulate ASO activity (Supplementary Fig. S3.8C). As for SH-BC-893 (Fig. 3.2H-J), the synergy between ARF6 inhibitors and PIKfyve inhibitors was not cell type- or platform-specific. PIKfyve/ARF6 inhibitor combinations also improved the activity of a *Malat1*-targeting cEt gapmer in MEFs and a *HPRT1*-targeting siRNA in HeLa cells (Supplementary Fig. S3.8D,E and Fig. 3.4C,D). In sum, structurally distinct chemical inhibitors and genetic studies indicate that simultaneous ARF6 and PIKfyve inhibition synergistically improve ASO activity.

Genetic experiments confirmed that simultaneous ARF6 and PIKfyve inhibition was required for ASO potentiation. Similar to ARF6 knockdown, PIKfyve knockdown severely limited cell viability and growth. As small molecule inhibition of ARF6 or PIKfyve is well tolerated (Supplementary Fig. S3.8C), these proteins likely have essential non-enzymatic functions in cells. As was done for ARF6 (Fig. 3.3E,F), PIKfyve activity was modulated indirectly. PIKfyve functions as part of a heterotrimeric complex, and can be inhibited by over-expressing its scaffold VAC14 (Burack and Shaw, 2000; Schulze et al., 2014). VAC14 over-expression produced robust cytoplasmic vacuolation (Supplementary Fig. S3.8F). Consistent with published reports that PIKfyve-dependent vacuolation is not cytotoxic (Giridharan et al., 2022; Zhang et al., 2012), VAC14 over-expressing cells were fully viable and proliferated normally for several weeks of continuous culture despite their highly vacuolated state. Recapitulating the effects of chemical PIKfyve inhibitors (Fig. 3.4A-B and Supplementary Fig. S3.8A-B,D-E), VAC14 over-

expression increased ASO activity by ~2-fold (Supplementary Fig. S3.8G-H). This result confirms that PIKfyve inhibition alone is not sufficient to promote ASO activity.

Consistent with the model that dual ARF6 and PIKfyve inactivation is required to phenocopy the effects of SH-BC-893, VAC14 over-expression synergized with the otherwise ineffective ARF6 inhibitor NAV2729 to potentiate ASO activity (Supplementary Fig. S3.8G-H). Conversely, inhibition of ARF6-mediated endocytic recycling was necessary for SH-BC-893-mediated ASO potentiation. $GRP1^{DD}$ expressing cells that are resistant to endocytic recycling inhibition by SH-BC-893 ((Finicle et al., 2018) and Fig. 3.3E-F) were also significantly less sensitive to the ASO-potentiating effects of SH-BC-893 (Fig. 3.4E,F). In summary, studies with chemical inhibitors and genetic approaches both support the model that simultaneous ARF6 and PIKfyve inhibition is necessary and sufficient to account for the effects of SH-BC-893 on ASO uptake, distribution, and activity.

SH-BC-893 disrupts both endocytic recycling and lysosomal fusion by activating PP2A (Fig. 3.1A and (Finicle et al., 2018; Kim et al., 2016; Kubiniok et al., 2019)). The dopaminergic antagonist perphenazine (PPZ) is structurally distinct from SH-BC-893 (Supplementary Fig. S3.1) but also activates PP2A (Gutierrez et al., 2014; Morita et al., 2020). Like SH-BC-893, PPZ inhibits ARF6-dependent endocytic recycling (Finicle et al., 2018) and vacuolates cells similar to PIKfyve inhibitors (Supplementary Fig. S3.9A). Consistent with the model that SH-BC-893's effects on ASO trafficking and activity lie downstream of PP2A-dependent ARF6 and PIKfyve inactivation (Fig. 3.1A), PPZ enhanced the intracellular accumulation of ASOs, blocked endocytic recycling, and increased the extralysosomal fraction of ASOs phenocopying the effects of SH-BC-893 (Supplementary Fig. S3.9B-E). Like SH-BC-893, PPZ is also not cytotoxic under the conditions where it disrupts endolysosomal trafficking (Supplementary Fig. S3.9F). Consistent with its effects on intracellular ASO levels and localization (Supplementary Fig. S3.9B-E), PPZ increased ASO activity to a similar extent as SH-BC-

893 (Fig. 3.4G-H). Notably, SH-BC-893 is 3 times more potent than PPZ. As with SH-BC-893, potentiation by the PP2A activator PPZ was independent of the RNA target or cell type (Supplementary Fig. S3.9G-I). Together, these results with molecules that are structurally unrelated to SH-BC-893, the ARF6 inhibitors NAV2729 and SecinH3, the PIKfyve inhibitors YM201636 and apilimod, and the PP2A activator PPZ, support the model that SH-BC-893 improves oligonucleotide activity via PP2A-dependent changes in ARF6- and PIKfyve-dependent endolysosomal trafficking (Fig. 3.1A and (Finicle et al., 2018; Kim et al., 2016)).

Oral administration of SH-BC-893 safely potentiates systemically delivered ASOs in both the liver and extra-hepatic tissues

Inefficient oligonucleotide uptake and endosomal escape limits target engagement in all tissues, including the liver (Dowdy, 2017; Dowdy et al., 2022; Gökirmak et al., 2021). Prior work established that SH-BC-893 reaches active concentrations in the liver 4 h after oral administration of 120 mg/kg (Jayashankar et al., 2021). To determine whether SH-BC-893 potentiated ASO activity in the liver, the cEt gapmer targeting *Malat1* was administered to mice subcutaneously. *Malat1* is often targeted in proof-of-concept studies as this lncRNA is ubiquitously expressed and not essential for cellular homeostasis (Arun et al., 2020). To control for sequence-independent effects of oligonucleotides on *Malat1* expression (Gagnon and Corey, 2019), a non-targeting, control ASO was also utilized (Supplementary Table 3.1). As expected, 50 mg/kg of targeted but not control ASO administered subcutaneously reduced *Malat1* RNA levels in the liver by 80% (Fig. 3.5A). At this high ASO dose, knockdown efficiency was not significantly improved by SH-BC-893. At lower ASO doses, the potentiating effect of SH-BC-893 became apparent (Fig. 3.5B,C). With SH-BC-893 co-administration, 5 and 0.5 mg/kg Malat1-targeted ASO produced similar *Malat1* knockdown as the 50 and 5 mg/kg doses in the absence of SH-BC-893 (Fig. 3.5A-C and Supplementary Fig. S3.10A). Fitting a curve to the dose response shown in Fig. 3.5C, the ED50 for knockdown was 15 mg/kg in control mice and 1 mg/kg in

SH-BC-893-treated mice. Targeted delivery via GalNAc conjugation increases ASO uptake and activity in hepatocytes (Crooke et al., 2019; Prakash et al., 2014). As expected, the $GalNAc_3$-conjugated form of the MALAT1 ASO (GN3-ASO) was already extremely potent in the liver (Supplementary Fig. S3.10B). SH-BC-893 only modestly improved its activity. Given the different route of entry and pharmacology, a kinetic study combined with a full dose response curve would be required to fully appreciate the extent to which SH-BC-893 would further improve ASO potency for GalNAc-conjugates. In sum, SH-BC-893 increases the activity of systemically delivered ASOs in the liver.

Orally administered SH-BC-893 also reaches active concentrations in the brain (Jayashankar et al., 2021). Many CNS diseases, including lethal neurodegenerative diseases where there is a high unmet need, could be treated with oligonucleotide therapeutics. Because unconjugated oligonucleotides do not cross the blood brain barrier (BBB), intrathecal administration is required to access CNS targets (Dowdy, 2017; Gökirmak et al., 2021). However, intrathecal or intracerebroventricular administration is not patient-friendly. If oligonucleotides could engage CNS targets after systemic delivery, it could allow home administration and improve provider and patient uptake. It was recently discovered that systemically-delivered oligonucleotides can cross the BBB if duplexed with a cholesterol-conjugated sense strand (Nagata et al., 2021). However, multiple high doses of these duplexes are required to achieve significant knockdown in the CNS. We therefore evaluated whether SH-BC-893 could improve target RNA knockdown in the CNS of mice treated with the *Malat1* targeting cEt ASO duplexed with a cholesterol-functionalized DNA sense strand (Supplementary Table 3.4). Consistent with prior reports (Nagata et al., 2021), two subcutaneous 50 mg/kg doses of duplexed ASOs were insufficient to produce robust *Malat1* knockdown in CNS tissues (Fig. 3.6A-E). However, co-administration with SH-BC-893 enabled statistically significant knockdown of ~30% in the brain stem and spinal cord with a promising trend in the hippocampus and cerebellum. No knockdown was observed in the cortex in control or 893-treated mice. The lack of activity in the cortex could be due to low penetration of ASOs in

this region as SH-BC-893 has been shown to reach active concentrations in the cortex (Jayashankar et al., 2021). These results clearly demonstrate that SH-BC-893 can improve oligonucleotide activity in at least a subset of CNS tissues.

To predict which additional extrahepatic tissues might be susceptible to SH-BC-893-mediated ASO potentiation, SH-BC-893 levels were determined in a variety of organs after oral administration (Fig. 3.7A). SH-BC-893 levels were highest in the lung (Fig. 3.7A,B), a tissue that is basally resistant to systemically administered ASOs due to limited ASO accumulation at this site (Geary et al., 2015; Kumar and Moschos, 2017). As expected, a single 50 or 5 mg/kg subcutaneous dose of ASO did not produce knockdown in the lung (Fig. 3.7C,D). In contrast, oral administration of SH-BC-893 enabled ASO-dependent reductions in lung *Malat1* RNA levels of 54% or 26% 24 h after a single 50 or 5 mg/kg subcutaneous ASO dose, respectively. Potentiation by SH-BC-893 was similarly robust when measured 3 d after dosing (Supplementary Fig. S3.10C). Although ASOs and SH-BC-893 are both present at reasonably high levels in the kidney and spleen ((Geary, 2009) and Fig. 3.7A and Supplementary Fig. S3.10D), no potentiation was observed in these tissues (Supplementary Fig. S3.10E-I). The lack of potentiation could reflect different limitations on ASO delivery in different tissues, accumulation of ASO and SH-BC-893 in different cell types, and/or the fact that tissue-level LC-MS/MS measurements fail to discriminate between intracellular and extracellular ASOs and/or SH-BC-893. Statistically significant ASO potentiation was not observed in tissues with low SH-BC-893 levels such as skeletal and heart muscle, although a promising trend was observed in the quadriceps that might be improved with repeated dosing (Fig. 3.7A and Supplementary Fig. S3.10J,K). In summary, co-administration of SH-BC-893 rendered systemically administered ASO active in the lung.

Potentiating effects in the lung were intriguing as oligonucleotide therapeutics are being developed to treat lung diseases (Crosby et al., 2017; Kumar and Moschos, 2017; Zhao et al., 2019). An ASO

targeting the *Scnn1a* mRNA that encodes a subunit of the ENaC sodium channel has been tested in cystic fibrosis patients and may also have benefits in other lung diseases characterized by mucus dehydration such as chronic obstructive pulmonary disease (COPD) (Crosby et al., 2017; Ghosh et al., 2015; Zhao et al., 2019). SH-BC-893-dependent potentiation may vary with different ASO sequences and targets. Because the MALAT1 ASO widely used in proof-of-concept studies is 2-3-fold more potent than most other cEt gapmers, other oligonucleotides may exhibit less potentiation with SH-BC-893. Additionally, individual cell types present within a tissue may be differentially sensitive to SH-BC-893-dependent potentiation (Geary, 2009; Geary et al., 2015; Kumar and Moschos, 2017). For these reasons, SH-BC-893 was also tested with a cEt gapmer ASO targeting the *Scnn1a* mRNA expressed in lung epithelial cells. At the 50 mg/kg ASO dose, SH-BC-893 improved *Scnn1a* knockdown from 17% to 59% (Fig. 3.7F). While ENaC is also expressed in the kidney, statistically significant knockdown was not observed with subcutaneous administration of the Scnn1a ASO even in mice treated with SH-BC-893 (Supplementary Fig. S3.10L). Although knockdown did not achieve statistical significance after a single 5 mg/kg dose of Scnn1a ASO and SH-BC-893, 30% knockdown was achieved after repeat dosing with the combination while Scnn1a ASO alone was ineffective (Fig. 3.7G,H and Supplementary Fig. S3.10M). Thus, SH-BC-893 improves ASO activity in lung epithelial cells that are targeted by oligonucleotide therapeutics designed to treat cystic fibrosis. In sum, the results presented here establish the feasibility of improving therapeutic oligonucleotide delivery to both hepatic and extrahepatic tissues by co-administering small molecules like SH-BC-893 that block endocytic recycling and lysosomal fusion.

In contrast to the historical toxicity problems associated with endolytic agents, even chronic daily administration of SH-BC-893 is well tolerated (Kim et al., 2016). After 11 weeks of daily oral administration of the effective dose of SH-BC-893 (120 mg/kg), blood chemistry revealed no signs of organ toxicity. Rapidly proliferating cells in the bone marrow and intestinal crypts were not

compromised based on normal complete blood counts and grossly normal histopathology. In fact, oral administration of 120 mg/kg SH-BC-893 every other day promotes metabolic homeostasis in mice maintained on a high fat diet (Jayashankar et al., 2021). In this study, mice provided with a running wheel engaged in the same amount of voluntary exercise whether they were treated with vehicle or with 120 mg/kg SH-BC-893 PO over the 4-week study. Voluntary wheel running is a holistic and sensitive measure of animal health (Häger et al., 2018). Together, these studies clearly establish the safety of chronic administration of the effective dose of SH-BC-893.

To confirm that SH-BC-893 did not induce acute toxicity that might have been missed in the published long-term studies, we evaluated blood chemistry in mice 24 h after treatment with vehicle, 120, or 240 mg/kg SH-BC-893 (Supplementary Fig. S3.11C). Neither the effective dose (120 mg/kg) nor twice the effective dose (240 mg/kg) disrupted blood chemistry values, indicating that SH-BC-893 is not acutely toxic to the liver, kidney, or muscle. Consistent with the bloodwork, no significant changes in body weight were noted in mice that were maintained for more than 24 h after administration of SH-BC-893 and oligonucleotide (Supplementary Fig. S3.11D-F). When used as an oligonucleotide potentiator, the safety margin would be further enhanced compared to published studies with repeat dosing because SH-BC-893 would only be administered as frequently as the oligonucleotide (weekly, monthly or even every 6 months) (Brown et al., 2020). Taken together, the data presented here and in published studies clearly establish that SH-BC-893 is not toxic to mice at the effective dose.

3.4 Discussion

Here we demonstrate that the small molecule SH-BC-893 increases the activity of ASOs and siRNAs by up to 100-fold in multiple cell types without lysing endosomes. Rather than disrupting membranes, SH-BC-893 traps oligonucleotides in a pre-lysosomal compartment where they likely escape when fission and fusion reactions deform the lipid bilayer increasing permeability (Bennett and Tieleman, 2014; Cullis et al., 1986; Juliano, 2018; Renard et al., 2018; Wang et al., 2009; Wickner and Rizo, 2017). Consistent with this mechanism of action and the well-established low permeability of the lysosomal membrane, SH-BC-893 cannot increase oligonucleotide activity if it is added after ASOs have reached lysosomes (Supplementary Fig. S3.6C-D). Genetic approaches and multiple, structurally distinct chemical inhibitors confirmed that simultaneous inhibition of ARF6-dependent endocytic recycling and PIKfyve-dependent lysosomal fusion was necessary and sufficient for SH-BC-893 to boost intracellular ASO levels, increase accumulation of ASOs within extra-lysosomal compartments, and enhance oligonucleotide activity (Figs. 3.3 & 3.4 and Supplementary Fig. S3.8). As single agents, ARF6 inhibitors increase intracellular ASO levels but fail to potentiate ASO activity because ASOs still end up in lysosomes (Fig. 3.3A-B,G and 3.4A-B and Supplementary Fig. S3.8A-B,D-E). Similarly, inactivating the PIKfyve-dependent lysosomal fusion pathway in isolation fails to block recycling and produces only a 2-4 fold increase in oligonucleotide activity similar to what can be achieved with previously reported small molecule potentiators (Fig. 3.3C-D and 3.4A-D and Supplementary Figs. S3.6G-H and S3.8A-B,D-H). In contrast, the synergistic effects of blocking recycling out of the cell and preventing ASO transit to lysosomes allows SH-BC-893 to dramatically increase oligonucleotide activity (Fig. 3.3 & 3.4 and Supplementary Fig. S3.8). SH-BC-893 is distinct from previously identified small molecule potentiators in that it robustly increases oligonucleotide activity without lysing endosomes, avoiding the toxic consequences that have prevented endolytic agents from advancing to the clinic.

Agents like SH-BC-893 may have some utility for liver-targeted ASOs. The 15-fold increase in ASO activity observed in the livers of mice treated with SH-BC-893 (Fig. 3.5C) is on par with the potency

increase reported with GalNAc conjugation, a clinically validated means to improve oligonucleotide delivery to hepatocytes (Gökirmak et al., 2021; Prakash et al., 2014). Thus, for liver targets, SH-BC-893 might offer greater access to cell types that do not express the ASGPR or offer an alternative approach to GalNAc conjugation. SH-BC-893 slightly enhanced the activity of the already quite potent $GalNAc_3$-MALAT1 ASO (Supplementary Fig. S3.10B). Additional studies with GalNAc-conjugates and other targeted oligonucleotides would be required to fully assess the potential of SH-BC-893 to improve ligand-conjugated oligonucleotide uptake in the liver and extrahepatic tissues (Ämmälä et al., 2018; Seth et al., 2019; Sugo et al., 2016).

Agents that act like SH-BC-893 are poised to render new targets in extrahepatic tissues accessible even without ligand-receptor targeting strategies. In the CNS, SH-BC-893 increased the activity of cholesterol-functionalized ASO duplexes in the brainstem and spinal cord (Figs. 3.6A,B) with positive trends noted in the hippocampus and cerebellum (Fig. 3.6C,D). The most sensitive extrahepatic tissue was the lung (Fig. 3.7C-E) likely due to the accumulation of SH-BC-893 in this tissue (Fig. 3.7A,B). Interestingly, although both ASOs and SH-BC-893 accumulate in the kidney and spleen (Fig. 3.7A, Supplementary Fig. S3.10D, and (Geary, 2009)), potentiation was limited or absent in these tissues (Supplementary Fig. S3.10E-I,L). These results could be explained by lower basal levels of ARF6-dependent ASO recycling, reduced PIKfyve-dependent lysosomal fusion, and/or differences in the endocytic trafficking pathways used for oligonucleotide entry in these tissues. Alternatively, SH-BC-893 and ASOs may not accumulate in the same cell types in these organs; ASOs accumulate primarily in proximal tubular epithelial cells in the kidney and endothelial cells in the spleen. In heart and skeletal muscle, limited potentiation is likely explained by the low concentrations of both SH-BC-893 and ASOs in these tissues ((Geary, 2009; Geary et al., 2015) and Supplementary Fig. S3.10D,J-K). Given the ubiquitous expression of PP2A, ARF6, and PIKfyve, additional tissues with SH-BC-893 levels higher than the brain (Fig. 3.7A) may also be sensitive to potentiation. The results reported here offer an important proof of concept, but additional studies will be required to produce a comprehensive inventory

of the tissues and cell types that are responsive to SH-BC-893-mediated potentiation with single or repeat oligonucleotide dosing.

While this study utilized systemic ASO delivery, SH-BC-893 should also improve the efficacy of locally administered oligonucleotide therapeutics. Administration of ASOs directly at the site of action (e.g., intravitreal, intrathecal, or aerosol delivery) increases uptake by elevating local concentrations but does not address the negative effects of ARF6-dependent recycling or PIKfyve-dependent lysosomal fusion on delivery (Fig. 3.1A). Local administration of SH-BC-893 along with the oligonucleotide might additionally overcome any limitations imposed by the tissue pharmacokinetics of SH-BC-893. In some cases, local delivery of oligonucleotide is preferred to limit target engagement to specific tissues. For example, in cystic fibrosis therapy it is desirable to reduce ENaC levels in the lung while leaving ENaC expression in the kidney unaffected (Christopher Boyd et al., 2020). Notably, SH-BC-893 increased ENaC knockdown in the lung (Fig. 3.7F-H) but not in the kidney (Supplementary Fig. S3.10L). Formulation work would be required to evaluate whether SH-BC-893 could be administered intrathecally or via inhalation along with the oligonucleotide, but local delivery of oligonucleotide and/or SH-BC-893 might further extend the clinical reach of small molecule-mediated potentiation.

It is also worth noting that SH-BC-893 is unlikely to diminish any long-term activity that might be sustained by slow leak of oligonucleotides from lysosomes (Brown et al., 2020). A single dose of SH-BC-893 administered with oligonucleotides would be cleared from the body in 24-48 h releasing the trafficking block and allowing trapped oligonucleotides to continue their progress through the endocytic pathway. Long-term activity likely tracks with the level of initial oligonucleotide uptake by target cells, and thus SH-BC-893 may improve knockdown duration by increasing the intracellular amount of oligonucleotide (Figs. 3.1D-E and 3.3A-B and Supplementary Fig. S3.2B,D,E,G). In summary, SH-BC-893 is likely to be compatible with other approaches that improve extrahepatic oligonucleotide delivery.

The in vivo results with SH-BC-893 are noteworthy both due to the significant gain in oligonucleotide activity and the surprising tolerability of this compound despite its profound effects on endolysosomal trafficking (Jayashankar et al., 2021; Kim et al., 2016). SH-BC-893 does not harm even rapidly proliferating normal tissues after chronic administration of the effective dose; bone marrow suppression was not observed and rapidly dividing intestinal crypts were not compromised (Kim et al., 2016). In fact, SH-BC-893 promotes metabolic homeostasis in mice, and treated animals engage in normal levels of voluntary exercise, a holistic measure of animal health (Häger et al., 2018; Jayashankar et al., 2021). When used as an oligonucleotide delivery potentiator, the safety margin would be further increased by infrequent dosing. Consistent with these earlier studies, acute administration of even twice the effective dose of SH-BC-893 produced no detectable changes in liver, kidney, or muscle function by blood chemistry analysis (Supplementary Fig. S3.11C).

The tolerability of SH-BC-893 likely stems from its origin as a synthetic analog of the natural sphingolipid, phytosphingosine, that promotes survival in yeast under stress (Dickson et al., 1997). This sphingolipid-responsive signaling pathway is conserved in mammalian cells suggesting that it was fine-tuned by evolution to modulate intracellular trafficking in a manner that preserves cell viability and tissue homeostasis (Finicle et al., 2018; Jayashankar et al., 2021; Kim et al., 2016; Kubiniok et al., 2019; Perryman et al., 2016). Consistent with this hypothesis, SH-BC-893 selectively kills cancer cells while sparing non-transformed cells (Kim et al., 2016). Oncogenic mutations make cancer cells constitutively anabolic and therefore hypersensitive to nutrient limitation. Indeed, this liability provides the therapeutic index for many standard-of-care cancer therapies (Luengo et al., 2017). While cancer cells starve to death secondary to SH-BC-893-induced changes in endolysosomal trafficking, normal cells adapt to the moderate nutrient restriction by reducing their energy demands (Kim et al., 2016). In summary, the low toxicity of the anti-neoplastic agent SH-BC-893 in non-transformed cells and tissues likely augurs well for its use in combination with oligonucleotide therapeutics.

Going forward, oligonucleotide therapeutics will need to compete with next-generation small molecules that are also capable of hitting what were previously “undruggable” targets (Makurvet, 2021). A potentiator like SH-BC-893 that permits at-home oligonucleotide administration could improve the ability of oligonucleotide therapeutics to compete with new orally administered small molecule alternatives (Paik, 2022). By lowering the required dose, a small molecule potentiator like SH-BC-893 could make expensive oligonucleotide therapeutics accessible to more patients. Given the established pre-clinical activities of SH-BC-893 as a single agent in cancer and obesity models (Jayashankar et al., 2021; Kim et al., 2016), oligonucleotide therapeutics targeting these diseases might be prioritized for assessing the therapeutic value of combination therapy. For example, several oligonucleotides that entered cancer trials failed to reach efficacy benchmarks. SH-BC-893 slows autochthonous prostate tumor growth (Kim et al., 2016) and could be even more effective in combination with relevant oncology ASOs (De Velasco et al., 2019; Xiao et al., 2018). Given its accumulation in the lung (Fig. 3.7A), primary or metastatic lung tumors might also be responsive to an SH-BC-893/ASO combination targeting KRAS (Ross et al., 2017). The oligonucleotide-independent actions of SH-BC-893 on mitochondrial dynamics (Jayashankar et al., 2021) may complement the activities of oligonucleotides designed to treat cancer (Chen and Chan, 2017), non-alcoholic steatohepatitis (NASH) (Friedman et al., 2018), and/or neurodegenerative diseases (Burté et al., 2015; Gökirmak et al., 2021; Jayashankar et al., 2021). In conclusion, the proof-of-concept studies presented here provide a strong rationale for future work exploring the therapeutic value and safety of SH-BC-893 and/or related small molecules as oligonucleotide potentiating agents.

3.5 Materials and Methods

Cell lines and cell culture. MDA-MB-468, MDA-MB-231, SW620, NCI-H358, A549, BxPC3, and PANC1 were obtained from the ATCC. HeLa cells were obtained from Steve Caplan (University of Nebraska Medical Center, Omaha, NE, USA). *p53*$^{-/-}$ MEFs were generated in-house from embryos from C57BL/6 mice (stock no. 008462, The Jackson Laboratory) using standard techniques. All cells were maintained at 37°C in 5% CO_2. HeLa, MEFs, A549, BxPC3, and PANC1 cells were cultured in DMEM media supplemented with 10% fetal bovine serum (FBS) without antibiotics. MDA-MB-468, MDA-MB-231, and SW620 were cultured in DMEM media supplemented with 10% FBS and 1% sodium pyruvate without antibiotics. All cells were maintained in culture for no more than 3 weeks before low-passage vials were thawed. *Mycoplasma* testing was performed monthly using the published PCR protocol from Uphoff and Drexeler (Uphoff and Drexler, 2014).

Chemicals and reagents. SH-BC-893 was synthesized by IntelliSyn RD (Montreal, Quebec, Canada) following the methods in (Chen et al., 2016) and with advice from S. Hanessian. The following chemicals were purchased: YM201636 (Cayman Chemicals, cat# 13576), apilimod (SelleckChem, cat# S6414), NAV2729 (R&D systems, cat# 5986), SecinH3 (Cayman Chemicals, cat# 10009570), perphenazine (PPZ, Sigma, cat# P6402-1G), UNC10217938A (Medchemexpress, cat# HY-136151), 6BIO (Cayman Chemicals, cat# 13123), AZD8055 (Cayman Chemicals, cat# 16978), and retro-2 (Sigma, cat# SML1085-5MG). Stock solutions were prepared as follows, aliquoted, and stored at -20°C: SH-BC-893 (5 mM in H_2O), YM201636 (1.6 mM in DMSO), apilimod (100 µM in DMSO), NAV2729 (12.5 mM in DMSO), SecinH3 (30 mM in DMSO), perphenazine (50 mM in DMSO), UNC10217938A (10 mM in DMSO), 6BIO (15 mM in DMSO), AZD8055 (1 mM in DMSO), and retro-2 (100 mM in DMSO). All chemical structures of compounds are shown in Supplementary Fig. S1. Oligonucleotides used are shown in Supplementary Tables 1, 3, & 4 and were obtained from Ionis Pharmaceuticals.

Fluorescence microscopy sample preparation. Cells were seeded into glass bottom 8-chamber slides at 12,000 cells per chamber (Cellvis, cat# C8-1.5H-N). 16-24 h after seeding, cells were incubated with ASOs (2 μM) for indicated time points. Post-incubation, cells were washed three times with PBS, fixed in 4% paraformaldehyde (VWR, cat# 100503-917) for 15 min, and then washed again with PBS. For samples where no other proteins were immunostained, cells were imaged following DAPI staining (1 mg/ml in PBS, VWR, cat# 422801-BL) for 5 min. For samples where other proteins or molecules were immunostained (e.g., LAMP1, LAMP2, PS-ASOs, or myc-tag), samples were permeabilized and incubated in blocking solution for 30 min at RT (10% FCS, 0.3% saponin, 0.05% azide in PBS). Samples were incubated with primary antibody diluted in block solution for 1 h at RT or overnight at 4°C, washed three times with PBS, and then stained in Alexa Fluor-conjugated secondary antibody solution at RT for 1 h with rocking. Samples were washed again three times, stained with DAPI, washed, and then imaged in PBS by confocal microscopy. Antibodies: anti-LAMP1 (Cell Signaling Technologies, cat# 9091S, 1:400 dilution), anti-LAMP2 (Developmental Studies Hybridoma Bank, cat# H4B4, 1:200 dilution), anti-PS-ASOs (provided by Ionis Pharmaceuticals, 1:200 dilution), anti-myc-tag (Cell Signaling Technologies, cat# 2278S, 1:200 dilution), Alexa Fluor 594 goat anti-mouse (Fisher Scientific, cat# A11032, 1:200 dilution), and Alexa Fluor 594 goat anti-rabbit (Fisher Scientific, cat# A-11012, 1:200 dilution).

Microscopy, image analysis, and quantification. All microscopy images were collected with ZEN digital imaging software on a Zeiss LSM780 confocal microscope with a Plan-Apochromat 63x/1.40 Oil DIC objective or a Zeiss LSM900 with Airyscan 2 with a Plan-Apochromat 63x/1.40 Oil DIC objective. All quantification of microscopy data was performed using ImageJ. In brief, regions of interest (ROIs) enclosing individual cells in each field of view were drawn using cell autofluorescence to define cell boundaries. LAMP1/2-positive area was defined by turning LAMP1 or LAMP2 fluorescent images into a binary image and utilizing ImageJ to automatically draw a ROI around each LAMP1- or LAMP2-positive

lysosome. LAMP1/2-negative area was defined by subtracting the LAMP1/2-positive ROI from the ROI enclosing the total cell. ASO fluorescence that did or did not colocalize with LAMP1/2-positive pixels was measured as Integrated Density per cell. Total intracellular ASO fluorescence was measured by adding the fluorescence of ASOs within LAMP1/2-positive or LAMP1/2-negative ROIs. For cytoplasmic ASO quantification, endosomal ASO signal was eliminated by generating regions of interest (ROIs) on thresholded images. With the diffuse cytoplasmic signal remaining, the Integrated Density per cell was measured. Background subtraction was performed by quantifying fluorescent signal in cells that were not exposed to ASOs but stained with both primary and secondary antibodies. At least 100 cells per experiment from a total of 2-3 independent experiments were analyzed for each experiment.

RNA isolation and RT-qPCR. To monitor ASO or siRNA activity in vitro, 3,000 cells were plated in duplicate or triplicate wells of a 96-well flat bottom plate. After 16-24 h, cells were treated with a serial dilution of ASOs starting at 20 μM and including 3-fold serial dilutions. Cells were lysed 24 h after ASO addition in GTC lysis buffer (4 M guanidine isothiocyanate, 50 mM Tris HCl pH 7.5, 25 mM EDTA). RNA was immediately purified or lysates were stored in this buffer at -20°C for later purification. Samples were mixed with an equal amount of 70% EtOH and pipetted into a Pall 96-well glass fiber filter plate (VWR, cat# 97052-104) fitted onto a vacuum manifold. Samples were then washed twice with RNA wash buffer (60 mM potassium acetate, 10 mM Tris HCl pH 7.5, 60% EtOH) before digesting genomic DNA using DNaseI (Fisher, cat# 18047019) in DNaseI buffer (400 mM Tris HCl pH 7.5, 100 mM NaCl, 100 mM CaCl2, 100 mM MgCl2) for 15 min at RT. Samples were then washed twice with GTC wash buffer (1 M guanidine isothiocyanate, 12.5 mM Tris HCl (pH 7.5), 6.25 mM EDTA) followed by three washes in RNA wash buffer. After the final wash, residual buffers were removed from the glass fiber plate by spinning in a tabletop centrifuge for 5 min at 3,696 x g. RNA was eluted in nuclease-free water into a 96-well round bottom plate. Following RNA elution, RT-qPCR reaction plates were set up by loading 5 μL of RNA into each well and using the Taqman AgPath-ID™ One-Step RT-PCR

Reagents (Fisher, cat# 4387391) according to supplier's recommendations. Taqman primers and probes are described in Supplementary Table 2. RNA levels were quantified using a StepOnePlus Real-Time PCR system (Applied Biosystems) and normalized to total RNA loaded using Quant-iT™ RiboGreen™ RNA Assay Kit (Invitrogen, cat# R11490) according to supplier's recommendations. RNA levels are expressed relative to control or drug-treated samples that received no ASOs. Two to three technical replicates each were performed for each ASO activity assay. At least three independent experiments were performed to produce biological replicates.

To monitor ASO activity in tissues in vivo, approximately 10-100 mg of flash-frozen tissue were lysed in 1 ml of Trizol using a Bullet Blender Storm Pro Tissue Homogenizer (Next Advance, cat# BT24M). After complete tissue homogenization, samples were transferred to a new Eppendorf tube and incubated at RT for 5 min to permit complete dissociation of nucleoprotein complexes. Following addition of 0.2 ml of chloroform to the Trizol-homogenate, the tube was inverted vigorously 3-4 times and then by vortexing for 20 seconds. Samples were then centrifuged at 13,000 rpm in a microcentrifuge at 4°C for at least 15 min. Following centrifugation, the upper aqueous layer containing RNA was transferred to a new tube. RNA was precipitated by adding 0.5 ml of ice-cold isopropanol followed by centrifugation at 13,000 rpm in a microcentrifuge at 4°C for 30-60 min. The resulting RNA pellet was washed twice with 1 ml of 70% EtOH (centrifuging for 5 min at 13,000 rpm to clear washes). The washed RNA pellet was dissolved in 40-100 µl of nuclease-free water, and then quantified using a NanoDrop™ 2000 spectrophotometer. To achieve pure RNA, approximately 10 µg of RNA was treated with DNaseI (Zymo Research Corporation, cat# E1010) and then cleaned up on spin columns (New England Biolabs, cat# T2030L) according to the supplier's recommendations. qRT-PCR reaction plates were set up by loading 50 ng of RNA into each well and using the Taqman AgPath-ID™ One-Step RT-PCR Reagents (Fisher, cat# 4387391) according to the supplier's recommendations. Taqman primers and probes are described in Supplementary Table 2. RNA levels were quantified using a StepOnePlus Real-Time PCR system

(Applied Biosystems) and expressed relative to housekeeping gene *Ppia* using the $2^{-\Delta\Delta Ct}$ method prior to normalization as described in the figure legends.

Viability measurement by flow cytometry. Viability was measured by vital dye exclusion using DAPI. In brief, adherent cells were plated in 24-well plates at 30,000 cells per well (matching the confluency of the cells in 96-well plates in the RT-qPCR experiments). After 16-24 h, cells were treated with indicated compounds at indicated concentrations for 24 h. After 24 h, the following was collected in FACS tubes: media containing floating dead cells, a PBS wash, trypsinized cells, and a final media wash to collect all remaining cells and debris. This live and dead cell containing solution was pelleted by centrifugation and the supernatant discarded. The pellet was placed back in single-cell suspension with 0.6 mL of media containing 1 µg/ml of DAPI. Samples were evaluated on a BD Fortessa X20.

Plasmids and stable cell line generation. pQCXIP-mCherry and pQCXIP-mCherry-VAC14 were generously provided by Thomas Weide (University Hospital of Muenster, Germany). The pQCXIB Firefly Luciferase plasmid was a gift from Reuben Shaw (Addgene plasmid # 74445; http://n2t.net/addgene:74445; RRID:Addgene_74445). myc-GRP1^{DD} was produced by PCR amplification of the insert in pEF6-myc-GRP$^{S155D/T240D}$ (a generous gift from Victor Hsu, Harvard Medical School, Boston, MA, USA) and subsequent Gateway cloning into pQCXIB CMV/TO DEST (w320-1), a gift from Eric Campeau & Paul Kaufman (Addgene plasmid # 17400; http://n2t.net/addgene:17400; RRID:Addgene_17400). Stable cell lines were generated by transducing target cells with retrovirus and drug selection.

General animal procedures. All experiments measuring ASO activity in animals were approved by the Institutional Animal Care and Use Committee of University of California, Irvine. Six- to eight-week old,

male Balbc/J mice were purchased from the Jackson Laboratory and acclimated to the university vivarium for at least 7 days prior to experimentation. Mice were housed under a 12 h light/dark cycle at 20-22°C in groups of 2-4. Cages contained 1/8" corncob bedding (7092A, Envigo, Huntingdon, UK) enriched with ~6 g of cotton fiber nestlets (Ancare, Corp., Bellmore, NY). Mice were fed the vivarium stock diet (chow, 2020x, Envigo). Access to food and water was ad libitum. For oral administration of SH-BC-893, polypropylene feeding tubes (20 g × 38 mm; Instech Laboratories Inc., Plymouth, PA) were used to dose 120 mg/kg of SH-BC-893 dissolved in H_2O (stock = 24 mg/ml). To aid gavage by inducing salivation, feeding tubes were dipped into a 1 g/ml sucrose solution immediately prior to treatment. For subcutaneous administration, ASOs were dissolved in PBS at a concentration such that 10 ml/kg was administered using a 27 G needle. For blood chemistry analysis, blood was collected by decapitation from nine-week old male Balbc/J mice. Serum was separated from whole blood in a SST-MINI tube with clot activator gel (Greiner, cat# 450571VET). Serum samples were sent to IDEXX Bioanalytics for a comprehensive chemistry panel (cat# 6006).

Tissue distribution and pharmacokinetics of SH-BC-893. Tissue PK studies were performed at Pharmaron (Beijing, China) on a fee-for-service basis and were approved by their Institutional Animal Care and Use Committee. Six- to eight-week old male or female CD1 mice were treated daily for 5 d with 120 mg/kg SH-BC-893 dissolved in H_2O (P.O., stock = 12 mg/ml) and then sacrificed 0.5, 1, 2, 4, 8, or 24 h after the last dose. Tissues were perfused with 10 mL saline and prior to collection and snap frozen in liquid nitrogen. Frozen tissue was homogenized in PBS (W/V 1:4). 10 µL of tissue or plasma homogenate was mixed with 10 µL blank solution and added to 200 µL acetonitrile containing FTY720 as an internal standard. Samples were vortexed and then spun for 30 min at 4700 rpm at 4˚C to precipitate protein. The resultant supernatant was diluted 2-fold with water and 10 µL of diluted supernatant was injected into the LC-MS/MS for quantitative analysis. SH-BC-893 was quantified by LC-MS/MS using a HALO 90A AQ-C18, 2.7 µm 2.1×50 mm column and an AB Sciex Triple Quad 5500

LC-MS/MS instrument (serial no. BB214861610) and corrected for extraction efficiency using the FTY720 internal standard.

Statistical analysis. For microscopy experiments, box and whisker plots showing median and quartiles are presented because data was not normally distributed. In bar graphs depicting ASO or siRNA IC50s or target RNA levels in tissues, mean ± SD is presented. All experimental data are from ≥ 3 independent biological replicates except where otherwise indicated. Statistical analysis was performed using GraphPad Prism software. Corrections for multiple comparisons were made as indicated in the legends and adjusted P-values reported: n.s., not significant, $P \geq 0.05$; * $P < 0.05$; ** $P < 0.01$; *** $P < 0.001$; key comparisons are shown in the figures.

3.6 Acknowledgements

The authors would like to thank the following colleagues for generously sharing equipment, reagents, and/or providing technical advice: Wenqi Wang and Scott Atwood (UCI) for access to their StepOnePlus Real-Time PCR systems (Applied Biosystems), Katrina Waymire (UCI) for access to mice for practice dissections, and Michael Migawa (Ionis) for assistance arranging ASO synthesis. The authors also thank Thomas Weide (University Hospital Münster) for generously providing the pQCXIP-mCherry-VAC14 plasmid.

3.7 Competing interest statement

ALE, SH, PPS, and BTF are inventors on patents relevant to the use of SH-BC-893 and agents with similar activities for oligonucleotide potentiation. ANM, DG, SH, and ALE own shares in Siege Pharmaceuticals which has licensed these patents and is developing SH-BC-893 for clinical use. ASR, BAA, WBW, and PPS were employees of Ionis Pharmaceuticals during the project. PPS is currently an employee of Alnylam Pharmaceuticals. ALE has consulted for Alnylam Pharmaceuticals. Other authors declare no conflicts of interest.

3.8 Author contributions

BTF, PPS, and ALE designed the research. BTF performed all experiments except tissue PK studies; KHE assisted with the animal experiments. ANM, DG, and ALE designed and coordinated tissue PK studies. ASR, BAA, WBW, and PPS selected or designed all oligonucleotide-related reagents obtained from Ionis. DAF provided conflict of interest oversight. ALE supervised the research; SH supervised synthesis of SH-BC-893 at Intellisyn. BTF and ALE analyzed the results and wrote the manuscript; all authors provided feedback and approved the manuscript. ALE and BTF obtained funding for the project.

3.9 Funding

This work was supported by an Ono Pharma Foundation Breakthrough Science Initiative grant (G-1902-0039) and an unrestricted gift from Ionis Pharmaceuticals to ALE and by NIH 1R44CA257568 to DG. BTF was supported by NCI T32 CA009054, F31 CA261085, and F99 CA264430. The authors also wish to acknowledge the support of the Chao Family Comprehensive Cancer Center Optical Biology Center shared resource, supported by the National Cancer Institute of the National Institutes of Health under award number P30 CA062203. The content is solely the responsibility of the authors and does not necessarily represent the official views of the National Institutes of Health.

3.10 Data availability

All data generated and analyzed in this study are included in the manuscript and supplementary data.

3.11 References

Ämmälä, C., Drury, W.J., Knerr, L., Ahlstedt, I., Stillemark-Billton, P., Wennberg-Huldt, C., Andersson, E.M., Valeur, E., Jansson-Löfmark, R., Janzén, D., et al. (2018). Targeted delivery of antisense oligonucleotides to pancreatic β-cells. Sci. Adv. *4*, eaat3386.

Arun, G., Aggarwal, D., and Spector, D.L. (2020). MALAT1 Long Non-Coding RNA: Functional Implications. Noncoding RNA *6*.

Bennett, W.F.D., and Tieleman, D.P. (2014). The importance of membrane defects-lessons from simulations. Acc. Chem. Res. *47*, 2244–2251.

Brown, C.R., Gupta, S., Qin, J., Racie, T., He, G., Lentini, S., Malone, R., Yu, M., Matsuda, S., Shulga-Morskaya, S., et al. (2020). Investigating the pharmacodynamic durability of GalNAc-siRNA conjugates. Nucleic Acids Res. *48*, 11827–11844.

Burack, W.R., and Shaw, A.S. (2000). Signal transduction: hanging on a scaffold. Curr. Opin. Cell Biol. *12*, 211–216.

Burté, F., Carelli, V., Chinnery, P.F., and Yu-Wai-Man, P. (2015). Disturbed mitochondrial dynamics and neurodegenerative disorders. Nat. Rev. Neurol. *11*, 11–24.

Chen, H., and Chan, D.C. (2017). Mitochondrial dynamics in regulating the unique phenotypes of cancer and stem cells. Cell Metab. *26*, 39–48.

Chen, B., Roy, S.G., McMonigle, R.J., Keebaugh, A., McCracken, A.N., Selwan, E., Fransson, R., Fallegger, D., Huwiler, A., Kleinman, M.T., et al. (2016). Azacyclic FTY720 analogues that limit nutrient transporter expression but lack S1P receptor activity and negative chronotropic effects offer a novel and effective strategy to kill cancer cells in vivo. ACS Chem. Biol. *11*, 409–414.

Christopher Boyd, A., Guo, S., Huang, L., Kerem, B., Oren, Y.S., Walker, A.J., and Hart, S.L. (2020). New approaches to genetic therapies for cystic fibrosis. J Cyst Fibros *19 Suppl 1*, S54–S59.

Corey, D.R., Damha, M.J., and Manoharan, M. (2022). Challenges and opportunities for nucleic acid therapeutics. Nucleic Acid Ther. *32*, 8–13.

Crooke, S.T., Wang, S., Vickers, T.A., Shen, W., and Liang, X.-H. (2017). Cellular uptake and trafficking of antisense oligonucleotides. Nat. Biotechnol. *35*, 230–237.

Crooke, S.T., Baker, B.F., Xia, S., Yu, R.Z., Viney, N.J., Wang, Y., Tsimikas, S., and Geary, R.S. (2019). Integrated Assessment of the Clinical Performance of GalNAc3-Conjugated 2'-O-Methoxyethyl Chimeric Antisense Oligonucleotides: I. Human Volunteer Experience. Nucleic Acid Ther. *29*, 16–32.

Crosby, J.R., Zhao, C., Jiang, C., Bai, D., Katz, M., Greenlee, S., Kawabe, H., McCaleb, M., Rotin, D., Guo, S., et al. (2017). Inhaled ENaC antisense oligonucleotide ameliorates cystic fibrosis-like lung disease in mice. J Cyst Fibros *16*, 671–680.

Cullis, P.R., Hope, M.J., and Tilcock, C.P. (1986). Lipid polymorphism and the roles of lipids in membranes. Chem Phys Lipids *40*, 127–144.

Dickson, R.C., Nagiec, E.E., Skrzypek, M., Tillman, P., Wells, G.B., and Lester, R.L. (1997). Sphingolipids are potential heat stress signals in Saccharomyces. J. Biol. Chem. *272*, 30196–30200.

Dominska, M., and Dykxhoorn, D.M. (2010). Breaking down the barriers: siRNA delivery and endosome escape. J. Cell Sci. *123*, 1183–1189.

Dowdy, S.F. (2017). Overcoming cellular barriers for RNA therapeutics. Nat. Biotechnol. *35*, 222–229.

Dowdy, S.F., Setten, R.L., Cui, X.-S., and Jadhav, S.G. (2022). Delivery of RNA therapeutics: the great endosomal escape! Nucleic Acid Ther. *32*, 361–368.

Finicle, B.T., Ramirez, M.U., Liu, G., Selwan, E.M., McCracken, A.N., Yu, J., Joo, Y., Nguyen, J., Ou, K., Roy, S.G., et al. (2018). Sphingolipids inhibit endosomal recycling of nutrient transporters by inactivating ARF6. J. Cell Sci. *131*.

Friedman, S.L., Neuschwander-Tetri, B.A., Rinella, M., and Sanyal, A.J. (2018). Mechanisms of NAFLD development and therapeutic strategies. Nat. Med. *24*, 908–922.

Gagnon, K.T., and Corey, D.R. (2019). Guidelines for Experiments Using Antisense Oligonucleotides and Double-Stranded RNAs. Nucleic Acid Ther. *29*, 116–122.

Geary, R.S. (2009). Antisense oligonucleotide pharmacokinetics and metabolism. Expert Opin Drug Metab Toxicol *5*, 381–391.

Geary, R.S., Norris, D., Yu, R., and Bennett, C.F. (2015). Pharmacokinetics, biodistribution and cell uptake of antisense oligonucleotides. Adv. Drug Deliv. Rev. *87*, 46–51.

Ghosh, A., Boucher, R.C., and Tarran, R. (2015). Airway hydration and COPD. Cell Mol. Life Sci. *72*, 3637–3652.

Gilleron, J., Paramasivam, P., Zeigerer, A., Querbes, W., Marsico, G., Andree, C., Seifert, S., Amaya, P., Stöter, M., Koteliansky, V., et al. (2015). Identification of siRNA delivery enhancers by a chemical library screen. Nucleic Acids Res. *43*, 7984–8001.

Giridharan, S.S.P., Luo, G., Rivero-Rios, P., Steinfeld, N., Tronchere, H., Singla, A., Burstein, E., Billadeau, D.D., Sutton, M.A., and Weisman, L.S. (2022). Lipid kinases VPS34 and PIKfyve coordinate a phosphoinositide cascade to regulate retriever-mediated recycling on endosomes. Elife *11*.

Gökirmak, T., Nikan, M., Wiechmann, S., Prakash, T.P., Tanowitz, M., and Seth, P.P. (2021). Overcoming the challenges of tissue delivery for oligonucleotide therapeutics. Trends Pharmacol. Sci. *42*, 588–604.

Grant, B.D., and Donaldson, J.G. (2009). Pathways and mechanisms of endocytic recycling. Nat. Rev. Mol. Cell Biol. *10*, 597–608.

Gutierrez, A., Pan, L., Groen, R.W.J., Baleydier, F., Kentsis, A., Marineau, J., Grebliunaite, R., Kozakewich, E., Reed, C., Pflumio, F., et al. (2014). Phenothiazines induce PP2A-mediated apoptosis in T cell acute lymphoblastic leukemia. J. Clin. Invest. *124*, 644–655.

Häger, C., Keubler, L.M., Talbot, S.R., Biernot, S., Weegh, N., Buchheister, S., Buettner, M., Glage, S., and Bleich, A. (2018). Running in the wheel: Defining individual severity levels in mice. PLoS Biol. *16*, e2006159.

He, C., Migawa, M.T., Chen, K., Weston, T.A., Tanowitz, M., Song, W., Guagliardo, P., Iyer, K.S., Bennett, C.F., Fong, L.G., et al. (2021). High-resolution visualization and quantification of nucleic acid-

based therapeutics in cells and tissues using Nanoscale secondary ion mass spectrometry (NanoSIMS). Nucleic Acids Res. *49*, 1–14.

Hong, D., Kurzrock, R., Kim, Y., Woessner, R., Younes, A., Nemunaitis, J., Fowler, N., Zhou, T., Schmidt, J., Jo, M., et al. (2015). AZD9150, a next-generation antisense oligonucleotide inhibitor of STAT3 with early evidence of clinical activity in lymphoma and lung cancer. Sci. Transl. Med. *7*, 314ra185.

Jayashankar, V., Selwan, E., Hancock, S.E., Verlande, A., Goodson, M.O., Eckenstein, K.H., Milinkeviciute, G., Hoover, B.M., Chen, B., Fleischman, A.G., et al. (2021). Drug-like sphingolipid SH-BC-893 opposes ceramide-induced mitochondrial fission and corrects diet-induced obesity. EMBO Mol. Med. *13*, e13086.

Juliano, R.L. (2018). Intracellular trafficking and endosomal release of oligonucleotides: what we know and what we don't. Nucleic Acid Ther. *28*, 166–177.

Juliano, R.L. (2021). Chemical manipulation of the endosome trafficking machinery: implications for oligonucleotide delivery. Biomedicines *9*.

Kendall, G.C., Mokhonova, E.I., Moran, M., Sejbuk, N.E., Wang, D.W., Silva, O., Wang, R.T., Martinez, L., Lu, Q.L., Damoiseaux, R., et al. (2012). Dantrolene enhances antisense-mediated exon skipping in human and mouse models of Duchenne muscular dystrophy. Sci. Transl. Med. *4*, 164ra160.

Kim, S.M., Roy, S.G., Chen, B., Nguyen, T.M., McMonigle, R.J., McCracken, A.N., Zhang, Y., Kofuji, S., Hou, J., Selwan, E., et al. (2016). Targeting cancer metabolism by simultaneously disrupting parallel nutrient access pathways. J. Clin. Invest. *126*, 4088–4102.

Kubiniok, P., Finicle, B.T., Piffaretti, F., McCracken, A.N., Perryman, M., Hanessian, S., Edinger, A.L., and Thibault, P. (2019). Dynamic Phosphoproteomics Uncovers Signaling Pathways Modulated by Anti-oncogenic Sphingolipid Analogs. Mol. Cell Proteomics *18*, 408–422.

Kumar, M., and Moschos, S.A. (2017). Oligonucleotide therapies for the lung: ready to return to the clinic? Mol. Ther. *25*, 2604–2606.

Li, J., Malaby, A.W., Famulok, M., Sabe, H., Lambright, D.G., and Hsu, V.W. (2012). Grp1 plays a key role in linking insulin signaling to glut4 recycling. Dev. Cell *22*, 1286–1298.

Liang, X.-H., Sun, H., Hsu, C.-W., Nichols, J.G., Vickers, T.A., De Hoyos, C.L., and Crooke, S.T. (2020). Golgi-endosome transport mediated by M6PR facilitates release of antisense oligonucleotides from endosomes. Nucleic Acids Res. *48*, 1372–1391.

Linnane, E., Davey, P., Zhang, P., Puri, S., Edbrooke, M., Chiarparin, E., Revenko, A.S., Macleod, A.R., Norman, J.C., and Ross, S.J. (2019). Differential uptake, kinetics and mechanisms of intracellular trafficking of next-generation antisense oligonucleotides across human cancer cell lines. Nucleic Acids Res. *47*, 4375–4392.

Luengo, A., Gui, D.Y., and Vander Heiden, M.G. (2017). Targeting metabolism for cancer therapy. Cell Chem. Biol. *24*, 1161–1180.

Makurvet, F.D. (2021). Biologics vs. small molecules: Drug costs and patient access. Medicine in Drug Discovery *9*, 100075.

Ming, X., Carver, K., Fisher, M., Noel, R., Cintrat, J.-C., Gillet, D., Barbier, J., Cao, C., Bauman, J., and Juliano, R.L. (2013). The small molecule Retro-1 enhances the pharmacological actions of antisense and splice switching oligonucleotides. Nucleic Acids Res. *41*, 3673–3687.

Morita, K., He, S., Nowak, R.P., Wang, J., Zimmerman, M.W., Fu, C., Durbin, A.D., Martel, M.W., Prutsch, N., Gray, N.S., et al. (2020). Allosteric activators of protein phosphatase 2A display broad antitumor activity mediated by dephosphorylation of MYBL2. Cell *181*, 702–715.e20.

Nagata, T., Dwyer, C.A., Yoshida-Tanaka, K., Ihara, K., Ohyagi, M., Kaburagi, H., Miyata, H., Ebihara, S., Yoshioka, K., Ishii, T., et al. (2021). Cholesterol-functionalized DNA/RNA heteroduplexes cross the blood-brain barrier and knock down genes in the rodent CNS. Nat. Biotechnol. *39*, 1529–1536.

Ochaba, J., Powers, A.F., Tremble, K.A., Greenlee, S., Post, N.M., Matson, J.E., MacLeod, A.R., Guo, S., and Aghajan, M. (2019). A novel and translational role for autophagy in antisense oligonucleotide trafficking and activity. Nucleic Acids Res.

Odate, S., Veschi, V., Yan, S., Lam, N., Woessner, R., and Thiele, C.J. (2017). Inhibition of STAT3 with the Generation 2.5 Antisense Oligonucleotide, AZD9150, Decreases Neuroblastoma Tumorigenicity and Increases Chemosensitivity. Clin. Cancer Res. *23*, 1771–1784.

Osborn, M.F., Alterman, J.F., Nikan, M., Cao, H., Didiot, M.C., Hassler, M.R., Coles, A.H., and Khvorova, A. (2015). Guanabenz (Wytensin™) selectively enhances uptake and efficacy of hydrophobically modified siRNAs. Nucleic Acids Res. *43*, 8664–8672.

Paik, J. (2022). Risdiplam: A review in spinal muscular atrophy. CNS Drugs *36*, 401–410.

Paramasivam, P., Franke, C., Stöter, M., Höijer, A., Bartesaghi, S., Sabirsh, A., Lindfors, L., Arteta, M.Y., Dahlén, A., Bak, A., et al. (2022). Endosomal escape of delivered mRNA from endosomal recycling tubules visualized at the nanoscale. J. Cell Biol. *221*.

Perryman, M.S., Tessier, J., Wiher, T., O'Donoghue, H., McCracken, A.N., Kim, S.M., Nguyen, D.G., Simitian, G.S., Viana, M., Rafelski, S., et al. (2016). Effects of stereochemistry, saturation, and hydrocarbon chain length on the ability of synthetic constrained azacyclic sphingolipids to trigger nutrient transporter down-regulation, vacuolation, and cell death. Bioorg. Med. Chem. *24*, 4390–4397.

Prakash, T.P., Graham, M.J., Yu, J., Carty, R., Low, A., Chappell, A., Schmidt, K., Zhao, C., Aghajan, M., Murray, H.F., et al. (2014). Targeted delivery of antisense oligonucleotides to hepatocytes using triantennary N-acetyl galactosamine improves potency 10-fold in mice. Nucleic Acids Res. *42*, 8796–8807.

Raal, F.J., Santos, R.D., Blom, D.J., Marais, A.D., Charng, M.-J., Cromwell, W.C., Lachmann, R.H., Gaudet, D., Tan, J.L., Chasan-Taber, S., et al. (2010). Mipomersen, an apolipoprotein B synthesis inhibitor, for lowering of LDL cholesterol concentrations in patients with homozygous familial hypercholesterolaemia: a randomised, double-blind, placebo-controlled trial. Lancet *375*, 998–1006.

Renard, H.-F., Johannes, L., and Morsomme, P. (2018). Increasing diversity of biological membrane fission mechanisms. Trends Cell Biol. *28*, 274–286.

Roberts, T.C., Langer, R., and Wood, M.J.A. (2020). Advances in oligonucleotide drug delivery. Nat. Rev. Drug Discov. *19*, 673–694.

Ross, S.J., Revenko, A.S., Hanson, L.L., Ellston, R., Whalley, N., Pandey, S.K., Revill, M., Rooney, C., Buckett, K., Klein, S.K., et al. (2017). Targeting KRAS dependent tumors with AZD4785 , a high-affinity therapeutic antisense oligonucleotide inhibitor of KRAS. Sci Trans Med *5253*, 1–14.

Rudnik, S., and Damme, M. (2021). The lysosomal membrane-export of metabolites and beyond. FEBS J. *288*, 4168–4182.

Schulze, U., Vollenbröker, B., Braun, D.A., Van Le, T., Granado, D., Kremerskothen, J., Fränzel, B., Klosowski, R., Barth, J., Fufezan, C., et al. (2014). The Vac14-interaction network is linked to regulators of the endolysosomal and autophagic pathway. Mol. Cell Proteomics *13*, 1397–1411.

Seth, P.P., Tanowitz, M., and Bennett, C.F. (2019). Selective tissue targeting of synthetic nucleic acid drugs. J. Clin. Invest. *129*, 915–925.

Shen, X., and Corey, D.R. (2018). Chemistry, mechanism and clinical status of antisense oligonucleotides and duplex RNAs. Nucleic Acids Res. *46*, 1584–1600.

Stechmann, B., Bai, S.-K., Gobbo, E., Lopez, R., Merer, G., Pinchard, S., Panigai, L., Tenza, D., Raposo, G., Beaumelle, B., et al. (2010). Inhibition of retrograde transport protects mice from lethal ricin challenge. Cell *141*, 231–242.

Sugo, T., Terada, M., Oikawa, T., Miyata, K., Nishimura, S., Kenjo, E., Ogasawara-Shimizu, M., Makita, Y., Imaichi, S., Murata, S., et al. (2016). Development of antibody-siRNA conjugate targeted to cardiac and skeletal muscles. J. Control. Release *237*, 1–13.

Tanowitz, M., Hettrick, L., Revenko, A., Kinberger, G.A., Prakash, T.P., and Seth, P.P. (2017). Asialoglycoprotein receptor 1 mediates productive uptake of N-acetylgalactosamine-conjugated and unconjugated phosphorothioate antisense oligonucleotides into liver hepatocytes. Nucleic Acids Res. *45*, 12388–12400.

Uphoff, C.C., and Drexler, H.G. (2014). Detection of Mycoplasma contamination in cell cultures. Curr. Protoc. Mol. Biol. *106*, 28.4.1–14.

De Velasco, M.A., Kura, Y., Sakai, K., Hatanaka, Y., Davies, B.R., Campbell, H., Klein, S., Kim, Y., MacLeod, A.R., Sugimoto, K., et al. (2019). Targeting castration-resistant prostate cancer with androgen receptor antisense oligonucleotide therapy. JCI Insight *4*.

Wagenaar, T.R., Tolstykh, T., Shi, C., Jiang, L., Zhang, J., Li, Z., Yu, Q., Qu, H., Sun, F., Cao, H., et al. (2015). Identification of the endosomal sorting complex required for transport-I (ESCRT-I) as an important modulator of anti-miR uptake by cancer cells. Nucleic Acids Res. *43*, 1204–1215.

Wang, S., Sun, H., Tanowitz, M., Liang, X.-H., and Crooke, S.T. (2016). Annexin A2 facilitates endocytic trafficking of antisense oligonucleotides. Nucleic Acids Res. *44*, 7314–7330.

Wang, S., Sun, H., Tanowitz, M., Liang, X.-H., and Crooke, S.T. (2017). Intra-endosomal trafficking mediated by lysobisphosphatidic acid contributes to intracellular release of phosphorothioate-modified antisense oligonucleotides. Nucleic Acids Res. *45*, 5309–5322.

Wang, T., Smith, E.A., Chapman, E.R., and Weisshaar, J.C. (2009). Lipid mixing and content release in single-vesicle, SNARE-driven fusion assay with 1-5 ms resolution. Biophys. J. *96*, 4122–4131.

Wickner, W., and Rizo, J. (2017). A cascade of multiple proteins and lipids catalyzes membrane fusion. Mol. Biol. Cell *28*, 707–711.

Wilke, S., Krausze, J., and Büssow, K. (2012). Crystal structure of the conserved domain of the DC lysosomal associated membrane protein: implications for the lysosomal glycocalyx. BMC Biol. *10*, 62.

Wittrup, A., Ai, A., Liu, X., Hamar, P., Trifonova, R., Charisse, K., Manoharan, M., Kirchhausen, T., and Lieberman, J. (2015). Visualizing lipid-formulated siRNA release from endosomes and target gene knockdown. Nat. Biotechnol. *33*, 870–876.

Xiao, L., Tien, J.C., Vo, J., Tan, M., Parolia, A., Zhang, Y., Wang, L., Qiao, Y., Shukla, S., Wang, X., et al. (2018). Epigenetic Reprogramming with Antisense Oligonucleotides Enhances the Effectiveness of Androgen Receptor Inhibition in Castration-Resistant Prostate Cancer. Cancer Res. *78*, 5731–5740.

Yamamoto, Y., Loriot, Y., Beraldi, E., Zhang, F., Wyatt, A.W., Al Nakouzi, N., Mo, F., Zhou, T., Kim, Y., Monia, B.P., et al. (2015). Generation 2.5 antisense oligonucleotides targeting the androgen receptor and its splice variants suppress enzalutamide-resistant prostate cancer cell growth. Clin. Cancer Res. *21*, 1675–1687.

Yang, B., Ming, X., Cao, C., Laing, B., Yuan, A., Porter, M.A., Hull-Ryde, E.A., Maddry, J., Suto, M., Janzen, W.P., et al. (2015). High-throughput screening identifies small molecules that enhance the pharmacological effects of oligonucleotides. Nucleic Acids Res. *43*, 1987–1996.

Zhang, X., Castanotto, D., Nam, S., Horne, D., and Stein, C. (2017). 6BIO Enhances Oligonucleotide Activity in Cells: A Potential Combinatorial Anti-androgen Receptor Therapy in Prostate Cancer Cells. Mol. Ther. *25*, 79–91.

Zhang, Y., McCartney, A.J., Zolov, S.N., Ferguson, C.J., Meisler, M.H., Sutton, M.A., and Weisman, L.S. (2012). Modulation of synaptic function by VAC14, a protein that regulates the phosphoinositides PI(3,5)P_2 and PI(5)P. EMBO J. *31*, 3442–3456.

Zhao, C., Crosby, J., Lv, T., Bai, D., Monia, B.P., and Guo, S. (2019). Antisense oligonucleotide targeting of mRNAs encoding ENaC subunits α, β, and γ improves cystic fibrosis-like disease in mice. J Cyst Fibros *18*, 334–341.

3.12 Figures

Figure 3.1

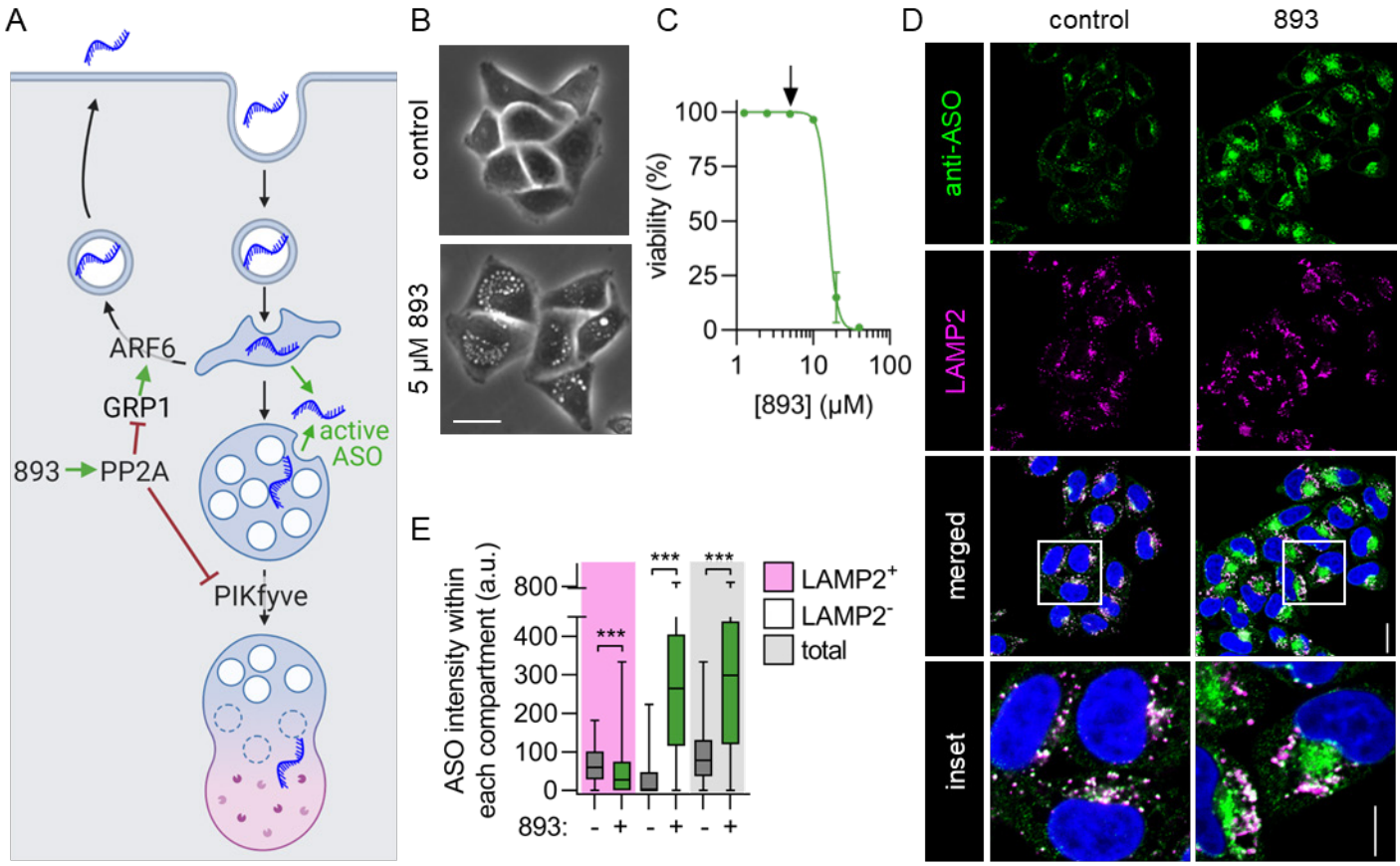

Figure 3.1: SH-BC-893 increases oligonucleotide accumulation in non-lysosomal compartments. **(A)** Model showing how SH-BC-893 (893) alters intracellular trafficking. **(B)** Phase contrast images of HeLa cells treated with SH-BC-893 (5 μM) for 3 h. Scale bar = 20 μm. **(C)** Viability measured by vital dye (DAPI) exclusion through flow cytometry in HeLa cells treated with indicated concentrations of SH-BC-893 for 24 h. Arrow indicates concentration used in all in vitro oligonucleotide assays. Mean ± SD shown, n=3. **(D)** HeLa cells treated with a 3-10-3 cEt ASO targeting *MALAT1* (2 μM) ± SH-BC-893 (5 μM) for 6 h and stained with antibodies to endogenous LAMP2 or PS-ASOs. Scale bar = 20 μm. For inset, scale bar = 10 μm. **(E)** Quantification of the raw intensity values for ASO from images in (D) within LAMP2-positive, LAMP2-negative, and total cellular areas. At least 100 cells were quantified

from each of 2 independent experiments. Using a Mann-Whitney t test to correct for data that is not normally distributed, ***, $p<0.001$.

Figure 3.2

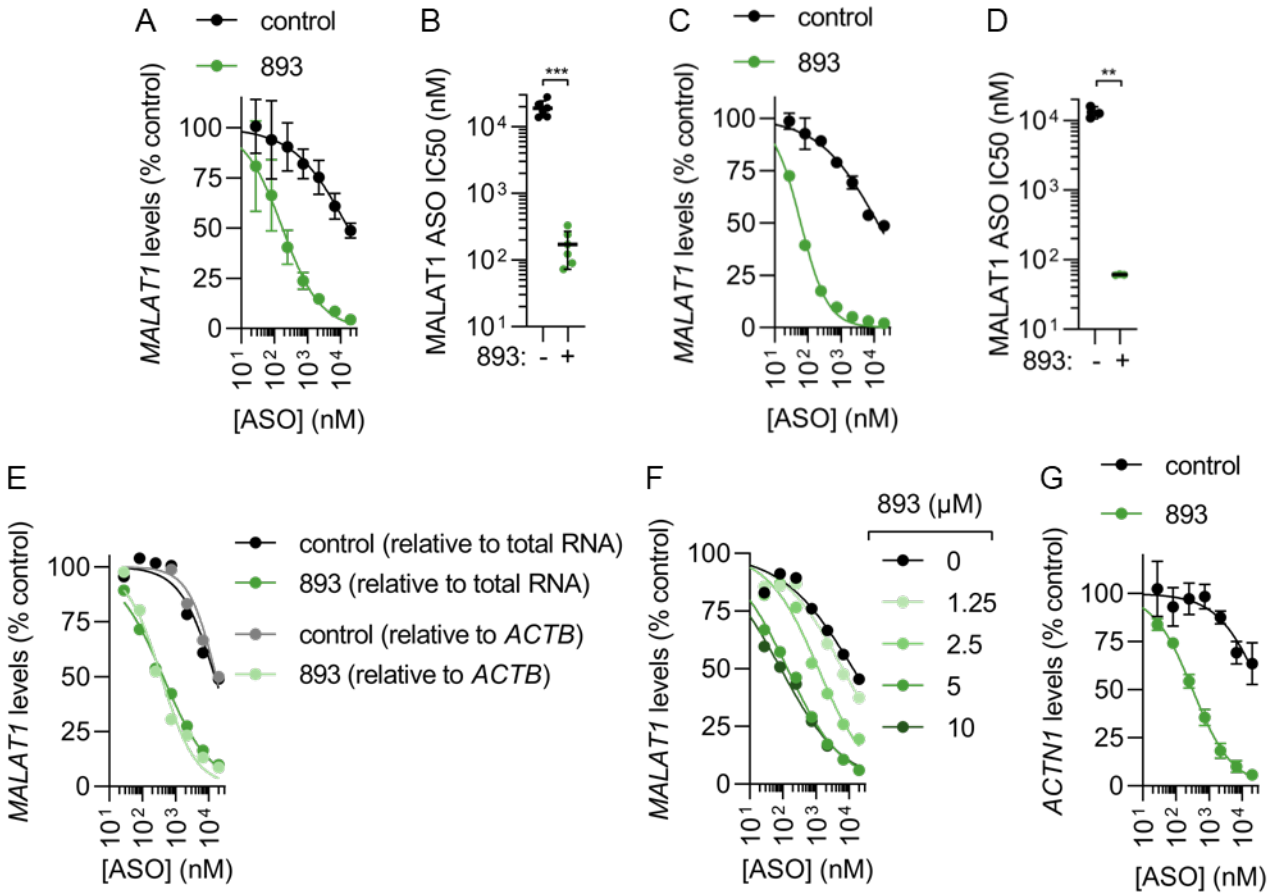

H

	Basal IC50 (nM)	IC50 (nM) + 893	Fold decrease in IC50	Cell type
MEF	4,065	27	151	Fibroblast
MDA-MB-468	>20,000	171	>117	Breast
MDA-MB-231	7,763	331	23	Breast
HeLa	18,975	171	111	Cervical
SW620	>20,000	207	>97	Colon
NCI-H358	8,995	468	19	Lung
A549	761	38	20	Lung
BxPC3	19,015	640	30	Pancreas
PANC1	522	67	8	Pancreas

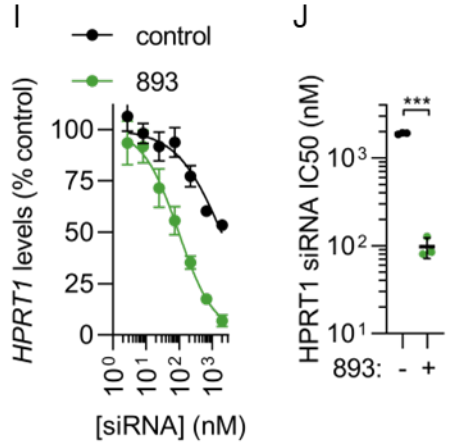

Figure 3.2: SH-BC-893 enhances oligonucleotide activity. (A) *MALAT1* levels in HeLa cells treated with the indicated concentrations of 3-10-3 cEt gapmer targeting *MALAT1* ± SH-BC-893 (5 μM) for 24 h. Mean ± SD shown, n=6. **(B)** IC50s from each biological replicate in (A); mean ± SD shown. Using a

Welch's t test to correct for unequal SD, ***, p<0.001. **(C-D)** As in (A-B), except using a 5-10-5 2'MOE gapmer; mean ± SD shown, n=3. Using a Welch's t test to correct for unequal SD's, **, p<0.01. **(E)** As in (A), except data expressed relative to total RNA or to housekeeping gene *ACTB*, n=1. **(F)** As in (A), except with indicated concentrations of 893, n=1. **(G)** As in (A), except using a 3-10-3 cEt gapmer targeting the *ACTN1* mRNA and n=3. IC50 values for control could not be calculated due to the low basal activity of this ASO. **(H)** The indicated cell lines were treated with the cEt *MALAT1* ASO ± SH-BC-893 (5 μM) for 24 h and an IC50 (nM) calculated. Dose response curves shown in Supplementary Fig. S3.5. **(I)** *HPRT1* mRNA levels in HeLa cells treated with the indicated doses of a palmitate-conjugated siRNA targeting *HPRT1* ± SH-BC-893 (5 μM) for 24 h. Mean ± SD shown, n=3. **(J)** IC50s from each biological replicate in (I); mean ± SD shown. Using a Welch's t test to correct for unequal SD, ***, p<0.001.

Figure 3.3

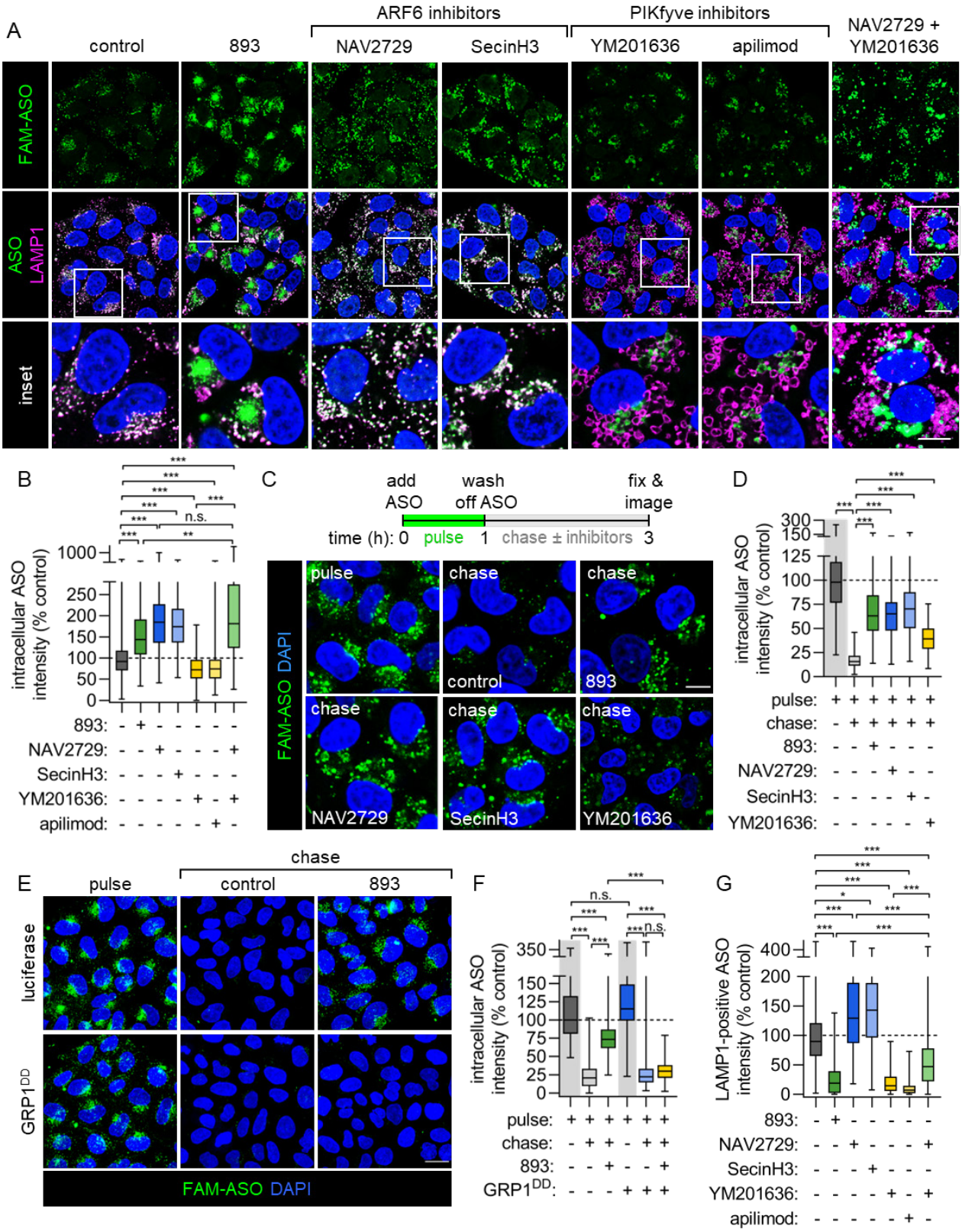
A
control
893
ARF6 inhibitors
NAV2729
SecinH3
PIKfyve inhibitors
YM201636
apilimod
NAV2729 + YM201636
FAM-ASO
ASO LAMP1
inset
B
intracellular ASO intensity (% control)
n.s.
893:
NAV2729:
SecinH3:
YM201636:
apilimod:
C
add ASO
wash off ASO
fix & image
time (h): 0 pulse 1 chase ± inhibitors 3
FAM-ASO DAPI
pulse
chase
control
893
NAV2729
SecinH3
YM201636
D
intracellular ASO intensity (% control)
pulse:
chase:
893:
NAV2729:
SecinH3:
YM201636:
E
chase
pulse
control
893
luciferase
GRP1DD
FAM-ASO DAPI
F
intracellular ASO intensity (% control)
n.s.
pulse:
chase:
893:
GRP1DD:
G
LAMP1-positive ASO intensity (% control)
893:
NAV2729:
SecinH3:
YM201636:
apilimod:

Figure 3.3: Simultaneous PIKfyve and ARF6 inhibition is both necessary and sufficient to recapitulate the effects of SH-BC-893 on ASO uptake and localization. (A) FAM-tagged cEt 3-10-3 ASO and LAMP1 localization in HeLa cells treated with SH-BC-893 (5 μM), NAV2729 (12.5 μM), SecinH3 (30 μM), YM201636 (800 nM), apilimod (100 nM), or both NAV2729 and YM20636 for 6 h. **(B)** Quantification of the total intracellular ASO fluorescence intensity from the images in (A). At least 100 cells were quantified from each of 3-4-independent experiments. Because the data is not normally distributed, a Kruskal-Wallis ANOVA was used with Dunn's test to correct for multiple comparisons. ***, $p < 0.001$. **(C)** HeLa cells were pulsed with FAM-tagged 3-10-3 cEt ASO (2 μM) for 1 h, washed, and then chased in media containing vehicle (DMSO), SH-BC-893 (5 μM), NAV2729 (12.5 μM), SecinH3 (30 μM), or YM201636 (800 nM) for 2 h prior to imaging. **(D)** Quantification of the intracellular ASO fluorescence of cells in (C). At least 100 cells were quantified from each of 2 independent experiments. Because data is not normally distributed, a Kruskal-Wallis ANOVA was used with Dunn's test to correct for multiple comparisons. ***, $p<0.001$. **(E)** HeLa cells expressing luciferase or $GRP1^{DD}$ were subjected to an ASO pulse-chase as in (C). **(F)** Quantification of the intracellular ASO fluorescence intensity in (E) performed as in (D). Scale bars, 20 μm (A and E) or 10 μm (inset in A and in C). **(G)** As in (B), except ASO fluorescence intensity within LAMP1-positive pixels is measured. **, $p<0.01$; ***, $p<0.001$.

Figure 3.4

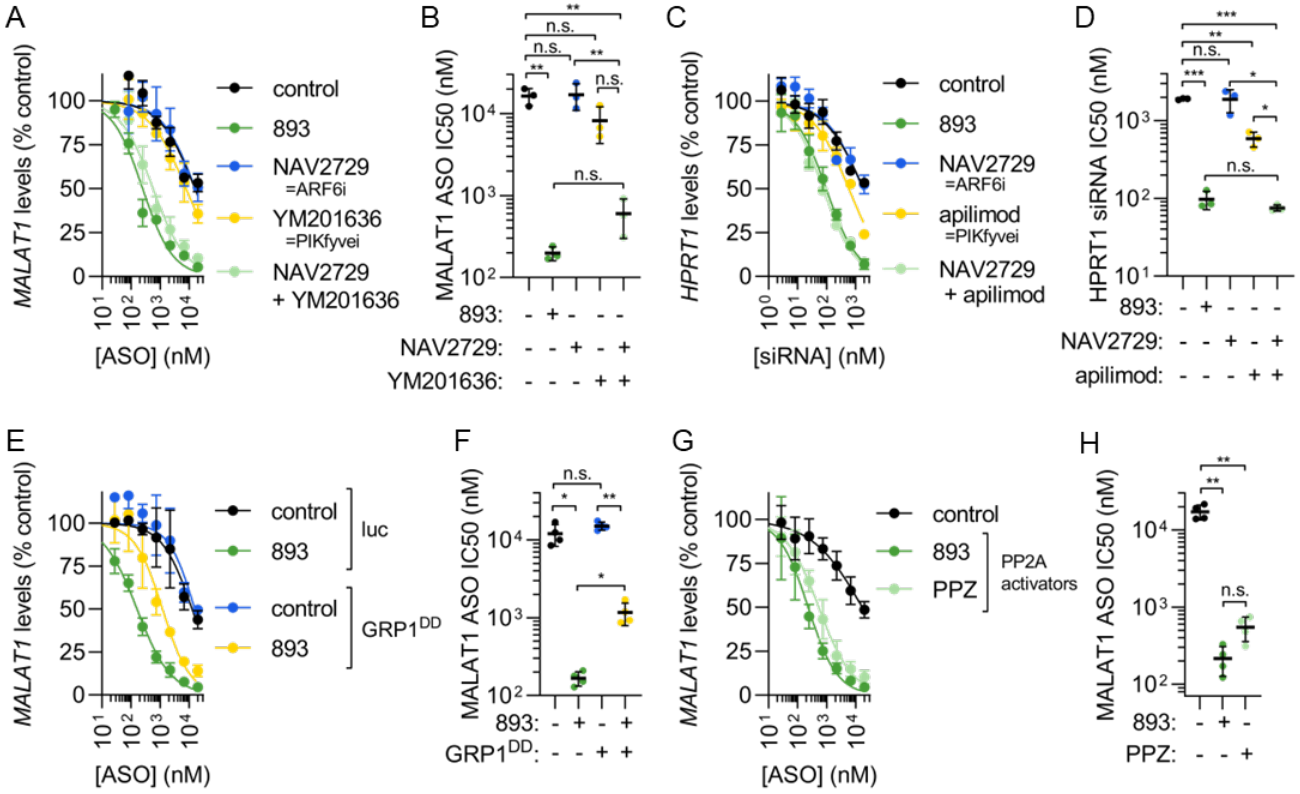

Figure 3.4: Simultaneous PIKfyve and ARF6 inhibition is both necessary and sufficient to account for the increase in ASO and siRNA activity in SH-BC-893-treated cells. (A) *MALAT1* levels in HeLa cells treated with the indicated concentrations of cEt gapmer ASO targeting *MALAT1* ± SH-BC-893 (5 μM), NAV2729 (12.5 μM), YM201636 (800 nM), or both for 24 h. Mean ± SD shown, n=3. **(B)** IC50s from each biological replicate in (A); mean ± SD shown. Due to unequal SD, a Brown-Forsythe and Welch ANOVA test was used with Dunnett's T3 test to correct for multiple comparisons; **, p<0.01. **(C)** *HPRT1* mRNA levels in HeLa cells treated with the indicated concentrations of a palmitate-conjugated siRNA targeting *HPRT1* ± SH-BC-893 (5 μM), NAV2729 (12.5 μM), apilimod (100 nM), or NAV2729 and apilimod for 24 h. Mean ± SD shown, n=3. **(D)** IC50s from each biological replicate in (C); mean ± SD shown. Using an ordinary one-way ANOVA with Sidak's multiple comparison test, **, p<0.01; ***, p<0.001. **(E)** *MALAT1* levels in HeLa cells stably expressing luciferase or $GRP1^{DD}$ treated with the indicated concentrations of cEt ASO targeting *MALAT1* ± SH-BC-893 (5

μM) for 24 h. Mean ± SD shown, n=3. **(F)** IC50s from each biological replicate in (E); mean ± SD shown. **(G)** *MALAT1* levels in HeLa cells treated with the cEt ASO targeting MALAT1 ± SH-BC-893 (5 μM) or PPZ (15 μM) for 24 h. Mean ± SD shown, n=3. **(H)** IC50s from each biological replicate in (G); mean ± SD shown. Because SD are not equal, Brown-Forsythe and Welch ANOVA test was used with Dunnett's T3 test to correct for multiple comparisons; **, $P<0.01$.

Figure 3.5

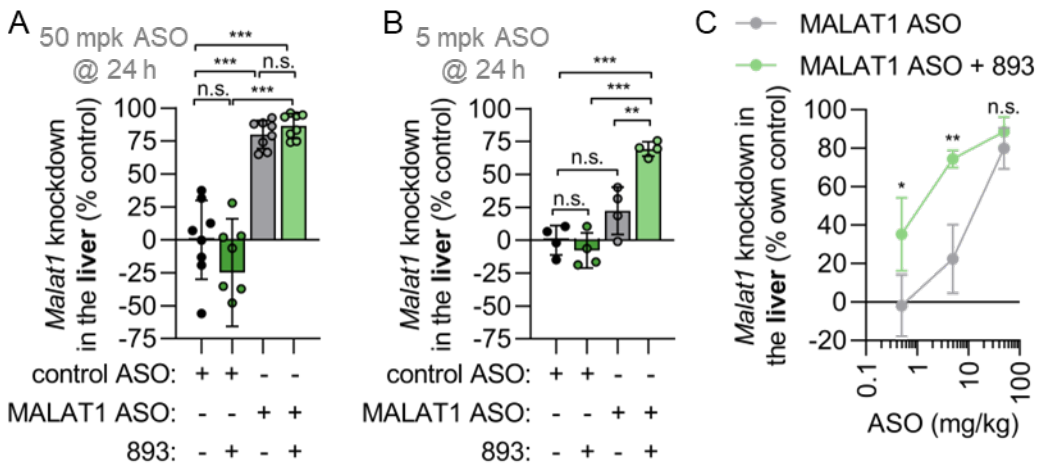

Figure 3.5: SH-BC-893 enhances activity of systemically administered ASOs in the liver. (A) *Malat1* knockdown in the livers of male Balbc/J mice treated with SH-BC-893 (120 mg/kg P.O.) 2 h before ASO (50 mg/kg S.C.) and sacrificed 24 h after a single dose. Non-targeting (control) or *Malat1*-targeting cEt gapmer ASO were used. Mean ± SD shown, n=8. Using an ordinary one-way ANOVA with Tukey's correction for multiple comparisons, ***, p<0.001. **(B)** As in (A), except mice were given 5 mg/kg ASO and n=4. **(C)** *Malat1* knockdown in mice treated as in (A) with 120 mg/kg SH-BC-893 and the indicated dose of cEt *Malat1* ASO. Mean ± SD shown, n=4 except 50 mg/kg group where n=8. Using an unpaired t-test to compare results ± SH-BC-893, *, p<0.05 and **, p<0.01. RNA levels are expressed relative to the housekeeping gene *Ppia* using the $2^{-\Delta\Delta Ct}$ method. In (A-B), knockdown is calculated relative to the mean from the mice receiving the non-targeting ASO and water vehicle. In (C), knockdown is expressed relative to the mean from the non-targeting ASO group for either the vehicle- or SH-BC-893-treated mice.

Figure 3.6

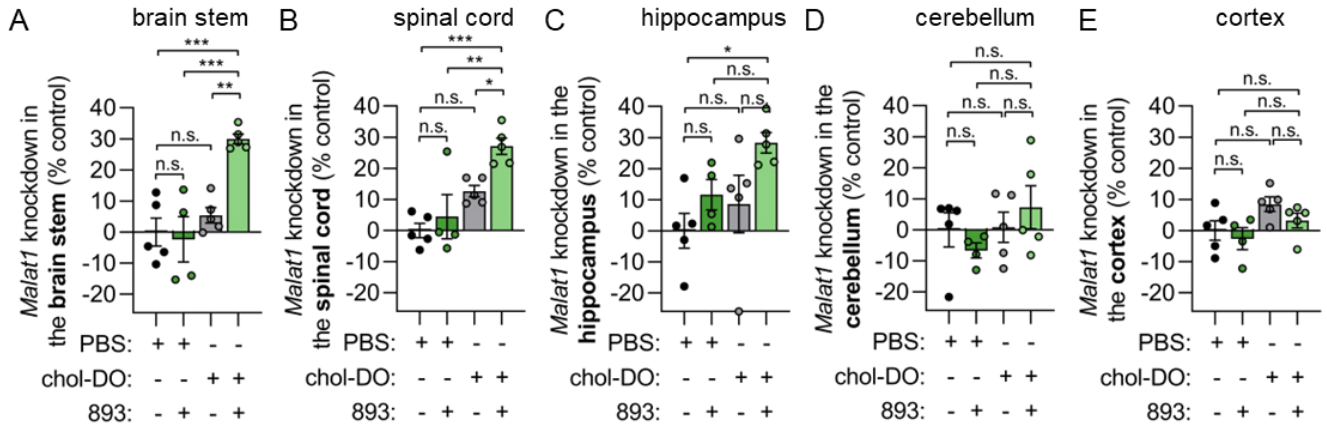

Figure 3.6: SH-BC-893 increases the activity of systemically-delivered, cholesterol-functionalized DNA/DNA duplexed oligonucleotides in the CNS. (A-E) *Malat1* knockdown in the brain stem (A), spinal cord (B), hippocampus (C), cerebellum (D), or cortex (E) of male Balbc/J mice treated with SH-BC-893 (120 mg/kg P.O.) 2 h before subcutaneous dosing with cholesterol-functionalized duplexed cEt gapmer targeting *Malat1* (100 mg/kg of duplex, 50 mg/kg of ASO strand S.C.). Mice received 2 doses 2 d apart and were sacrificed 5 d after the last dose. Mean ± SEM shown, n=5. Using an ordinary one-way ANOVA with Tukey's correction for multiple comparisons, ***, $p<0.001$. RNA levels were expressed relative to the housekeeping gene *Ppia* using the $2^{-\Delta\Delta Ct}$ method and knockdown expressed relative to the mean of the group receiving both vehicles.

Figure 3.7

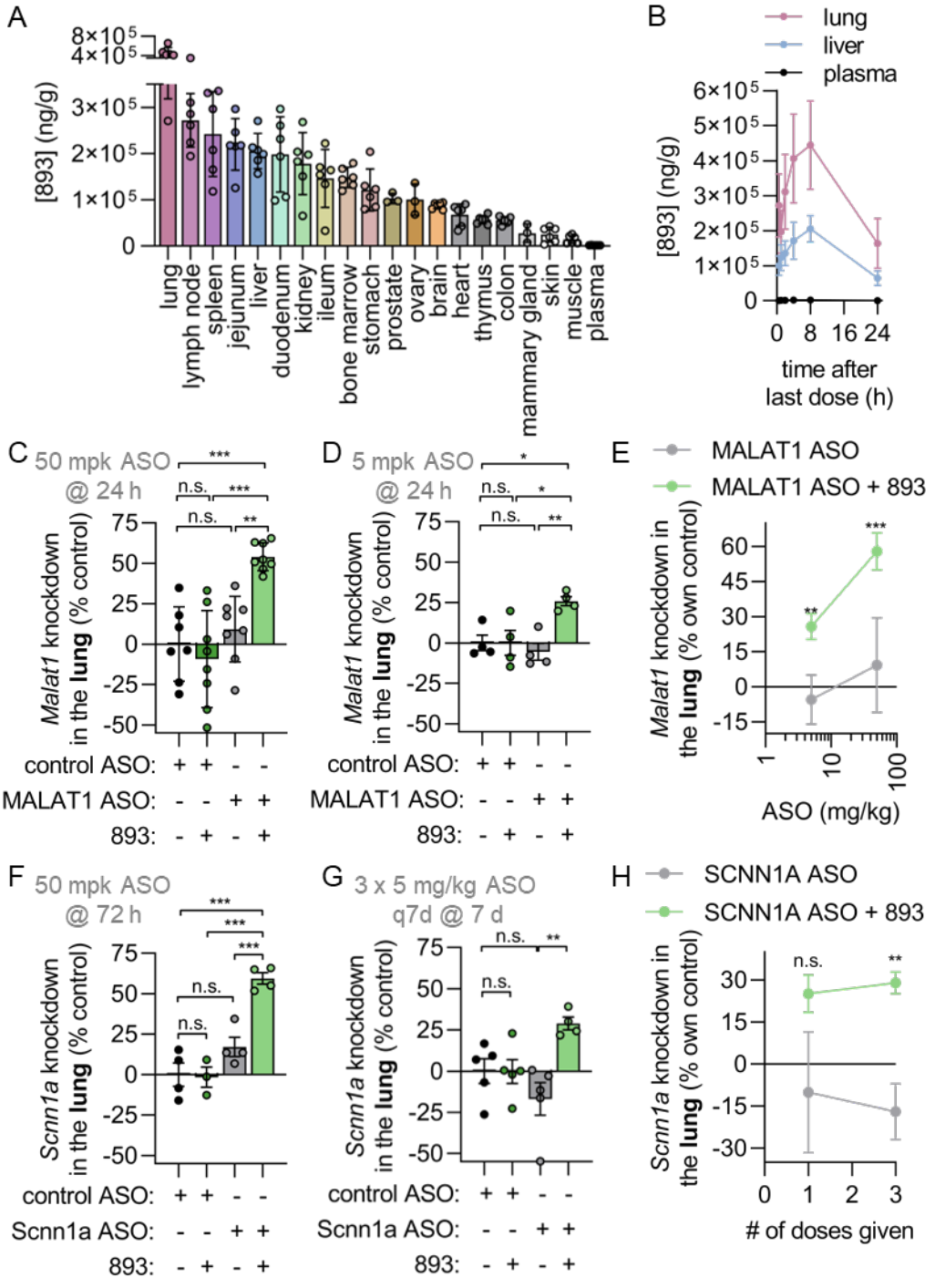

Figure 3.7: SH-BC-893 sensitizes the lung to systemically administered ASOs. (A) Tissue SH-BC-893 levels in male (n=3) or female (n=3) CD1 mice treated with 120 mg/kg P.O. Q.D. for 5 d and sacrificed 8 h after the last dose. Mean ± SD shown, n=6. **(B)** As in (A) but in mice sacrificed at the

indicated time points after the last dose. **(C)** *Malat1* knockdown in the lungs of male Balbc/J mice treated with SH-BC-893 (120 mg/kg P.O.) 2 h before ASO (50 mg/kg S.C.) and sacrificed 24 h after a single dose. Non-targeting (control) or *Malat1*-targeting cEt gapmer ASO were used. Mean ± SD shown, n=8. Using an ordinary one-way ANOVA with Tukey's correction for multiple comparisons, ***, $p<0.001$. **(D)** As in (C), except mice were given 5 mg/kg ASO and n=4. **(E)** *Malat1* knockdown in mice treated as in (C) with 120 mg/kg SH-BC-893 and the indicated dose of cEt *Malat1* ASO. Mean ± SD shown, n=4 except 50 mg/kg group where n=8. Using an unpaired t-test to compare results ± SH-BC-893, *, $p<0.05$ and **, $p<0.01$. **(F)** *Scnn1a* (aka ENaCα) knockdown in the lungs of male Balbc/J mice treated with SH-BC-893 (120 mg/kg P.O.) 2 h before ASO (50 mg/kg S.C.) and sacrificed 72 h after a single dose. Non-targeting (control) or *Scnn1a*-targeting cEt gapmers was used. Mean ± SD shown, n=4. Using a 1-way ANOVA with Tukey's correction for multiple comparisons, ***, $p<0.001$. **(G)** As in (F), except 3 doses of 5 mg/kg ASO were given at 7 d intervals and mice sacrificed 7 d after the last dose. **(H)** As in (G), except expressed as a function of number of doses received and normalized to the non-targeting ASO control. Using an unpaired t-test to compare results ± SH-BC-893, **, $p<0.01$. RNA levels are expressed relative to the housekeeping gene *Ppia* using the $2^{-\Delta\Delta Ct}$ method. In (C,D,F, & G), knockdown is calculated relative to the mean from the mice receiving the non-targeting ASO and water vehicle. In (E & H), knockdown is expressed relative to the mean from the non-targeting ASO group for either the vehicle- or SH-BC-893-treated mice.

3.13 Supplementary Tables

Supplementary Table 3.1

Summary of ASOs used in this study.

Target	Description of chemistry	Sequence (5' → 3')
MALAT1 (mouse & human)	3-10-3 cEt gapmer	**GCA**TTCTAATAGC**AGC**
MALAT1 (mouse & human)	6-FAM-tagged 3-10-3 cEt gapmer for fluorescence microscopy	**6-FAM-GCA**TTCTAATAGC**AGC**
MALAT1 (mouse & human)	5-10-5 2'MOE gapmer	**CCAGG**CTGGTTATGA**CTCAG**
MALAT1 (mouse & human)	6-FAM-tagged 5-10-5 2'MOE gapmer for fluorescence microscopy	**6-FAM-CCAGG**CTGGTTATGA**CTCAG**
ACTN1 (human)	3-10-3 cEt gapmer	**TAA**CTTTGTGCTT**GGT**
MALAT1 (mouse & human)	5'tagged $GalNAc_3$ (GN3) tagged 3-10-3 cEt gapmer	**GN3-GCA**TTCTAATAGC**AGC**
Scnn1a (mouse)	3-10-3 cEt gapmer	**GAG**CATCTAATAC**AGC**
non-targeting	3-10-3 cEt gapmer control ASO	**CGC**CGATAAGGTA**CAC**

All gapmers contain ten 2'-deoxynucleosides flanked by either three **2',4'-constrained ethyl (cEt)** modified or five **2'-O-methoxyethyl (2'MOE)** modified riboses on the 5' and 3' ends. All cytosine residues throughout the modified oligonucleotide are 5-methyl cytosines. The internucleoside linkages are all phosphorothioate (PS). Some oligonucleotides are tagged on the 5' end with a **6-carboxyfluorescein (6-FAM)**.

Supplementary Table 3.2

Primers and Probes used in this study for qRT-PCR:

target	Primers (5' → 3')	Taqman Probe (5' → 3') 6-FAM on 5' end TAMRA on 3' end
MALAT1 (human)	Fwd: AGGCGTTGTGCGTAGAGGAT Rev: AAAGGTTACCATAAGTAAGTTCCAGAAAA	AGTGGTTGGTAAAAATCCGTGAGGTCGG
Malat1 (mouse)	Fwd: TGGGTTAGAGAAGGCGTGTACTG Rev: TCAGCGGCAACTGGGAAA	CGTTGGCACGACACCTTCAGGGACT
ACTN1 (human)	Fwd: CAATATGGCGGGCACCAA Rev: GGTCCCATTTGCCATTGATC	CCCTACACAACCATCACGCCTCAGG
Ppia (mouse)	Fwd: TCGCCGCTTGCTGCA Rev: ATCGGCCGTGATGTCGA	CCATGGTCAACCCCACCGTGTTC
Scnn1a (mouse)	Fwd: GGTGTAGAGTTCTGTGACTACC Rev: AGCTTGTAGTTGGTCACACTG	CTGCCTTCTCCTTGGATAGCCTGG
ACTB (human)	Fwd: CGGACTATGACTTAGTTGCGTTACA Rev: GCCATGCCAATCTCATCTTGT	CCTTTCTTGACAAAACCTAACTTGCGCAGA

target	Taqman Assay Primer/Probe Mix from Applied Biosystems
HPRT1 (human)	Taqman Assay ID: Hs99999909_m1 Catalog #: 4333768F

Supplementary Table 3.3

Summary of siRNAs used in this study.

Target	Sequence & Chemistry
HPRT1 (human)	5′-pAsUsAAAAUCUACAGUCAUAGGAsAsU-3′ 3′-UsAsUUUUAGAUGUCAGUAUCCU-5′-C_{16}-palmitate 2′-OMe 2′-F-RNA s = phosphorothioate p = 5′-phosphate

Red = 2'-O-methyl (2'-OMe) modified riboses
Green = 2'fluorine (2'-F-RNA) modified riboses
s = phosphorothioate (PS) internucleoside linkage

Supplementary Table 3.4

Description of cholesterol-functionalized DNA/DNA duplexed oligos

Target	Sequence & Chemistry
MALAT1 (human & mouse)	$^{5'}$GsCsAsTsTsCsTsAsAsTsAsGsCsAsGsC$^{3'}$ $^{3'}$CsGsU A A G A T T A T C G UsCsG$^{5'}$-TEG-cholesterol

Blue = 2',4'-constrained ethyl (cEt)
Yellow = 2'fluorine (2'-F-RNA) modified riboses
s = phosphorothioate (PS) internucleoside linkage

3.14 Supplementary Figures

Supplementary Fig. S3.1

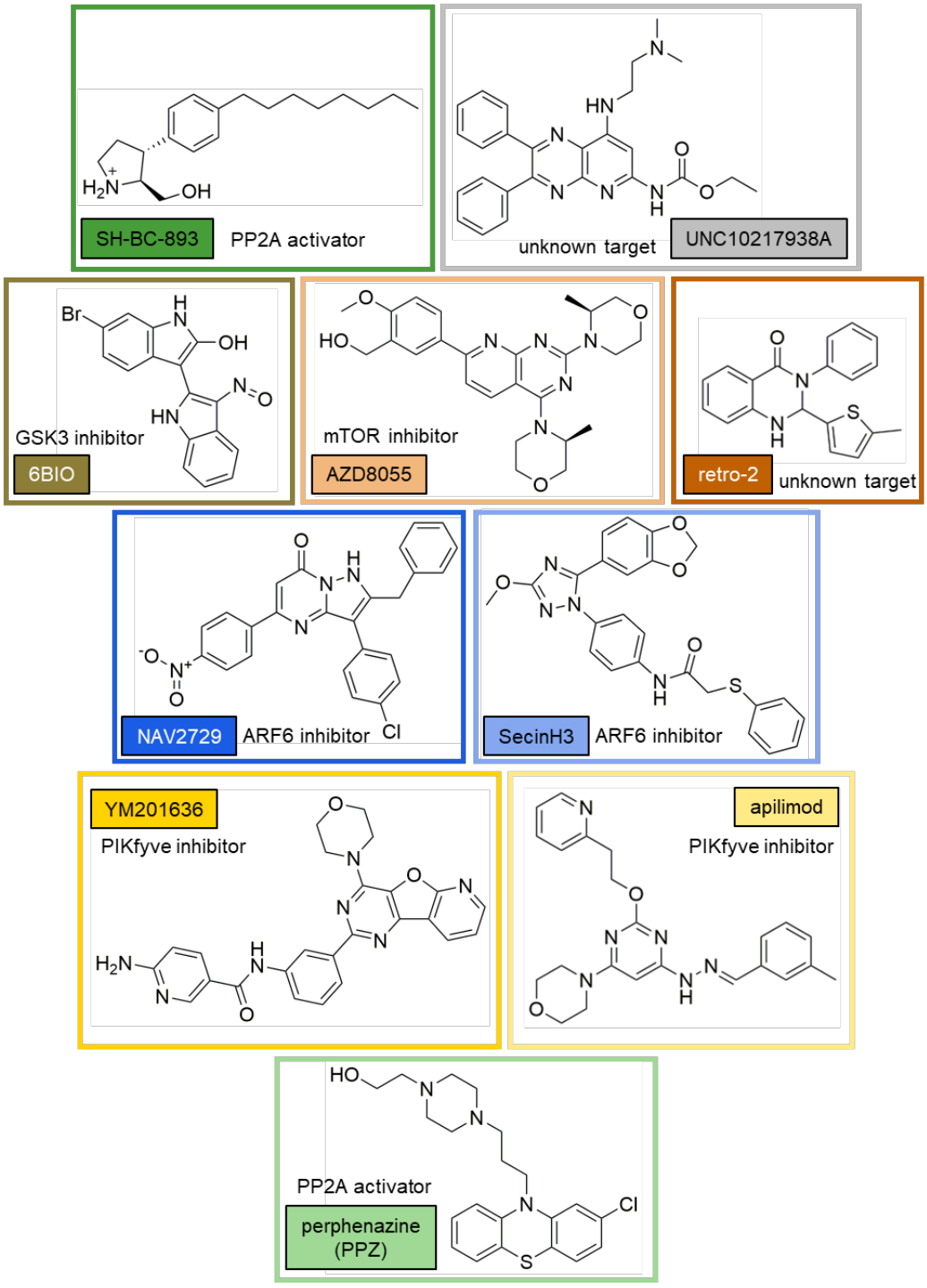

Supplementary Fig. S3.1: Chemical structures of all small molecules used in this study.

Molecular targets are indicated.

Supplementary Fig. S3.2

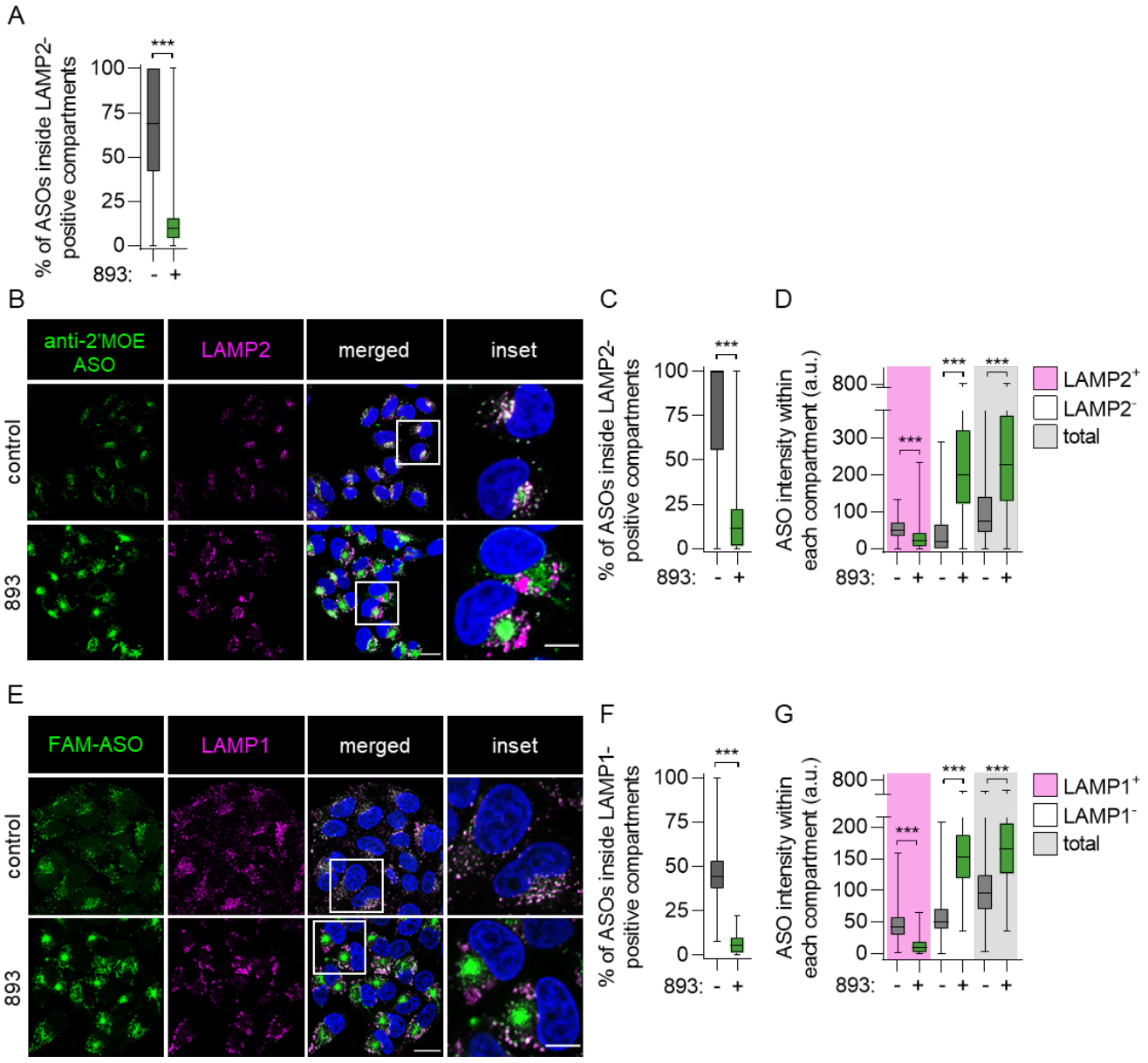

Supplementary Fig. S3.2: SH-BC-893 increases ASO delivery to extra-lysosomal compartments. **(A)** Quantification of the images in (Fig. 1B). Percent of the total intracellular ASO that is within LAMP2-positive lysosomes is quantified. **(B)** HeLa cells treated with an untagged 5-10-5 2'MOE gapmer (2 μM) ± SH-BC-893 (5 μM) for 6 h then stained with antibodies for PS-ASOs and endogenous LAMP2. Scale bar = 20 μm. **(C)** Quantification of the images in (B). Percent of the total intracellular ASO that is within LAMP2-positive lysosomes is quantified. **(D)** Quantification of the raw intensity values for ASO from

images in (B) within LAMP2-positive, LAMP2-negative, and total cellular areas. At least 100 cells were quantified from 2 independent experiments. Using a Mann-Whitney t test to correct for data that is not normally distributed, ***, $p<0.001$. **(E-G)** As in (B-D), except FAM-tagged 3-10-3 cEt gapmer used and lysosomes marked with antibodies to endogenous LAMP1. Scale bar = 20 μm.

Supplementary Fig. S3.3

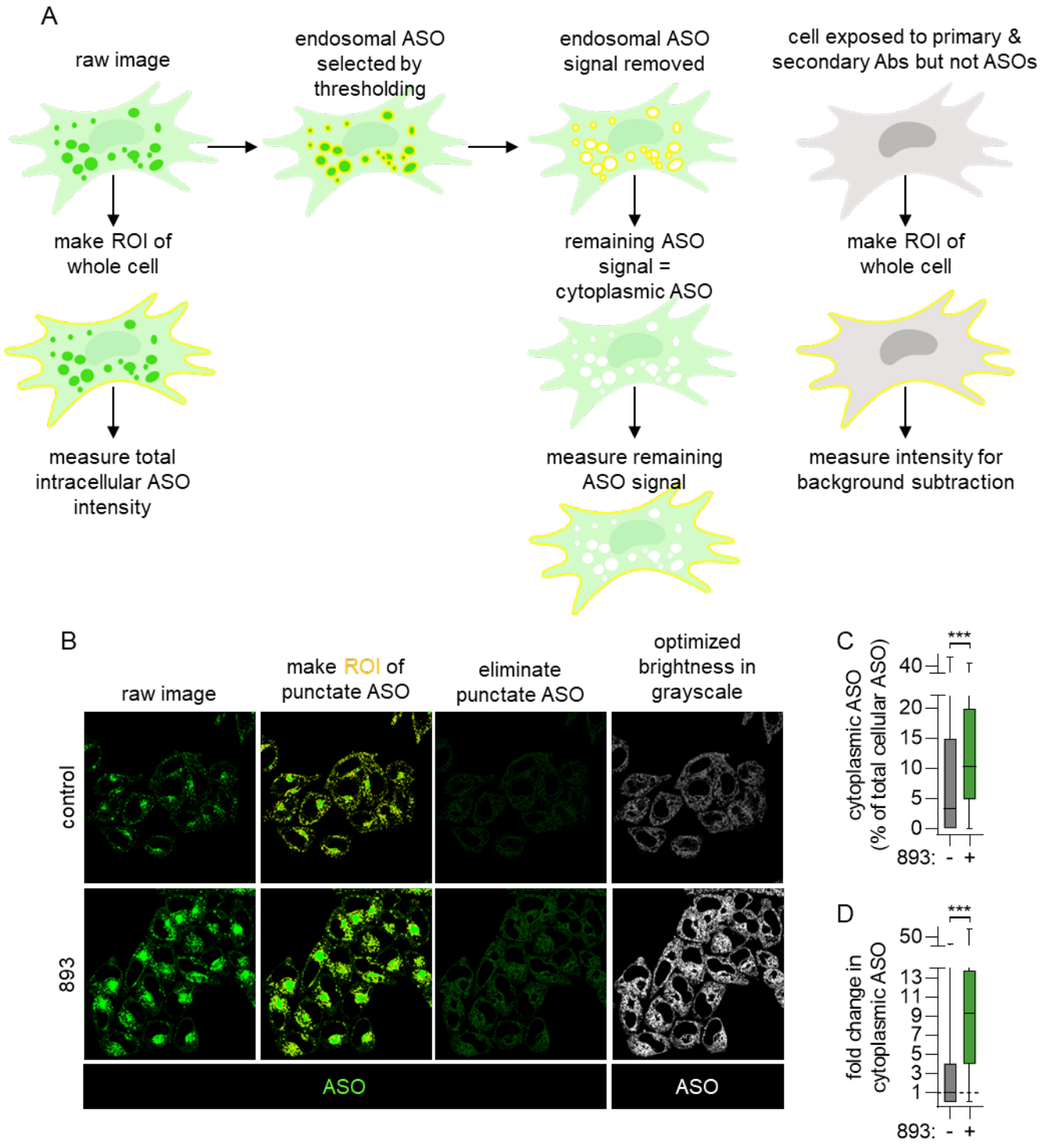

Supplementary Fig. S3.3: SH-BC-893 increases cytoplasmic ASO levels. (A) Figure depicting method to measure cytoplasmic ASO levels. In brief, endosomal ASO signal was eliminated by

generating regions of interest (ROIs) on thresholded images, leaving the diffuse cytoplasmic signal remaining. Background elimination was performed by quantifying fluorescent signal in cells that were not exposed to ASOs but stained with both primary and secondary antibodies. **(B)** HeLa cells treated with a 3-10-3 cEt ASO targeting *MALAT1* (2 μM) ± SH-BC-893 (5 μM) for 6 h and stained with antibodies to PS-ASOs. Scale bar = 20 μm. For inset, scale bar = 10 μm. Showing multiple steps of the quantification method described in A. **(C-D)** Quantification of (B), showing percent of total intracellular ASOs that is cytoplasmic (C) or the total raw signal of ASOs in the cytoplasm (D). Using a Mann-Whitney t test to correct for data that is not normally distributed, ***, $p<0.001$.

Supplementary Fig. S3.4

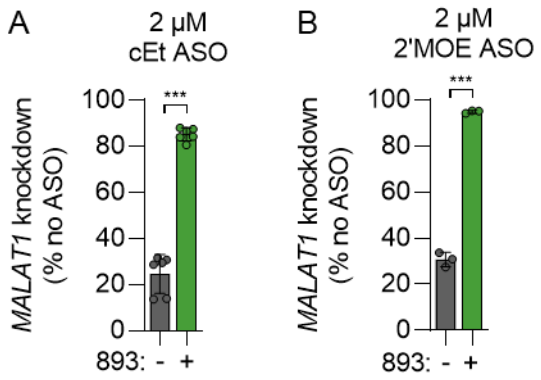

Supplementary Fig. S4: SH-BC-893 increases ASO activity. (A) MALAT1 knockdown in HeLa cells treated with a 3-10-3 cEt gapmer (2 μM) targeting MALAT1 ± SH-BC-893 (5 μM) for 24 h. Mean ± SD shown, n=6. Using an unpaired two-tailed t test, ***, $p<0.001$. **(B)** As in (A), except with a 5-10-5 2'MOE gapmer, n=3.

Supplementary Fig. S3.5

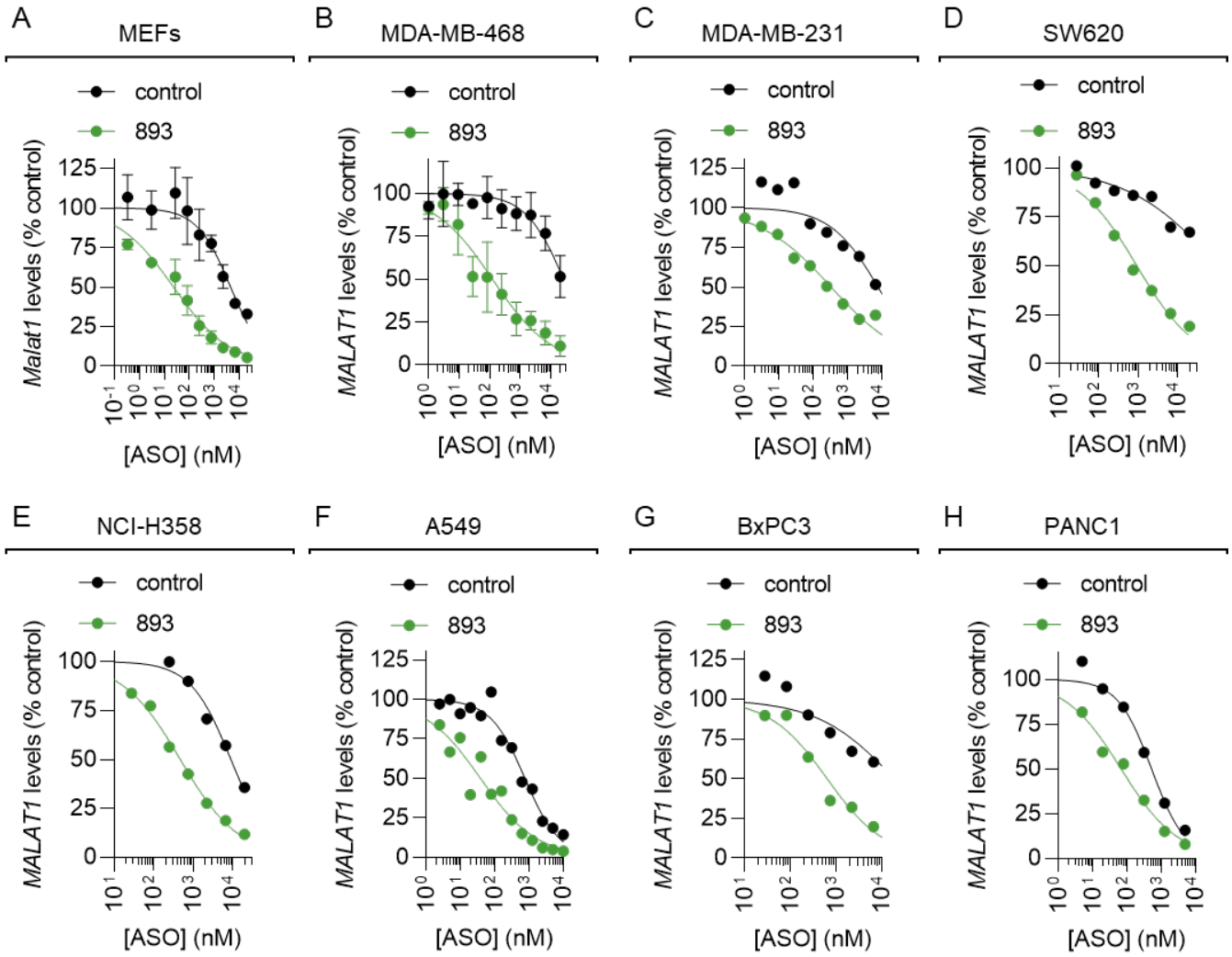

Supplementary Fig. S3.5: Individual graphs for the IC50s presented in Fig. 3.2H. (A) *Malat1* levels in MEFs treated with a 3-10-3 cEt gapmer targeting *Malat1* ± SH-BC-893 (5 μM) for 24 h. Mean ± SD shown, n=3. **(B-H)** As in (A), except MDA-MB-468 cells (B), MDA-MB-231 cells & n=1 (C), SW620 cells & n=1 (D), NCI-H358 cells & n=1 (E), A549 cells & n=2 (F), BxPC3 cells & n=1 (G), and PANC1 cells & n=1 (H).

Supplementary Fig. S3.6

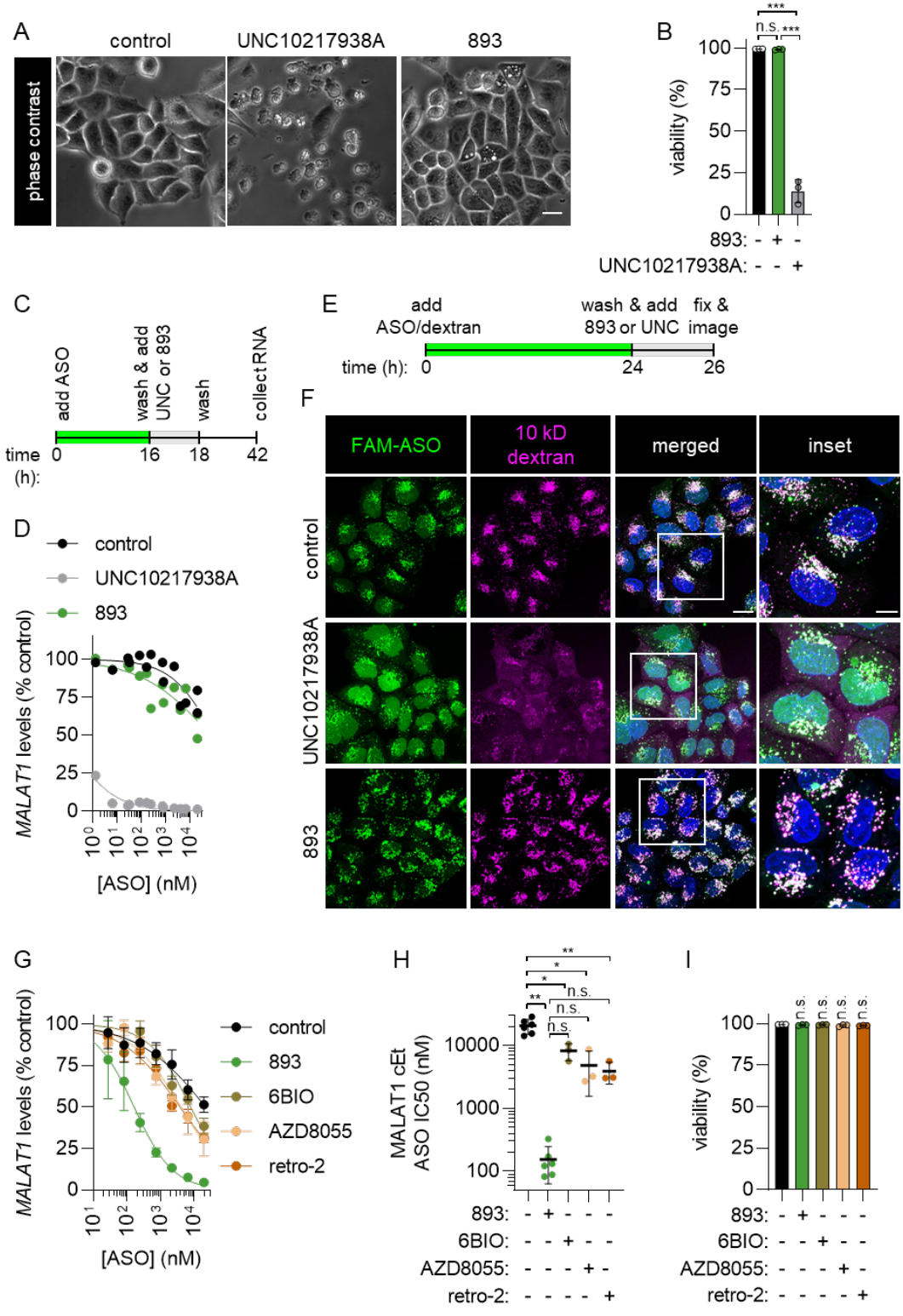

Supplementary Fig. S3.6: SH-BC-893 is distinct from endolytic agents and more effective than

previously identified oligonucleotide-potentiating small molecules. (A) Phase contrast microscopy of HeLa cells treated with UNC10217938A (10 μM) or SH-BC-893 (5 μM) for 24 h. Scale bar = 20 μm. **(B)** Viability measured by vital dye (DAPI) exclusion through flow cytometry analysis in HeLa cells treated as in (A). Using an ordinary one-way ANOVA with Tukey's correction for multiple comparisons. Mean ± SD shown, n=3. **(C)** Timeline for the published experiments performed evaluating UNC10217938A's ability to potentiate ASO. **(D)** *MALAT1* levels in HeLa cells treated with the indicated concentrations of 3-10-3 cEt gapmer targeting *MALAT1* ± SH-BC-893 (5 μM) or UNC10217938A (10 μM) using the timeline in (C). **(E)** Timeline for (F). **(F)** HeLa cells loaded with a FAM-tagged 3-10-3 cEt gapmer (2 μM) and Alexa Fluor 594-tagged 10 kD dextran (200 μg/ml) for 24 h before treating with UNC10217938A (10 μM) or SH-BC-893 (5 μM) for 2 h before fixing and imaging by confocal microscopy. Scale bar = 20 μm. For inset, scale bar = 10 μm. n.s. = not significant. **(G)** *MALAT1* levels in HeLa cells treated with the indicated concentrations of 3-10-3 cEt gapmer targeting *MALAT1* ± SH-BC-893 (5 μM), 6BIO (3 μM), AZD8055 (500 nM), or retro-2 (100 μM) for 24 h. Mean ± SD shown, n=3-6. **(H)** IC50s from each biological replicate in (G); mean ± SD shown. Due to unequal SD, a Brown-Forsythe and Welch ANOVA test was used with Dunnett's T3 test to correct for multiple comparisons; **, $p<0.01$, *, $p<0.05$. **(I)** Viability measured by vital dye (DAPI) exclusion through flow cytometry analysis in HeLa cells treated as in (G). Using an ordinary one-way ANOVA with Tukey's correction for multiple comparisons. Mean ± SD shown, n=3.

Supplementary Fig. S3.7

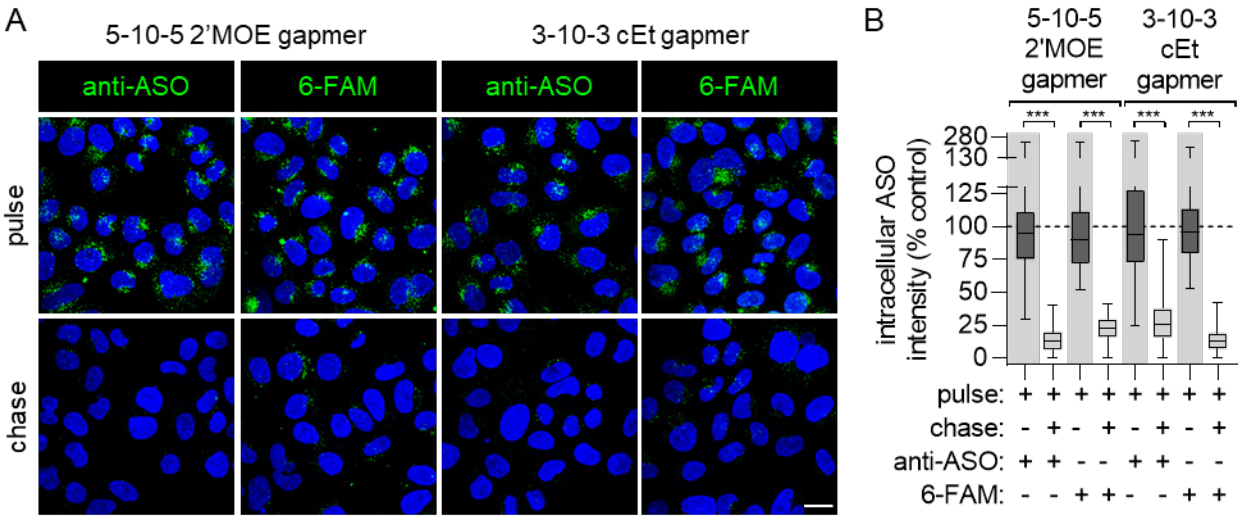

Supplementary Fig. S3.7: The loss of ASO signal during the chase is not due to a quenching effect on the 6-FAM fluorophore. **(A)** HeLa cells were pulsed with untagged or 6-FAM-tagged 5-10-5 2'MOE or 3-10-3 cEt gapmers (2 μM) for 1 h, washed, and then chased in media lacking ASOs for 2 h prior to staining with antibodies for PS-ASOs (for untagged ASOs) or imaging directly (for 6-FAM-tagged ASOs). Scale bar = 20 μm. **(B)** Quantification of the intracellular ASO fluorescence of cells in (A). At least 80 cells were quantified from 1 experiment. Because data is not normally distributed, a Kruskal-Wallis ANOVA was used with Dunn's test to correct for multiple comparisons. ***, $p<0.001$.

Supplementary Fig. S3.8

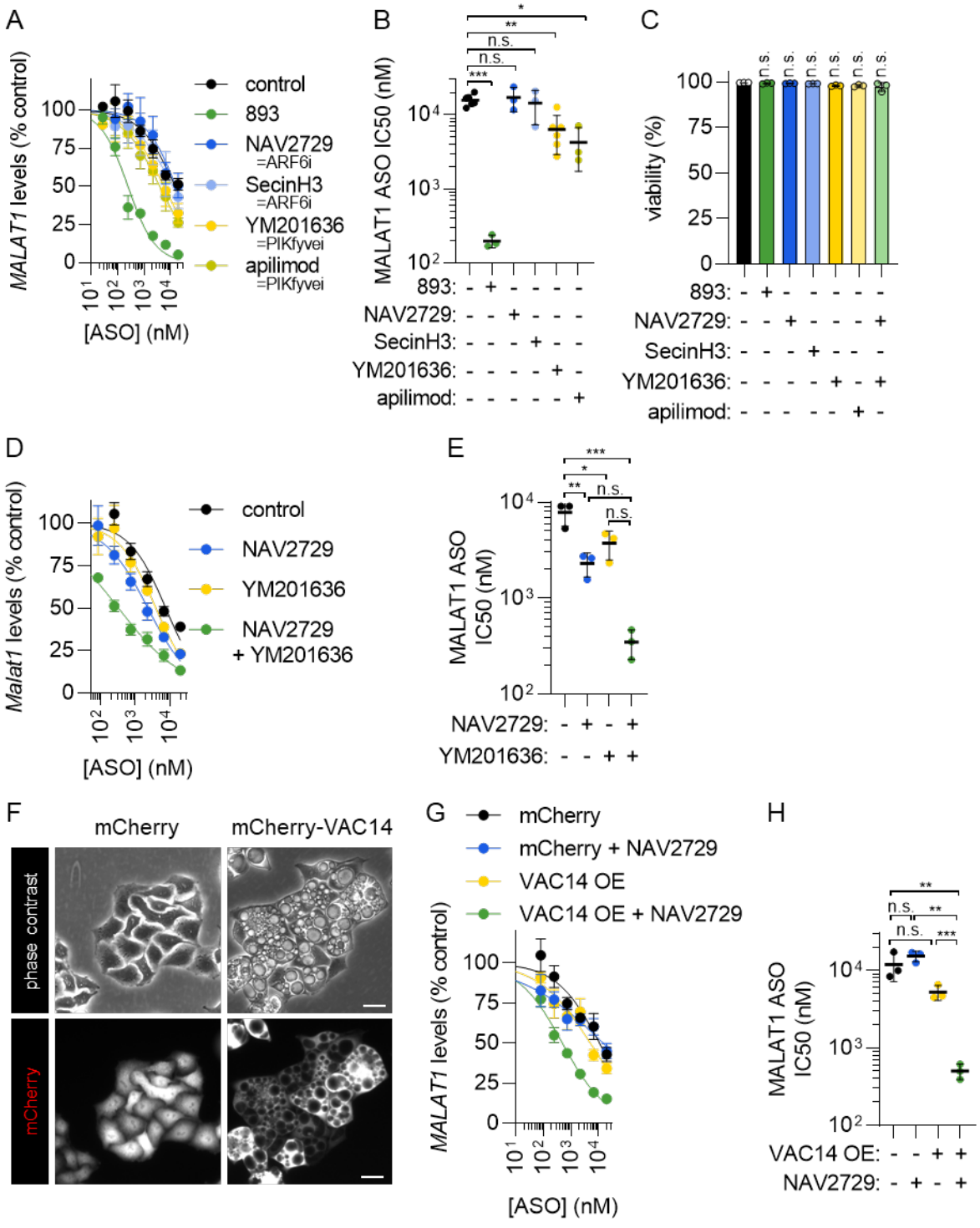

Supplementary Fig. S3.8: Simultaneous ARF6 and PIKfyve inhibition enhance ASO activity synergistically. (A) *MALAT1* levels in HeLa cells treated with the indicated concentrations of 3-10-3

cEt gapmer targeting *MALAT1* ± SH-BC-893 (5 μM), NAV2729 (12.5 μM), SecinH3 (30 μM), YM201636 (800 nM), or apilimod (100 nM) for 24 h. Mean ± SD shown, n=3-5. **(B)** IC50s of each biological replicate in (A); mean ± SD shown. Due to unequal SD, a Brown-Forsythe and Welch ANOVA test was used with Dunnett's T3 test to correct for multiple comparisons; ***, $p<0.001$; **, $p<0.01$; *, $p<0.05$. **(C)** Viability measured by vital dye (DAPI) exclusion through flow cytometry analysis in HeLa cells treated as in (A). Using an ordinary one-way ANOVA with Tukey's correction for multiple comparisons. Mean ± SD shown, n=3. **(D-E)** Same as (A-B), except in MEFs and NAV2729 and YM201636 in combination. Mean ± SD shown, n=3. **(F)** Phase contrast microscopy or mCherry fluorescence of HeLa cells transduced with pQCXIP-mCherry or mQCXIP-mCherry-VAC14. Scale bar = 20 μm. **(G)** *MALAT1* levels in HeLa cells expressing mCherry or mCherry-VAC14 treated with the indicated concentrations of 3-10-3 cEt gapmer targeting *MALAT1* ± NAV2729 (12.5 μM) for 24 h. Mean ± SD shown, n=3. **(H)** IC50s from each biological replicate in (G); mean ± SD shown. Due to unequal SD, a Brown-Forsythe and Welch ANOVA test was used with Dunnett's T3 test to correct for multiple comparisons; ***, $p<0.001$; **, $p<0.01$. n.s. = not significant.

Supplementary Fig. S3.9

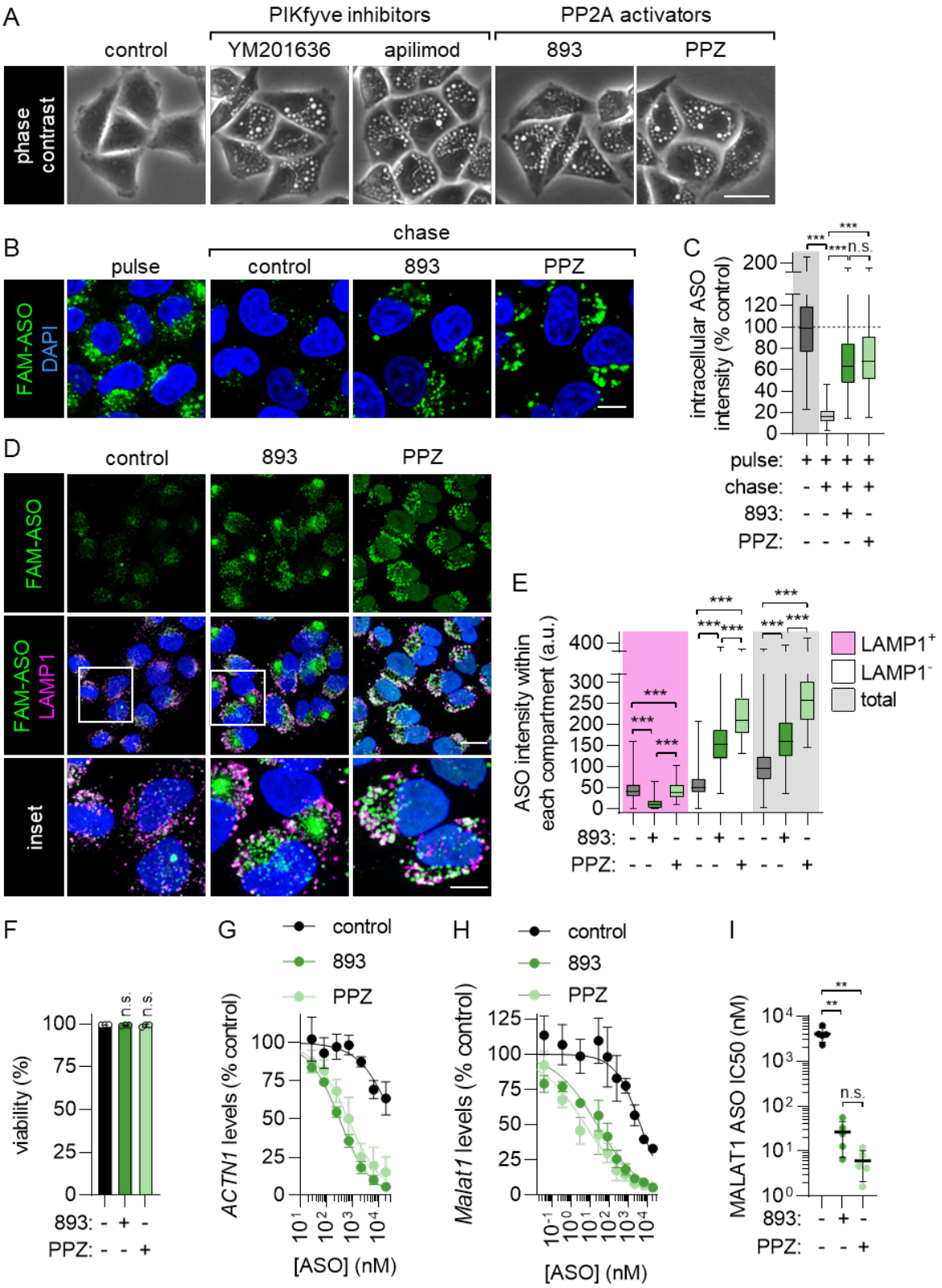

Supplementary Fig. S3.9: PP2A activation blocks endocytic recycling and lysosomal fusion and increases ASO activity. (A) Phase contrast images of HeLa cells treated with YM201636 (800 nM), apilimod (100 nM), SH-BC-893 (5 μM), or PPZ (15 μM) for 3 h. Scale bar = 20 μm. **(B)** HeLa cells were pulsed with FAM-tagged 3-10-3 cEt ASO (2 μM) for 1 h, washed, and then chased in media containing vehicle (DMSO), SH-BC-893 (5 μM), or PPZ (15 μM) for 2 h prior to imaging. **(C)** Quantification of the intracellular ASO fluorescence of cells in (B). At least 100 cells were quantified from each of 2 independent experiments. Because data is not normally distributed, a Kruskal-Wallis ANOVA was used with Dunn's test to correct for multiple comparisons. ***, $p<0.001$. **(D)** FAM-tagged cEt 3-10-3 ASO and LAMP1 localization in HeLa cells treated with SH-BC-893 (5 μM) or PPZ (15 μM) for 6 h. Scale bar = 20 μm. For inset, scale bar = 10 μm. **(E)** Quantification of the raw intensity values for ASO from images in (D) within LAMP2-positive, LAMP2-negative, and total cellular areas. At least 50 cells were quantified from 2 independent experiments. Because data is not normally distributed, a Kruskal-Wallis ANOVA was used with Dunn's test to correct for multiple comparisons. ***, $p <0.001$. **(F)** Viability measured by vital dye (DAPI) exclusion through flow cytometry analysis in HeLa cells treated with SH-BC-893 (5 μM) or PPZ (15 μM) for 24 h. Using an ordinary one-way ANOVA with Tukey's correction for multiple comparisons. Mean ± SD shown, n=3. **(G)** *ACTN1* levels in HeLa cells treated with the indicated concentrations of a 3-10-3 cEt gapmer targeting *ACTN1* ± SH-BC-893 (5 μM) or PPZ (15 μM) for 24 h. Mean ± SD shown, n=3. IC50 for control could not be calculated due to low activity. **(H)** Same as (G), except with 3-10-3 cEt gapmer targeting *Malat1* in MEFs, n=4. **(I)** IC50s from each biological replicate in (H); mean ± SD shown. Using a Welch's t test to correct for unequal SD, **, $p<0.01$. n.s. = not significant.

Supplementary Fig. S3.10

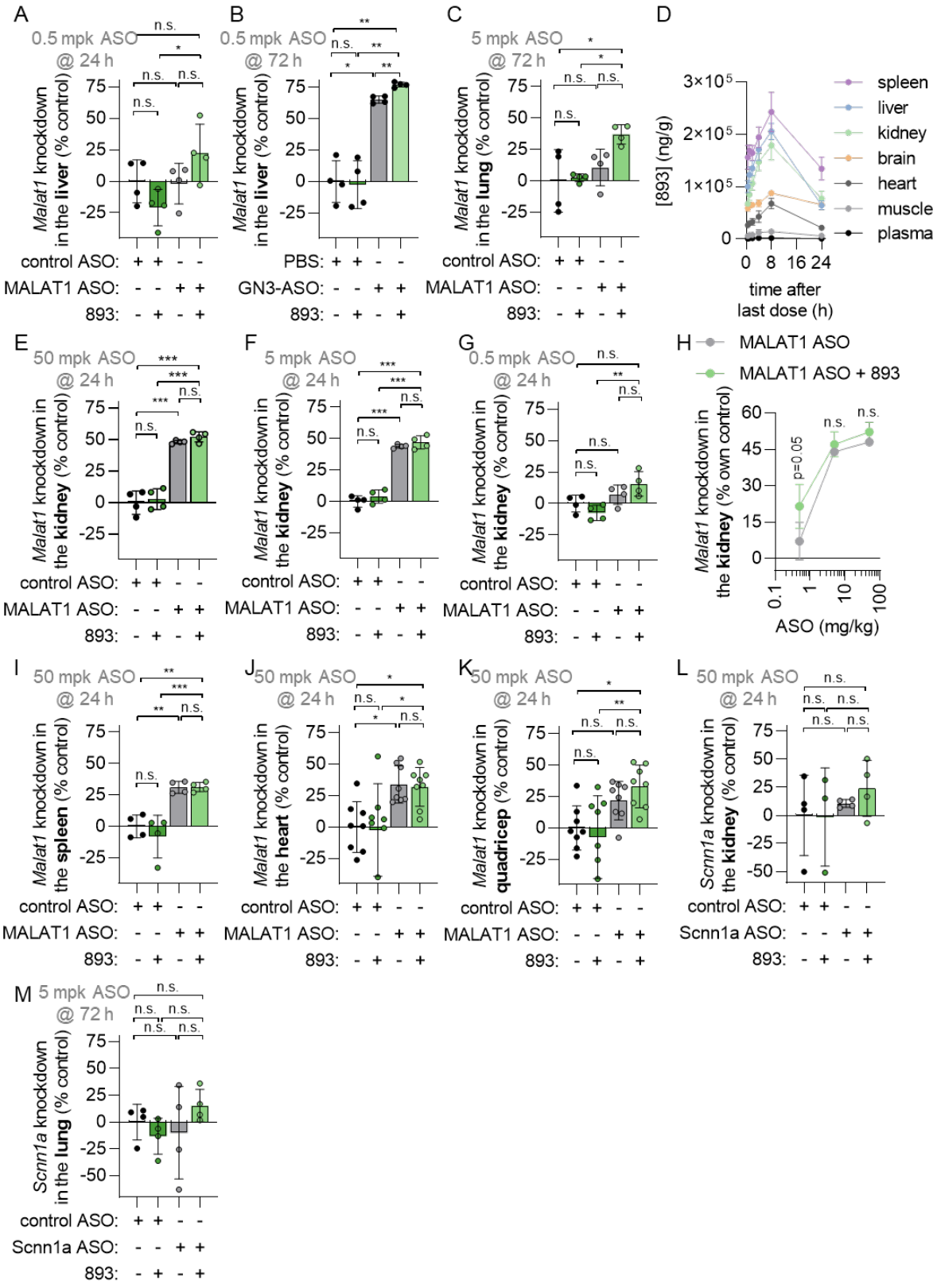

Supplementary Fig. S3.10: SH-BC-893 sensitizes lung and liver tissues to systemically-delivered ASO. (A) *Malat1* knockdown in the livers of male Balbc/J mice (n=4/group) treated with SH-BC-893 (120 mg/kg P.O.) 2 h before ASO (0.5 mg/kg S.C.) and sacrificed 24 h after a single dose. Non-targeting (control) or *Malat1*-targeting cEt gapmer were used. Mean ± SD shown. Using an ordinary one-way ANOVA with Tukey's correction for multiple comparisons, *, $p<0.05$. **(B)** As in (A), except using a $GalNAc_3$-conjugated (GN) form of the MALAT1 ASO and mice sacrificed 72 h after single dose. Due to unequal SD, a Brown-Forsythe and Welch ANOVA test was used with Dunnett's T3 test to correct for multiple comparisons, *, $p<0.05$; **, $p<0.01$. **(C)** As in (A), except 5 mg/kg ASO and in the lung. **(D)** Tissue SH-BC-893 levels in male (n=3) or female (n=3) CD1 mice treated with 120 mg/kg P.O. Q.D. for 5 d and sacrificed at the indicated time points after the last dose. Mean ± SD shown, n=6. **(E)** As in (A), except 50 mg/kg ASO and kidney tissue evaluated. **(F-G)** As in (E), except 5 mg/kg (F) or 0.5 mg/kg (G) ASO. **(H)** As in (E-G), except expressed as a function of the dose of ASO delivered in mg/kg. Mean ± SD shown (n=4 mice/group). Using an unpaired t-test to compare lung *Malat1* levels in ASO alone or ASO+893 groups, n.s., $p>0.05$. **(I-K)** As in (E), except spleen (I), heart (J), or quadricep muscle (K). **(L)** *Scnn1a* (aka ENaCα) knockdown in the kidney of male Balbc/J mice (n=4 mice/group) treated with SH-BC-893 (120 mg/kg P.O.) 2 h before ASO (50 mg/kg S.C.) and sacrificed 72 h after a single dose. A non-targeting (control) or Scnn1a-targeting cEt gapmer were used. Using an ordinary one-way ANOVA with Tukey's correction for multiple comparisons, ***, $p<0.001$. **(M)** Same as (L), except 5 mg/kg and in lung tissue. n.s. = not significant. RNA levels are expressed relative to the housekeeping gene *Ppia* using the $2^{-\Delta\Delta Ct}$ method. In (A,B,C,E-G,I-M), knockdown is calculated relative to the mean from the mice receiving the non-targeting ASO and water vehicle. In (H), knockdown is expressed relative to the mean from the non-targeting ASO group for either the vehicle- or SH-BC-893-treated mice.

Supplementary Fig. S3.11

A see *J Clin Invest* (2016) 126:4088. DOI: 10.1172/JCI87148 for detailed analysis of toxicity in mice dosed daily with 120 mg/kg SH-BC-893 for 11 weeks, includes body weight, complete blood chemistry panel, complete blood count, and histology of intestinal crypts.

B see EMBO Mol Med (2021)13:e13086 DOI: 10.15252/emmm.202013086 for a holistic measurement of SH-BC-893 toxicity by monitoring the time spent exercising and the distance ran of mice treated with 120 mg/kg SH-BC-893 P.O. every other day for 4 weeks.

C

Group ID	AST (U/L)	ALT (U/L)	ALP (U/L)	total bilirubin (mg/dL)	conjugated bilirubin (mg/dL)	albumin (g/dL)	globulin (g/dL)	ALB:GLOB ratio	total protein (g/dL)
water PO	85 ± 16	35 ± 8	142 ± 28	0.1 ± 0	0 ± 0	2.4 ± 0.1	1.8 ± 0.1	1.4 ± 0.1	4.1 ± 0.1
120 mg/kg 893 PO	92 ± 44	33 ± 7	138 ± 14	0.2 ± 0.1	0 ± 0	2.4 ± 0.1	1.8 ± 0.1	1.4 ± 0.1	4.2 ± 0.2
240 mg/kg 893 PO	74 ± 17	27 ± 3	125 ± 8	0.1 ± 0.1	0 ± 0	2.4 ± 0.1	1.7 ± 0.1	1.4 ± 0.1	4.1 ± 0.1

Group ID	BUN (mg/dL)	creatinine (mg/dL)	BUN:creatinine ratio	creatine kinase (U/L)	cholesterol (mg/dL)
water PO	21 ± 2	0.1 ± 0.1	171 ± 54	2531 ± 1005	98 ± 5
120 mg/kg 893 PO	25 ± 3	0.1 ± 0	247 ± 34	3914 ± 3298	103 ± 11
240 mg/kg 893 PO	19 ± 2	0.1 ± 0.1	160 ± 45	2243 ± 545	109 ± 14

Group ID	glucose (mg/dL)	calcium (mg/dL)	phosphorus (mg/dL)	bicarbonate (mmol/L)	chloride (mmol/L)	potassium (mmol/L)	sodium (mmol/L)	NA/K Ratio
water PO	310 ± 71	8.4 ± 0.6	9.7 ± 2.3	20 ± 5	110 ± 1	5.8 ± 1.6	146 ± 0	27 ± 5
120 mg/kg 893 PO	314 ± 44	8.3 ± 0.2	9.9 ± 1.0	20 ± 2	109 ± 1	5.5 ± 0.7	144 ± 1	27 ± 4
240 mg/kg 893 PO	375 ± 77	8.3 ± 0.6	10.7 ± 2.4	17 ± 1	109 ± 2	6.2 ± 1.7	144 ± 2	25 ± 6

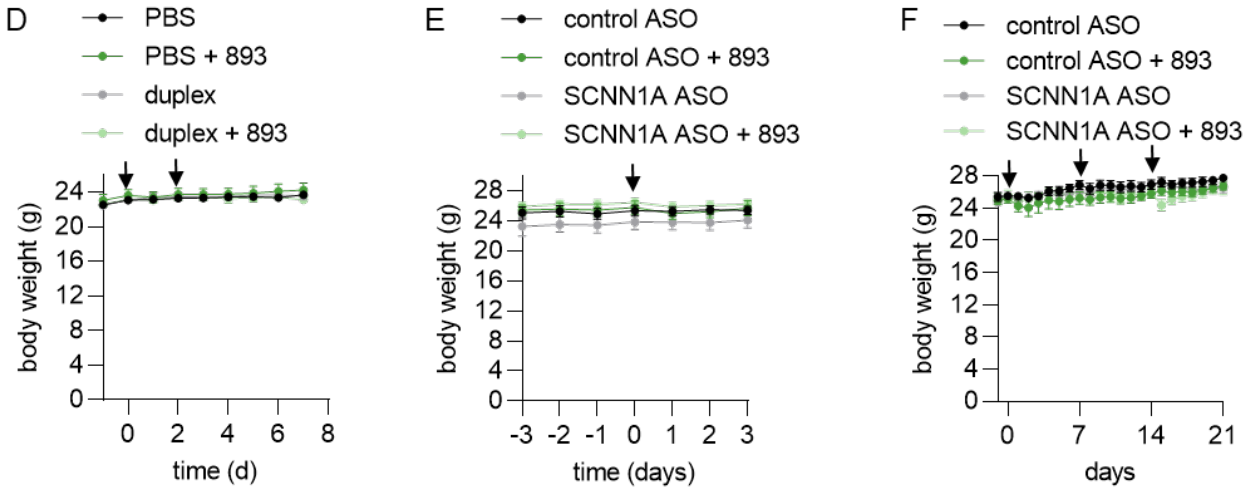

Supplementary Fig. S3.11: Acute toxicity profile of SH-BC-893 in mice. (A) Reference to publication showing toxicity profile of SH-BC-893 in mice treated with SH-BC-893 (120 mg/kg PO) for

11 weeks. **(B)** Reference to publication showing voluntary exercise in mice treated with SH-BC-893 (120 mg/kg PO) every Monday, Wednesday, and Friday for 4 weeks. **(C)** Blood chemistry in nine-week-old male Balbc/J mice treated with SH-BC-893 (120 or 240 mg/kg PO) and sacrificed 24 h after a single dose to look at acute toxicity. Blood was collected by decapitation and serum separated from whole blood after letting clot in a tube with clot activator gel. Mean ± SD shown, n=4-6 mice/group. **(D-F)** Mouse body weights from experiments in Fig. 5 (D), in Fig. 6E (E), and in Fig. 6G (F). Arrows indicate treatment days.

CHAPTER 4

Summary and Conclusions

4.1 Summary of results

The aim of this work was to identify a solution to the critical unmet need within the field of oligonucleotide therapeutics: inefficient delivery to the cytoplasm and nuclei of cells in extrahepatic tissues. We demonstrated that the synthetic sphingolipid analogs SH-BC-893 simultaneously blocks two endolysosomal trafficking pathways (PIKfyve-dependent lysosomal fusion and ARF6-dependent endocytic recycling) thereby resulting in accumulation of endocytosed oligonucleotides within pre-lysosomal compartments that are thought to be more susceptible to endosomal escape.

In Chapter 1 (published in (Finicle et al., 2018)), we show that ARF6-dependent endocytic recycling is blocked by SH-BC-893 and other sphingolipids by following the trafficking of cell surface nutrient transporter proteins. While it has been known for a long time that sphingolipids downregulate nutrient transporter proteins (Barthelemy et al., 2017; Bultynck et al., 2006; Chung et al., 2001; Guenther et al., 2008; Kim et al., 2016; Romero Rosales et al., 2011; Skrzypek et al., 1998; Summers et al., 1998), the molecular mechanism was incompletely defined. Specifically, we demonstrate that sphingolipids block endocytic recycling in mammalian cells by inactivating the small GTPase ARF6. ARF6 inhibition with the small molecules SecinH3 and NAV2729 was sufficient to block endocytic recycling and decrease surface levels of nutrient transporter proteins. Results using chemical inhibitors were validated using genetic approaches. SH-BC-893 and other sphingolipids have been shown to disrupt endolysosomal trafficking downstream of activation of the serine and threonine protein phosphatase 2A (PP2A) (Finicle et

al., 2018; Guenther et al., 2008; Kim et al., 2016; Romero Rosales et al., 2011). ARF6 is activated by its guanine nucleotide exchange factor GRP1 which is in turn activated by Akt-dependent phosphorylation of two residues: serine 255 and threonine 280 (Finicle et al., 2018; Li et al., 2012). We hypothesized that GRP1 could be inactivated by PP2A-dependent dephosphorylation of these residues; this would provide a mechanistic explanation for how PP2A activation by sphingolipids could inactivate ARF6. Indeed, replacing serine 255 and threonine 280 with aspartic acid residues ($GRP1^{DD}$), which would render GRP1 resistant to inactivation by PP2A, restores recycling and surface nutrient transporter expression in SH-BC-893-treated cells (Finicle et al., 2018). Combining this data with our previous work (Kim et al., 2016), we show that SH-BC-893 activates a unique program that simultaneously inhibits PIKfyve-dependent lysosomal fusion and ARF6-dependent endocytic recycling.

In Chapter 2, we further dissect the mechanism by which PP2A activation by sphingolipids SH-BC-893 and ceramide causes defects in intracellular trafficking. In this study, quantitative and kinetic phosphoproteomics was used to identify phosphoproteins that responded differentially to pharmacological compounds that modulate PP2A activity. With this data, our prior knowledge of PP2A-dependent phenotypes produced by these molecules helped to prioritize the large dataset to help us learn about the putative PP2A substrates that are responsible for intracellular trafficking disruption. Time-resolved phosphoproteome analyses of FL5.12 cells treated with the PP2A agonist SH-BC-893 or the PP2A inhibitor LB-100 enabled the identification of putative PP2A substrates. Approximately 75% of the phosphorylation sites (289 out of 384 sites) changed by SH-BC-893 were also changed by LB100 in the opposite direction, further confirming that SH-BC-893 was activating PP2A. A more detailed analysis of the dynamic changes in protein phosphorylation common to LB-100 and SH-BC-893 revealed that 40% of these profiles displayed the expected reciprocal response and could represent putative PP2A

substrates. A significant proportion of these targets are involved in the regulation of actin polymerization, including previously known PP2A substrates. One key finding that stemmed from this work was that SH-BC-893 induced actin polymerization in a PP2A-dependent manner. This finding was interesting because many endolysosomal trafficking events are powered by actin polymerization (Eitzen, 2003; Hong et al., 2015b; Wang et al., 2021, 2016b; Zech et al., 2012). Given that both PIKfyve- and ARF6-dependent trafficking is powered by actin polymerization and dynamics (Boulakirba et al., 2014; Cotton et al., 2007; Hong et al., 2015b; Jackson et al., 2000; Kanamarlapudi, 2014), this finding could provide additional mechanistic insight into sphingolipid- and PP2A-mediated endolysosomal trafficking disruption.

In Chapter 3, we combine the knowledge obtained from the above two chapters and our previously published studies (Finicle et al., 2018; Guenther et al., 2008; Kim et al., 2016; Kubiniok et al., 2019; Romero Rosales et al., 2011) and apply these findings towards the field of oligonucleotide therapeutics. Oligonucleotides in endocytic vesicles are either recycled back to the extracellular space through exocytosis or progress to lysosomes, the degradative compartment of the cell (Crooke et al., 2017; Gökirmak et al., 2021; Grant and Donaldson, 2009). Chemical modifications render therapeutic oligonucleotides resistant to lysosomal nucleases (Dowdy, 2017; Gökirmak et al., 2021; Roberts et al., 2020). Therefore, the majority of endocytosed oligonucleotides accumulate within lysosomes where they are stable but unable to reach their cytosolic targets. This is because the limiting membrane of the lysosome is heavily decorated with glycoproteins (e.g., LAMP1 and LAMP2) and glycolipids that reduce permeability relative to other endocytic structures (Rudnik and Damme, 2021; Wilke et al., 2012).

In the absence of permeabilizing agents, oligonucleotides likely escape from endocytic compartments at sites of membrane fission and fusion (Juliano, 2018; Wagenaar et al., 2015; Wang et al., 2017; Wittrup et al., 2015). During these dynamic membrane remodeling events, the lipid bilayer is deformed to create non-bilayer regions that have increased permeability (Bennett and Tieleman, 2014; Cullis et al., 1986; Renard et al., 2018; Wang et al., 2009; Wickner and Rizo, 2017). Consistent with this model, pre-lysosomal compartments that undergo high rates of vesicle budding and fusion have been identified as sites of oligonucleotide escape (Liang et al., 2020; Linnane et al., 2019; Paramasivam et al., 2022; Wang et al., 2016a). Approaches that increase oligonucleotide uptake and/or residency time in pre-lysosomal compartments where oligonucleotide escape is most efficient could offer significant gains in potency that would make extrahepatic tissues therapeutically accessible.

We hypothesized that SH-BC-893-mediated disruption of ARF6-dependent endocytic recycling and PIKfyve-dependent lysosomal fusion (Finicle et al., 2018; Jayashankar et al., 2021; Kim et al., 2016; Kubiniok et al., 2019) would synergistically increase oligonucleotide accumulation within pre-lysosomal compartments where endosomal release is most efficient and improve activity. In Chapter 3, we demonstrate that the parallel actions of SH-BC-893 on endocytic recycling and lysosomal fusion are necessary and sufficient to increase intracellular oligonucleotide levels in extra-lysosomal compartments and significantly enhance oligonucleotide activity both in vitro and in vivo with no toxicities detected. Importantly, these changes in trafficking are well tolerated as SH-BC-893 is non-toxic at the effective dose even with chronic administration (Finicle et al., 2018; Jayashankar et al., 2021; Kim et al., 2016). More specifically, SH-BC-893 improved ASO activity by 15-fold in the liver and completely sensitized the lungs to systemic delivery of ASOs. SH-BC-893 also sensitized certain areas of

the brain and CNS to systemically delivered cholesterol-functionalized duplexed oligonucleotides.

In sum, our deep understanding of the mechanism by which SH-BC-893 disrupts endolysosomal trafficking (evaluated in Chapters 1 & 2 and in published studies (Finicle et al., 2018; Guenther et al., 2008; Kim et al., 2016; Kubiniok et al., 2019; Romero Rosales et al., 2011)) facilitated our ability to solve the critical delivery barrier for oligonucleotide therapeutics.

4.2 Implications for therapeutics development

ASOs accumulate in the liver and kidney after systemic administration and do not cross the blood brain barrier. Tissues like the lung do not experience enough ASOs for clinical activity to be achieved with systemic administration. SH-BC-893 could render new targets in extrahepatic tissues accessible. For example, SH-BC-893 increased ASO activity in the brainstem and spinal cord with positive trends in the hippocampus. This result is consistent with prior studies showing SH-BC-893 is active in the brain (Jayashankar et al., 2021). Consistent with the high degree of accumulation of SH-BC-893, the lung was almost completely sensitized to two different systemically delivered ASOs by SH-BC-893. While this study utilized systemic ASO delivery, SH-BC-893 should also improve the efficacy of locally administered oligonucleotide therapeutics. Administration of ASOs at the site of action (e.g., intravitreal, intrathecal, or aerosol delivery to the lungs) elevates local concentrations and therefore uptake but does not address the negative effects of ARF6-dependent recycling or PIKfyve-dependent lysosomal fusion on delivery. Therefore, SH-BC-893 may also help with local delivery, especially in the lung. The lung is highly immunogenic and local delivery of oligonucleotides can cause

undesirable lung inflammation (Kumar and Moschos, 2017). Lowering the dose of oligonucleotide could circumvent this problem by reducing the levels of immunogenic oligonucleotides in the lung. Local administration of SH-BC-893 itself along with the oligonucleotide might overcome limitations imposed by the tissue pharmacokinetics of SH-BC-893 by allowing for both molecules to reach the target tissues at the same time. Formulation work would be required to evaluate whether SH-BC-893 could be administered intrathecally or via inhalation along with the oligonucleotide, but local delivery of oligonucleotide and/or SH-BC-893 might further extend the clinical reach of small molecule-mediated potentiation.

SH-BC-893 did not improve ASO activity in all tissues. Despite both ASOs and SH-BC-893 accumulating in the kidney and spleen (Geary, 2009), SH-BC-893 treatment failed to increase activity in these tissues. These results could be due to 1) lower basal levels of ARF6-dependent ASO recycling, 2) reduced PIKfyve-dependent lysosomal fusion, 3) differences in the endocytic trafficking pathways used for oligonucleotide entry in these tissues, and/or 4) failure for SH-BC-893 and/or ASOs to accumulate in the same cell types in these organs. In heart and skeletal muscle, limited potentiation is likely explained by the low concentrations of both SH-BC-893 and ASOs in these tissues (Geary, 2009; Geary et al., 2015). The results reported here offer an important proof of concept, but additional studies will be required to produce a comprehensive inventory of the tissues and cell types that are responsive to SH-BC-893-mediated potentiation with single or repeat oligonucleotide dosing.

SH-BC-893 disrupts both endocytic recycling and lysosomal fusion by activating (Finicle et al., 2018; Kim et al., 2016; Kubiniok et al., 2019). The dopaminergic antagonist perphenazine (PPZ) is structurally distinct from SH-BC-893 but also activates PP2A (Gutierrez et al., 2014; Morita et

al., 2020), inhibits ARF6-dependent endocytic recycling (Finicle et al., 2018), and vacuolates cells similar to PIKfyve inhibitors (Chapter 3). As one would expect based on these activities, PPZ also enhances the intracellular accumulation of ASOs by limiting endocytic recycling, increases the fraction of intracellular ASOs that accumulated outside of lysosomes, and increases ASO activity to a similar extent as SH-BC-893. There are also other small molecules that activate PP2A that also enhance ASO activity (data not shown). This result is important because it not only provides further evidence that PP2A activation is sufficient to enhance ASO activity, but it also provides small molecule alternatives that could be a backup in case there are unexpected pharmacological liabilities that arise during the development of SH-BC-893 as an oligonucleotide potentiator.

While SH-BC-893 slightly increased the activity of the $GalNAc_3$-MALAT1 ASO, it was nowhere near to the extent as it did with unconjugated ASOs. This could be due to many potential reasons. One possibility is that SH-BC-893 alters the steady state localization of ASGPR by inhibiting endocytic recycling, and therefore timing of administration of both molecules must be further optimized. Alternatively, $GalNAc_3$-conjugates could accumulate in pre-lysosomal compartments due to ASGPR trafficking to recycling endosomes. In this case, SH-BC-893-mediated inhibition of lysosomal fusion would not have additional benefit. In a similar line of thinking, SH-BC-893-mediated inhibition of endocytic recycling could have no benefit to $GalNAc_3$-conjugates if intracellular accumulation is already maximal due to ASGPR-facilitated endocytosis. Another attractive model could be that $GalNAc_3$-conjugates preferentially escape from lysosomes. Given that the lysosomal membrane is heavily decorated with glycoproteins and glycolipids, the addition of the GalNAc sugar could benefit interactions with and release from the lysosomal membrane. In sum, it could be one or some combination of the above listed possibilities or additional unanticipated mechanisms that contribute to the lower potentiation

observed with $GalNAc_3$-conjugates and therefore additional studies will be required to fully assess the potential of SH-BC-893 to improve ligand-conjugated oligonucleotide uptake.

The long-term activity of siRNAs (e.g., >6 months of activity from a single dose) is thought to be due to the accumulation of oligonucleotides within lysosomes (Brown et al., 2020). Despite blocking lysosomal delivery, it is unlikely that SH-BC-893 would diminish long-term activity that might be sustained by slow leak of oligonucleotides from lysosomes. This is because SH-BC-893 would only be dosed along with the oligonucleotide. And because a single dose of SH-BC-893 administered with oligonucleotides would be cleared from the body in 24-48 h, the trafficking block would be released and trapped oligonucleotides would progress on towards the lysosome. In addition, long-term activity should track with the level of initial oligonucleotide uptake by target cells, and thus SH-BC-893 may improve knockdown duration by increasing the intracellular amount of oligonucleotide. Future studies dedicated to looking at longevity of oligonucleotide activity are therefore warranted with SH-BC-893.

Going forward, oligonucleotide therapeutics will need to compete with next-generation small molecules that are also capable of hitting what were previously “undruggable” targets (Makurvet, 2021). A potentiator like SH-BC-893 that permits at-home oligonucleotide administration due to its oral bioavailability could improve the ability of oligonucleotide therapeutics to compete with new orally administered alternatives (Paik, 2022). By lowering the required dose, a small molecule potentiator like SH-BC-893 could make expensive oligonucleotide therapeutics accessible to more patients.

Given SH-BC-893 is an established anti-cancer and anti-obesity agent (Jayashankar et al., 2021; Kim et al., 2016), oligonucleotide therapeutics targeting these diseases might be prioritized for assessing the therapeutic value of combination therapy. In this case, SH-BC-893 would not only enhance the activity of the oligonucleotide therapeutic but also have efficacy on its own; the combination of these activities could synergize for treatment of cancer and/or obesity. For example, several oligonucleotides that entered cancer trials failed to reach efficacy benchmarks despite their enormous promise (MacLeod and Crooke, 2017). Because ASOs and siRNAs can target any sequence, these platforms can drug oncoproteins that lack a drug binding pocket (transcription factors, GTPases, splice variants like AR-V7) or non-coding RNAs (lncRNA, miRs, etc) expanding the ability to treat high-value drug targets. SH-BC-893 slows autochthonous prostate tumor growth (Kim et al., 2016) and could be even more effective in combination with the androgen receptor (AR) -targeting ASO that is currently in clinical trials (De Velasco et al., 2019). Given its accumulation in the lung, primary or metastatic lung tumors might also be responsive to an SH-BC-893/ASO combination targeting KRAS (Ross et al., 2017). Other ASOs targeting relevant oncology targets like the histone lysine-N-methyltransferase EZH2 or the transcription factor STAT3 could also benefit by combining with SH-BC-893 treatment (Hong et al., 2015a; Odate et al., 2017; Reilley et al., 2018; Xiao et al., 2018). The oligonucleotide-independent actions of SH-BC-893 on mitochondrial dynamics (Jayashankar et al., 2021) may complement the activities of oligonucleotides designed to treat cancer (Chen and Chan, 2017), non-alcoholic steatohepatitis (NASH) (Friedman et al., 2018), and/or neurodegenerative diseases (Burté et al., 2015; Gökirmak et al., 2021; Jayashankar et al., 2021). In conclusion, the proof-of-concept studies presented here provide a strong rationale for future work exploring the therapeutic value and safety of SH-BC-893 and/or related small molecules as oligonucleotide potentiating agents.

4.3 References

Barthelemy, C., Barry, A.O., Twyffels, L., and André, B. (2017). FTY720-induced endocytosis of yeast and human amino acid transporters is preceded by reduction of their inherent activity and TORC1 inhibition. Sci. Rep. *7*, 13816.

Bennett, W.F.D., and Tieleman, D.P. (2014). The importance of membrane defects-lessons from simulations. Acc. Chem. Res. *47*, 2244–2251.

Boulakirba, S., Macia, E., Partisani, M., Lacas-Gervais, S., Brau, F., Luton, F., and Franco, M. (2014). Arf6 exchange factor EFA6 and endophilin directly interact at the plasma membrane to control clathrin-mediated endocytosis. Proc. Natl. Acad. Sci. USA *111*, 9473–9478.

Brown, C.R., Gupta, S., Qin, J., Racie, T., He, G., Lentini, S., Malone, R., Yu, M., Matsuda, S., Shulga-Morskaya, S., et al. (2020). Investigating the pharmacodynamic durability of GalNAc-siRNA conjugates. Nucleic Acids Res. *48*, 11827–11844.

Bultynck, G., Heath, V.L., Majeed, A.P., Galan, J.-M., Haguenauer-Tsapis, R., and Cyert, M.S. (2006). Slm1 and slm2 are novel substrates of the calcineurin phosphatase required for heat stress-induced endocytosis of the yeast uracil permease. Mol. Cell. Biol. *26*, 4729–4745.

Burté, F., Carelli, V., Chinnery, P.F., and Yu-Wai-Man, P. (2015). Disturbed mitochondrial dynamics and neurodegenerative disorders. Nat. Rev. Neurol. *11*, 11–24.

Chen, H., and Chan, D.C. (2017). Mitochondrial dynamics in regulating the unique phenotypes of cancer and stem cells. Cell Metab. *26*, 39–48.

Chung, N., Mao, C., Heitman, J., Hannun, Y.A., and Obeid, L.M. (2001). Phytosphingosine as a specific inhibitor of growth and nutrient import in Saccharomyces cerevisiae. J. Biol. Chem. *276*, 35614–35621.

Cotton, M., Boulay, P.-L., Houndolo, T., Vitale, N., Pitcher, J.A., and Claing, A. (2007). Endogenous ARF6 interacts with Rac1 upon angiotensin II stimulation to regulate membrane ruffling and cell migration. Mol. Biol. Cell *18*, 501–511.

Crooke, S.T., Wang, S., Vickers, T.A., Shen, W., and Liang, X.-H. (2017). Cellular uptake and trafficking of antisense oligonucleotides. Nat. Biotechnol. *35*, 230–237.

Cullis, P.R., Hope, M.J., and Tilcock, C.P. (1986). Lipid polymorphism and the roles of lipids in membranes. Chem Phys Lipids *40*, 127–144.

Dowdy, S.F. (2017). Overcoming cellular barriers for RNA therapeutics. Nat. Biotechnol. *35*, 222–229.

Eitzen, G. (2003). Actin remodeling to facilitate membrane fusion. Biochim. Biophys. Acta *1641*, 175–181.

Finicle, B.T., Ramirez, M.U., Liu, G., Selwan, E.M., McCracken, A.N., Yu, J., Joo, Y., Nguyen, J., Ou, K., Roy, S.G., et al. (2018). Sphingolipids inhibit endosomal recycling of nutrient transporters by inactivating ARF6. J. Cell Sci. *131*.

Friedman, S.L., Neuschwander-Tetri, B.A., Rinella, M., and Sanyal, A.J. (2018). Mechanisms of NAFLD development and therapeutic strategies. Nat. Med. *24*, 908–922.

Geary, R.S. (2009). Antisense oligonucleotide pharmacokinetics and metabolism. Expert Opin Drug Metab Toxicol *5*, 381–391.

Geary, R.S., Norris, D., Yu, R., and Bennett, C.F. (2015). Pharmacokinetics, biodistribution and cell uptake of antisense oligonucleotides. Adv. Drug Deliv. Rev. *87*, 46–51.

Gökirmak, T., Nikan, M., Wiechmann, S., Prakash, T.P., Tanowitz, M., and Seth, P.P. (2021). Overcoming the challenges of tissue delivery for oligonucleotide therapeutics. Trends Pharmacol. Sci. *42*, 588–604.

Grant, B.D., and Donaldson, J.G. (2009). Pathways and mechanisms of endocytic recycling. Nat. Rev. Mol. Cell Biol. *10*, 597–608.

Guenther, G.G., Peralta, E.R., Rosales, K.R., Wong, S.Y., Siskind, L.J., and Edinger, A.L. (2008). Ceramide starves cells to death by downregulating nutrient transporter proteins. Proc. Natl. Acad. Sci. USA *105*, 17402–17407.

Gutierrez, A., Pan, L., Groen, R.W.J., Baleydier, F., Kentsis, A., Marineau, J., Grebliunaite, R., Kozakewich, E., Reed, C., Pflumio, F., et al. (2014). Phenothiazines induce PP2A-mediated apoptosis in T cell acute lymphoblastic leukemia. J. Clin. Invest. *124*, 644–655.

Hong, D., Kurzrock, R., Kim, Y., Woessner, R., Younes, A., Nemunaitis, J., Fowler, N., Zhou, T., Schmidt, J., Jo, M., et al. (2015a). AZD9150, a next-generation antisense oligonucleotide inhibitor of STAT3 with early evidence of clinical activity in lymphoma and lung cancer. Sci. Transl. Med. *7*, 314ra185.

Hong, N.H., Qi, A., and Weaver, A.M. (2015b). PI(3,5)P2 controls endosomal branched actin dynamics by regulating cortactin-actin interactions. J. Cell Biol. *210*, 753–769.

Jackson, T.R., Brown, F.D., Nie, Z., Miura, K., Foroni, L., Sun, J., Hsu, V.W., Donaldson, J.G., and Randazzo, P.A. (2000). ACAPs are arf6 GTPase-activating proteins that function in the cell periphery. J. Cell Biol. *151*, 627–638.

Jayashankar, V., Selwan, E., Hancock, S.E., Verlande, A., Goodson, M.O., Eckenstein, K.H., Milinkeviciute, G., Hoover, B.M., Chen, B., Fleischman, A.G., et al. (2021). Drug-like sphingolipid SH-BC-893 opposes ceramide-induced mitochondrial fission and corrects diet-induced obesity. EMBO Mol. Med. *13*, e13086.

Juliano, R.L. (2018). Intracellular trafficking and endosomal release of oligonucleotides: what we know and what we don’t. Nucleic Acid Ther. *28*, 166–177.

Kanamarlapudi, V. (2014). Exchange factor EFA6R requires C-terminal targeting to the plasma membrane to promote cytoskeletal rearrangement through the activation of ADP-ribosylation factor 6 (ARF6). J. Biol. Chem. *289*, 33378–33390.

Kim, S.M., Roy, S.G., Chen, B., Nguyen, T.M., McMonigle, R.J., McCracken, A.N., Zhang, Y., Kofuji, S., Hou, J., Selwan, E., et al. (2016). Targeting cancer metabolism by simultaneously disrupting parallel nutrient access pathways. J. Clin. Invest. *126*, 4088–4102.

Kubiniok, P., Finicle, B.T., Piffaretti, F., McCracken, A.N., Perryman, M., Hanessian, S., Edinger, A.L., and Thibault, P. (2019). Dynamic Phosphoproteomics Uncovers Signaling Pathways Modulated by Anti-oncogenic Sphingolipid Analogs. Mol. Cell Proteomics *18*, 408–422.

Kumar, M., and Moschos, S.A. (2017). Oligonucleotide therapies for the lung: ready to return to the clinic? Mol. Ther. *25*, 2604–2606.

Li, J., Malaby, A.W., Famulok, M., Sabe, H., Lambright, D.G., and Hsu, V.W. (2012). Grp1 plays a key role in linking insulin signaling to glut4 recycling. Dev. Cell *22*, 1286–1298.

Liang, X.-H., Sun, H., Hsu, C.-W., Nichols, J.G., Vickers, T.A., De Hoyos, C.L., and Crooke, S.T. (2020). Golgi-endosome transport mediated by M6PR facilitates release of antisense oligonucleotides from endosomes. Nucleic Acids Res. *48*, 1372–1391.

Linnane, E., Davey, P., Zhang, P., Puri, S., Edbrooke, M., Chiarparin, E., Revenko, A.S., Macleod, A.R., Norman, J.C., and Ross, S.J. (2019). Differential uptake, kinetics and mechanisms of intracellular trafficking of next-generation antisense oligonucleotides across human cancer cell lines. Nucleic Acids Res. *47*, 4375–4392.

MacLeod, A.R., and Crooke, S.T. (2017). RNA therapeutics in oncology: advances, challenges, and future directions. J. Clin. Pharmacol. *57 Suppl 10*, S43–S59.

Makurvet, F.D. (2021). Biologics vs. small molecules: Drug costs and patient access. Medicine in Drug Discovery *9*, 100075.

Morita, K., He, S., Nowak, R.P., Wang, J., Zimmerman, M.W., Fu, C., Durbin, A.D., Martel, M.W., Prutsch, N., Gray, N.S., et al. (2020). Allosteric activators of protein phosphatase 2A display broad antitumor activity mediated by dephosphorylation of MYBL2. Cell *181*, 702–715.e20.

Odate, S., Veschi, V., Yan, S., Lam, N., Woessner, R., and Thiele, C.J. (2017). Inhibition of STAT3 with the Generation 2.5 Antisense Oligonucleotide, AZD9150, Decreases Neuroblastoma Tumorigenicity and Increases Chemosensitivity. Clin. Cancer Res. *23*, 1771–1784.

Paik, J. (2022). Risdiplam: A review in spinal muscular atrophy. CNS Drugs *36*, 401–410.

Paramasivam, P., Franke, C., Stöter, M., Höijer, A., Bartesaghi, S., Sabirsh, A., Lindfors, L., Arteta, M.Y., Dahlén, A., Bak, A., et al. (2022). Endosomal escape of delivered mRNA from endosomal recycling tubules visualized at the nanoscale. J. Cell Biol. *221*.

Reilley, M.J., McCoon, P., Cook, C., Lyne, P., Kurzrock, R., Kim, Y., Woessner, R., Younes, A., Nemunaitis, J., Fowler, N., et al. (2018). STAT3 antisense oligonucleotide AZD9150 in a subset of patients with heavily pretreated lymphoma: results of a phase 1b trial. J. Immunother. Cancer *6*, 119.

Renard, H.-F., Johannes, L., and Morsomme, P. (2018). Increasing diversity of biological membrane fission mechanisms. Trends Cell Biol. *28*, 274–286.

Roberts, T.C., Langer, R., and Wood, M.J.A. (2020). Advances in oligonucleotide drug delivery. Nat. Rev. Drug Discov. *19*, 673–694.

Romero Rosales, K., Singh, G., Wu, K., Chen, J., Janes, M.R., Lilly, M.B., Peralta, E.R., Siskind, L.J., Bennett, M.J., Fruman, D.A., et al. (2011). Sphingolipid-based drugs selectively kill cancer cells by down-regulating nutrient transporter proteins. Biochem. J. *439*, 299–311.

Ross, S.J., Revenko, A.S., Hanson, L.L., Ellston, R., Whalley, N., Pandey, S.K., Revill, M., Rooney, C., Buckett, K., Klein, S.K., et al. (2017). Targeting KRAS dependent tumors with AZD4785 , a high-affinity therapeutic antisense oligonucleotide inhibitor of KRAS. Sci Trans Med *5253*, 1–14.

Rudnik, S., and Damme, M. (2021). The lysosomal membrane-export of metabolites and beyond. FEBS J. *288*, 4168–4182.

Skrzypek, M.S., Nagiec, M.M., Lester, R.L., and Dickson, R.C. (1998). Inhibition of amino acid transport by sphingoid long chain bases in Saccharomyces cerevisiae. J. Biol. Chem. *273*, 2829–2834.

Summers, S.A., Garza, L.A., Zhou, H., and Birnbaum, M.J. (1998). Regulation of insulin-stimulated glucose transporter GLUT4 translocation and Akt kinase activity by ceramide. Mol. Cell. Biol. *18*, 5457–5464.

De Velasco, M.A., Kura, Y., Sakai, K., Hatanaka, Y., Davies, B.R., Campbell, H., Klein, S., Kim, Y., MacLeod, A.R., Sugimoto, K., et al. (2019). Targeting castration-resistant prostate cancer with androgen receptor antisense oligonucleotide therapy. JCI Insight *4*.

Wagenaar, T.R., Tolstykh, T., Shi, C., Jiang, L., Zhang, J., Li, Z., Yu, Q., Qu, H., Sun, F., Cao, H., et al. (2015). Identification of the endosomal sorting complex required for transport-I (ESCRT-I) as an important modulator of anti-miR uptake by cancer cells. Nucleic Acids Res. *43*, 1204–1215.

Wang, D., Ye, Z., Wei, W., Yu, J., Huang, L., Zhang, H., and Yue, J. (2021). Capping protein regulates endosomal trafficking by controlling F-actin density around endocytic vesicles and recruiting RAB5 effectors. Elife *10*.

Wang, S., Sun, H., Tanowitz, M., Liang, X.-H., and Crooke, S.T. (2016a). Annexin A2 facilitates endocytic trafficking of antisense oligonucleotides. Nucleic Acids Res. *44*, 7314–7330.

Wang, S., Sun, H., Tanowitz, M., Liang, X.-H., and Crooke, S.T. (2017). Intra-endosomal trafficking mediated by lysobisphosphatidic acid contributes to intracellular release of phosphorothioate-modified antisense oligonucleotides. Nucleic Acids Res. *45*, 5309–5322.

Wang, T., Smith, E.A., Chapman, E.R., and Weisshaar, J.C. (2009). Lipid mixing and content release in single-vesicle, SNARE-driven fusion assay with 1-5 ms resolution. Biophys. J. *96*, 4122–4131.

Wang, X., Galletta, B.J., Cooper, J.A., and Carlsson, A.E. (2016b). Actin-Regulator Feedback Interactions during Endocytosis. Biophys. J. *110*, 1430–1443.

Wickner, W., and Rizo, J. (2017). A cascade of multiple proteins and lipids catalyzes membrane fusion. Mol. Biol. Cell *28*, 707–711.

Wilke, S., Krausze, J., and Büssow, K. (2012). Crystal structure of the conserved domain of the DC lysosomal associated membrane protein: implications for the lysosomal glycocalyx. BMC Biol. *10*, 62.

Wittrup, A., Ai, A., Liu, X., Hamar, P., Trifonova, R., Charisse, K., Manoharan, M., Kirchhausen, T., and Lieberman, J. (2015). Visualizing lipid-formulated siRNA release from endosomes and target gene knockdown. Nat. Biotechnol. *33*, 870–876.

Xiao, L., Tien, J.C., Vo, J., Tan, M., Parolia, A., Zhang, Y., Wang, L., Qiao, Y., Shukla, S., Wang, X., et al. (2018). Epigenetic Reprogramming with Antisense Oligonucleotides Enhances the Effectiveness of Androgen Receptor Inhibition in Castration-Resistant Prostate Cancer. Cancer Res. *78*, 5731–5740.

Zech, T., Calaminus, S.D.J., and Machesky, L.M. (2012). Actin on trafficking: could actin guide directed receptor transport? Cell Adh Migr *6*, 476–481.